

Diversity of the crustal structure in the northern Baffin Bay and the southern Nares Strait

Dissertation

zur Erlangung des Grades Dr. rer. nat.
vorgelegt dem Fachbereich Geowissenschaften
der Universität Bremen

vorgelegt von
Tabea Altenbernd



1. Gutachter: Prof. Dr. Wilfried Jokat

2. Gutachter: Prof. Dr. Cornelia Spiegel

Abgabe der Arbeit: 03.07.2015

Datum Promotionskolloquium: 09.11.2015

Erklärung

Hiermit versichere ich,

Tabea Altenbernd,

wohnhaft in der Bürgermeister-Smidt-Straße 112,

27568 Bremerhaven,

dass ich

- a) die vorliegende Arbeit ohne fremde Hilfe angefertigt habe,
- b) keine anderen als die von mir angegebenen Quellen und Hilfsmittel verwendet habe,
- c) die den benutzten Werken wörtlich oder inhaltlich entnommenen Stellen als solche kenntlich gemacht habe.

Bremerhaven, den 01.07.2015

Zusammenfassung

Die Baffin-Bucht und Nares-Straße liegen zwischen Grönland und Kanada. Obwohl die Region eine der ersten Beispiele für den Kontinentalaufbruch war, wird ihre Entstehung und Krustenstruktur noch heute diskutiert.

Von der Baffin-Bucht wird angenommen, daß sie die nördliche Fortsetzung des erloschenen Spreizungssystem der Labradorsee darstellt. Dennoch sind eindeutige magnetische Anomalien, welche die räumliche Ausdehnung und das Alter der ozeanischen Kruste in der Labradorsee belegen, in der Baffin-Bucht nicht vorhanden. In letzter Zeit akquirierte, moderne geophysikalische Datensätze enthüllten die Krustenstruktur der südlichen Baffin-Bucht und bestätigten, dass die Region von ozeanischer Kruste unterlagert ist. Allerdings ist die Krustenstruktur und der Kontinentalrandtyp der nördlichen Baffin-Bucht und südlichen Nares-Straße weiterhin umstritten, da hier bislang nur wenige moderne geophysikalische Daten erhoben wurden. Aussagen über die Ausdehnung von Krustentypen basieren auf wenigen Sonobojendaten, Schweredaten, reflexionsseismischen Profilen und plattenkinematische Modellierungen.

Um die strukturelle und tektonische Entwicklung zu verstehen wurden geophysikalische und geologische Untersuchungen im grönländischen Teil der Baffin-Bucht während einer Forschungsreise an Bord der FS Polarstern im Jahr 2010 durchgeführt. Unter anderem wurden drei refraktionsseismische Profile, dazugehörige reflexionsseismische Profile und Schweredatensätze in der Melville-Bucht, der nordöstlichen Baffin-Bucht sowie der südlichen Nares-Straße erhoben. Auf Grundlage dieser Datensätze wurden *P*-Wellen-Geschwindigkeits-, Dichte-, und geologische Modelle erstellt, die ich in dieser Doktorarbeit vorstellen werde. Aufgrund der Modelle kann ich die Krustenstruktur des Untersuchungsgebietes in der nordöstlichen Baffin-Bucht und südlichen Nares-Straße untersuchen. Durch Bestimmung der auftretenden Krustentypen und ihre Ausdehnung kann ich einen Beitrag zur Entwicklung der untersuchten Gebiete leisten. Des weiteren untersuche ich den Kontinentalrandtyp und die Verfüllung der tiefen Becken in der Melville-Bucht. Zusätzlich werde ich meine Ergebnisse mit früheren Modellen über die Krustenstruktur der Gegend vergleichen.

Meine Ergebnisse bestätigen, dass eine 3.5–7 km mächtige, von bis zu 6.5 km mächtigen Sedimenten überlagerte, ozeanische Kruste im zentralen Teil der nördlichen Baffin-Bucht vorhanden ist. Die teilweise geringe Mächtigkeit der Kruste und der unterlagernde, serpentinierte obere Mantel sind Hinweise für langsame bis sehr langsame Spreizungsraten während der Entstehung der ozeanischen Kruste.

Eine bis zu 80 km weite Kontinent-Ozean-Übergangszone trennt ozeanische von der kontinentalen Kruste. Die Kontinent-Ozean-Übergangszone in der Melville-Bucht Region wurde von intrusiven und extrusiven Magmatismus beeinflusst, während die Kontinent-Ozean-Übergangszone in der südlichen Nares-Straße keinerlei Anzeichen für magmatische Aktivität aufweist. Daher kann der Kontinentalrand in der südlichen Nares-Straße als nicht-vulkanisch klassifiziert werden. Der Kontinentalrand westlich der Melville-Bucht kann am ehesten als gerifteter Kontinentalrand mit nach Norden hin abnehmendem Einfluss von Magmatismus beschrieben werden, da klare Anzeichen für eine Klassifizierung als vulkanischer oder nicht vulkanischer Kontinentalrand fehlen.

Die bis zu dreilagige, kristalline kontinentale Kruste hat eine maximale Mächtigkeit von 30 km und ist teilweise von Sedimenten bedeckt. Tiefe Störungen und Becken charakterisieren die Region der Melville-Bucht. Zwei parallel verlaufende Profile in der nördlichen und südlichen Melville-Bucht enthüllen Änderungen in der Krustengeometrie und der Beckenverfüllung und weisen daher auf Unterschiede in der Entwicklung beider Gebiete hin.

Ein Vergleich meiner Ergebnisse mit vorherigen Studien über die räumliche Ausdehnung von Krustentypen zeigt, dass das Ausmaß der Kontinent-Ozean-Übergangszone und teilweise auch die Ausdehnung der ozeanischen Kruste in der nordöstlichen Baffin-Bucht bislang unterschätzt wurde.

Summary

The Baffin Bay and the Nares Strait are situated between Canada and Greenland. Although the regions were among the first subjects for scientist to study continental breakup, their genesis and crustal structure is still under discussion. The Baffin Bay is believed to be the northern prolongation of the extinct spreading system of the Labrador Sea. But clear magnetic spreading anomalies, which constrain the extent and age of oceanic crust in the Labrador Sea, are missing in the Baffin Bay. Recently acquired modern geophysical datasets revealed the crustal structure of the southern Baffin Bay and additionally confirmed that the region is underlain by oceanic crust. However, the crustal structure or type of margin in the northern Baffin Bay and southern Nares Strait is still controversial, because only sparse modern geophysical data have been acquired in this area. Statements about the extent of crustal types are based on few sonobuoy recordings, gravity data, reflection seismic profiles and plate kinematic modeling.

To reveal is structural and tectonic evolution, geophysical and geological investigations were conducted in the Greenlandic part of the Baffin Bay during a research cruise aboard RV Polarstern in 2010. Amongst others, three refraction seismic profiles and corresponding reflection- and gravity datasets were acquired in the Melville Bay area, the northeastern Baffin Bay and the southern Nares Strait. In this study I will present *P* wave velocity, density and geological models derived from raytracing, modeling and interpretation of these datasets. This allows me to study the crustal structure of my research area in northeastern Baffin Bay and southern Nares Strait. I will also classify the crustal types and map their extent, and thereby contribute information to the genesis of the study area. Furthermore, the type of margin and the infill of the deep basins in Melville Bay are investigated. I will also set my results in context with previous models on the crustal structure of the area.

My findings confirm that a 3.5–7 km thick oceanic crust is present in central northern Baffin Bay, which is covered by up to 6.5 km thick sediments. The partly small thickness of the crust and the underlying serpentinized upper mantle are indications for slow to ultraslow spreading rates during the formation of the oceanic crust.

An up to 80 km wide continent-ocean transition zone separates the oceanic crust from stretched and rifted continental crust. The continent-ocean transition in the Melville Bay area has been affected by intrusive and extrusive magmatism, while the transition between continental and oceanic crust in the southern Nares Strait does not show any signs of magmatic activity. Therefore, the margin in the southern Nares Strait can be classified as non-volcanic rifted margin. The margin west of the Melville Bay area can be described as rifted margins with decreasing influence of magmatism towards the north, since clear indications for a classification as non-volcanic or volcanic margins are missing.

The up to three-layered crystalline continental crust has a maximum thickness of 30 km and is partly covered by sediments. Steep faults and deep basins characterize the Melville Bay area. Two parallel extending profiles in northern and southern Melville Bay revealed changes in the crustal geometry as well as in basin infill and therefore indicate differences in the genesis of both regions.

A comparison of my results on the extent of crustal types in the research area with previous studies shows that the extent of the continent-ocean transition

and partly also the eastern extent of oceanic crust were underestimated in the northeastern Baffin Bay.

CONTENT

1	Introduction	1
1.1	Motivation.....	1
1.2	Geology and geophysical investigations in the Baffin Bay, Labrador Sea and Nares Strait	3
1.3	Outline and aim of this thesis.....	8
1.4	Central questions	8
2	Methods, data acquisition and processing	11
2.1	Data acquisition in the Baffin Bay	11
2.2	Seismics	12
2.2.1	Acquisition of refraction seismic data offshore.....	12
2.2.2	Processing of refraction seismic data	14
2.2.3	Phase determination and modeling of refraction seismic data	14
2.3	Gravity data	17
2.3.1	Acquisition and processing	17
2.3.1	Density Modeling	17
3	Contributions to scientific journals	19
3.1	A crustal model for northern Melville Bay, Baffin Bay	19
3.2	Insights in the crustal structure of the transition between Nares Strait and Baffin Bay	19
3.3	The crustal fabric of the northeastern Baffin Bay.....	20
4	A crustal model for northern Melville Bay, Baffin Bay	21
4.1	Abstract	21
4.2	Introduction.....	21
4.3	Geological setting	24
4.4	Data acquisition and data processing	26
4.4.1	Seismic refraction data.....	26
4.4.2	Gravity data.....	26
4.5	Modeling.....	26
4.5.1	Seismic refraction data.....	26
4.5.1.1	Error analysis and model uncertainty of the velocity model.....	30
4.5.2	Gravity data.....	35
4.6	Results and interpretation of crustal units	37
4.6.1	Velocity model of AWI-20100200	37
4.6.1.1	Oceanic crust (km 0–80).....	37
4.6.1.2	Continent-ocean transition (km 80–140).....	39
4.6.1.3	Rifted continental crust (km 140–321).....	40
4.6.2	Density model.....	41
4.7	Discussion.....	42
4.7.1	Continental crust.....	42
4.7.2	Continent-ocean transition.....	43
4.7.3	Oceanic crust.....	44
4.8	Conclusions	47
4.9	Acknowledgments.....	48
4.10	References.....	48
5	Insights into the crustal structure of the northern transition between Nares Strait and Baffin Bay	53
5.1	Abstract	53
5.2	Introduction	53
5.3	Geological setting	55
5.3.1	Regional geology of southern Nares Strait and Northern Baffin Bay.....	56

5.4	Data acquisition and processing.....	57
5.4.1	Seismic data	57
5.4.2	Gravity data.....	59
5.5	Modeling of seismic refraction data	60
5.5.1	Model uncertainty and error analysis	63
5.6	Results	66
5.6.1	Velocity model	66
5.6.1.1	Sedimentary layers and Thule Supergroup.....	67
5.6.1.2	Continental crust (km 0–200)	68
5.6.1.3	Oceanic crust (km 270–399)	68
5.6.1.4	Continent-ocean transition zone (km 200–270).....	69
5.6.2	Density model	70
5.7	Discussion.....	70
5.7.1	Intersection with line 3 (continental crust).....	72
5.7.2	Intersection with AWI-20100200 (oceanic crust)	73
5.7.3	Comparison with profile 91/3 of Jackson and Reid (1994).....	73
5.7.4	Crustal structure and origin of thin oceanic crust.....	73
5.7.5	COT and margin.....	76
5.8	Conclusions	77
5.9	Acknowledgements	78
5.10	References	78
6	The crustal fabric of the northeastern Baffin Bay	81
6.1	Abstract	81
6.2	Introduction.....	81
6.3	Geological setting of Baffin Bay and Melville Bay	82
6.4	Data acquisition and processing.....	85
6.5	Modeling	89
6.5.1	<i>P</i> wave velocity model	89
6.5.1.1	Ray coverage, resolution and uncertainty analysis	90
6.5.2	Density model	96
6.6	Results and interpretation	96
6.6.1	Oceanic crust (km 0–57)	97
6.6.2	COT (km 57–135)	99
6.6.3	Continental crust (km 135–270)	100
6.7	Discussion.....	101
6.7.1	Intersection with profile AWI-20100400	101
6.7.2	Comparison with the northern Melville Bay (AWI-20100200)	103
6.7.3	COT.....	105
6.7.4	Margin of the northeastern Melville Bay	105
6.7.5	Oceanic crust and upper mantle	107
6.7.6	Crustal units in the northeastern Baffin Bay	110
6.8	Conclusion	110
6.9	Acknowledgements	111
6.10	References	111
7	Conclusion.....	115
8	Outlook.....	117
	Bibliography.....	120
	Appendix	127
	Danksagung.....	197
	Curriculum Vitae	199

List of Figures

Figure 1.1: Bathymetry of the Labrador Sea, Baffin Bay and Davis Strait	1
Figure 1.2: Movement of North America relative to Greenland (Taylor, 1910).	2
Figure 1.3: Modified cutout of a map of Wegener (1915) showing continental plate boundaries.	3
Figure 1.4: Offshore Geology of Baffin Bay and adjacent regions, modified after Oakey and Chalmers (2012).	4
Figure 1.5: Movement of the Greenland Plate relative to the North American Plate	5
Figure 1.6: Geology of the Nares Strait and position of the Wegener Fault.	7
Figure 2.1: Investigated area in the Greenlandic part of Baffin Bay and Nares Strait.	11
Figure 2.2: Bathymetry and position of the three refraction seismic profiles in the research area.	12
Figure 2.3: A LOBSTER OBS and its components (Damm, 2010).	13
Figure 2.4: Acquisition of wide-angle seismic data	13
Figure 2.5: Examples for a seismic section, picked phases and <i>P</i> wave velocity modeling.	16
Figure 4.1: Bathymetric map of the Baffin Bay.	22
Figure 4.2: Geological map of the Baffin Bay, Davis Strait, and Labrador Sea.	23
Figure 4.3: Seismic sections, picked phases, and modeled raypaths of OBS 5.	27
Figure 4.4: Seismic sections, picked phases, and modeled raypaths of OBS 11.	28
Figure 4.5: Seismic sections, picked phases, and modeled raypaths of OBS 17.	29
Figure 4.6: Seismic sections, picked phases, and modeled raypaths of OBS 21.	30
Figure 4.7: Seismic sections, picked phases, and modeled raypaths of OBS 23.	31
Figure 4.8: Seismic reflection profile BGR10-302.	32
Figure 4.9: <i>P</i> wave velocity model and geological interpretation of AWI-20100200.	33
Figure 4.10: Reflected rays at the base of velocity layer 3 to 9.	34
Figure 4.11: Ray coverage of velocity layer 2 to 10.	35
Figure 4.12: Diagonal values of the resolution matrix of the <i>P</i> wave velocity model.	36
Figure 4.13: Gravity modeling along profile AWI-20100200.	37
Figure 4.14: Velocity-depth profiles from AWI-20100200, compared with typical Atlantic oceanic crust.	39
Figure 4.15: Spreading rate vs. crustal thickness.	45
Figure 4.16: Comparison between the extent of crustal units after Oakey and Chalmers (2012) and this study	47
Figure 5.1: Overview, bathymetry and free-air gravity of the region of interest.	54

Figure 5.2: Geological provinces and offshore geology of northern Baffin Bay and southern Nares Strait.....	55
Figure 5.3: Reflection seismic data along AWI-20100300.....	58
Figure 5.4: Parts of the recorded seismogram section, picked signals and modeled raypaths for OBS 1.....	59
Figure 5.5: Parts of the recorded seismogram section, picked signals and modeled raypaths for OBS 4.....	60
Figure 5.6: Parts of the recorded seismogram section, picked signals and modeled raypaths for OBS 12.....	61
Figure 5.7: Parts of the recorded seismogram section, picked signals and modeled raypaths for OBS 24.....	62
Figure 5.8: Parts of the recorded seismogram section, picked signals and modeled raypaths for OBS 27.....	63
Figure 5.9: <i>P</i> wave velocity model, resolution and geological interpretation of AWI-20100300.....	64
Figure 5.10: Ray coverage for different velocity layers of the <i>P</i> wave velocity model.....	65
Figure 5.11: Comparison of velocity-depth-functions from AWI-20100300 with normal oceanic crust.....	69
Figure 5.12: Gravity modeling along AWI-20100300.....	71
Figure 5.13: Velocity-depth profiles at the intersections between AWI-20100300, line 3 and AWI-20100200.....	72
Figure 5.14: Comparison between AWI-20100300 and profile 91/3.....	74
Figure 5.15: Comparison between the distribution of crustal types.....	75
Figure 6.1: Geological map of the Baffin Bay.....	82
Figure 6.2: Bathymetry and free-air gravity anomalies in the Melville Bay area.....	84
Figure 6.3: Western and eastern part of reflection seismic profile BGR10-311.....	86
Figure 6.4: Parts of the seismic section, picked signals, and modeled raypaths for OBS 1.....	87
Figure 6.5: Parts of the seismic section, picked signals and modeled raypaths for OBS 2.....	88
Figure 6.6: Parts of the seismic section, picked signals and modeled raypaths for OBS 6.....	89
Figure 6.7: Parts of the seismic section, picked signals and modeled raypaths for OBS 10.....	90
Figure 6.8: Parts of the seismic section, picked signals and modeled raypaths for OBS 11.....	91
Figure 6.9: Parts of the seismic section, picked signals and modeled raypaths for OBS 12.....	92
Figure 6.10: <i>P</i> wave velocity model, resolution matrix and geological interpretation of AWI-20100450.....	94
Figure 6.11: Ray coverage of the <i>P</i> wave velocity model.....	95
Figure 6.12: Density model of AWI-20100450.....	97
Figure 6.13: Comparison of velocity-depth functions from AWI-20100450 with typical Atlantic oceanic crust.....	98
Figure 6.14: Velocity-depth-profiles at the intersection between AWI-20100450 and AWI-20100400.....	102
Figure 6.15: Refraction seismic profile AWI-20100200.....	103

Figure 6.16: Comparison of oceanic crust from AWI-20100450 with oceanic crust in northern and southern Baffin Bay..	107
Figure 6.17: Distribution of crustal types in Baffin Bay.....	109
Figure 8.1: Geological map, modified after Oakey and Chalmers (2012), with proposed location of new refraction seismic profiles.	118
Figure A.1: Seismic section, picks and modeled raypaths of OBS 1 (AWI- 20100200)	127
Figure A.2: Seismic section, picks and modeled raypaths of OBS 2 (AWI- 20100200)	128
Figure A.3: Seismic section, picks and modeled raypaths of OBS 3 (AWI- 20100200)	129
Figure A.4: Seismic section, picks and modeled raypaths of OBS 4 (AWI- 20100200)	130
Figure A.5: Seismic section, picks and modeled raypaths of OBS 5 (AWI- 20100200)	131
Figure A.6: Seismic section, picks and modeled raypaths of OBS 6 (AWI- 20100200)	132
Figure A.7: Seismic section, picks and modeled raypaths of OBS 7 (AWI- 20100200)	133
Figure A.8: Seismic section, picks and modeled raypaths of OBS 8 (AWI- 20100200)	134
Figure A.9: Seismic section, picks and modeled raypaths of OBS 9 (AWI- 20100200)	135
Figure A.10: Seismic section, picks and modeled raypaths of OBS 10 (AWI- 20100200)	136
Figure A.11: Seismic section, picks and modeled raypaths of OBS 11 (AWI- 20100200)	137
Figure A.12: Seismic section, picks and modeled raypaths of OBS 12 (AWI- 20100200)	138
Figure A.13: Seismic section, picks and modeled raypaths of OBS 13 (AWI- 20100200)	139
Figure A.14: Seismic section, picks and modeled raypaths of OBS 14 (AWI- 20100200)	140
Figure A.15: Seismic section, picks and modeled raypaths of OBS 15 (AWI- 20100200)	141
Figure A.16: Seismic section, picks and modeled raypaths of OBS 16 (AWI- 20100200)	142
Figure A. 17: Seismic section, picks and modeled raypaths of OBS 17 (AWI- 20100200)	143
Figure A.18: Seismic section, picks and modeled raypaths of OBS 18 (AWI- 20100200)	144
Figure A.19: Seismic section, picks and modeled raypaths of OBS 19 (AWI- 20100200)	145
Figure A.20: Seismic section, picks and modeled raypaths of OBS 20 (AWI- 20100200)	146
Figure A.21: Seismic section, picks and modeled raypaths of OBS 21 (AWI- 20100200)	147
Figure A.22: Seismic section, picks and modeled raypaths of OBS 22 (AWI- 20100200)	148

Figure A.23: Seismic section, picks and modeled raypaths of OBS 23 (AWI-20100200).....	149
Figure A.24: Seismic section, picks and modeled raypaths of OBS 24 (AWI-20100200).....	150
Figure A.25: Seismic section, picks and modeled raypaths of OBS 25 (AWI-20100200).....	151
Figure B.1: Seismic section, picks and modeled raypaths of OBS 1 (AWI-20100300).....	152
Figure B.2: Seismic section, picks and modeled raypaths of OBS 2 (AWI-20100300).....	153
Figure B.3: Seismic section, picks and modeled raypaths of OBS 3 (AWI-20100300).....	154
Figure B.4: Seismic section, picks and modeled raypaths of OBS 4 (AWI-20100300).....	155
Figure B.5: Seismic section, picks and modeled raypaths of OBS 5 (AWI-20100300).....	156
Figure B.6: Seismic section, picks and modeled raypaths of OBS 6 (AWI-20100300).....	157
Figure B.7: Seismic section, picks and modeled raypaths of OBS 7 (AWI-20100300).....	158
Figure B.8: Seismic section, picks and modeled raypaths of OBS 8 (AWI-20100300).....	159
Figure B.9: Seismic section, picks and modeled raypaths of OBS 9 (AWI-20100300).....	160
Figure B.10: Seismic section, picks and modeled raypaths of OBS 10 (AWI-20100300).....	161
Figure B.11: Seismic section, picks and modeled raypaths of OBS 11 (AWI-20100300).....	162
Figure B.12: Seismic section, picks and modeled raypaths of OBS 12 (AWI-20100300).....	163
Figure B.13: Seismic section, picks and modeled raypaths of OBS 14 (AWI-20100300).....	164
Figure B.14: Seismic section, picks and modeled raypaths of OBS 15 (AWI-20100300).....	165
Figure B.15: Seismic section, picks and modeled raypaths of OBS 16 (AWI-20100300).....	166
Figure B.16: Seismic section, picks and modeled raypaths of OBS 17 (AWI-20100300).....	167
Figure B.17: Seismic section, picks and modeled raypaths of OBS 18 (AWI-20100300).....	168
Figure B.18: Seismic section, picks and modeled raypaths of OBS 19 (AWI-20100300).....	169
Figure B.19: Seismic section, picks and modeled raypaths of OBS 20 (AWI-20100300).....	170
Figure B.20: Seismic section, picks and modeled raypaths of OBS 21 (AWI-20100300).....	171
Figure B.21: Seismic section, picks and modeled raypaths of OBS 22 (AWI-20100300).....	172
Figure B.22: Seismic section, picks and modeled raypaths of OBS 23 (AWI-20100300).....	173

Figure B.23: Seismic section, picks and modeled raypaths of OBS 24 (AWI-20100300).....	174
Figure B.24: Seismic section, picks and modeled raypaths of OBS 25 (AWI-20100300).....	175
Figure B.25: Seismic section, picks and modeled raypaths of OBS 26 (AWI-20100300).....	176
Figure B.26: Seismic section, picks and modeled raypaths of OBS 27 (AWI-20100300).....	177
Figure B.27: Seismic section, picks and modeled raypaths of OBS 28 (AWI-20100300).....	178
Figure C.1: Seismic section, picks and modeled raypaths of OBS 1 (AWI-20100450).....	179
Figure C.2: Seismic section, picks and modeled raypaths of OBS 2 (AWI-20100450).....	180
Figure C.3: Seismic section, picks and modeled raypaths of OBS 3 (AWI-20100450).....	181
Figure C.4: Seismic section, picks and modeled raypaths of OBS 4 (AWI-20100450).....	182
Figure C.5: Seismic section, picks and modeled raypaths of OBS 5 (AWI-20100450).....	183
Figure C.6: Seismic section, picks and modeled raypaths of OBS 6 (AWI-20100450).....	184
Figure C.7: Seismic section, picks and modeled raypaths of OBS 7 (AWI-20100450).....	185
Figure C.8: Seismic section, picks and modeled raypaths of OBS 8 (AWI-20100450).....	186
Figure C.9: Seismic section, picks and modeled raypaths of OBS 9 (AWI-20100450).....	187
Figure C.10: Seismic section, picks and modeled raypaths of OBS 10 (AWI-20100450).....	188
Figure C.11: Seismic section, picks and modeled raypaths of OBS 11 (AWI-20100450).....	189
Figure C.12: Seismic section, picks and modeled raypaths of OBS 12 (AWI-20100450).....	190
Figure C.13: Seismic section, picks and modeled raypaths of OBS 13 (AWI-20100450).....	191
Figure C.14: Seismic section, picks and modeled raypaths of OBS 14 (AWI-20100450).....	192
Figure C.15: Seismic section, picks and modeled raypaths of OBS 15 (AWI-20100450).....	193
Figure C.16: Seismic section, picks and modeled raypaths of OBS 16 (AWI-20100450).....	194
Figure C.17: Seismic section, picks and modeled raypaths of OBS 17 (AWI-20100450).....	195

List of tables

Table 2.1: Information about refraction seismic profiles presented in this study.....	14
Table 2.2: Used channels for picking.....	15
Table 4.1: Nomenclature of picked phases, number of picks within the velocity layer (n), RMS misfit, and χ^2	32
Table 5.1: Nomenclature of picked refracted (rfr) and reflected (rfl) phases, number of picks within the velocity layers (n), RMS misfit and χ^2	66
Table 6.1: Number of picks (n), RMS misfit, and χ^2 for different velocity layers.....	93
Table 6.2: Velocity and thickness ranges of oceanic layer 2 and oceanic layer 3 along the profiles AWI-20100300, AWI-20100200, AWI-20100450, AWI-20080500, and AWI-20080600.	108

Abbreviations

AGC – Automatic Gain Control
AWI – Alfred Wegener Institute for Polar- and Marine Research
BB – Baffin Bay
BBB – Baffin Bay Basin
BGR – Federal Institute for Geosciences and Natural Resources
BH – Basement High
BI – Baffin Island
CA – Canada
CB – Carey Basin
CDP – Common Depth Point
COB – Continent-Ocean Boundary
COT – Continent-Ocean Transition
DEPAS – Deutsche Geräte-Pool für Amphibische Seismologie
DI – Devon Island
EI – Ellesmere Island
GB – Glacier Basin
GEBCO – General Bathymetric Chart of the Oceans
GL – Greenland
HFZ – Hudson Fracture Zone
IGSN – International Gravity Standardization Net
JS – Jones Sound
KB – Kivioq Basin
KR – Kivioq Ridge
LOBSTER – Longterm OBS for Tsunami and Earthquake Research
LS – Lancaster Sound
MB – Melville Bay
MBF – Melville Bay Fault
MBG – Melville Bay Graben
MBR – Melville Bay Ridge
MCS – Multi Channel Seismics
Moho – Mohorovičić Discontinuity
MS – Magmatic Structure
NBB – Northern Baffin Bay
NI – Northumberland Island
NS – Nares Strait
NWB – Northwater Basin
OBS – Ocean Bottom Seismometers
rfl – Reflection/s
rfr – Refraction/s
RMS – Root mean square
RV – Research Vessel
SB – Steensby Basin
SDR – Seaward dipping reflectors
SM – Smith Sound
TWT – Two-way traveltime
UFZ – Ungava Fault Zone
WE – Western Europe

1 Introduction

1.1 Motivation

The Baffin Bay is an up to 2400 m deep oceanic basin situated between Greenland and Ellesmere Island (Canada). The narrow Davis Strait links the Baffin Bay to the Labrador Sea. In the north, the Nares Strait and the Lancaster Sound provide a gateway to the Arctic Ocean (Figure 1.1).

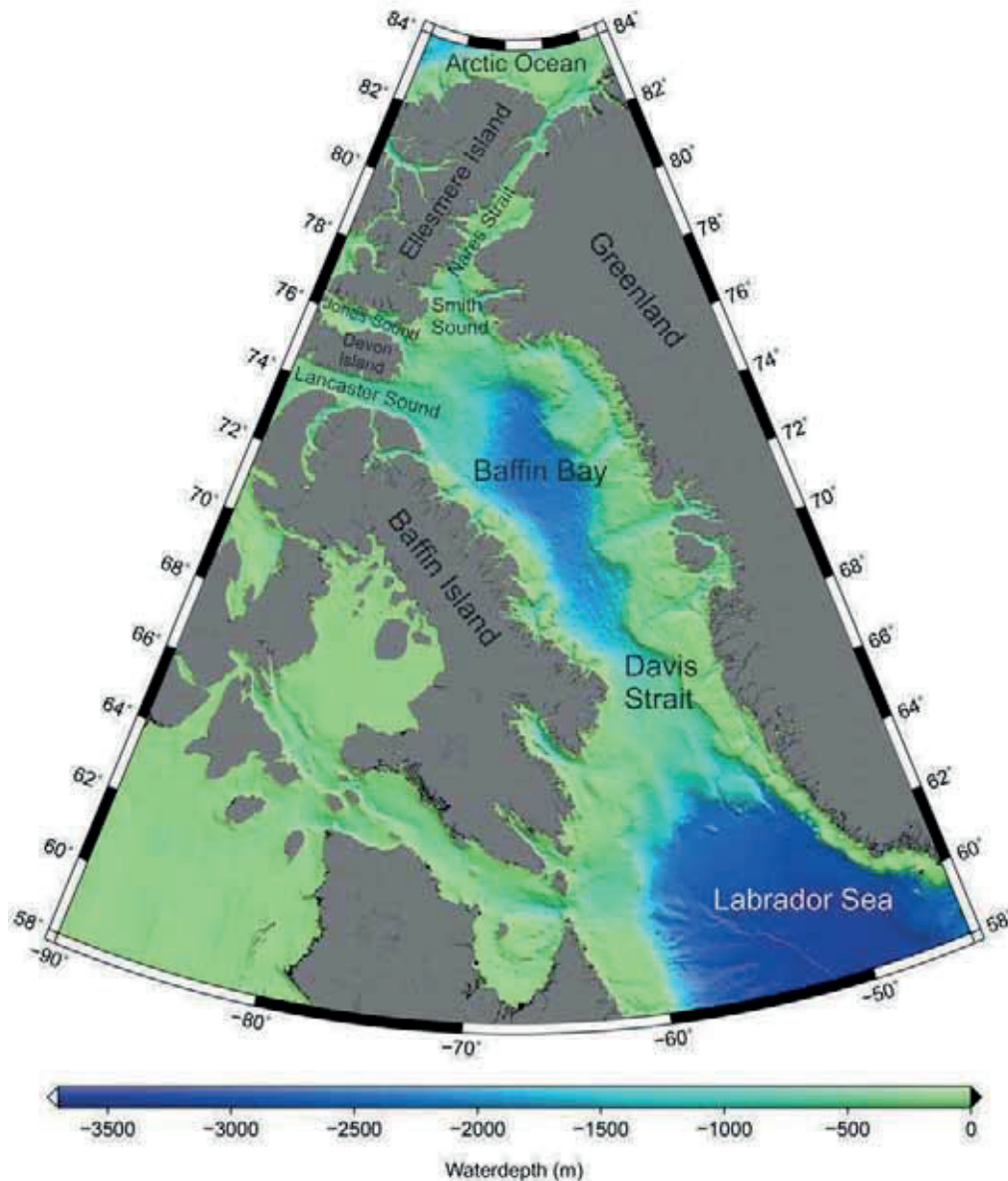


Figure 1.1: Bathymetry of the Labrador Sea, Baffin Bay and Davis Strait (GEBCO grid of 2014, version 2.0).

[Taylor \(1910\)](#) was the first who proposed that Baffin Bay, Labrador Sea and Davis Strait were created by movement between North America and Greenland. In his theory, North America moved away from Greenland while Greenland's position remained fixed (Figure 1.2), creating the Nares Strait as a product of this offsetting displacement.

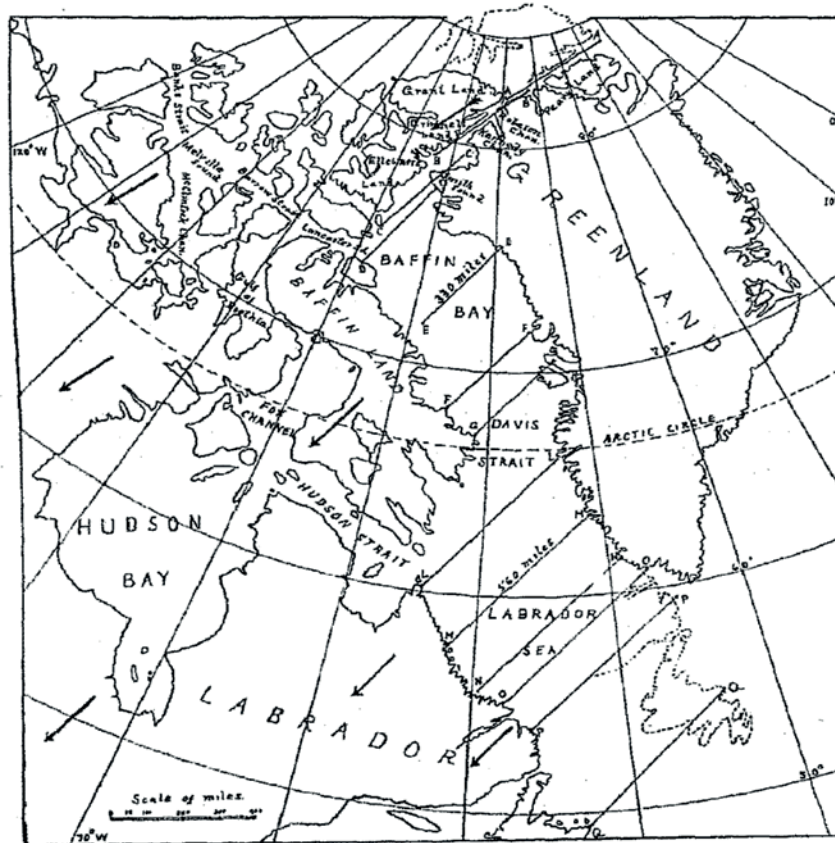


Figure 1.2: Movement of North America relative to Greenland (Taylor, 1910).

Two years after Taylor's article, Alfred Wegener published his global theory about continental drift in 1912. Between 1915 and 1929, four editions of his book "Die Entstehung der Kontinente und Ozeane" were published, in which he explained his theory about the drifting continents based on geological, palaeontological, biological and paleoclimate indications. The first edition already contained maps showing the assumed plate boundaries between the continents (Figure 1.3). Like Taylor (1910), Wegener (1915) also explained the horizontal displacement between Greenland and North America by movement along the Nares Strait (Figure 1.3, red line). Therefore, the assumed strike-slip fault in Nares Strait was named "Wegener Fault" by Wilson (1963).

A long time has passed since the introduction of the continental drift, in which scientific knowledge improved. The theory of plate tectonics has replaced the theory of continental drift in the scientific community. Today, the classifications of crustal types and localization of plate boundaries is based on geological, seismic and potential field data. Especially modern refraction seismic investigations can provide insights in the crustal fabric and extend of crustal types in examined areas.

Although the Baffin Bay and Nares Strait were among the first examples for oceanic basin development, their genesis was disputed for a long time. In the last century, contradicting scientific results of geophysical and geological investigations revealed that the opening history and tectonic evolution of the Baffin Bay is much more complicated than previously thought. Especially the presence of oceanic crust in the Baffin Bay, the plate tectonic evolution and the existence and location of the Wegener Fault was discussed. Since some years, the genesis of the shelf regions in the Baffin Bay is also of commercial interest.

Exploration activity of the oil and gas industry increased along the northwestern Greenland shelf because of assumed hydrocarbon potential.



Figure 1.3: Modified cutout of a map of Wegener (1915) showing continental plate boundaries. The “Wegener Fault” in the Nares Strait is highlighted in red. Abbreviations: GL: Greenland, CA: Canada, WE: Western Europe.

In the last 15 years, the Baffin Bay and Nares Strait was again the target area for researchers. The nature of the Baffin Bay crust, the type of margin, and the opening history of the Baffin Bay were examined. But since weather conditions and sea-ice coverage of the Baffin Bay region aggravate investigations, the data coverage with modern refraction seismic datasets is sparse and was reduced to the southern Baffin Bay and the Smith Sound region in the southern Nares Strait. Therefore, another research cruise was conducted in the Greenlandic part of Baffin Bay in 2010 to gain further information about the structural and tectonic evolution of the region. In the next chapter, I will summarize the genesis and geology of the Labrador Sea, Baffin Bay and Nares Strait and previously conducted investigations in these regions.

1.2 Geology and geophysical investigations in the Baffin Bay, Labrador Sea and Nares Strait

In the Labrador Sea and Baffin Bay, initial stretching between Greenland and North America probably started during Late Triassic at 223 Ma, as indicated by dyke swarms in West Greenland (Larssen et al., 2009). Extension starting during the Cretaceous caused the formation of rifted continental margins (e.g., Whittaker et al., 1997; Oakey and Chalmers 2012; Gregersen et al., 2013) off Greenland and Baffin Island, which contain thick sedimentary successions. For example, the rifted margins of the Melville Bay area in northeast Baffin Bay are characterized by deep grabens and halfgrabens, which are believed to contain up to 13 km thick Cretaceous and younger sediments (Whittaker et al., 1997). The arrival of the Iceland mantle plume underneath the Greenland lithosphere led to the formation of massive Paleocene volcanic rocks on- and offshore West Greenland and Baffin Island (Storey et al., 1998) and may have also triggered the

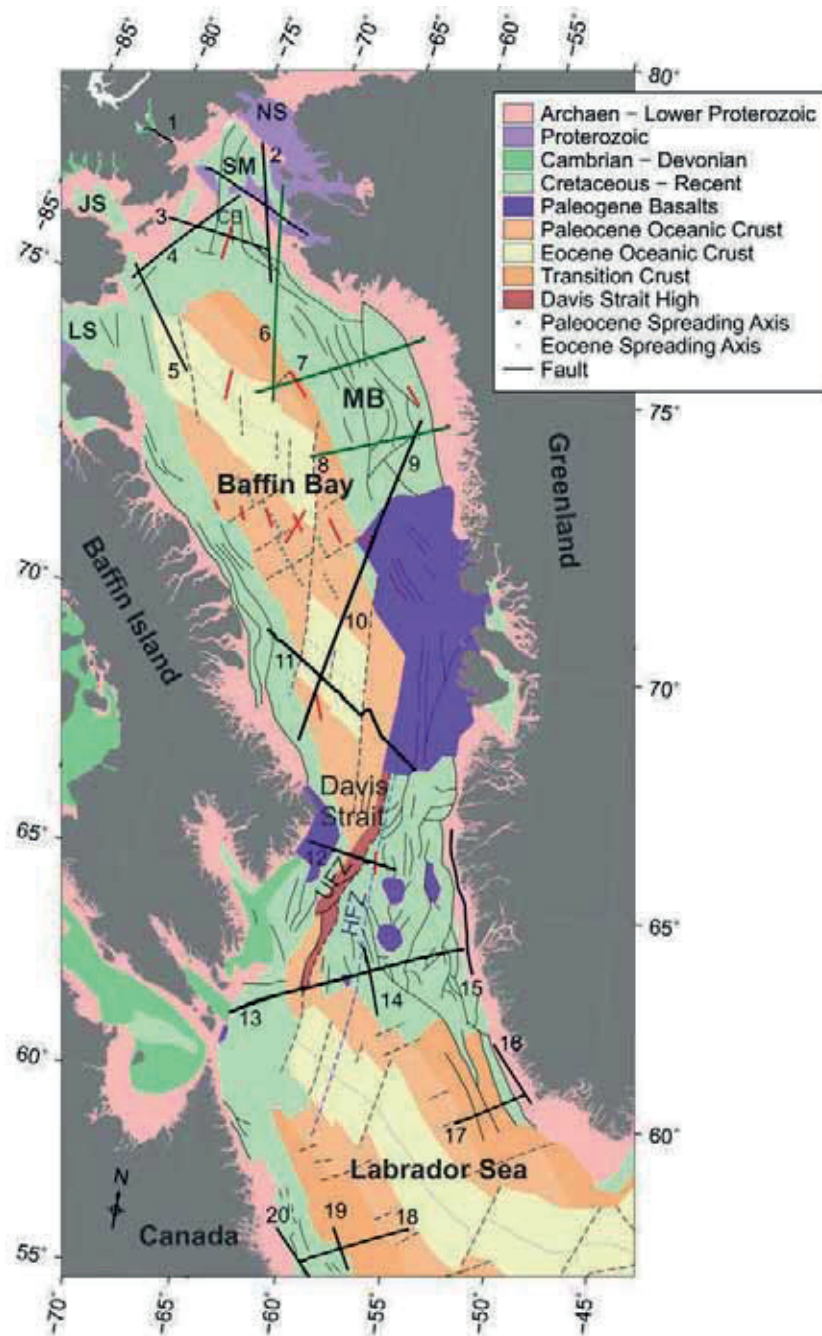


Figure 1.4: Offshore Geology of Baffin Bay and adjacent regions, modified after Oakey and Chalmers (2012). The position of the Hudson Fracture Zone (blue dashed line) is taken from Chalmers and Pulvertaft (2001). Bold red lines mark the position of sonobuoy recordings from Keen and Barrett (1972). Bold green lines mark the position of seismic refraction profiles presented in this thesis. Bold black lines with numbers mark the position of refraction seismic profiles: 1: line 3 (Funck et al., 2006); 2: profile 91/3 (Jackson and Reid, 1994); 3: profile 91/2 (Reid and Jackson, 1997); 4: profile 91/1 (Jackson and Reid, 1994); 5: profile 91/4 (Reid and Jackson, 1997); 6: profile AWI-20100300 (this thesis); 7: profile AWI-20100200, (this thesis); 8: AWI_20100450 (this thesis); 9: profile AWI-20100400 (Suckro et al., 2012); 10: profile AWI-20080500 (Suckro et al., 2012); 11: profile AWI-20080600 (Funck et al., 2012); 12: AWI-20080700 (Suckro et al., 2013); 13: profile NUGGET-1 (Funck et al., 2007); 14: profile NUGGET-2 (Gerlings et al., 2009); 15: GR89-WA (Gohl and Smithson, 1993) 16: 88R1 (Chian and Loudon, 1992) 17: profile 88R2 (Chian and Loudon, 1994) 18: profile 90R1 (Chian et al., 1995b) 19: 90R2, (Chian et al., 1995b) 20: 90R3 (Chian et al., 1995b). Abbreviations: MB: Melville Bay, NS: Nares Strait, SM: Smith Sound, JS: Jones Sound, LS: Lancaster Sound, HFZ: Hudson Fracture Zone, UFZ: Ungava Fault Zone, CB: Carey Basin.

onset of seafloor spreading in Labrador Sea. The Baffin Bay is believed to be the northern extension of the extinct Labrador Sea rift system.

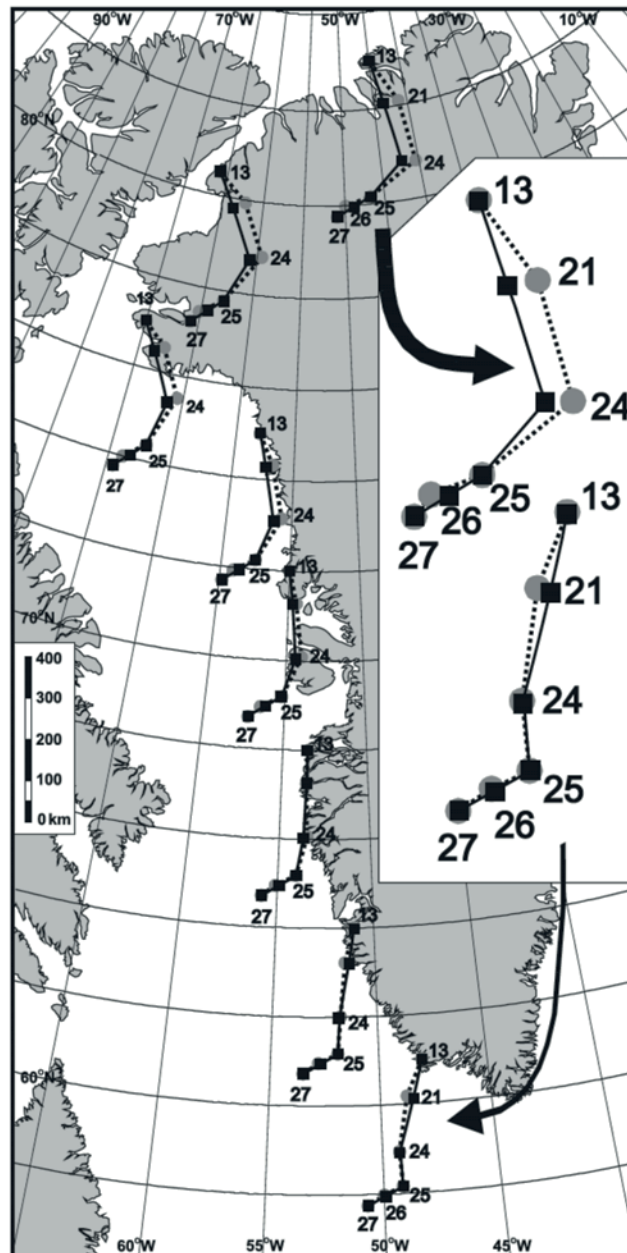


Figure 1.5: Movement of the Greenland Plate relative to the North American Plate (Oakey and Chalmers, 2012). Solid black lines (Oakey and Chalmers, 2012) and dotted black lines (Roest and Srivastava, 1989) mark the motion paths of Greenland relative to North America at Chron 27N, 26N, 25N, 24N and 21N (dots and squares).

In contrast to the Baffin Bay, the crustal types of the Labrador Sea and their extent are well investigated: refraction and reflection seismic measurements revealed that oceanic crust is present in its central part (Chian et al., 1995a; Chian and Loudon, 1994)(Figure 1.4). Based on magnetic lineations, the onset and timing of seafloor spreading was examined (e.g., Roest and Srivastava, 1989). The oldest, undisputed magnetic anomaly in Labrador Sea is chron 27N, therefore spreading probably started during the Paleocene at 61.3-60.9 Ma (Chalmers and Laursen, 1995). The onset of seafloor spreading between East Greenland and Europe caused a change in spreading direction at ~55 Ma

(Srivastava, 1978) (Figure 1.5) and separated the oceanic crust of the Labrador Sea in Paleocene and Eocene segments.

The type of margin in the Labrador Sea changes from the south to the north: While non-volcanic margins and a wide transition zones, composed of serpentized upper mantle, are present in the southern Labrador Sea (Chian et al., 1995b, Funck and Loudon, 1999), volcanic margins characterize the northern transition between oceanic and stretched continental crust (Chalmers and Laursen 1995, Chalmers 1997; Keen et al., 2012).

Volcanic margins are also present in southern Davis Strait (Funck et al. 2007). The crust underneath Davis Strait is mainly composed of continental crust, which incorporates slices of thick oceanic crust (Funck et al., 2007) or stretched and intruded igneous crust (Suckro et al., 2013) within the transform fault system of the Ungava Fault Zone.

Since the Ungava Fault Zone (Chalmers et al., 1993) and the Hudson Fracture Zone (Suckro et al., 2013) in the Davis Strait are believed to link the spreading systems of Labrador Sea and Baffin Bay, one can expect that the crustal structure and the opening history of Baffin Bay is similar to that of the Labrador Sea, but in fact, there are many differences.

Magnetic measurements revealed no clear magnetic lineations in the Baffin Bay in contrast to the Labrador Sea. Oakey and Chalmers (2012) were the first who identified weak magnetic lineations in central Baffin Bay. Due to missing clear magnetic anomalies in wide parts of the Baffin Bay, the existence of oceanic crust and therefore the timing and onset of spreading was unclear.

First refraction seismic measurements in central Baffin Bay showed that abnormally thin, ~4km thick oceanic crust is overlain by thick sediments (Keen and Barrett, 1972). In contrast to the probably oceanic crust in central Baffin Bay, thin crust in northern Baffin Bay was interpreted by Jackson and Reid (1994) and Reid and Jackson (1997) to consists of serpentized upper mantle, formed during amagmatic rifting. A gravity low in the Baffin Bay, which is aligned nearly in the same direction as the Eocene spreading center in Labrador Sea, gave further evidence that an Eocene spreading ridge and therefore oceanic crust is present in central Baffin Bay (Whittaker et al. 1997). The existence of 7 to 9 km thick oceanic crust and volcanic margins in the southern Baffin Bay has recently been confirmed on basis of modern refraction and reflection seismic datasets (Suckro et al., 2012, Funck et al., 2012, Skaarup et al., 2006). However, the crustal structure and type of margin of the northeastern, Greenlandic part and nearly the whole Canadian part of the Baffin Bay have not been investigated and the onset of change from a volcanic southern margin to the non-volcanic northern margin have not been described yet.

Estimations on the extent of Eocene and Paleocene oceanic crust in Baffin Bay are in wide parts based on potential field data and/or plate tectonic reconstructions, which take the sparse refraction seismic measurements in northern and southern Baffin Bay into account. However, another unsolved problem for reconstructing the movement between Greenland and North America is the “Wegener Fault”. In different opening scenarios for Baffin Bay and Labrador Sea, spreading and accumulation of oceanic crust between Canada and Greenland requires between 300 to 150 km of transform motion in the Nares Strait (Johnson and Srivastava 1982, Srivastava & Falconer 1982, Roest & Srivastava 1989, Srivastava 1985, Srivastava & Tapscott 1986) However, geological features on both sides of the Strait do not show a lateral offset in the

Smith Sound (southern Nares Strait), or only show a small offset in the northern Nares Strait along the Judge Daly Fault Zone in the Kennedy Channel (e.g., Kerr 1967; Frisch and Dawes, 1982; Dawes 2009; Harrison 2006)(Figure 1.6). Refraction seismic measurements in the Smith Sound area revealed up to 36 km thick, continental crust (Funck et al., 2006). Reid and Jackson (1997) proposed that an only ~7km thick crust underneath the Carey Basin along their profile 91/2 is caused by a plate boundary. But no clear indications for a transform plate boundary have been found only 80 km north along the parallel profile line 3 (Funck et al., 2006) (Figure 1.4).

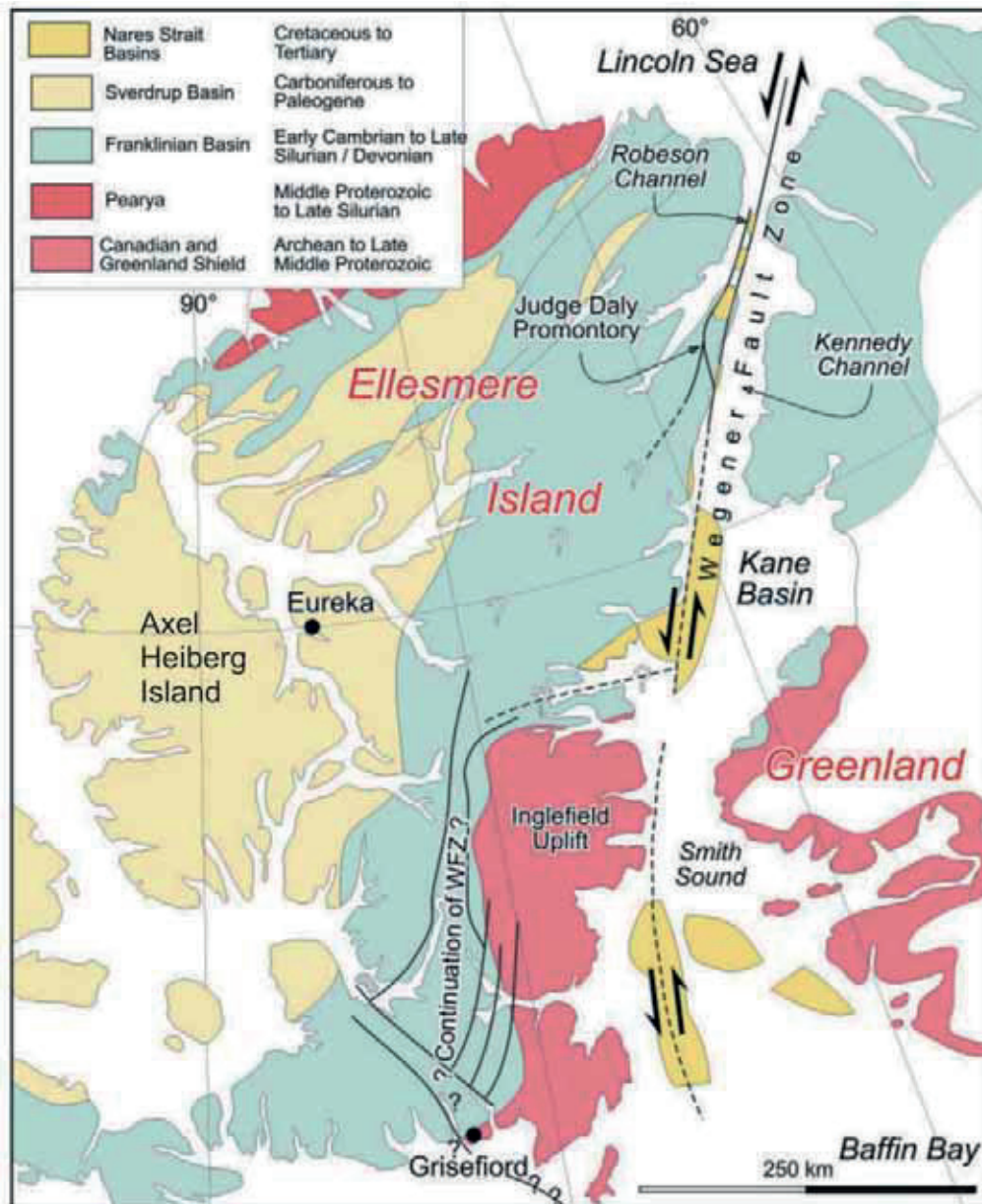


Figure 1.6: Geology of the Nares Strait and position of the Wegener Fault (modified after Tessensohn et al., 2006).

Some authors propose an onshore continuation of the strike-slip system at southern Ellesmere Island (e.g., Tessensohn et al., 2006; Figure 1.6) or more to the south at Axel Heiberg Island (e.g., Harrison, 2006). Until today, no consent about the existence or location of the “Wegener Fault” or a comparable plate tectonic margin in the Nares Strait and adjacent regions has been found.

1.3 Outline and aim of this thesis

Three seismic refraction profiles as well as corresponding reflection seismic profiles and shipborne gravity data were acquired during the research cruise in 2010. The aim of my thesis is to examine the crustal structure, the type of margin and extent of crustal types in northeastern and central Baffin Bay and southern Nares Strait based on these geophysical datasets.

The central questions and main objectives of my thesis are presented in the chapter 1.4.

P wave velocity models for the three refraction seismic profiles were calculated by raytracing and forward modeling. The obtained *P* wave velocity models together with the recorded ship-borne gravity data were used to calculate density models. An overview about the datasets and methods used is provided in chapter 2.

Findings of the geophysical datasets were combined to generate geological models for all three profiles. Three articles for scientific peer-reviewed journals were prepared which discuss the main objectives of this thesis. In chapter 3, an overview about my contributions to every publication and the content of the publication is given. The articles are presented in chapter 4 to 6.

chapter 7 summarizes the results of this study. An outlook of further geophysical investigations in the Baffin Bay is provided in chapter 8.

1.4 Central questions

In the following, I will summarize the central questions of my thesis.

The Melville Bay in northeast Baffin Bay is characterized by deep basins and grabens, containing thick successions of probably Cretaceous and younger sediments (e.g., Whittaker et al., 1997). Although the rifted margin of Melville Bay was in the focus of the industry during the last years, its crustal structure is not well investigated due to the lack of modern refraction seismic data. The thickness of the crust, its velocity structure and the depth of the Moho (Mohorovičić discontinuity) are unclear. Statements about the depth of basins and their infill are based on reflection seismic data.

- What kind of crust is present in the Melville Bay area? How is the crustal structure composed? How thick is the crust?

- How is the infill of the basins within Melville Bay characterized?

The profile AWI-20100450 (southern Melville Bay) is located parallel to the profile AWI-20100200 (northern Melville Bay). Both profiles cross the same major tectonic features in the Melville Bay area.

- Can we detect major differences between the crustal structure of northern and southern Melville Bay?

The type of margin in the Labrador Sea changes from a volcanic margin in the north to a non-volcanic margin in the south. Like in the Labrador Sea, the different types of margins have been identified in Baffin Bay: Southern Baffin Bay is characterized by volcanic margins (e.g., Suckro et al., 2012), northeastern Baffin Bay by non-volcanic margins (Reid and Jackson, 1997), but the location of the transition between both margin types is unclear.

- What type of margin is present in the Melville Bay area?

Refraction seismic measurements in the northern Nares Strait area revealed up to 36 km thick, continental crust (Funck et al., 2006). The transition between the continental crust in Smith Sound and the assumed oceanic crust in northern Baffin Bay is unexplored.

- How is the transition between assumed oceanic and continental crust in the Smith Sound characterized? What type of margin is present?

Reid and Jackson (1997a) found thin crust with a velocity of 6.8 km/s in northeastern Baffin Bay (Figure 1.4, line 91/4). They proposed that it was formed by amagmatic rifting and consists of unroofed serpentinized mantle rather than oceanic layer 3. In contrast, modern refraction seismic data showed, that southern Baffin Bay is underlain by oceanic crust (Suckro et al., 2012; Funck et al., 2012). The crustal structure of the thin oceanic crust in central Baffin Bay has only been examined by few sonobuoy recordings from Keen and Barrett (1972), but no modern refraction seismic data are available for this region. The composition and structure of the thin crust in central northern Baffin Bay and the transition from oceanic crust in the southern Baffin Bay to thin crust consisting of serpentinized upper mantle in the northern Baffin Bay remains uncertain.

- Is oceanic crust is present in central northern Baffin Bay? If so, how is it characterized?

- Does the crustal structure provide indications for the genesis of the region?

The onset of spreading in Baffin Bay remains unclear due to the lack of clear magnetic spreading anomalies in Baffin Bay. Statements on the extent of continental, oceanic and transitional crust in central and northern Baffin Bay are in wide parts based on plate tectonic reconstructions. These reconstructions take gravity data, reflection seismic and the few refraction seismic profiles acquired in Baffin Bay and plate kinematic rotation poles derived from the magnetic data in the Labrador Sea into account (e.g. Suckro et al., 2012; Oakey and Chalmers, 2012; Hosseinpour, 2013). Especially in the central and northern Baffin Bay, the extent of crustal types is not verified by deep sounding profiles.

- What is the extent of different crustal types in Northeastern Baffin Bay?

- Do my results confirm previous models about the extent of crustal types in Baffin Bay?

2 Methods, data acquisition and processing

2.1 Data acquisition in the Baffin Bay

During the cruise ARK-XXV/3 on board of RV Polarstern, datasets of various geophysical and geological methods were acquired. The cruise was a cooperation between the Alfred-Wegener-Institute for Polar- and Marine Research in Bremerhaven (AWI) and the Federal Institute for Geosciences and Natural Resources in Hanover (BGR). Besides Multi channel seismic (MCS) profiles, gravity and magnetic data, four refraction seismic profiles were acquired. Offshore and onshore seismic measurements, potential field methods, onshore and offshore sampling and heatflow measurements were conducted in the Greenlandic part of Baffin Bay (Figure 2.1). The reflection/refraction seismic datasets as well as the shipborne gravity datasets used in this study were acquired during this expedition. The three northern refraction seismic profiles (AWI-20100200, AWI-20100300, AWI-20100450) are taken as a basis for this dissertation (Figure 2.2).

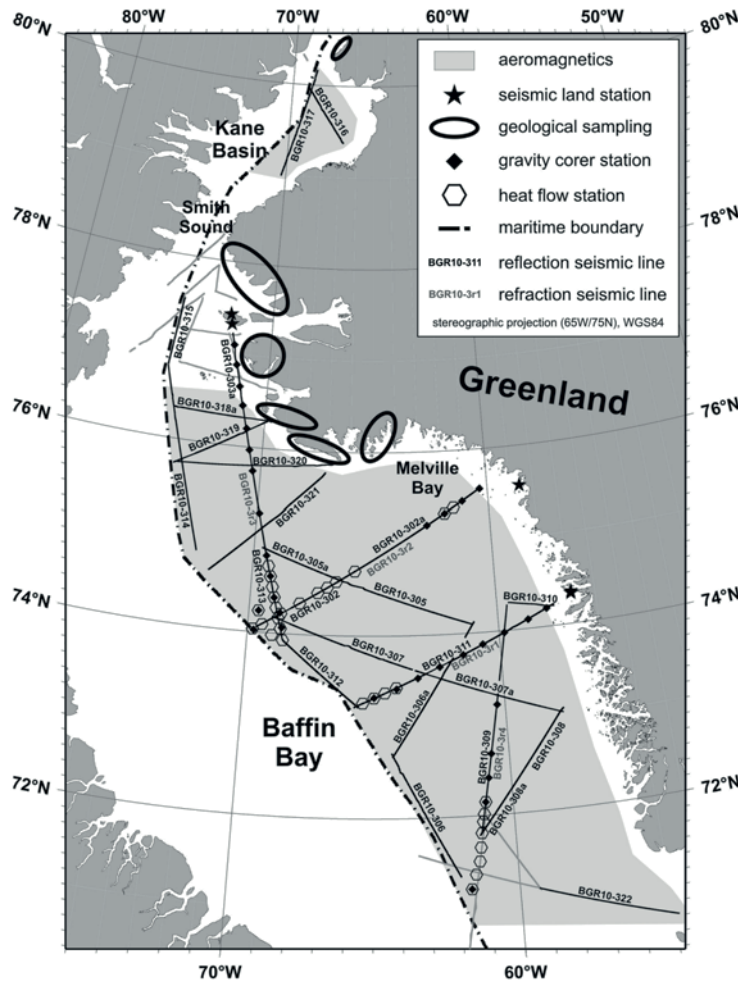


Figure 2.1: Investigated area in the Greenlandic part of Baffin Bay and Nares Strait and the position of conducted experiments during the expedition ARK-XXV/3 in 2010, taken from Damm (2010). Black lines mark the position of reflection and refraction seismic data acquired in 2010, light grey lines the position of profiles acquired during previous expeditions.

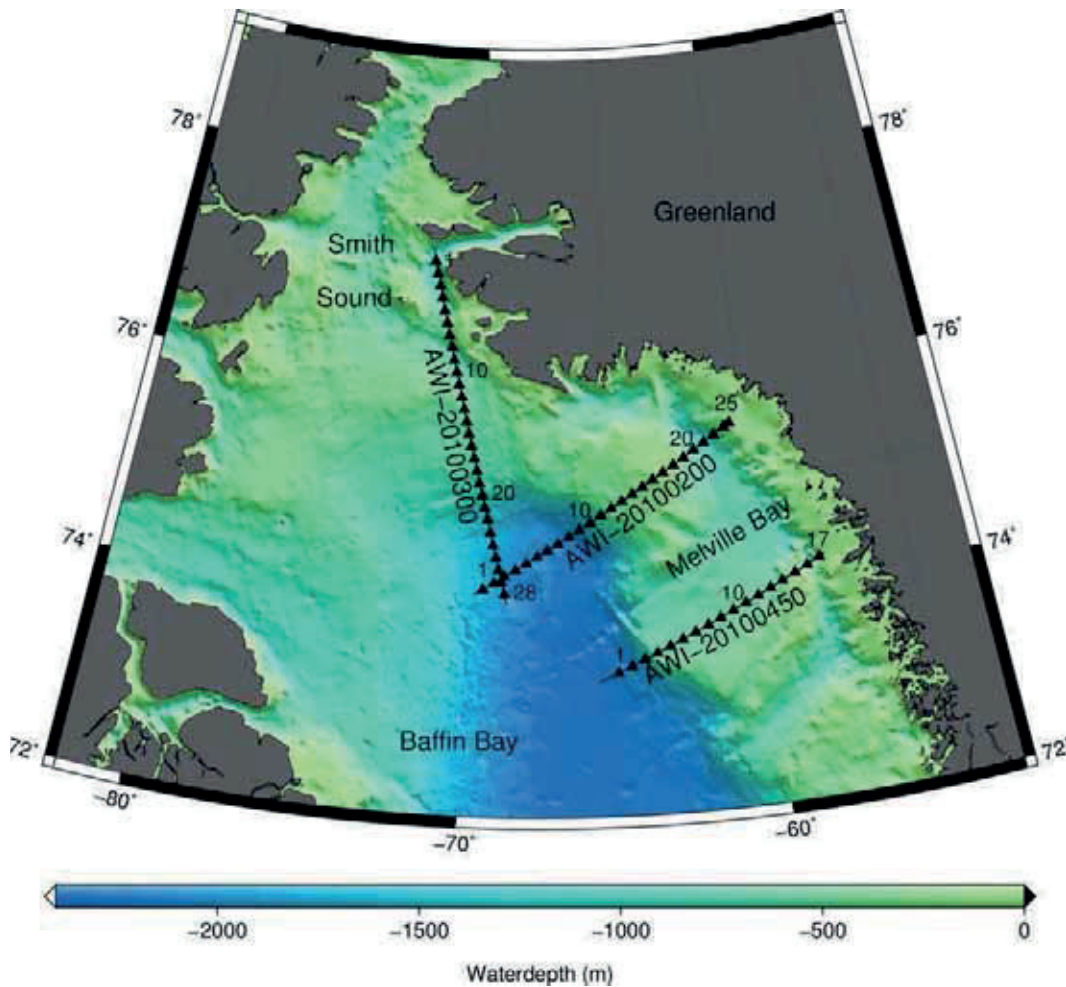


Figure 2.2: Bathymetry (GEBCO grid of 2014, version 2.0) and position of the three refraction seismic profiles in the research area. Black triangles mark the position of OBS along the profiles, the black numbers are the OBS numbers.

2.2 Seismics

2.2.1 Acquisition of refraction seismic data offshore

During ARK-XXV/3, offshore refraction seismic data were collected with Ocean Bottom Seismometers (OBS), type LOBSTER (Longterm OBS for Tsunami and Earthquake Research). Every OBS consisted of an aluminum frame, flotation units and a pressure cylinder (Figure 2.3). The pressure cylinder contained a hard drive and batteries for running different instruments, which were fixed to the aluminum frame. During the cruise, every OBS used was equipped with a Gralp CMG-40T 60 sec 3-component broadband seismometer and a High Tech Inc. hydrophone. An anchor weight was fixed to the OBS frame via a release-unit. Due to the weight of the anchor, the OBS sink to the seafloor during deployment.

In total, 70 OBS-stations were deployed along the three northern refraction seismic profiles during the cruise. Along the SW-NE orientated profile AWI-20100200, 25 OBS were deployed (Figure 2.2). Also SW-NE aligned, profile AWI-20100450 consists of 17 OBS; the northernmost, N-S orientated profile AWI-20100300 is composed of 28 OBS. Start- and endpoint of the profiles, the

length of the P wave velocity models, and the average spacing between the deployed OBS are presented in Table 2.1.

An array of 8 airguns with a total volume of 67.2 l was towed behind the ship at a depth of 10m and used as seismic source. Every 60 s, the airgun-array generated seismic signal, called “shot”. The distance between each shot was ~150m. The traveltimes of resulting reflected, refracted and direct waves of the signal (Figure 2.4) were recorded by the recording device inside the pressure cylinder. The data were recorded with a sampling rate of 250 Hz.

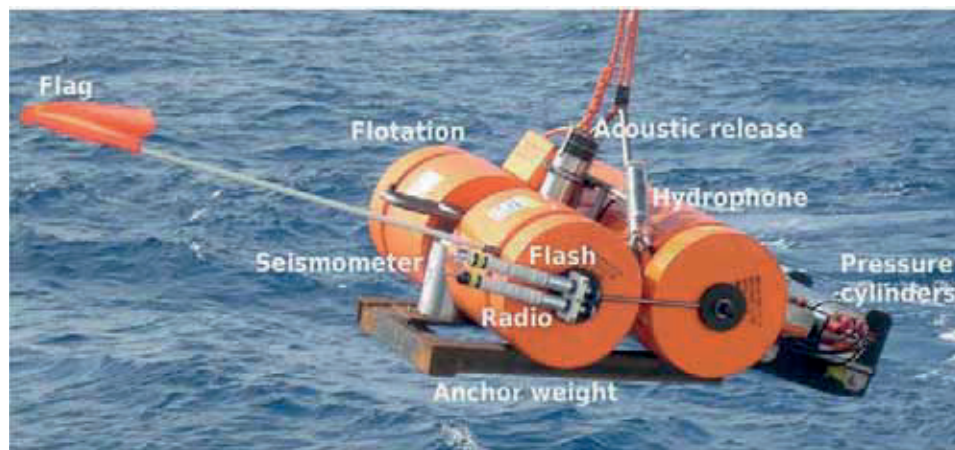


Figure 2.3: A LOBSTER OBS and its components (Damm, 2010).

After successful completion of the data acquisition, a signal was sent to the release unit to disconnect the OBS from the anchor. Because of its floating units, the OBS returned to the sea surface and was recovered by members of the scientific crew.

Fortunately, no OBS was lost during recovery. Nevertheless, not all recorders and/or seismometers and hydrophones worked properly due to technical failures or a damages of the equipment. Table 2.2 illustrates, which OBS worked without failure and where data-losses occurred.

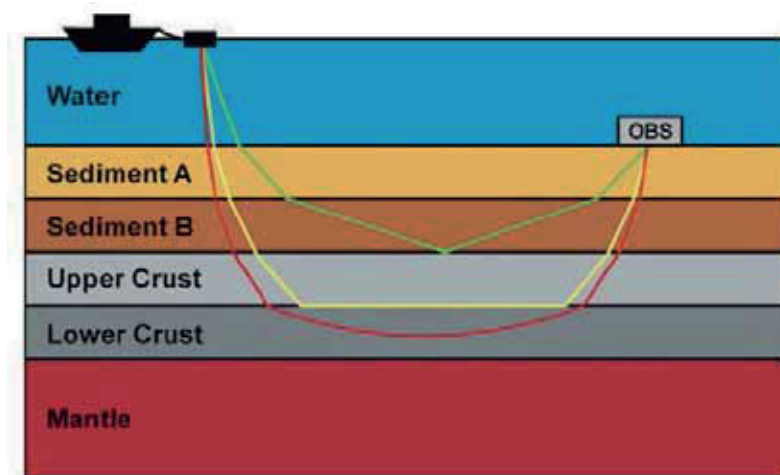


Figure 2.4: Acquisition of wide-angle seismic data (Leinweber, 2011). The travelpaths of different waves are colored in green, yellow and red: The green line represents the travelpath of a reflected wave, the yellow line the travelpath of a head wave. The red line marks the travelpath of a refracted wave.

The recording of data was stopped after the recovery of the OBS. At first, the internal clock of the recorder unit was synchronized with a GPS signal. Then the synchronized data was downloaded to a PC for processing.

Table 2.1: Information about refraction seismic profiles presented in this study.

	AWI-20100200	AWI-20100300	AWI-20100450
Number of deployed OBS	25	28	17
Average spacing between OBS	~13 km	~13 km	~15 km
Length (km) of <i>P</i> wave velocity model	321 km	399 km	270 km
Start of refraction seismic profile	-69.74753 W 74.04276 N	-72.1162 W 77.4263 N	-65.73424W 73.21505 N
End of refraction seismic profile	-60.41610 W 75.55662 N	-68.61022 W 73.95862 N	-56.69702 W 74.35228 N

2.2.2 Processing of refraction seismic data

As a first step of processing, the recorded data were cut into 60s traces. Segy-files for every OBS were created. The offsets between the shot positions and the OBS locations were calculated and written into the segy-files. During deployment, the OBS normally drift away from their deployment position due to water currents. Therefore, most OBS need to be relocalized in order to correct the position of the OBS along the profile. For this, the direct water-wave within every seismogram was picked with the software *zp* (by B. Zelt, <http://www.soest.hawaii.edu/users/bzelt/zp/zp.html>) and the trace with the shortest travel time was determined. Every trace of an OBS was shifted by the same value to obtain that the trace with the shortest traveltime was shifted to zero offset. An automatic gain control (AGC) of 1 s was applied to the dataset. The used bandpass filter was 4.0–13.5 Hz for all seismograms.

For the geometry-setup of every profile, the start- and endpoint was determined (Table 2.1). The relocated OBS were projected on a line, while the distance between the positions of the OBS and the shots remained unchanged.

2.2.3 Phase determination and modeling of refraction seismic data

Identification and picking of *P* waves was done with the free software *zp*. Since the data-quality of the seismic sections was different along the three profiles, the channel with the best data-quality and signal-to-noise ratio was used for picking (Table 2.2). In the seismic sections of profile AWI-20100200, the channel of the hydrophone-component displays the best data quality. For profile 20100300, the hydrophone or the vertical *z*-component of the seismometer was used for picking, depending on the data-quality. For profile 20100450, the hydrophone component, and for OBS 7 also the *z*-component was used.

On basis of their traveltimes, curvature and appearance of the *P* waves, different reflected and refracted phases were determined. These phases were subdivided into sediment-, crustal- and mantle phases. Examples for a seismic section and picked phases are given in Figure 2.5a-b.

Modeling was conducted with software *Rayinvr* (Zelt and Smith, 1992) and the graphical user interface *Pray*, which was written by Tanja Fromm at AWI and is available under <http://aforge.awi.de/gf/project/pray/>. A *P* wave velocity profile was generated for every profile by forward modeling. Since *S* waves were

sparse or absent in the data, it was not possible to calculate an *S* wave model as well.

With the software rayinvr, the position of the different layer boundaries and the velocities within each layer can be selected and changed by the user. Additionally, an inversion algorithm can be used to model either single or several phases.

During the modeling of the three profiles, reflected phases were used to determine the depth of layer boundaries, while refracted phases provided information about the velocities within a layer. If possible, the position of the basement and structural elements were determined in the corresponding reflection seismic profiles and also incorporated in the velocity model. BGR and Cairn Energy provided the already processed reflection seismic profiles. The picked *P* wave velocities were applied to each layer and the velocity nodes were changed until a satisfying fit was obtained (Figure 2.5c-d). The inversion algorithm was used for some layers to obtain a better fit between the picked phases and the model.

Table 2.2: Used channels for picking

AWI-20100200					AWI-20100300					AWI-20100450				
OBS 1	H	X	Y	Z	OBS 1	H	X	Y	Z	OBS 1	H	X	Y	Z
OBS 2	H	X	Y	Z	OBS 2	H	X	Y	Z	OBS 2	H	X	Y	Z
OBS 3	H	X	Y	Z	OBS 3	H	X	Y	Z	OBS 3	H	X	Y	Z
OBS 4	H	X	Y	Z	OBS 4	H	X	Y	Z	OBS 4	H	X	Y	Z
OBS 5	H	X	Y	Z	OBS 5	H	X	Y	Z	OBS 5	H	X	Y	Z
OBS 6	H	X	Y	Z	OBS 6	H	X	Y	Z	OBS 6	H	X	Y	Z
OBS 7	H	X	Y	Z	OBS 7	H	X	Y	Z	OBS 7	H	X	Y	Z
OBS 8	H	X	Y	Z	OBS 8	H	X	Y	Z	OBS 8	H	X	Y	Z
OBS 9	H	X	Y	Z	OBS 9	H	X	Y	Z	OBS 9	H	X	Y	Z
OBS 10	H	X	Y	Z	OBS 10	H	X	Y	Z	OBS 10	H	X	Y	Z
OBS 11	H	X	Y	Z	OBS 11	H	X	Y	Z	OBS 11	H	X	Y	Z
OBS 12	H	X	Y	Z	OBS 12	H	X	Y	Z	OBS 12	H	X	Y	Z
OBS 13	H	X	Y	Z	OBS 13	H	X	Y	Z	OBS 13	H	X	Y	Z
OBS 14	H	X	Y	Z	OBS 14	H	X	Y	Z	OBS 14	H	X	Y	Z
OBS 15	H	X	Y	Z	OBS 15	H	X	Y	Z	OBS 15	H	X	Y	Z
OBS 16	H	X	Y	Z	OBS 16	H	X	Y	Z	OBS 16	H	X	Y	Z
OBS 17	H	X	Y	Z	OBS 17	H	X	Y	Z	OBS 17	H	X	Y	Z
OBS 18	H	X	Y	Z	OBS 18	H	X	Y	Z					
OBS 19	H	X	Y	Z	OBS 19	H	X	Y	Z					
OBS 20	H	X	Y	Z	OBS 20	H	X	Y	Z					
OBS 21	H	X	Y	Z	OBS 21	H	X	Y	Z					
OBS 22	H	X	Y	Z	OBS 22	H	X	Y	Z					
OBS 23	H	X	Y	Z	OBS 23	H	X	Y	Z					
OBS 24	H	X	Y	Z	OBS 24	H	X	Y	Z					
OBS 25	H	X	Y	Z	OBS 25	H	X	Y	Z					
					OBS 26	H	X	Y	Z					
					OBS 27	H	X	Y	Z					
					OBS 28	H	X	Y	Z					

H: hydrophone channel; X, Y, and Z: seismometer channels. Acquired channels are written in black, channels which were used for acquisition but did not record any data are written in grey. Channels used for picking phases are highlighted in green.

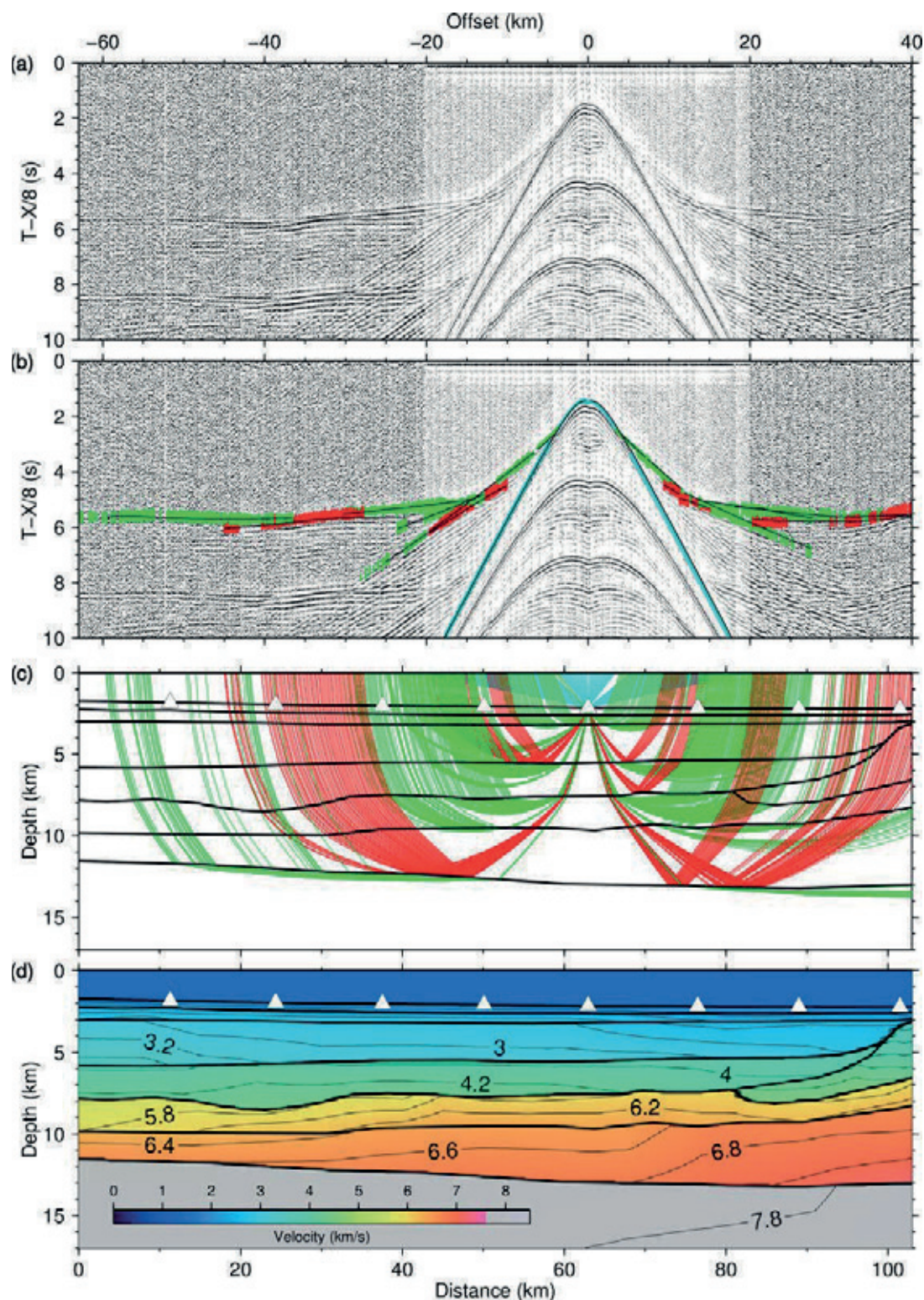


Figure 2.5: Examples for a seismic section, picked phases and P wave velocity modeling.

a) Example for a seismic section.

b) Seismic section with picked phases. Reflected rays are colored red, refracted rays are colored green. The waterwave (reflected wave) is colored blue. Black lines mark the modeled raypaths in the P wave velocity model (see c)

c) Modeled reflected and refracted raypaths in the P wave velocity model. Triangles mark the positions of OBS stations.

d) Modeled P wave velocity-model. Triangles mark the positions of OBS at the seafloor.

2.3 Gravity data

2.3.1 Acquisition and processing

The logging and processing of the gravity data was done by the BGR. Therefore, I will give only a short overview on the acquisition and processing of the gravity data.

During the acquisition of refraction seismic data, gravity measurements were conducted continuously with the sea gravimeter system KSS31 on board of RV Polarstern. Calibration measurements in Reykjavik and Bremerhaven at the beginning and end of the cruise were performed with a LaCoste and Romberg gravity meter. With the help of these calibration measurements, the instrumental drift of the sea gravimeter system during the cruise (8.6 mGal) was determined and the acquired dataset was linked to the International Gravity Standardization Net IGSN 71. Additionally, the normal gravity (WGS84) was subtracted from the measured gravity data. The Eötvös correction was applied to obtain the free-air gravity anomalies. For further information, please refer to Damm (2010).

2.3.1 Density Modeling

Density modeling was conducted at BGR together with Ingo Heyde. To set up the density start model, the layer boundaries of the velocity model were transferred to the density model. The average *P* wave velocities of every layer were converted into densities, using values of Barton (1986). If a velocity layer was characterized by great lateral velocity changes, it was divided into 2 or more blocks and different density values were assigned to every block.

If the observed calculated and measured gravity data did not show a good fit, the density values were changed within a reasonable range that still corresponds to the values of Barton (1986). If density adjustments were not enough to enhance the fit, the vertical boundaries between the density blocks or in some cases also the boundaries of the density model were slightly adjusted.

3 Contributions to scientific journals

3.1 A crustal model for northern Melville Bay, Baffin Bay

In: Journal of Geophysical Research - Solid Earth

DOI:10.1002/2014JB011559

Received: 22. August, 2014

Accepted: 12. November, 2014

Published: 14. December, 2014

Authors: Tabea Altenbernd¹, Wilfried Jokat¹, Ingo Heyde², Volkmar Damm²

¹Alfred Wegener Institute Helmholtz Centre for Polar and Marine Research, Am Alten Hafen 26, D-27568 Bremerhaven, Germany

²Federal Institute for Geosciences and Natural Resources, Stilleweg 2, D-30655, Hanover, Germany

Content and contributions to the article

Based on a *P* wave velocity model and a density model, the crust along the 321km long profile AWI-20100200 in the northern Melville Bay is examined. The crust along the profile is subdivided into thin oceanic, transitional and rifted continental crust. The extent of crustal types is compared with a geological map of Oakey and Chalmers (2012). The paper provides insights into the rifted continental crust and the thickness and velocity structure of the thick sedimentary successions of Melville Bay. A possible relationship between unusually thin, oceanic crust in northern Baffin Bay and slow to ultraslow spreading rates during its formation is discussed.

Wilfried Jokat supervised my scientific work at AWI. Sonja Suckro conducted the first onboard basic processing steps of the OBS data. I relocalized the OBS, identified and picked the reflected and refracted signals in the seismic sections of the OBS and calculated the *P* wave velocity model. The processing of gravity data was done by Ingo Heyde, BGR. The already processed reflection seismic data was provided by BGR and Cairn Energy. On basis of my velocity model, I calculated the density-model together with Ingo Heyde at BGR. I wrote the manuscript and prepared all figures for the article. Wilfried Jokat, Ingo Heyde and Volkmar Damm, who improved this article with their useful comments, did proofreading of the article.

3.2 Insights in the crustal structure of the transition between Nares Strait and Baffin Bay

Submitted to: Tectonophysics

Received: 23. June, 2015

Authors: Tabea Altenbernd¹, Wilfried Jokat¹, Ingo Heyde², Volkmar Damm²

¹Alfred Wegener Institute Helmholtz Centre for Polar and Marine Research, Am Alten Hafen 26, D-27568 Bremerhaven, Germany

²Federal Institute for Geosciences and Natural Resources, Stilleweg 2, D-30655, Hanover, Germany

Content and contributions to the article

The article provides new insights into the crustal structure of Northern Baffin Bay and southern Nares Strait along the profile AWI-20100300. For the first time, the transition between continental crust in the Smith Sound and oceanic crust in the northeastern Baffin Bay, and the type of margin were investigated based on refraction seismic data. Also, differences in the velocity distribution and crustal structure of Paleocene and Eocene oceanic crust along the profile are discussed.

Wilfried Jokat supervised my scientific work at AWI. Sonja Suckro (AWI) did the onboard processing of the OBS data. Further data processing, relocalization, modeling and interpretation of the refraction seismic data was done by myself. BGR and Cairn Energy provided the processed reflection seismic sections. The processed gravity data was provided by BGR. On basis of my *P* wave velocity model, I calculated the density-model together with Ingo Heyde at the BGR. I wrote the manuscript for the article and prepared all figures. The co-authors Wilfried Jokat, Ingo Heyde and Volkmar Damm improved the article with useful discussions.

3.3 The crustal fabric of the northeastern Baffin Bay

Submitted to: Journal of Geophysical Research - Solid Earth

Received: 26. June, 2015

Authors: Tabea Altenbernd¹, Wilfried Jokat¹, Ingo Heyde², Volkmar Damm²

¹Alfred Wegener Institute Helmholtz Centre for Polar and Marine Research, Am Alten Hafen 26, D-27568 Bremerhaven, Germany

²Federal Institute for Geosciences and Natural Resources, Stilleweg 2, D-30655, Hanover, Germany

Content and contributions to the article

The profile AWI-20100450 extends from the southern part of the Melville Bay area into the adjacent deep oceanic part of Baffin Bay. Since it is located parallel to the refraction seismic profile AWI-20100200, the crustal structure of different crustal types and the geometry of major tectonic features in northern and southern Melville Bay can be compared. Based on a compilation with the results of the two previous studies, the extent of crustal types and type of margin in the northeastern Baffin Bay is discussed.

Wilfried Jokat supervised my scientific work at AWI. The onboard-processing of the OBS data was done by Sonja Suckro. OBS relocalization, further processing, modeling and interpretation of the refraction seismic data was done by myself. Processed reflection seismic data was provided by BGR and Cairn Energy, processing of gravity data was conducted at the BGR by Ingo Heyde. On basis of my velocity model, I calculated the density-model together with Ingo Heyde at BGR. I wrote the manuscript and prepared all figures for the article. Wilfried Jokat, Ingo Heyde and Volkmar Damm revised the manuscript.

4 A crustal model for northern Melville Bay, Baffin Bay

Tabea Altenbernd¹, Wilfried Jokat¹, Ingo Heyde², Volkmar Damm²

¹Alfred Wegener Institute Helmholtz Centre for Polar and Marine Research, Am Alten Hafen 26, D-27568 Bremerhaven, Germany

²Federal Institute for Geosciences and Natural Resources, Stilleweg 2, D-30655, Hanover, Germany

4.1 Abstract

The interpretation of seismic refraction and gravity data acquired in 2010 gives new insights into the crustal structure of the West Greenland coast and the adjacent deep central Baffin Bay basin. Underneath Melville Bay, the depth of the Moho varies between 26 and 17 km. Stretched continental crust with a thickness of 25 to 14 km and deep sedimentary basins are present in this area. The deep Melville Bay Graben contains an up to ~11km thick infill of consolidated and unconsolidated sediments with velocities of 1.6 to 4.9 km/s. Seaward, at the ~60 km wide transition between oceanic and stretched continental crust, a mount-shaped magmatic structure is observed, which most likely formed prior to the initial formation of oceanic crust. The up to 4 km high magmatic structure is underlain by a ~2 km thick and ~50 km wide high velocity lower crust. More to the west, in the oceanic part of the Baffin Bay basin, we identify a two-layered, 3.5 to 6 km thin igneous oceanic crust with increasing thickness toward the shelf. Beneath the oceanic crust, the depth of the Moho ranges between 11.5 and 13.5 km. In the western part of the profile, oceanic layer 3 is unusually thin (~1.5 km). A possible explanation for the thin crust is accretion due to slow spreading, although the basement is notably smooth compared to the basement of other regions formed by ultra-slow spreading. The oceanic crust is underlain by partly serpentinized upper mantle with velocities of 7.6 to 7.8 km/s.

4.2 Introduction

The Baffin Bay is situated between Greenland and the Canadian Arctic archipelago. To the south the Baffin Bay is bounded by the Davis Strait. In the north the Greenland/Canadian continental margin and the Nares Strait bound the basin. All existing geodynamic models for the area propose that the Baffin Bay was formed during the separation of Greenland and North America.

While the crustal fabric of northern and southern Baffin Bay has been studied based on modern seismic refraction data (e.g., Suckro et al., 2012; Funck et al., 2012; Funck et al., 2006), the nature of crust in the deep, central Baffin Bay as well as the crustal type and thickness of the West Greenland continental margin, the Melville Bay, is still a matter of debate due to sparse deep seismic sounding lines. Previous work about the type of crust in central Baffin Bay and Melville Bay were based on the interpretation of potential field data (e.g., Chalmers and Pulvertaft, 2001; Oakey and Chalmers, 2012), seismic reflection data (e.g., Whittaker et al., 1997; Gregersen et al., 2013) and a few sonobuoy recordings (Keen and Barrett, 1972). All these models were lacking convincing deep

sounding seismic data sets to provide non-ambiguous evidence for the presence and distribution of oceanic crust, the location of the continent-ocean boundary, and stretched continental crust in this part of Baffin Bay. It remained unclear if oceanic crust or hyper-extended continental crust is present in central Baffin Bay.

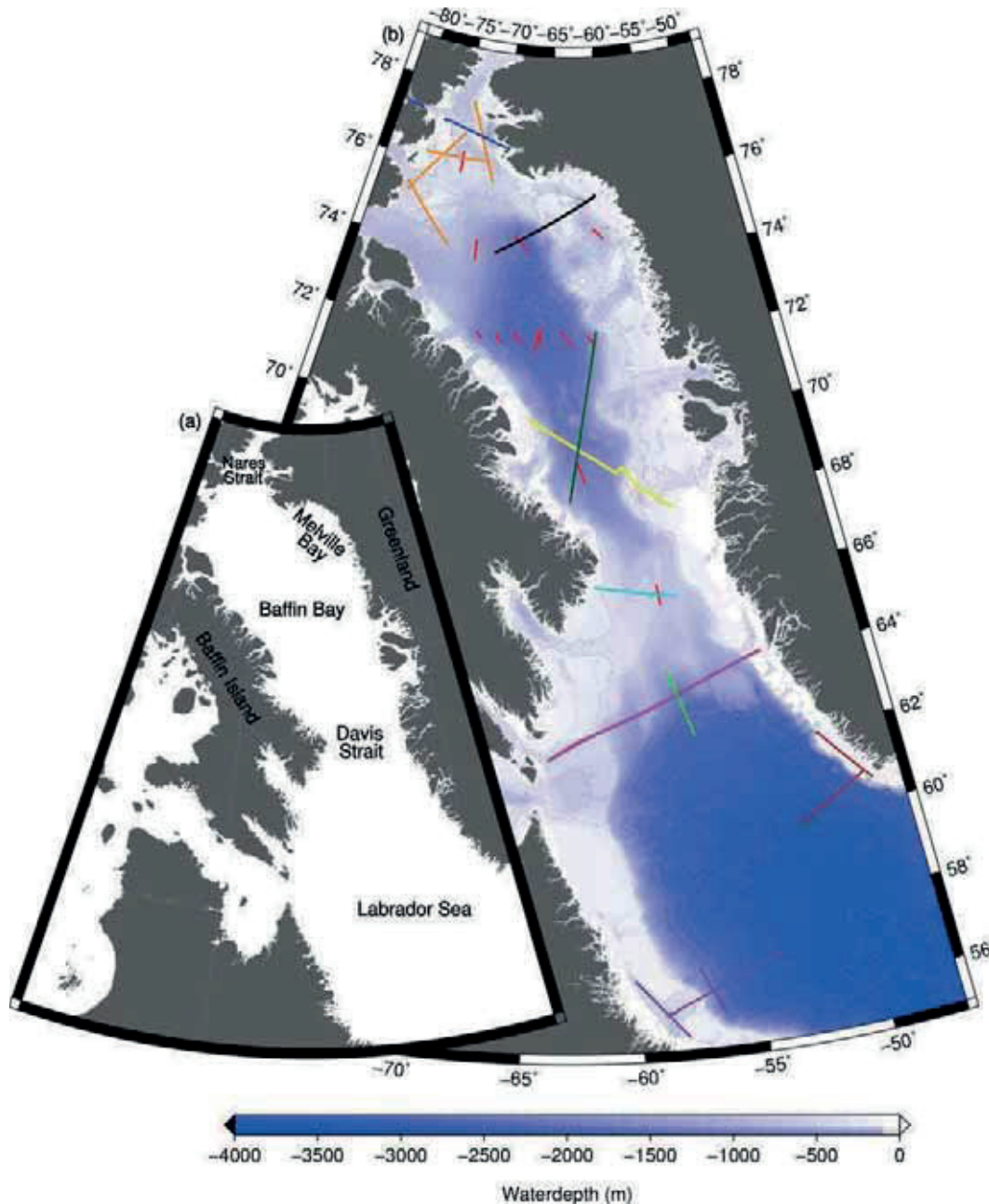


Figure 4.1: Bathymetric map of the Baffin Bay. Bathymetry is taken from the GEBCO Grid 2008. The colored lines mark locations of refraction seismic data already published: Blue line: Funck et al. (2006), orange lines: Reid and Jackson (1997), red lines: Keen and Barrett (1978), black line: AWI-20100200 (this study), dark green line: Suckro et al. (2012), yellow line: Funck et al. (2012), cyan line: Suckro et al. (2013), pink line: Funck et al. (2007), light green line: Gerlings et al. (2009), brown lines: Chian and Loudon (1994), and purple lines: Chian et al. (1995).

In summer 2010 a joint AWI (Alfred Wegener Institute Helmholtz Centre for Polar and Marine Research)-/BGR (Federal Institute for Geoscience and Natural Resources) geophysical experiment was conducted in the Baffin Bay to provide good constraints on the crustal composition of the area discussed above. During

the cruise, multi-channel and wide-angle seismic, gravity, and magnetic data were acquired on several profiles in the Greenlandic part of Baffin Bay (Damm, 2010).

In this study, we present a P wave velocity/density model of one of these profiles, which extends from the deep-sea area of northern Baffin Bay to the shelf area of Melville Bay (Figure 4.1). We will introduce the general geological structural units for the Melville Bay, which are typical for large parts of the NW Greenland margin.

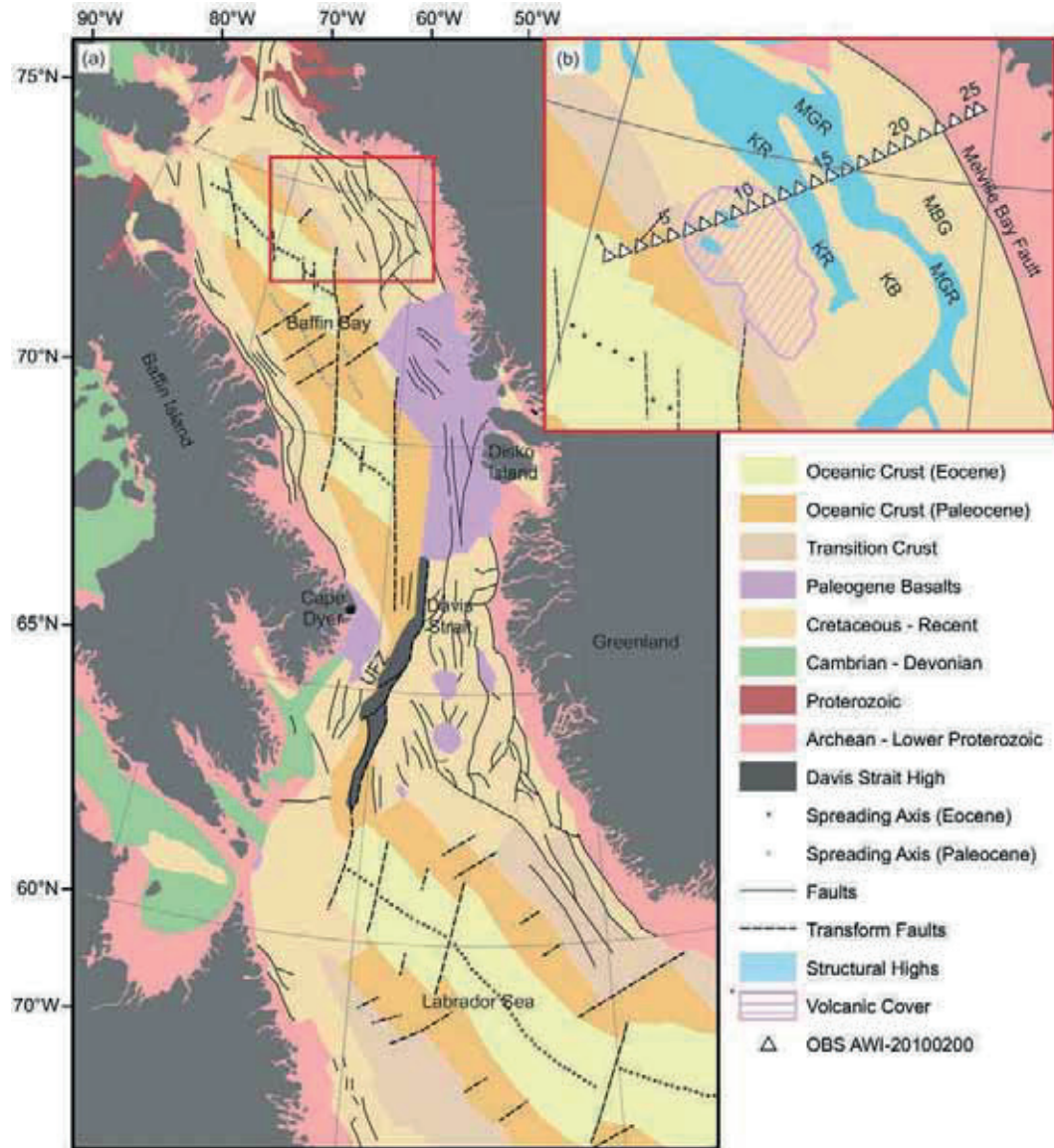


Figure 4.2: Geological map of the Baffin Bay, Davis Strait, and Labrador Sea (modified, after Oakey and Chalmers (2012) and Gregersen et al. (2013)).

(a) The red box marks the position of the close-up on the upper right corner.

(b) Close-up of the Melville Bay region. The location of structural highs in the Melville Bay (colored in light blue) and the volcanic cover in northern Melville Bay (purple hachure) are taken from Gregersen et al. (2013). White triangles mark the deployment positions of the OBS of refraction seismic profile AWI-20100200. OBS 1, 5, 10, 15, 20, and 25 are labeled with numbers. MBG: Melville Bay Graben, MBR: Melville Bay Ridge, KB: Kivioq Basin, KR: Kivioq Ridge, UFZ: Ungava Fault Zone.

4.3 Geological setting

The Melville Bay is part of the broad shelf area off West Greenland (Figure 4.1). The formation of the Baffin Bay is associated with the opening of the North Atlantic Ocean and is a continuation of the more southerly Labrador Rift system. The Ungava Fault Zone in the Davis Strait connects the extinct rift systems of the Labrador Sea and the Baffin Bay (Figure 4.2a).

Initial stretching in the Labrador Sea between Greenland and Canada started 223–150 Myrs ago during Late Triassic to Late Jurassic (Larsen et al., 2009). The initial breakup and the onset of volcanic activity in Baffin Bay may be explained by the arrival of the Greenland-Iceland mantle plume (Storey et al., 1998).

Magnetic spreading anomalies in the Labrador Sea are a consequence of seafloor spreading during the separation between Greenland and North America. The identification of the oldest spreading anomaly is still under debate; therefore, the exact location of the onset of oceanic crust is uncertain. Roest and Srivastava (1989) proposed initial spreading during the Cretaceous (chron 33), while Chalmers and Laursen (1995) assume that spreading started during the Paleocene (chron 27N).

The first period of rifting in the northern Labrador Sea was probably characterized by a long period of non-volcanic rifting (Funck et al., 2007). After the arrival of the Greenland-Iceland mantle plume underneath the Davis Strait region, plume-material led to underplating underneath southern Davis Strait (Gerlings et al., 2009) and also overprinted the originally non-volcanic margin of northern Labrador Sea (Funck et al., 2007). Up to 12 km thick oceanic crust formed after the beginning of seafloor spreading in northern Labrador Sea (Gerlings et al., 2009), while the central part of the southern Labrador Sea is underlain by 5.5 to 7 km thick oceanic crust (Chian and Loudon, 1994; Chian et al., 1995b). On the basis of seismic refraction data, Chian et al. (1995a and b) divided the crust of both conjugate margins in the southern Labrador Sea in three zones: The first, landward zone consists of 27 to 30 km thick, stretched continental crust, which thins seaward. In the adjacent seaward zone (zone 2), a high-velocity lower crust (6.4–7.7 km/s), probably consisting of serpentinized peridotite, is overlain by a 1 to 2 km thick upper crust with velocities of 4 to 5 km/s. Zone 3 is composed of a two-layered oceanic crust. In contrast to the Labrador Sea, no clear magnetic spreading anomalies have been identified in Baffin Bay, making an unambiguous classification of the Baffin Bay crust difficult. Furthermore, no deep seismic data have directly confirmed the presence of oceanic crust. However, Oakey (2005) and Oakey and Chalmers (2012) interpreted some diffuse magnetic anomalies in central Baffin Bay as indicators for Paleocene spreading. The location of the extinct spreading axis is proposed on the basis of a NW-SE trending linear gravity low present in central Baffin Bay (Whittaker et al., 1997). The main rifting episode and creation of oceanic crust in the Baffin Bay occurred during Paleocene and Eocene in two phases with different spreading directions (Roest and Srivastava, 1989; Oakey, 2005) (Figure 4.2a). During the reorientation of the spreading axis in the Eocene (chron 24 and 25), the NE motion of Greenland relative to North America changed to a NNW motion (Oakey, 2005). This change in plate kinematics is probably related to the opening of the North Atlantic Ocean between Greenland and Europe, which started about the same time (Talwani and Endholm, 1977).

Flood basalts are distributed over a wide domain within Baffin Bay. Offshore Paleogene flood basalts and outcrops of Paleogene volcanics can be found in the Disko Island region and also around Cape Dyer on Baffin Island (Figure 4.2a). Storey et al. (1998) dated two phases of volcanic activity in West Greenland: Paleocene flood basalt volcanism started at chron 27N (60.9–61.3 Ma) and lasted 1 to 2 Myrs. The onset of later Eocene volcanism in the region coincides with the reorientation in spreading direction at 55 Ma. During the Late Eocene or Early Oligocene, seafloor spreading in Baffin Bay ceased (Srivastava, 1978; Oakey and Chalmers, 2012).

Keen and Barrett (1972) published the first evidence for the presence of oceanic crust in Baffin Bay based on seismic refraction data recorded by a few sonobuoys (Figure 4.1). They reported that the central Baffin Bay is underlain by abnormally thin oceanic crust, which consists of oceanic layer 2, with velocities of 5–6.3 km/s and oceanic layer 3 with 6.5–6.9 km/s. In contrast, Reid and Jackson (1997) found no evidence for an oceanic layer 2 in the northern Baffin Bay. On their southernmost seismic refraction profile (Figure 4.1), they interpreted a layer with a velocity of 6.8 km/s as serpentinized mantle formed as a result of amagmatic rifting. Along their profile the crustal thickness of the serpentinized mantle varies from 6 to 13 km. The most recent deep seismic sounding results from the northern Davis Strait and southern Baffin Bay are reported by Suckro et al. (2012) and Funck et al. (2012). Both authors showed that oceanic crust is present in the southern Baffin Bay. In the *P* wave velocity model of Suckro et al. (2012), the average thickness of the oceanic crust is 7.5 km, covered by sediments of up to 6 km thickness. The crust consists of oceanic layer 2 with velocities of 4.8 to 6.4 km/s, and oceanic layer 3 with velocities between 6.4 and 7.2 km/s. The onset of oceanic crust is marked by the seaward termination of volcanic seaward dipping reflectors (SDRs). Therefore, like the northern Labrador Sea, the West Greenland margin of southern Baffin Bay is of volcanic origin. The oceanic crust in the central southern Baffin Bay (Funck et al., 2012) has a thickness of 5 to 9 km. Oceanic layer 3 shows a homogenous (6.8–7.2 km/s) and fairly constant velocity-distribution, while oceanic layer 2 is divided into segments by its velocity structure of 5.5 to 6 km/s or 6.1 to 6.5 km/s.

In the northeastern shelf area of Baffin Bay, extension and rifting of the crust during Cretaceous to Early Paleocene led to the formation of sediment-filled basins in the Melville Bay (Whittaker et al., 1997). The coast-parallel, NW trending basins are separated by ridges (Figure 4.2b). Gregersen et al. (2013) found indications for episodic rifting during their formation. The largest basin, the Melville Bay Graben (Figure 4.2b), is located between the Melville Bay Fault in the west and the Melville Bay Ridge in the east. The Melville Bay Graben infill is up to 13 km thick and consists of sediments and sedimentary rocks (Whittaker et al., 1997); some of the sedimentary rocks may already be metamorphosed and may contain intrusions (Gregersen et al., 2013). The Melville Bay Ridge separates the Melville Bay Graben from the parallel extending Kivioq Basin, where indications for a more than 10 km thick sedimentary infill have been found (Gregersen et al., 2013). To the west, the Kivioq Ridge limits the extent of the Kivioq Basin.

Numerous inversion structures caused by compression are present in the basins of northern Baffin Bay, like in the northern part of the Melville Bay Graben and the Kivioq Ridge (Oakey and Chalmers, 2012; Gregersen et al., 2013; Whittaker

et al., 1997). They probably developed during the Eocene, when the change in spreading direction in Baffin Bay also caused convergence, folding, and thrusting in the Canadian Arctic (Oakey and Chalmers, 2012).

4.4 Data acquisition and data processing

4.4.1 Seismic refraction data

Seismic refraction data along profile AWI-20100200 were collected with 25 DEPAS (Deutsche Geräte-Pool für amphibische Seismologie) ocean bottom seismometers (OBS). The 25 OBS were deployed with an average spacing of ~13 km. Each OBS was equipped with a 60 s three component broadband seismometer and a broadband hydrophone. The data were recorded with a sampling rate of 250 Hz.

For acquisition of seismic refraction data, an air gun array consisting of 8 G-Guns with a total volume of 68.2 L was used as seismic source. The shot interval was 60 s for all seismic refraction lines acquired during the cruise. The average shot distance was 150 m (for further information, see Damm, 2010).

A multichannel seismic reflection profile BGR10-302 was acquired separately along the deep seismic sounding line AWI-20100200 to constrain the geometry of the basement and distribution of the sediments.

After acquisition of the OBS data, the raw data of the four channels were converted to SEG-Y-format. Unfortunately, the recorder of OBS 10 was not working properly. Therefore, a time-offset of one second of recording time had to be subtracted from the data set. After that, the fit of the direct water wave was excellent. If necessary, the positions of the OBS were relocalized using direct arrivals for estimating the amount of the drift during the descent of the OBS to the seafloor.

4.4.2 Gravity data

Gravity data were continuously acquired throughout the entire cruise with the sea gravimeter system KSS31, serial No. 25. The observed gravity data were tied to the International Gravity Standardization Net IGSN 71 by harbor measurements conducted in Reykjavik and Bremerhaven. After the termination of the cruise, the instrumental drift was determined to 8.6 mGal in 70 days. However, the correction of the instrumental drift increased the crossover errors and led also to a greater mismatch between the measured gravity and the gravity data of satellite altimetry. It is possible that the mismatch between the measured gravity values in Bremerhaven and Reykjavik results from a slightly inaccurate scale factor of the KSS31. Therefore, the instrumental drift was not corrected. The normal gravity (WGS84) and the Eötvös effect were subtracted to calculate the free-air gravity anomalies.

4.5 Modeling

4.5.1 Seismic refraction data

The software zp (written by Barry Zelt, see <http://www.soest.hawaii.edu/~bzelt/zp/zp.html>) was used to pick refracted and reflected phases. Prior to picking, a band-pass filter from 4 to 13.5 Hz and an automatic gain control (AGC) with a time window of 1 s was applied. Because

of its good quality, the data of the OBS hydrophone channel were used to pick P wave travel time arrivals of sedimentary layers, crustal layers, and the upper mantle. Sediment, crustal, and upper mantle phases were identified within the seismic sections of most of the OBS.

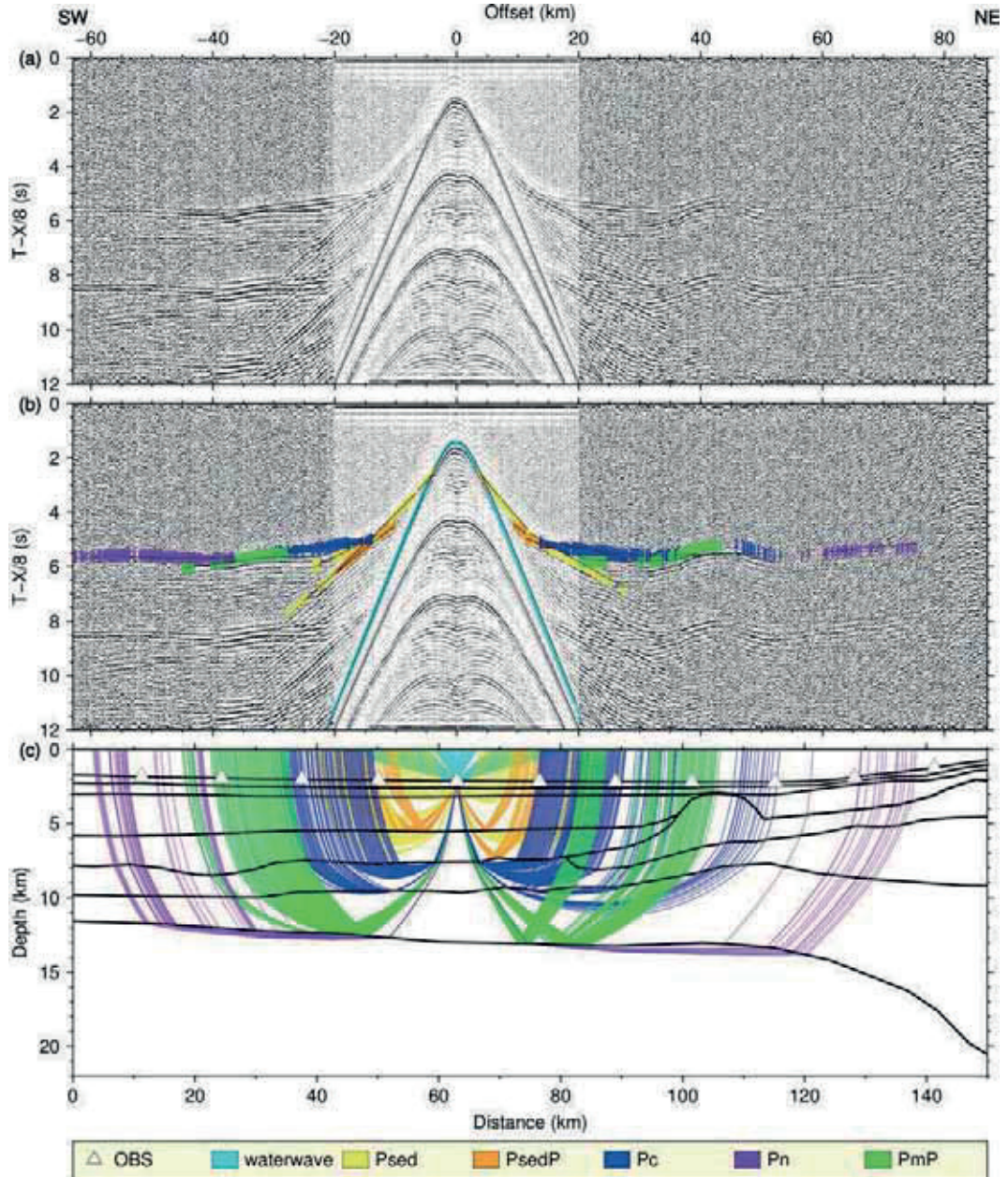


Figure 4.3: Seismic sections, picked phases, and modeled raypaths of OBS 5.

(a) Seismic section of OBS 5 (hydrophone component), with a reduction velocity of 8 km/s.

(b) Picked phases (colored lines) and modeled travel times (black lines) within the seismic section shown above. The length of the picks corresponds to the assigned pick uncertainties.

(c) Modeled raypaths of the picks shown above within the P wave velocity model.

Examples of picked phases of OBS 5, OBS 11, OBS 17, OBS 21, and OBS 23 are shown in Figures 4.3 to 4.7. Reflected phases in the unconsolidated and consolidated sedimentary layers of the model are named $P_{sed}P$, refracted phases P_{sed} . The oceanic crust is divided in oceanic layer 2 and 3: refracted phases of oceanic layer 2 are labeled P_{c1} , while P_{c2} corresponds to the refracted phases of oceanic layer 3. Reflected phases on top of volcanic layers are named P_bP ,

refracted phases within volcanic phases P_b . Moho reflections are named P_mP ; P_n indicates refracted signals from the upper mantle.

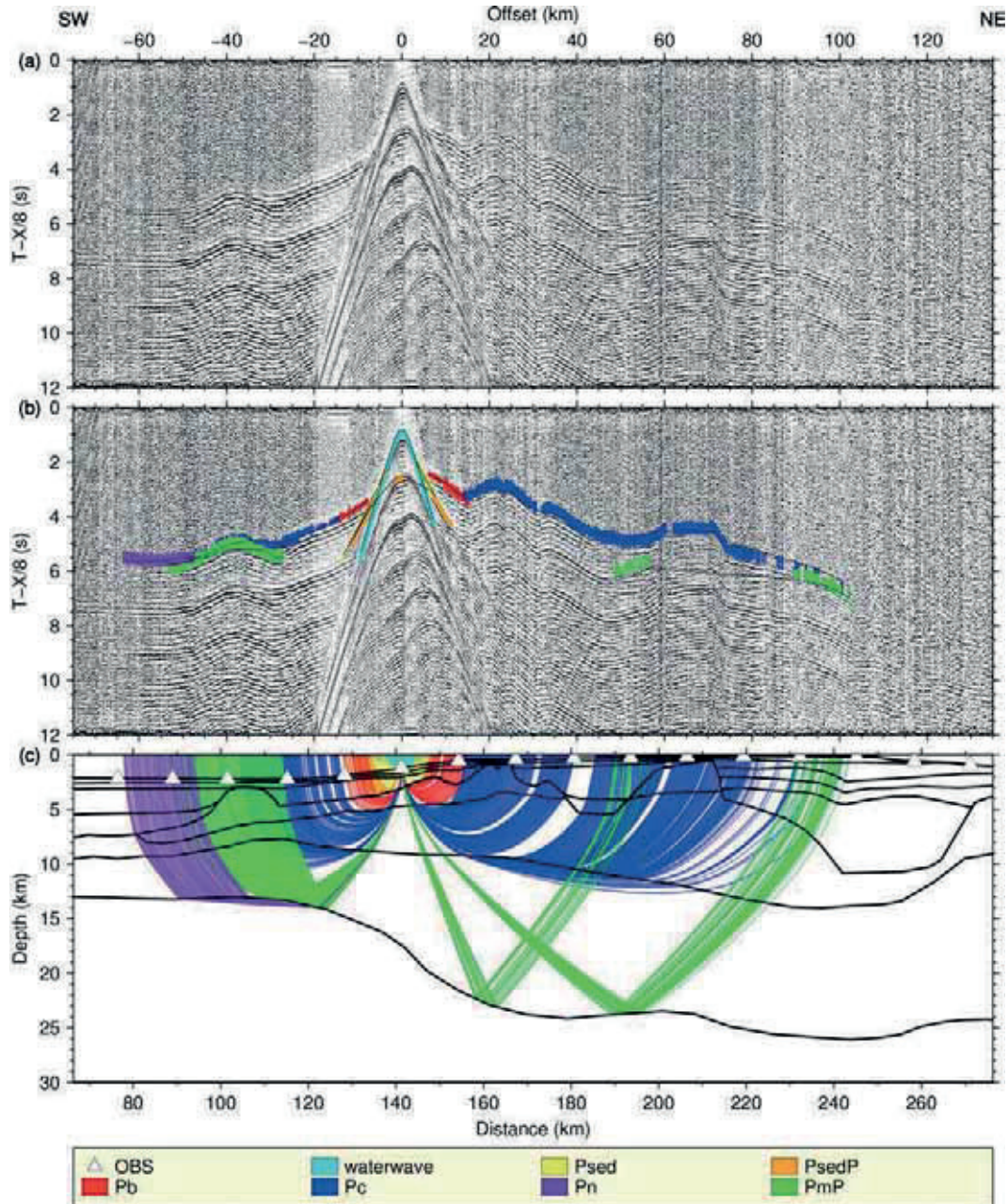


Figure 4.4: Seismic sections, picked phases, and modeled raypaths of OBS 11.

(a) Seismic section of OBS 11 (hydrophone component), with a reduction velocity of 8 km/s.
(b) Picked phases (colored lines) and modeled travel times (black lines) within the seismic section shown above. The length of the picks corresponds to the assigned pick uncertainties.
(c) Modeled raypaths of the picks shown above within the P wave velocity model.

For the geometry setup of the 321 km long starting model, the relocated OBS were projected on a line. Starting point of that line was in the west (shot point 1). Its endpoint in the east was the last shot point of the seismic reflection profile BGR10-302. Distances between shots and OBS locations remained unchanged.

For most of the profile, the position of the main structural elements, like ridges and basins, and the topography of the crustal basement were taken from

seismic reflection profile BGR10-302 (Figure 4.8) and incorporated into the velocity model. The top of the crustal basement beneath the sediment packages in the western parts of the profile (km 40–80) could not be imaged by the seismic reflection profile BGR10-302.

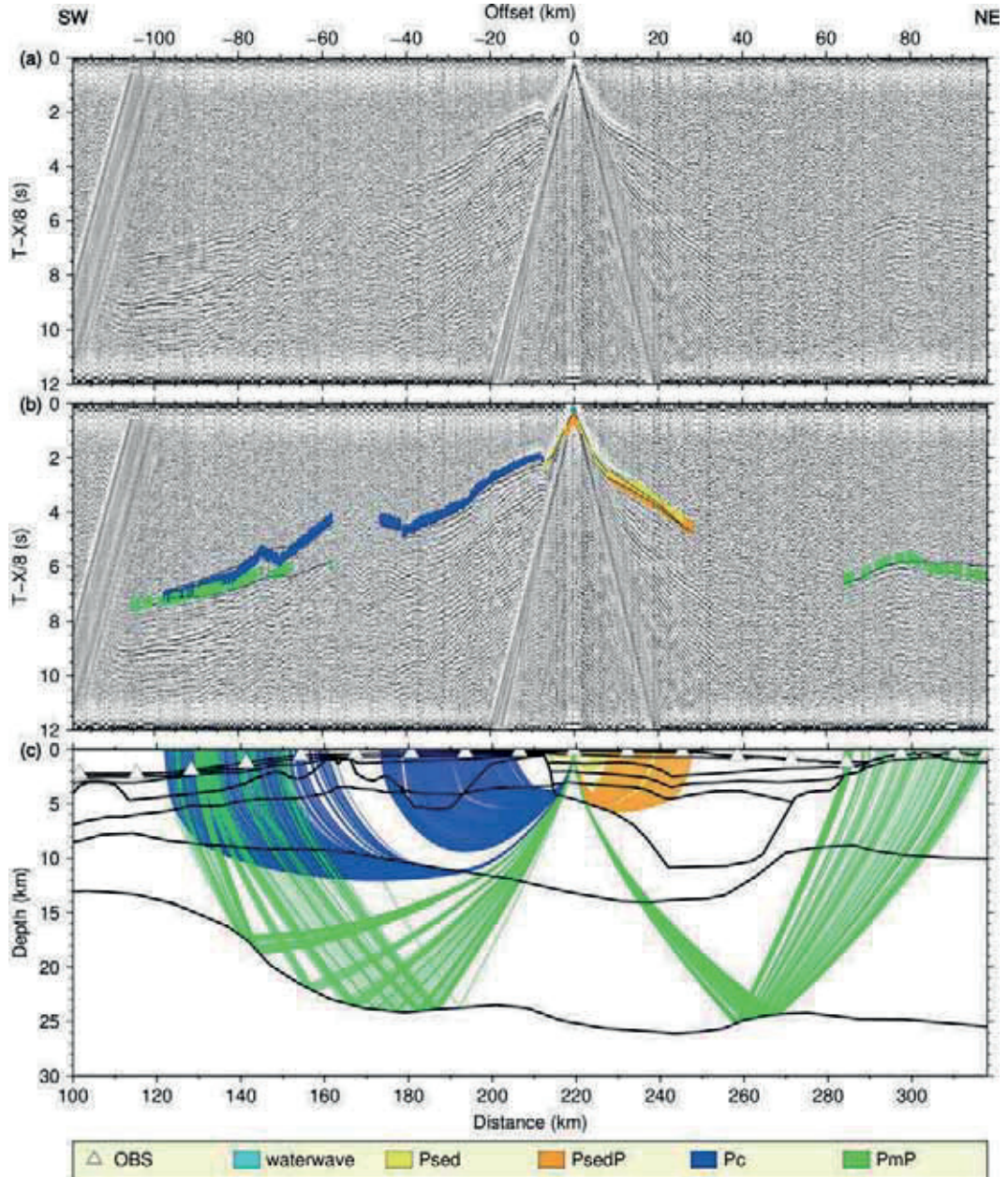


Figure 4.5: Seismic sections, picked phases, and modeled raypaths of OBS 17.

(a) Seismic section of OBS 17 (hydrophone component), with a reduction velocity of 8 km/s.

(b) Picked phases (colored lines) and modeled travel times (black lines) within the seismic section shown above. The length of the picks corresponds to the assigned pick uncertainties.

(c) Modeled raypaths of the picks shown above within the *P* wave velocity model.

Forward modeling of the *P* waves was performed with the raytracing software RAYINVR (Zelt and Smith, 1992). The final velocity model is shown in Figure 4.9a. The model comprises in total 10 velocity layers.

For an easy handling of the software, the amount of layers was kept to a minimum. Therefore, velocity layer 7 was used to model basaltic, sedimentary, and crustal phases in different parts of the profile. Figure 4.9b represents a

structural interpretation of the velocity model and divides or combines velocity layers in geological units. More details of the models will be discussed later.

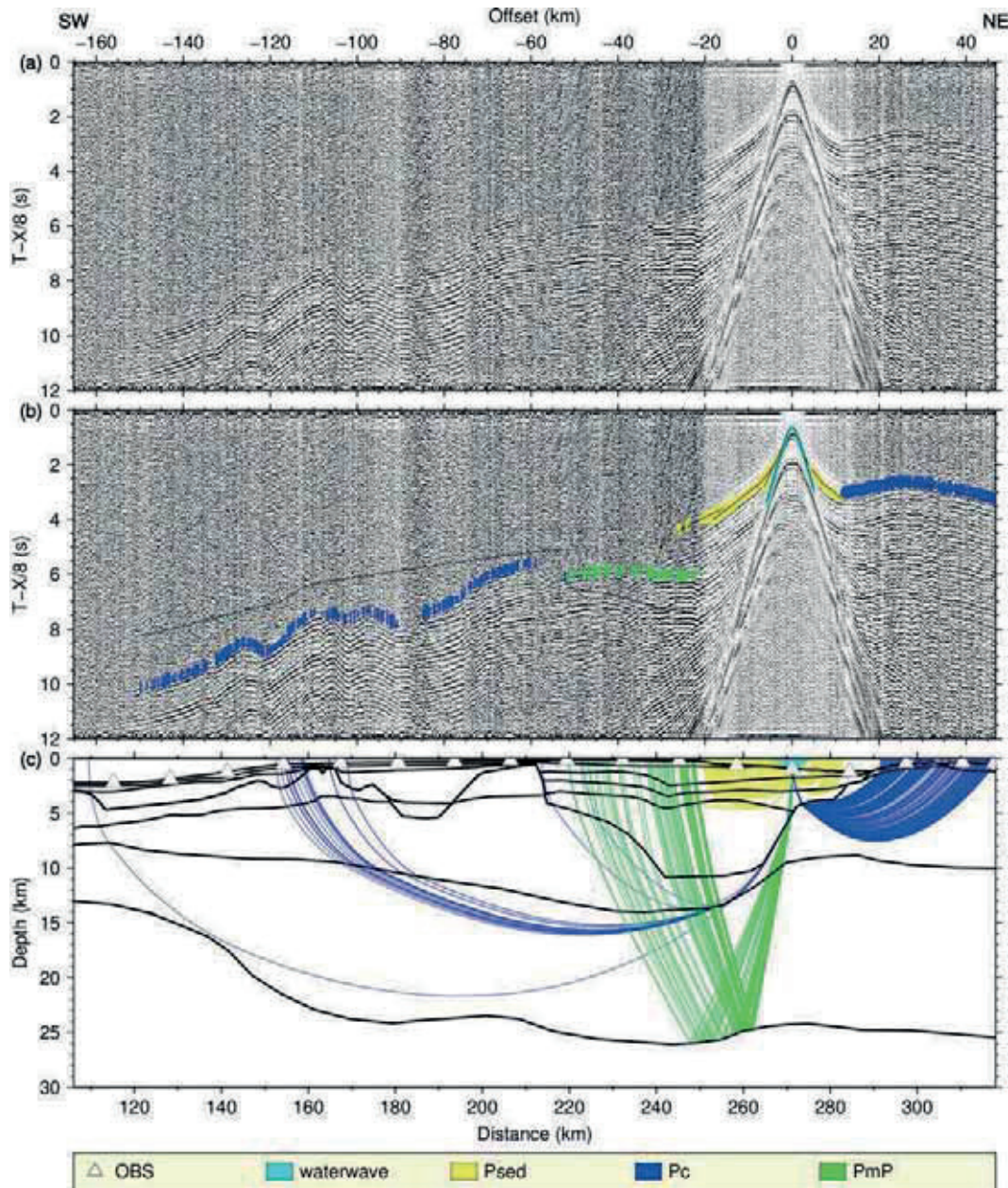


Figure 4.6: Seismic sections, picked phases, and modeled raypaths of OBS 21.

- (a) Seismic section of OBS 21 (hydrophone component), with a reduction velocity of 8 km/s.
- (b) Picked phases (colored lines) and modeled travel times (black lines) within the seismic section shown above. The length of the picks corresponds to the assigned pick uncertainties.
- (c) Modeled raypaths of the picks shown above within the *P* wave velocity model.

4.5.1.1 Error analysis and model uncertainty of the velocity model

It was difficult to accurately model the crustal phases of OBS 21 (Figure 4.6). The modeled raypaths of the crustal units did not reasonably fit the observed crustal phases. Therefore, it was decided to model the ray paths of the nearby OBS as good as possible and to neglect the accuracy of modeling the crustal phases of OBS 21. The problematic fit is probably caused by complex geological structures beneath OBS 21, which was situated above the steep Melville Bay Fault.

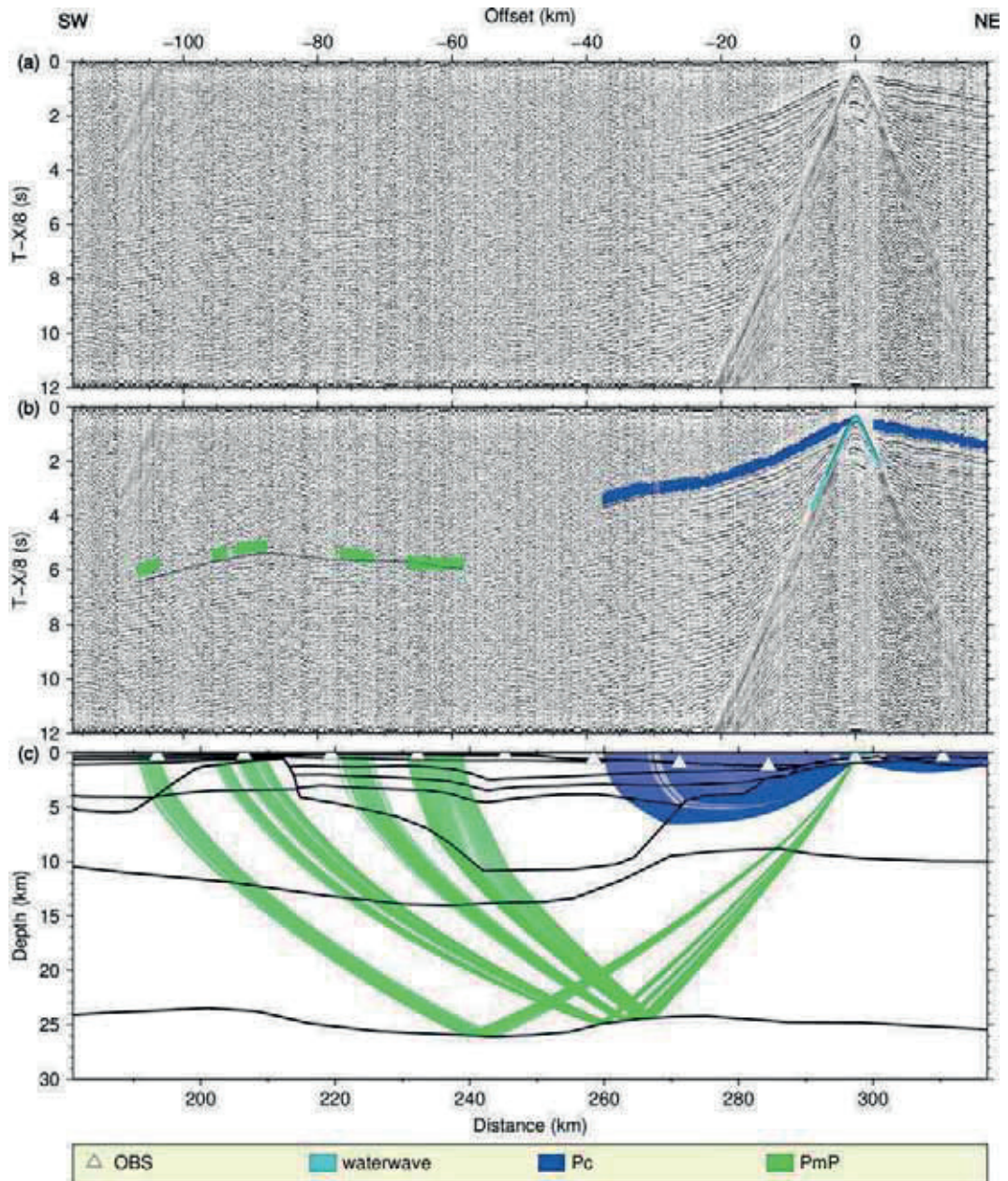


Figure 4.7: Seismic sections, picked phases, and modeled raypaths of OBS 23.
(a) Seismic section of OBS 23 (hydrophone component), with a reduction velocity of 8 km/s.
(b) Picked phases (colored lines) and modeled travel times (black lines) within the seismic section shown above. The length of the picks corresponds to the assigned pick uncertainties.
(c) Modeled raypaths of the picks shown above within the P wave velocity model.

Table 4.1 shows the number of picks, the RMS misfit and the χ^2 value for the 10 velocity layers. In total, 23,594 picks were used for modeling. As a result of the described problem, the picks of the deep crustal phases (velocity layer 9) of OBS 21 were excluded for the error analysis. Depending on the signal-to-noise ratio and the quality of the picks, pick uncertainties between 55 and 200 ms were assigned. The root mean square (RMS) misfit between calculated and picked travel times for different velocity layers lies in a range of 45 ms to 198 ms. The average RMS misfit is 144 ms. The normalized χ^2 value is 0.97, which is close to the perfect value of 1.

Table 4.1: Nomenclature of picked phases, number of picks within the velocity layer (n), RMS misfit, and χ^2 .

Velocity layer	Phase	n	RMS (s)	χ^2
1, rfl	waterwave	2176	0.089	0.790
2, rfr	P_{sed}	49	0.076	0.907
3, rfr	P_{sed}	305	0.060	0.487
3, rfl	$P_{sed}P$	47	0.158	0.661
4, rfr	P_{sed}	1306	0.062	0.392
4, rfl	$P_{sed}P$	691	0.077	0.291
5, rfr	P	233	0.045	0.214
5, rfl	$P_{sed}P$	9	0.081	0.206
6, rfr	P_{sed}	1210	0.078	0.338
6, rfl	P_{sed}	353	0.099	0.506
7, rfr	P_b, P_c, P_{sed}	966	0.101	0.623
7, rfl	P_bP	302	0.111	0.535
8, rfr	P_c	4794	0.148	0.969
8, rfl	P_cP	63	0.176	0.961
9, rfr	P_c	5043	0.164	1.157
9, rfl	P_mP	4306	0.198	1.718
10, rfr	P_n	1741	0.120	0.563
All layers	All phases	23594	0.144	0.974

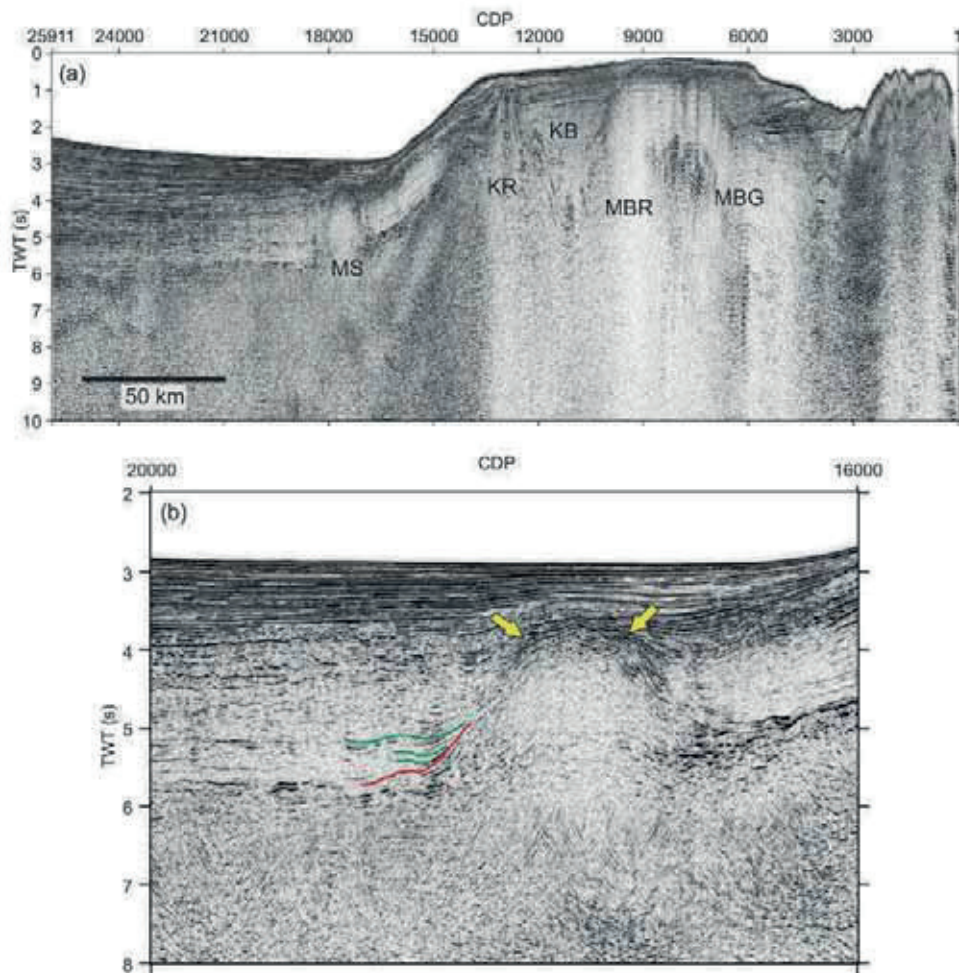


Figure 4.8: Seismic reflection profile BGR10-302.

(a) The main structural features are labeled. KR: Kivioq Ridge, KB: Kivioq Basin, MBR: Melville Bay Ridge, MBG: Melville Bay Graben, MS: magmatic structure.

(b) Close-up of the magmatic structure in the western part of the profile. The green lines mark sediment phases, which onlap on the lower part of the magmatic structure (red line). The yellow arrows show where horizons on top of the magmatic structure are pulled up.

Depth and velocity uncertainties of the model have been determined with the method described by Schlindwein and Jokat (1999). The *P* wave velocity uncertainties for the sedimentary layers range from ± 0.1 km/s for the upper sedimentary layers (velocity layers 2 to 5) to ± 0.2 km/s for lower sedimentary layers on top of the thin crust in the western part of the profile and for the lowermost sediment layer in the Melville Bay Graben. Within the crust and the upper mantle, a velocity error of ± 0.2 km/s is determined. Sedimentary layers have a depth uncertainty of ± 0.1 km, with exception of the lowermost sedimentary layer in the Melville Bay Graben (velocity layer 7), which depth can be varied ± 0.3 km at its top and ± 0.5 km at its base. The depth uncertainty for the crustal layers is ± 0.2 km. The depth of the crust-mantle boundary (Moho) is constrained to ± 0.3 km in the western part and ± 1 km below the thick continental crust in the eastern part of the profile.

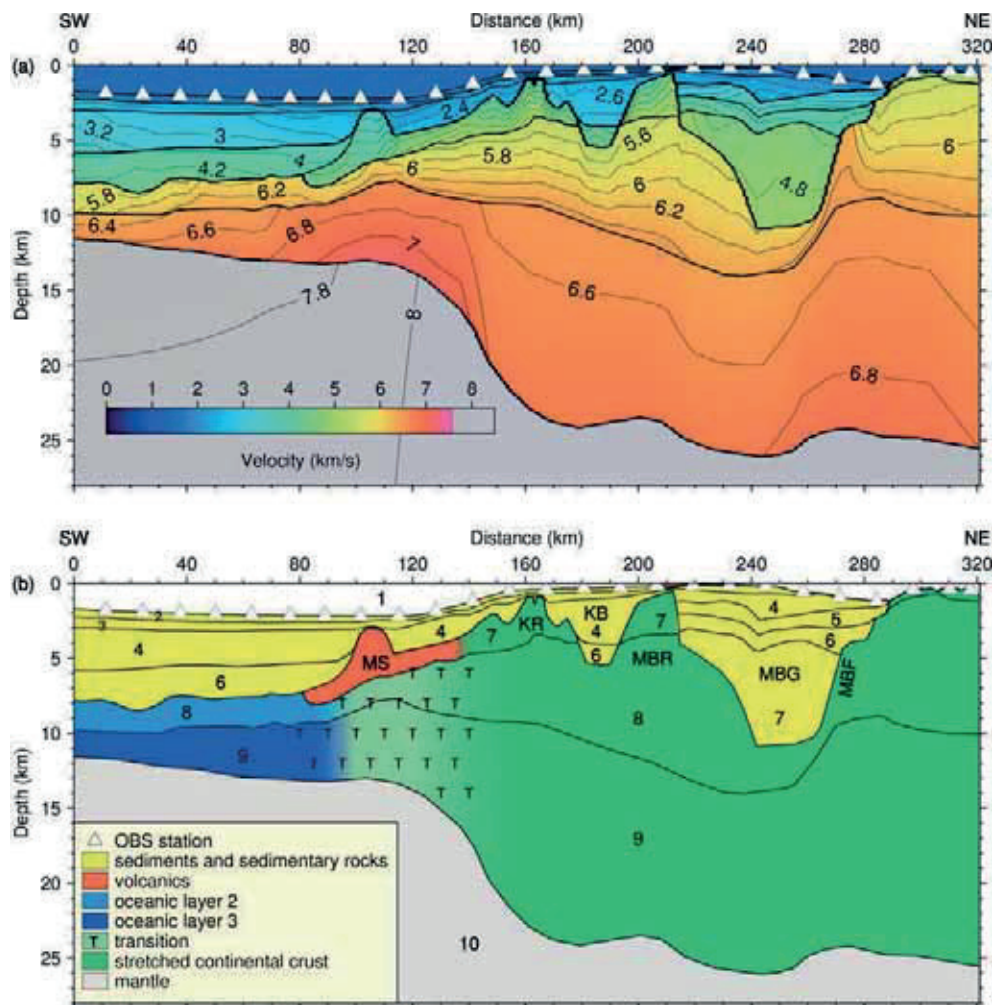


Figure 4.9: (a) *P* wave velocity model and (b) geological interpretation of AWI-20100200.

(a) Thick black lines mark the layer boundaries between the velocity layers, thin black lines are the contour lines of *P* wave velocities.

(b) The black lines mark the layer boundaries between the velocity layers. The different velocity layers are labeled with numbers. MS: magmatic structure, MBR: Melville Bay Ridge, KR: Kivioq Ridge, KB: Kivioq Basin, MBG: Melville Bay Graben, MBR: Melville Bay Ridge, T: transition.

The ray coverage for different velocity layers of the velocity model is shown in Figures 4.10 and 4.11. For most of the model, the ray coverage is excellent except for the deep crustal parts in the easternmost parts of the profile.

Refracted arrivals of the lower crust (velocity layer 9) are rare between km 230 to 320 and km 0 to 60. Also, the uppermost sedimentary layers are often not constrained by refracted arrivals. One explanation is that the water wave masks the signals from these uppermost layers. Furthermore, only the uppermost part of layer 7 in the Melville Bay Graben and layer 4 in the Kivioq Basin is well constrained by refractions. In both cases, reflections from the base of these layers were taken to model the thickness of these units. The boundary between the layers 8 and 9 is only constrained by reflections at km 220–250 (Figure 4.10). Between km 110 and 321 (Figure 4.9), the position of the boundary was chosen for a better adjustment of the velocity gradient in this region. The depth of crust-mantle boundary (Moho) is well constrained by numerous reflections between km 20 and 270. Eastward of km 140, no P_n phases are present (Figure 4.11). Also, the modeled velocity gradient in the upper mantle east of km 140 is not constrained by refractions.

The velocity resolution model (Figure 4.12) shows how well the velocities are constrained by rays. To obtain the velocity resolution, the resolution matrix diagonals for the velocity nodes were gridded. A resolution matrix value of 1 is the optimum for an excellent resolution, but values greater than 0.5 are usually considered to be well resolved (Lutter and Nowack, 1990). Altogether, the resolution of our model is good; however, lower resolution is generally observed where there is sparse or absent ray coverage, for example beneath the Melville Bay Graben and on the edges of the model. Low resolution of velocity layer 7 between km 80 and 180 and velocity layer 5 between km 240 and 290 can be explained by only little or no overlap of the rays of nearby OBS in these regions.

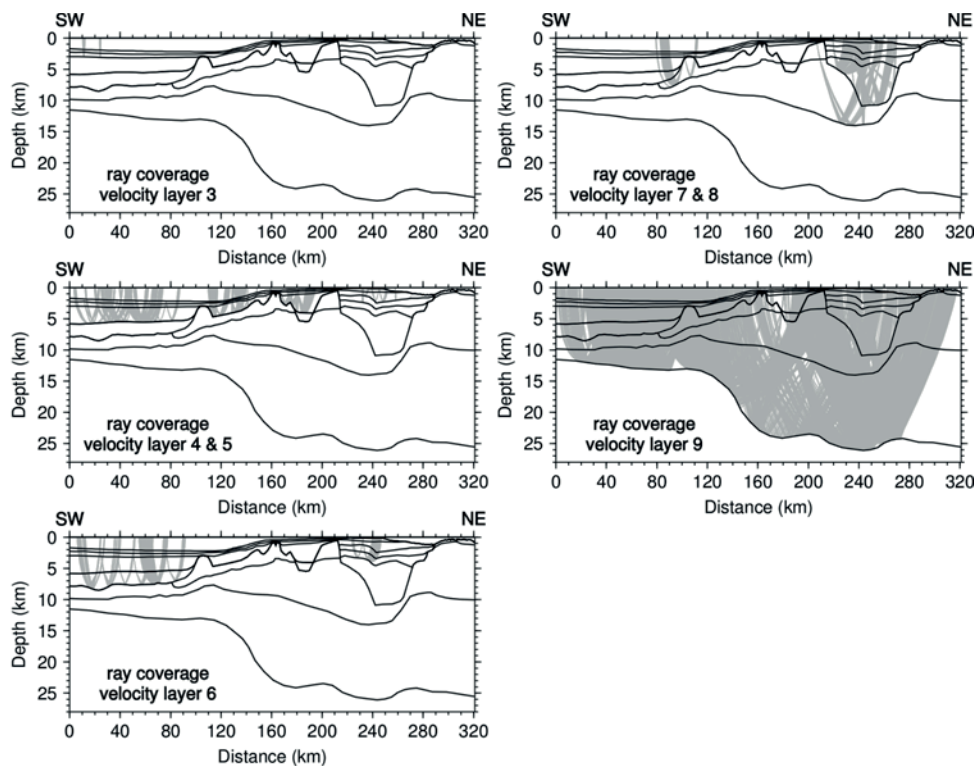


Figure 4.10: Reflected rays at the base of velocity layer 3 to 9. The reflected rays are colored gray; black lines mark the layer boundaries.

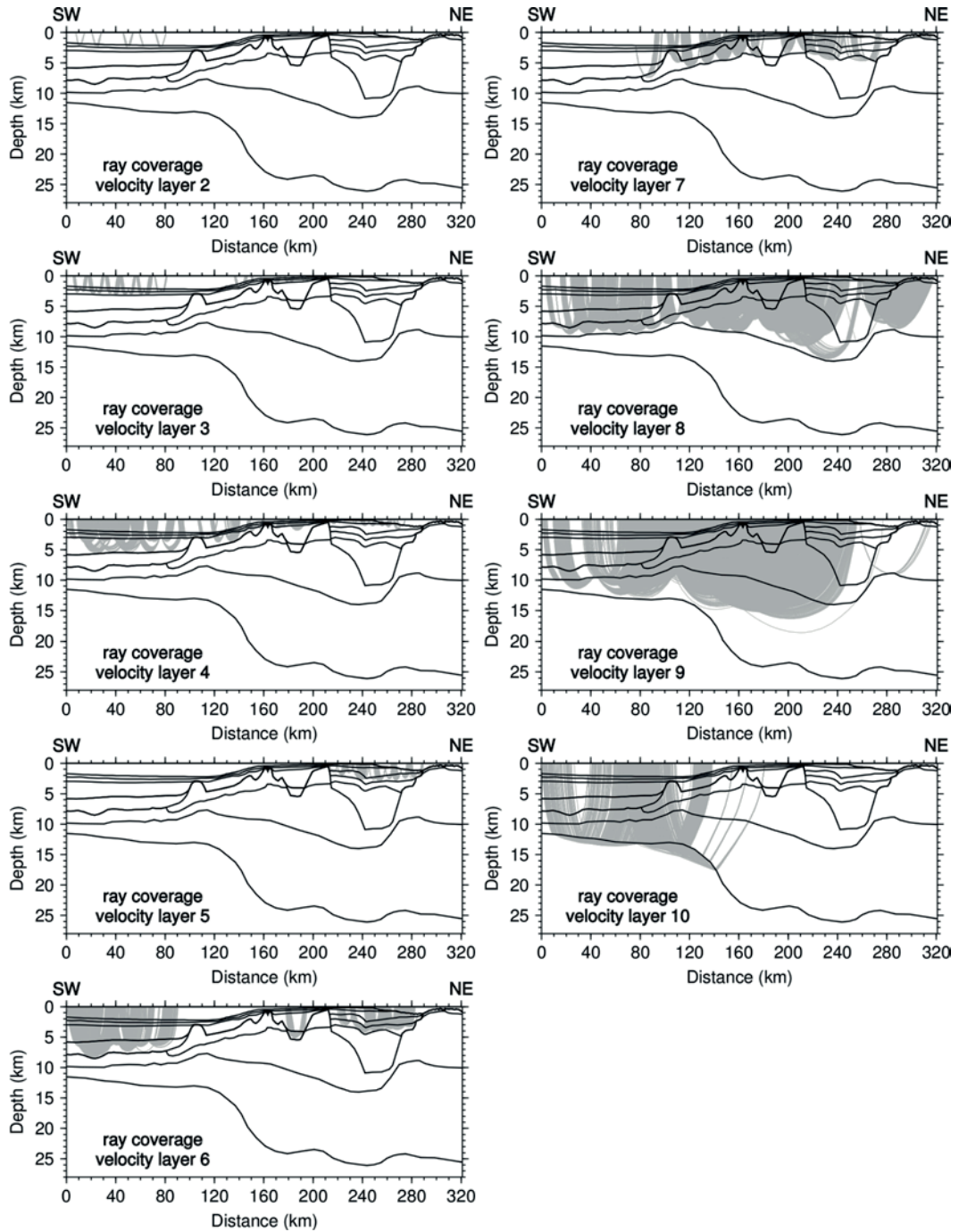


Figure 4.11: Ray coverage (refracted rays) of velocity layer 2 to 10. The refracted rays are colored gray; black lines mark the layer boundaries.

4.5.2 Gravity data

Density modeling was conducted to ensure that the crustal model derived from seismic data is consistent with the observed gravity data. The software GM-SYS (Northwest Geophysical Associates, Inc.) was used for forward modeling.

The geometry and layer boundaries of the seismic velocity model were taken as an input for the density model. Average velocities within the units were taken from the velocity model to calculate densities according to a velocity-density function from Barton (1986). To keep the model simple some sedimentary layers are combined into one density unit, for example sedimentary layers in the Melville Bay Graben.

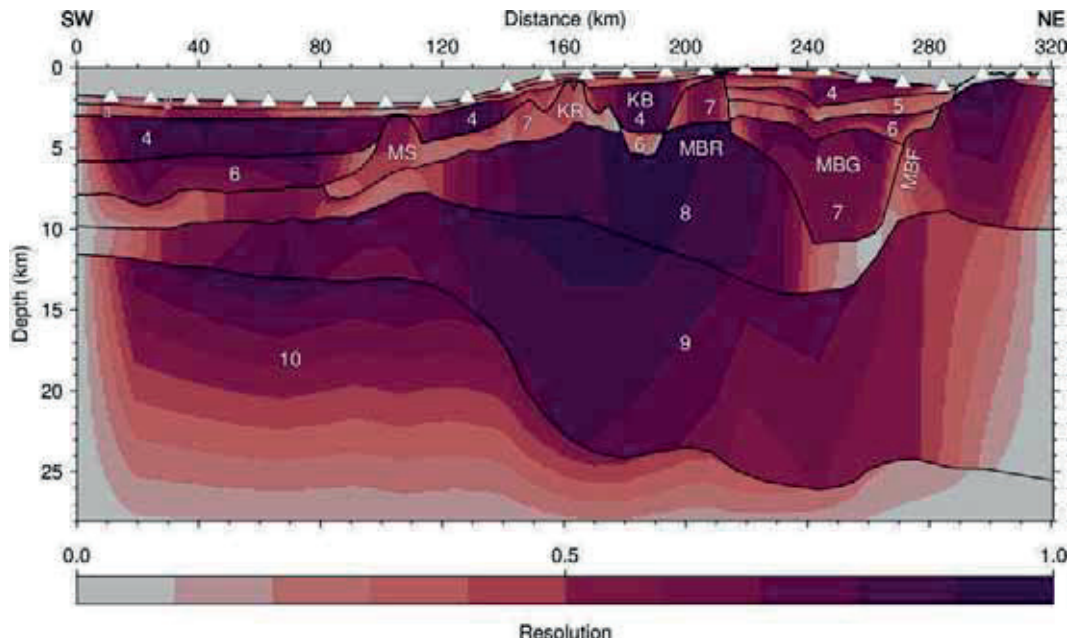


Figure 4.12: Diagonal values of the resolution matrix of the *P* wave velocity model. White triangles mark the location of OBS stations; thick black lines mark the layer boundaries between the velocity layers. The different velocity layers are labeled with white numbers. MS: magmatic structure, MBR: Melville Bay Ridge, KR: Kivioq Ridge, KB: Kivioq Basin, MBG: Melville Bay Graben, MBF: Melville Bay Fault.

The starting model already showed a good fit between the observed and calculated gravity data in the eastern part of the model. The greatest misfit was located in the western Melville Bay Graben, where the observed gravity was 30 mGal higher than the calculated values. Therefore, in some areas minor adjustments in the model were necessary to achieve a better fit between calculated and observed values (Figure 4.13). To allow density variations within a layer, some of them were divided into two, for example in the Melville Bay Graben. Also, smaller density bodies were added in the Melville Bay Ridge and Kivioq Basin to better fit the observed data and to include sedimentary layers visible in the seismic reflection data, which were not resolvable in the wide-angle data, because of their limited thickness. Between km 120 and 200, the layer boundaries between upper and lower continental crust were slightly changed ± 1 km. The largest adjustments were necessary between km 200 and 300. The velocity model in this area is only constrained by few reflections between km 220 and 250, and was mainly introduced to adjust the velocity gradient in this part of the model. Between km 200 and 265, the boundary between upper and lower crust was shifted upward (maximum 3 km). Due to higher velocities in the upper crust observed eastward of the Melville Bay Fault (km 265–300), a wedge-shaped structure of the lower crust, which almost reaches the top of the upper crust, was included. The geometry of this structure was also adjusted to obtain a good fit. Other misfits of about 15 mGal were present in the locations of pronounced features like Kivioq Ridge and Melville Bay Ridge. Underneath the Kivioq Ridge, the boundary between upper and lower continental crust was shifted less than 1 km upward between km 150 and 170. Also, a body of lower density (2500 kg/m^3) was included in the upper part of the Melville Bay Ridge for a better fit.

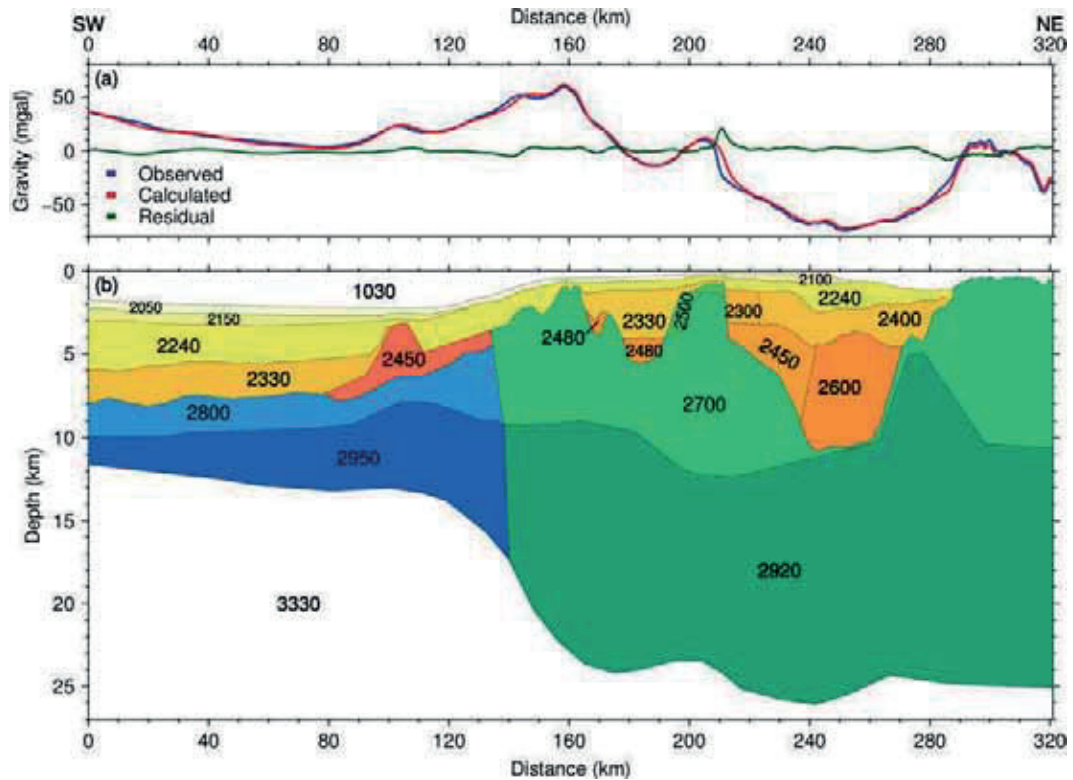


Figure 4.13: Gravity modeling along profile AWI-20100200.
(a) Observed and calculated free-air gravity anomalies.
(b) Density model, the used density values are given in kg/m³.

4.6 Results and interpretation of crustal units

Due to variations in the *P* wave velocity structure and thickness of the crust, profile AWI-20100200 has been divided into three parts: oceanic crust, transitional crust, and rifted continental crust. We introduce in the following chapter the results and present an interpretation of this part of the velocity and density model.

4.6.1 Velocity model of AWI-20100200

4.6.1.1 Oceanic crust (km 0–80)

This part of the Baffin Bay Basin is underlain by a 3 to 6 km thick, two-layered crust (Figure 4.9). The igneous oceanic crust is covered with 6 to 8 km thick sediments with seismic velocities of 1.7 to 4.5 km/s. Toward the shelf edge, the average sediment thickness and the sediment velocity decrease. Four sedimentary layers can be distinguished (velocity layer 2, 3, 4, and 6). Velocity layers 2 and 3 have velocities between 1.7 and 2.95 km/s. The modeled velocities of layer 4 range between 2.5 and 3.5 km/s and decrease from west to east. The base of velocity layer 4 is well documented by reflections, which can be identified in the data sets of OBS 1 to 8. This reflection is caused by a high impedance contrast between velocity layer 4 and 6. The velocities of velocity layer 6 range between 3.95 and 4.4 km/s and are, therefore, much higher than the velocities in layer 4. The observed velocities of the lowermost sediment layer (velocity layer 6) are unusually high (~4 km/s) and lie in a range also typical for basalts. Therefore, we try to classify the nature of layer 6 by using the reflection pattern of BGR10-302. The seismic reflection pattern in the western

part of profile BGR10-302 (Figure 4.8a, km 0 to 50) does not show a hummocky surface typical of volcanic rocks. In contrast, between km 50 and 80, it is not clear, if only sediments or also intercalated basalts are present. Sedimentary layers with similarly high velocities, which are located on top of the oceanic crust, have already been observed by Keen and Barrett (1972) in the central Baffin Bay: In their model, oceanic layer 2 is overlain by consolidated sediments with velocities of 3.9 to 4.2 km/s. As the high-velocity sediments found in this study are present in depths greater than 5.5 km and are overlain by 3 to 4 km thick sediments, compaction and consolidation seem to be a reasonable explanation for the high velocity values. Also, the density model shows a relatively low density of 2330 kg/m³ for this unit. Therefore, we interpret this layer to consist of consolidated sediments. Thin basaltic layers from km 50 to 80 might be intercalated.

In general, the velocities of the igneous crust increase toward the shelf. The depth of the uppermost crustal layer (velocity layer 8) is constrained by various reflections. While the average thickness of the first layer is fairly constant at 2 km, the observed velocities range between 5.6 and 6.4 km/s. The underlying layer (velocity layer 9) shows velocities ranging from 6.25 to 7.0 km/s, and has a thickness of 1.8 to 3.9 km. The layer thickens toward the east/shelf. Between both layers, no intra-crustal reflections have been observed. The depth of the Moho is well constrained by reflections and lies in a depth range of 11.5 to 13.5 km.

The velocities at the top of the upper mantle are constrained by P_n phases between km 10 and 90. The upper mantle velocities are relatively low (7.65 km/s). These velocities increase to 7.8 km/s toward the West Greenland shelf.

We classify the thin crust to be composed of oceanic layer 2 and a thin oceanic layer 3. To check if the thin crust found is of oceanic origin, we compare our results with the findings of White et al. (1992) (Figure 4.14) and compare the velocity-depth-profiles taken every 10 km with velocity-depth profiles typical for Atlantic oceanic crust of an age between 58 and 112 Myrs.

According to White et al. (1992), the mean thickness of normal igneous oceanic crust is about 7.1 km, with oceanic layer 3 having smaller velocity gradients than the overlying layer. Oceanic layer 3 is normally more than twice as thick as oceanic layer 2. Along our profile, the crustal thickness is well below the values for normal oceanic crust (Figure 4.14). Instead, oceanic layer 3 in the western part of the profile is unusually thin (~1.5 km). Its thickness is similar to oceanic layer 2 or even thinner in some parts of the profile. Landward, the thickness of layer 3 increases. With exception of the very eastern part of the crust, which is not well constrained by refractions, the velocity gradient of the underlying layer 3 is lower than the velocity gradient in oceanic layer 2.

In normal oceanic crust, oceanic layer 2 has velocities within a range of 2.5 to 6.6 km/s, typical velocities for layer 3 are 6.6 to 7.6 km/s (White et al., 1992). The velocities of the oceanic layer 2 along our line are within the range for oceanic crust (5.6–6.4 km/s). Velocities between 2.7 and 5.5 km/s are missing in oceanic layer 2. Therefore, the velocity-depth profiles taken from km 10 to 90 are not within the range typical for the upper first kilometer of normal oceanic crust (Figure 4.14). Additionally, the velocity on top of layer 3 in the western part of the profile is lower than expected for a typical layer 3, described by White et al. (1992). However, crustal velocities of less than 6.6 km/s in the

upper parts of layer 3 have also been reported by Suckro et al. (2012) in the southern part of Baffin Bay.

Since examples for thin oceanic crust accumulated at ultra-slow spreading ridges have been found beneath the Mohns Ridge (Klingelhöfer et al., 2000), Gakkel Ridge (Jokat et al., 2003; Jokat and Schmidt-Aursch, 2007) and Boreas Basin (Hermann and Jokat, 2013), we suggest that the observed thin oceanic crust accumulated during slow or even ultra-slow spreading.

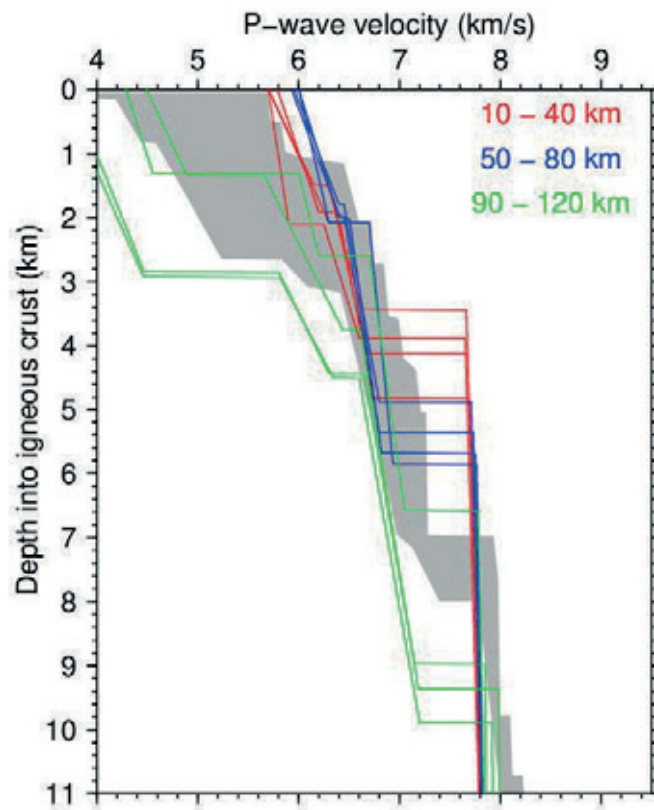


Figure 4.14: Velocity-depth profiles from AWI-20100200, compared with typical Atlantic oceanic crust. The gray shaded area marks the typical velocity-depth field for Atlantic oceanic crust with an age between 59 and 127 Myrs, taken from White et al. (1992). The colored lines are velocity-depth profiles taken every 10 km between km 10 and 120 of our *P* wave velocity profile AWI-20100200.

4.6.1.2 Continent-ocean transition (km 80–140)

Between km 90 and 170, the crustal thickness increases considerably. A buried magmatic structure at the shelf edge (Figure 4.9b) marks the onset of the transition between oceanic crust and stretched continental crust. Sediment velocities range between 1.7 and 4.1 km/s west of and 1.7 and 3.1 km/s east of a magmatic structure at km 100 to 120.

In the data sets, there are indications that the magmatic structure evolved in several steps: The lowermost sediments at the western flank of the magmatic structures (Figure 4.8b; between 4.5 and 5.5 s TWT) onlap onto the high, which might be an indication for a pre-sedimentary origin of this part of the magmatic structure. In contrast, the sedimentary layers close to and on top of the magmatic structure seem to be pulled up, which points to a later reactivation of magmatism and syn- or post-sedimentary development of the upper parts of the

structure. Also, the low velocities of 3.4 km/s in the upper part of the structure (Figure 4.9a) support this assumption, since the low velocity could be the result of interbedded sedimentary rocks between magmatic layers at the top of the structure.

East of the magmatic structure, the shape of the crustal refracted phases displays the morphology of the basement blocks. The velocities of the crust range between 5.4 and 7.2 km/s and have been divided into two units. A high-velocity lower crustal body located underneath the magmatic structure was modeled above the crust-mantle boundary. Constrained by numerous reflections, the depth of the Moho increases in this part of the profile from 13 to 18 km. Also, the velocity of the upper mantle increases toward the shelf from 7.7 to 8.0 km/s and is constrained by P_n phases.

Because we cannot clearly identify the onset of oceanic crust in this part of the profile, we classify this part of the crust as “transitional”. Main characteristics of this transition are the increasing crustal thickness and the magmatic structure, which is accompanied by the high-velocity lower crust. Unusually low velocities of 3.5 km/s in the upper part of the magmatic structure can originate from interbedded sedimentary rocks between the volcanic layers.

4.6.1.3 Rifted continental crust (km 140–321)

Between km 140 and 321, tilted fault blocks, deep sediment basins, and several faults characterize the area. The maximum thickness of the crust is ~25 km; the minimum thickness underneath the Melville Bay Graben and close to the transitional crust is ~14 km.

Thick sediments (200–700 m) cover the Kivioq and Melville Bay ridges. Low velocities of 4.0 km/s (velocity layer 7) are observed in the upper parts of both ridges. The refracted crustal phases of velocity layer 8 and 9 display the morphology of the ridges and basins and cannot be divided in upper and lower crustal units. Since intra-crustal reflections are only present between km 220 and 250, the border between both crustal units was chosen to fit the velocity gradient. The velocities of the upper unit range between 5.4 and 6.5 km/s (velocity layer 8), while the lower crust was modeled with velocities of 6.4 to 7.1 km/s (velocity layer 9). With the exception of the easternmost part of the profile, sufficient P_mP phases constrain the depth and morphology of the Moho underneath the stretched continental crust (Figure 4.10). P_n phases were not observed for this part of the model (Figure 4.11). However, we modeled the upper mantle with velocities of 8.0 km/s. Eastward of the Melville Bay Fault, crystalline basement is exposed. In the upper part, the basement has velocities ranging between 4.6 and 6.9 km/s.

Within the basins between the ridges, different thicknesses and velocities of sedimentary layers are found. The Melville Bay Graben is up to 10.7 km deep. It contains well-stratified sediments and sedimentary rocks (Figure 4.9b) with velocities between 1.6 and 4.9 km/s. Different layers of the infill may be distinguished by their velocity and reflection characteristics from the base of velocity layer 4 to 7. The uppermost layers (velocity layer 3 and 4) have partly been eroded in the eastern part of the Melville Bay Graben and show velocities ranging from 1.6 to 2.7 km/s. Reflections mark the onset of the underlying layers (velocity layer 5, 6, and 7), which contain inversion structures caused by compression (Figure 4.8b). They have velocities ranging from 2.8 to 4.9 km/s. The lowermost layer (velocity layer 7) has velocities of 4.5 to 4.9 km/s, and its

thickness ranges from 1.5 km to 7 km. The velocities are only well constrained in the upper parts of the layer (Figure 4.11) but can be identified on the seismograms of OBS 17 to 21. The base of the sediment layer is confined by reflections (Figures 4.10 and 4.11).

The sediments and sedimentary rocks in the Kivioq Basin have a thickness of ~5 km and show velocities of 1.6 to 4.7 km/s (Figure 4.9). The base of the thickest layer (velocity layer 4) is very well constrained by reflections. In contrast, its velocity is not well constrained in the deeper parts of the layer. However, this layer has been modeled with velocities of 2.4 to 3.0 km/s. The lowermost layer (velocity layer 6) has velocities of 4.0 to 4.7 km/s and is well constrained by refractions.

Thus, both deep sedimentary basins in Melville Bay differ in their depth, sedimentary infill, and velocity structure. As already observed by other authors (Whittaker et al., 1997; Gregersen et al., 2013) there are clear signs of compression in the Melville Bay Graben in this part of the profile, but no signs for compression in the Kivioq Basin (Figure 4.8a). On the contrary, more sedimentary layers have been identified in Melville Bay Graben based on their velocity structure compared to the Kivioq Basin.

4.6.2 Density model

Free-air gravity anomaly values along the seismic refraction profile range from +60 to -74 mGal (Figure 4.13a), with the lowest value measured in the Melville Bay Graben and the highest measured value above the Kivioq Ridge. The anomaly values decrease above the oceanic crust from km 0 (+36 mGal) to km 76 (+4 mGal). At the transition between oceanic and continental crust, the free-air gravity anomalies increase again above the magmatic structure and toward the shelf. Along the continental part of the profile, the shape of the anomalies displays the morphology of the basins and highs, with gravity lows measured in the Melville Bay Graben (-74 mGal) and Kivioq Basin (-14 mGal) and gravity highs above the Kivioq Ridge (+60 mGal) and Melville Bay Ridge (+10 mGal).

The densities of the uppermost sedimentary layers range between 2050 and 2240 kg/m³ throughout the model. Compacted sediments on top of the oceanic crust have been modeled with densities of 2330 kg/m³. Sediments and sedimentary rocks in the Kivioq Basin have been modeled with densities of 2050 to 2480 kg/m³. The densities of unconsolidated and consolidated sediments within Melville Bay Graben vary between 2050 kg/m³ for the uppermost layer and 2600 kg/m³ for the eventually already metamorphosed sedimentary rocks in the deepest part of the basin. Subsequent to the eastern boundary of the Melville Bay Graben a unit of higher density (2920 kg/m³) in the continental crust is necessary to explain the observed gravity increase. East of the graben practically no sediments are present on the continental basement with a density of 2700 kg/m³.

For oceanic layer 2, a density of 2800 kg/m³ and for oceanic layer 3, a density of 2950 kg/m³ was used for modeling. The volcanics in the transition zone have densities of 2450 kg/m³. For upper and lower continental crust, densities of 2700 and 2920 kg/m³ have been used, respectively. The mantle density was kept constant throughout the model (3330 kg/m³).

The maximum misfits between observed and modeled gravity are present in areas with strong lateral changes in morphology, e.g., at the eastern edge of the

Melville Bay High (20 mGal), in the Kivioq Ridge area (<10 mGal) and at the onset of the Melville Bay Fault (11 mGal). Since the model is a two-dimensional model, three-dimensional effects can cause these misfits. The greatest adjustments have been conducted in the very eastern part of the profile, which is also poorly resolved in the velocity model.

A good fit between observed and calculated free-air anomalies in the western part of the density model supports our findings, that a thin, two-layered oceanic crust is present in northern Baffin Bay. For modeling the densities of the deep transitional crust, we used the same density values as for oceanic layer 2 and 3 to keep the model simple. This also supports the results of the velocity model, that a clear onset of oceanic crust cannot be identified and that a transition between oceanic and continental crust exists in this area. The onset of clearly identified continental crust at km 135–145 is only slightly different to the onset of continental crust in the velocity model (km 140). In our velocity model, the continental crust consists of an upper and lower unit. Because of the poor ray coverage of the refracted phases in the lower crust in the eastern part of the velocity model and the adjustments of the boundary between upper and lower continental crust in the density model, additional crustal units might be present but cannot be resolved based on our current data set.

4.7 Discussion

Previous models of the crustal structure of northern Melville Bay and the deep parts of northern Baffin Bay were based on the interpretation of seismic reflection data, potential field data and <10 sonobuoy recordings only (e.g., Keen and Barrett, 1972; Whittaker et al., 1997, Oakey, 2005; Oakey and Chalmers, 2012; Gregersen et al., 2013). Thus, the model presented in this study is the first reliable information on crustal thickness in the northern Melville Bay.

4.7.1 Continental crust

The continental crust underneath Melville Bay is highly stretched and faulted. The maximum thickness (~25 km) of the continental crust is located underneath the eastern part of our profile at km 300–321 (Figure 4.9). The minimum crustal thickness (~14 km) of the continental crust is located close to the transitional crust (Figure 4.9, km 140). Braun et al. (2007) calculated an average crustal thickness of 37 km for Greenland based on gravity data. The differences between the minimum and maximum continental crustal thicknesses in our model and the average crustal thickness of Greenland calculated by Braun et al. (2007) amount to a minimum stretching factor of ~1.5 and a maximum stretching factor of ~2.6.

Hosseinpour et al. (2013) calculated a crustal thinning factor grid for the Baffin Bay and the Labrador Sea. Underneath the eastern part of our profile, the calculated thinning factors of Hosseinpour et al. (2013) range between 0.2 and 0.4. At the eastern end of our profile (km 321), their crustal thinning factor grid shows thinning factors of 0.6 to 0.7. The calculated thinning factors of the continental crust along our profile amount to 0.6 at km 321 and 0.3 at km 140 and therefore fit very well to the calculated data of Hosseinpour et al. (2013).

For the density model some adjustments of the boundary between upper and lower continental units were necessary to fit the observed free-air gravity anomalies in the eastern part of the profile. Hence, it is necessary to discuss how

reliable our modeled thickness of the continental crust is in this part of the model. The only interpreted seismic refraction profile in the vicinity of our seismic profile is line AWI-20100400 (Suckro et al., 2012) (Figure 4.1, dark green line), some 160 km to the south. The depth of the Moho on AWI-20100400 ranges between 26 and 30 km and is therefore partly deeper than observed in our model (~25 km). In contrast to our model, three continental crustal units instead of a two-layered continental crust were observed on profile AWI-20100400. Refractions of the lower crustal units are rare in both profiles, but P_mP phases constrain the depth of the Moho very well.

Sedimentary rocks with velocities around 4.5 to 4.9 km/s have been found within the basins of Melville Bay. An explanation for these rather high velocities is proposed by Gregersen et al. (2013), who suggest that the reflection pattern visible in reflection seismic data is caused by sedimentary rocks, which could already be metamorphosed, or may even represent intrusions. The high velocities found in this area as well as the high densities of 2450 to 2600 kg/m³, which have to be used for the density model, support this hypothesis.

4.7.2 Continent-ocean transition

Between the oceanic and stretched continental crust, we found a zone, which we denominated to be “transitional”. This area was affected by volcanism close to the initial formation of oceanic crust in our research area and also after the deposition of overlying sediments. Based on seismic reflection data Gregersen et al. (2013) identified volcanic units west of Kivioq Ridge. Our profile crosses the area (Figure 4.2b) in which the volcanic rocks were proposed. We confirm the interpretation of Gregersen et al. (2013) based on their seismic velocities ranging between 3.4 and 5.0 km/s. The high-velocity lower crust is probably caused by intrusions related to the formation of the volcanics. The presence of the magmatic structure in the middle of the volcanic province and its high velocities of up to 7.2 km/s in the lower transitional crust are clear indications for a significant volcanic activity in the transition zone before the initial formation of oceanic crust.

SDRs and/or underplating have been identified in southern Baffin Bay (Suckro et al., 2012), off Cape Dyer (Skaarup et al., 2006), and also in the northern Labrador Sea and southern Davis Strait (Chalmers, 1997; Funck et al., 2007). Apart from the volcanic province, we could not identify SDRs or massive underplating in our profile, which are typical characteristics of volcanic margins. Also, the thickness of the oceanic crust and the amount of volcanic rocks in the investigated area is rather small compared to other volcanic rifted margins, for example offshore Namibia (Gladczenko et al., 1998) or Mozambique (Leinweber et al., 2013).

The extent of the transition between continental and oceanic crust in AWI-20100200 (~60 km) is comparable to the 50 to 80 km wide transition zones in southern Labrador Sea (Figure 4.2a) or the ~55 to 80 km wide transition zones off Newfoundland (Lau et al., 2006; Funck et al., 2003; van Avendonk et al., 2006), where non-volcanic margins are present. However, there are some major differences in the velocity structure between these regions. On the Greenland and Labrador margins, the transition zone between highly thinned continental crust and oceanic crust is composed of a two-layered crust. The upper crust probably consists of block-faulted continental crust and is fairly thin (1–3 km)

(Chian and Loudon, 1994), with velocities ranging between 4.3 and 5.0 km/s (Chian and Loudon, 1994; Chian et al., 1995). Funck et al. (2003) reported a similar crustal thickness (2–3 km) and velocity distribution (4.7–4.9 km/s) of the upper transitional crust at the Flemish Cap margin along profile SCREECH-1. These are much lower velocities than observed in the upper crust underneath the magmatic structure of the transitional crust along our profile AWI-20100200 (5.5–6.5 km/s). In contrast, the velocity and velocity gradient in the thin upper transitional crust in the Newfoundland Basin (Lau et al., 2006) is greater (4.4–6.4 km/s). In southern Labrador Sea, the thin upper crust is underlain by a 4 to 5 km thick high-velocity lower crust (6.2–7.8 km/s), probably composed of serpentinites (Chian and Loudon, 1994; Chian et al., 1995), which are characterized by a high velocity gradient. A high velocity gradient (6.4–7.8 km/s) has also been observed in the lower transitional crust of the Newfoundland Basin margin (Lau et al., 2006), but not along SCREECH-1, where Funck et al. (2003) found an average velocity of 6.9 km/s in the up to 2 km thick lower transitional crust. Although we also found velocities of up to 7.2 km/s at the base of the lower transitional crust in AWI-20100200, the gradients and velocities (6.6–7.2 km/s) of the lower crust in our profile are much lower than in southern Labrador Sea or in the Newfoundland Basin.

4.7.3 Oceanic crust

Based on our *P* wave velocity and the density models we showed that the crust in the western part of our profile is oceanic. Our findings of a thin, oceanic crust are mostly consistent with the work of Keen and Barrett (1972), who reported only 4 km thick oceanic crust in the center of the Baffin Bay (around 72°N) from sonobuoy recordings. However, on the basis of its velocity structure and thickness it cannot be described as normal oceanic crust, which has been found in southern Baffin Bay or the adjacent Labrador Sea. The crust in our study area is partly much thinner (~3.5–6 km) compared to the oceanic crust found in southern Labrador Sea, which has a thickness between ~5.5 km (Chian et al., 1995) and 7 km (Chian and Loudon, 1994), or the oceanic crust in southern Baffin Bay, where crustal thicknesses of 7.5 km (Suckro et al., 2012) and 5 to 9 km (Funck et al., 2012) have been reported. Also, the velocity structure differs. In the western part of the profile, oceanic layer 3 has low velocities of only 6.2 to 6.6 km/s. It has to be taken into account, however, that the ray-coverage is rather sparse in this area.

After White et al. (1992), one explanation for thin oceanic crust can be slow spreading rates. Ultra-slow spreading with full spreading rates less than 20 mm/a leads to a decrease and high variability in crustal thickness (Reid and Jackson, 1981; Bown and White, 1994; Chen 1992; Jokat et al. 2003).

Since clear seafloor spreading anomalies are missing, estimates on spreading rates in Baffin Bay are speculative. Müller et al. (2008) introduced full spreading rates of 6 to 30 mm/a in Baffin Bay between chron 27N and 13N. In their model, the spreading rates in northern Baffin Bay, where our profile is located, range between 14 and 18 mm/a between chron 27N and 13N. Oakey (2005) describes three episodes of spreading for the region between Nares Strait and Labrador Sea. He calculated full spreading rates of ~18 mm/a during chron 27N–25N, which were followed by faster spreading (~35 mm/a) during chron 25N–24N when Greenland moved as a separated plate. Afterward slow

spreading occurred during chrons 24N–13N, with spreading rates of only ~ 12 mm/a.

Figure 4.15 shows a compilation of the relationship between crustal thickness and spreading rates. The blue bars mark the crustal thickness measured along our profile at km 20, 40, and 80. Applying these observations, the thin crust at km 20 can be explained by a slow spreading rate of only 10–15 mm/a. At km 40, the possible spreading rate ranges between 10 and 22 mm/a. At km 80, the possible spreading rate ranges between ~ 15 and 35 mm/a. In Figure 4.15, we can also compare the crustal thickness found along our profile and the resulting spreading rates with the spreading rates proposed by Oakey (2005) and Müller et al. (2008). Our results narrow the proposed spreading rates by Oakey (2005) and Müller et al. (2008) down to mainly ultra-slow spreading rates.

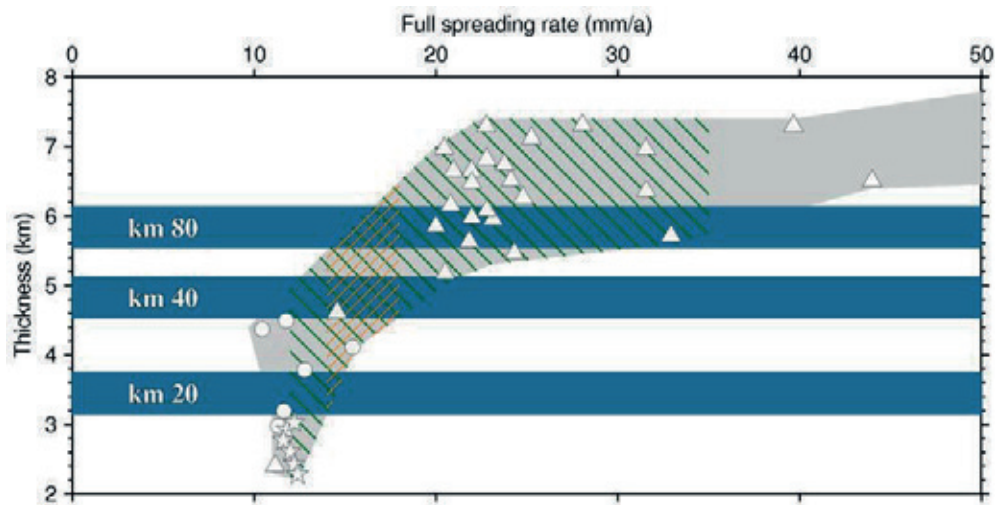


Figure 4.15: Spreading rate vs. crustal thickness. The datasets used to determine the gray area are taken from White et al. (2001) (white circles), Bown and White (1994) (white triangles), and Jokat et al. (2003) (white stars). Green hachures mark the area between lowest and highest spreading rate in Baffin Bay published by Oakey (2005). Orange hachures represent spreading rates taken from the spreading rate grid of Müller et al. (2008) along our profile. Blue bars represent the crustal thickness of igneous oceanic crust taken at km 20, 40, and 80 (± 0.3 km) along profile AWI-20100200.

Recently, several examples from the North Atlantic and Arctic Ocean of abnormal thin oceanic crust, caused by ultra-slow spreading, have been observed elsewhere and can therefore be compared to the thin crust in Baffin Bay. Jokat et al. (2003) found very thin 1.7–3.3 km thick oceanic crust along the Gakkel Ridge valley, while Hermann and Jokat (2013) identified an only 3 km thick oceanic crust underneath the Boreas Basin, also formed during ultra-slow spreading. The velocity structure and crustal composition of both examples differ from normal oceanic crust, which can also be observed in our model. On the contrary to our findings, no oceanic layer 3, in general, has been identified below the Gakkel Ridge and Boreas Basin. At specific locations on and off the ridge axis, seismic velocities typical for oceanic layer 3 were found below volcanic centers at an along-axis spacing of approximately 100 km (Jokat et al., 2003; Jokat and Schmidt-Aursch, 2007; Jokat et al., 2012; Hermann and Jokat, 2013). Klingelhöfer et al. (2000) identified thin oceanic crust close to the Mohns Ridge with a mean thickness of 4 ± 0.5 km. The thickness of oceanic layer 2 ranges between 1.5 and 2 km and is close to the global average of 2.11 ± 0.55 km

(White et al., 1992), while the thickness of oceanic layer 3 is smaller (2.45 ± 0.5 km) than the average thickness (4.97 ± 0.5) (White et al., 1992). Also, the velocity of oceanic layer 3 is partly lower than global averages and shows a wide range between ~ 5.5 and ~ 7.2 km/s. In the western part of our profile, we also found low velocities of oceanic layer 3, especially in the thinner part of the oceanic crust, which is caused by a decrease in the thickness of layer 3. Because of the existence and thickness of oceanic layer 3, the thin crust in northern Baffin Bay has more in common with the crust underneath the Mohns Ridge than with the crust underneath Gakkel Ridge and Boreas Basin. After Jokat et al. (2003), crustal thickness does not only depend on spreading rates but also on the magma supply along a ridge. Observations at the ultra-slow spreading Gakkel Ridge showed that crustal thickness is not only directly related to its spreading rates but is also controlled by its magmatic activity (Jokat et al., 2003). There, the oceanic crust formed at magmatic centers is thicker (up to 3.5 km) than the 1.4 to 2.9 km thick crust formed at amagmatic centers (Jokat et al., 2003). Funck et al. (2012) and Suckro et al. (2012) proposed with respect to the northward decrease in crustal thickness in Baffin Bay that a decrease in magma production and supply might have led to the formation of thin oceanic crust. After Funck et al. (2012), the up to 9 km thick oceanic crust in southern Baffin Bay can be explained by a greater magma supply provided by the Iceland mantle plume in the Davis Strait area. A decrease in crustal thickness with greater distance to the Davis Strait area can also be observed in the Labrador Sea. In the very northern Labrador Sea, Gerlings et al. (2009) reported ~ 12 km thick crust. After Gerlings et al. (2009), the interaction of the Iceland mantle plume and the spreading system led to the creation of the thick oceanic crust in northern Labrador Sea. In southern Labrador Sea, 5.5 (Chian et al., 1995) to 7 km (Chian and Loudon, 1994) thick oceanic crust has been observed. Nevertheless, the oceanic crust discovered along our profile in northern Baffin Bay is partly much thinner (3.5–6 km) than further south in the Labrador Sea. Therefore, variations in crustal thickness along our profile could be the product of changes in magma supply along the ridge axes.

Another important observation is the low, upper mantle velocity (>7.6 km/s) below the thin oceanic crust in our model. Comparing these findings with the results of Klingelhöfer et al. (2000), *P* wave velocities of the upper mantle beneath the thin crust of the Mohns Ridge are also relatively low (~ 7.5 km/s). Similar results have also been reported by Jokat et al. (2012) for the Knipovich Ridge and Hermann and Jokat (2013) for the Boreas Basin. Underneath the thin oceanic crust of the Boreas Basin, they modeled slow upper mantle velocities of less than 7.9 km/s, partly only 7.5 km/s. The observed low velocities of the upper mantle could be explained by seawater, which penetrated the thin crust and caused serpentinization of upper mantle rocks (peridotite). According to Horen et al. (1996), *P* wave velocities of 7.6 km/s can be caused by a serpentinization of $\sim 10\%$ of the upper mantle peridotite.

The thin oceanic crust, its velocity structure, and the presence of a low-velocity upper mantle strongly point to a mainly ultra-slow spreading regime during the formation of the northern Baffin Bay. Thickness variations of the oceanic crust can be the product of changes in magma supply along the spreading ridge. Nevertheless, the identified surface morphology of the oceanic basement along the seismic profile is untypical for such an assumption. Previous studies indicate that ultra-slow spreading ridges cause rough oceanic basement (Ehlers

and Jokat, 2009). Our profile is unfortunately not long enough to provide sufficient information on the basement morphology closer to the ridge axis, which is located ~50 km away from the western end of our profile. However, it should be noted that the shape of the oceanic basement in our profile is unusually smooth for ultra-slow spreading crust.

Our findings confirm assumptions that oceanic crust is present in the central northern Baffin Bay and that the Melville Bay area is underlain by stretched and rifted continental crust. A compilation for the crustal fabric in the Baffin Basin published by Oakey and Chalmers (2012) was based on gravity and magnetic data. In general, our results support the interpretation of Oakey and Chalmers (2012). However, based on our velocity and density model, the onset of oceanic crust and transitional crust must be shifted ~20 km to the east (Figure 4.16).

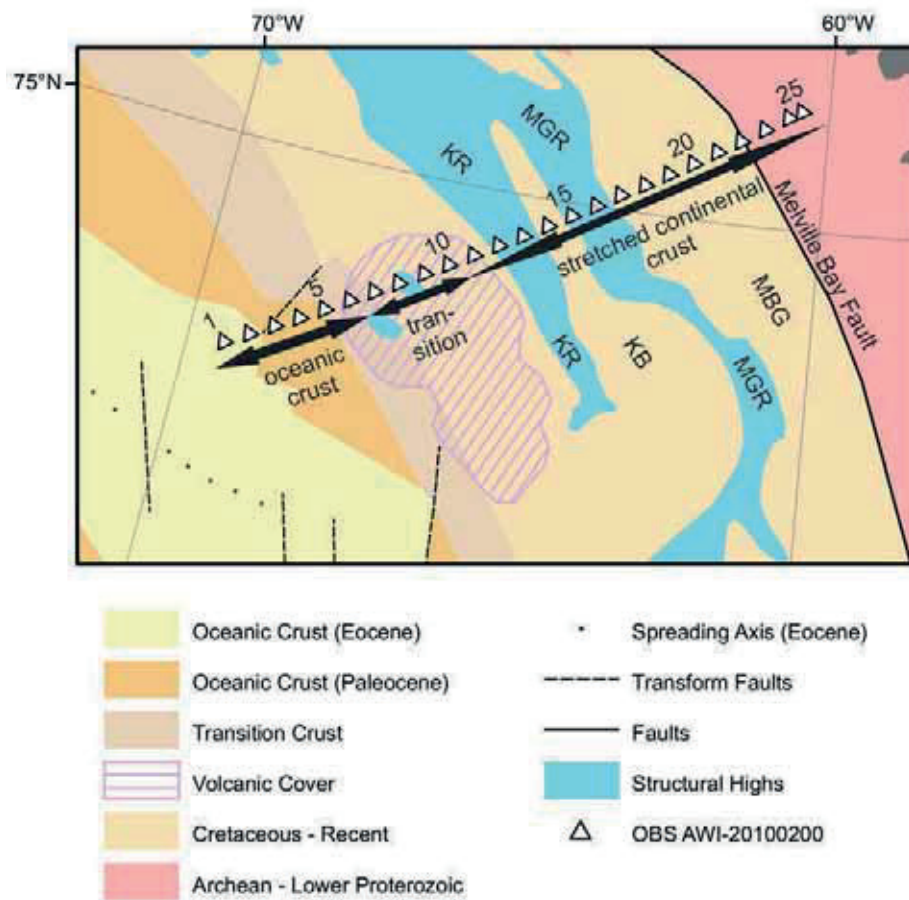


Figure 4.16: Comparison between the extent of crustal units after Oakey and Chalmers (2012) (see Figure 4.2b) and this study (black arrows). The location of structural highs in the Melville Bay (light blue) and the volcanic cover in northern Melville Bay (purple hachure) are taken from Gregersen et al. (2013). White triangles mark the deployment positions of the OBS of refraction seismic profile AWI-20100200. OBS 1, 5, 10, 15, 20, and 25 are labeled with numbers. MBG: Melville Bay Graben, MGR: Melville Bay Ridge, KB: Kivioq Basin, KR: Kivioq Ridge.

4.8 Conclusions

Our crustal model for the northern Melville Bay is the first one based on seismic refraction data in this region. Our findings confirm previous models that oceanic crust is present in the central northern Baffin Bay. The extent of oceanic crust toward the Greenland shelf is larger (~20 km) than previously postulated by

Oakey and Chalmers (2012) for our research area. The oceanic crust is unusually thin and consists of oceanic layer 2 and an unusually thin and partly slow (6.25–7.0 km/s) oceanic layer 3. Below the thin oceanic crust, the upper mantle velocities (7.6 km/s) are abnormally low, probably attributed to a 10% serpentinization of the upper mantle. With increasing thickness of the overlying crust, the velocity of the upper mantle increases. The abnormally thin (3.5–6 km) oceanic crust could be explained by its formation along an ultra-slow spreading ridge system. Thickness variations may result from changing magma supply at the ridge axis during the formation of the crust.

The oceanic crust is covered by up to 6.5 km thick sediments. High velocities observed in sedimentary layers on top of the oceanic crust (3.95 to 4.4 km/s) could be explained by compaction and may also be caused by interbedded basalts, while the deeper sedimentary rocks showing high velocities (~4.5 to 4.9 km/s) in the Melville Bay Graben may already be metamorphosed.

A 60 km wide transition zone between oceanic and stretched continental crust is identified. The transition is characterized by a magmatic structure, high crustal velocities in the lower crust and thickening of the crust. The presence of the magmatic structure in this area can be explained by increased volcanic activity right before and after the breakup and initiation of seafloor spreading, followed by at least one phase of magmatic intrusions into overlying sediments. Underneath Melville Bay, stretched and rifted 14 to 25 km thick continental crust is present.

4.9 Acknowledgments

We thank the captain and crew of R/V Polarstern for their great support and the on-board seismic team for their excellent work during expedition ARK-XXV/3. We also acknowledge the DEPAS-Pool for providing the OBS. We thank Cairn Energy for providing the processed data of reflection seismic profile BGR10-302. We also thank two anonymous reviewers for their useful and helpful comments that improved this article. The refraction seismic data sets used for this study are available upon request at Alfred Wegener Institute Helmholtz Centre for Polar and Marine Research in Bremerhaven. The reflection seismic data are available upon request at Federal Institute for Geosciences and Natural Resources in Hanover.

4.10 References

- Barton, P. (1986), The relationship between seismic velocity and density in continental crust—a useful constraint?, *Geophys. J. R. Astr. Soc.*, 87, 195–208.
- Bown, J.W., and White, R. S. (1994), Variation with spreading rate of oceanic crustal thickness and geochemistry, *Earth Planet. Sci. Lett.*, 121, 435–449, doi:10.1016/0012-821X(94)90082-5.
- Chalmers, J. A. (1997), The continental margin off southern Greenland: Along-strike transition from an amagmatic to a volcanic margin, *J. Geol. Soc. London*, 154, 571–576, doi:10.1144/gsjgs.154.3.0571.
- Chalmers, J. A., and K. Laursen (1995), Labrador Sea: the extent of continental and oceanic crust and the timing of the onset of seafloor spreading, *Mar. Petrol. Geol.*, 12, 205–217, doi:10.1016/0264-8172(95)92840-S.

Chalmers, J. A., and T. C. R. Pulvertaft (2001), Development of the continental margins of the Labrador Sea: A review, in *Non-Volcanic Rifting of Continental Margins: A Comparison of Evidence From Land and Sea*, edited by R. C. L. Wilson et al., Geol. Soc. Spec. Publ., 187, 77–105, doi:10.1144/GSL.SP.2001.187.01.05.

Chen, Y. (1992), Oceanic crustal thickness versus spreading rate, *Geophys. Res. Lett.*, 19, 743–756, doi:10.1029/92GL00161.

Chian, D., and K. E. Loudon (1994), The continent-ocean crustal transition across the southwest Greenland margin, *J. Geophys. Res.*, 99, 9117–9135, doi:10.1029/93JB03404.

Chian, D., K. E. Loudon, and I. Reid (1995), Crustal structure of the Labrador Sea conjugate margin and implications for the formation of non-volcanic continental margins, *J. Geophys. Res.*, 100, 24, 239–24, 253, doi:10.1029/95JB02162.

Damm, V. (2010), The Expedition of the Research Vessel “Polarstern” to the Arctic in 2010 (ARK-XXV/3), *Berichte zur Polar- und Meeresforschung*, 621, 234pp., Alfred Wegener Inst. for Polar and Mar. Res., Bremerhaven, Germany.

Ehlers, B. M., and W. Jokat (2009), Subsidence and crustal roughness of ultra-slow spreading ridges in the northern North Atlantic and the Arctic Ocean, *Geophys. J. Int.*, 177, 451–462, doi:10.1111/j.1365-246X.2009.04078.x.

Funck, T., and K. E. Loudon (1999), Wide-angle seismic transect across the Torngat Orogen, northern Labrador: Evidence for a Proterozoic crustal root, *J. Geophys. Res.*, 104, 7463–7480, doi:10.1029/1999JB900010.

Funck, T., J. R. Hopper, H. C. Larsen, K. E. Loudon, B. E. Tucholke, and W. S. Holbrook (2003), Crustal structure of the ocean-continent transition at Flemish Cap: Seismic refraction results, *J. Geophys. Res.*, 108, B11, 2531, doi:10.1029/2003JB002434.

Funck, T., H. R. Jackson, S. A. Dehler, and I. D. Reid (2006), A refraction seismic transect from Greenland to Ellesmere Island, Canada: The crustal structure in southern Nares Strait, *Polarforschung*, 74, 97–112.

Funck, T., H. Jackson, K. Loudon, and F. Klingelhöfer (2007), Seismic study of the transform-rifted margin in Davis Strait between Baffin Island (Canada) and Greenland: what happens when a plume meets a transform, *J. Geophys. Res.*, 112, B04402, doi:10.1029/2006JB004308.

Gerlings, J., T. Funck, H. Jackson, K. Loudon, and F. Klingelhöfer (2009), Seismic evidence for plume-derived volcanism during formation of the continental margin in southern Davis Strait and northern Labrador Sea, *Geophys. J. Int.*, 176, 980–994, doi:10.1111/j.1365-246X.2008.04021.x.

Gladchenko, T. P., J. Skogseid, and O. Eldholm (1998), Namibia volcanic margin, *Mar. Geophys. Res.*, 20, 313–341, doi:10.1023/A:1004746101320.

Gregersen, U., J. R. Hopper, and P. C. Knutz (2013), Basin seismic stratigraphy and aspects of prospectivity in the NE Baffin Bay, Northwest Greenland, *Mar. Pet. Geol.*, 46, 1–18, doi:10.1016/j.marpetgeo.2013.05.013.

Hermann, T., and W. Jokat (2013), Crustal structures of the Boreas Basin and the Knipovich Ridge, North Atlantic, *Geophys. J. Int.*, 193, 1399–1414, doi:10.1093/gji/ggt048.

Horen, H., M. Zamora, and G. Dubuisson (1996), Seismic waves velocities and anisotropy in serpentinized peridotites from Xigaze ophiolite: abundance of serpentine in slow spreading ridge, *Geophys. Res. Lett.*, 23(1), 9–12, doi:10.1029/95GL03594.

Hosseinpour, M., R. D. Müller, S. E. Williams and J. M. Whittaker (2013), Full-fit reconstruction of the Labrador Sea and Baffin Bay, *Solid Earth*, 4, 461–479, doi:10.5194/se-4-461-2013.

Jokat, W., and M. C. Schmidt-Aursch (2007), Geophysical characteristics of the ultra-slow spreading Gakkel Ridge, Arctic Ocean, *Geophys. J. Int.*, 168, 983–998, doi:10.1111/j.1365-246X.2006.03278.x.

Jokat, W., O. Ritzmann, M. C. Schmidt-Aursch, S. Drachev, S. Gauger, and J. Snow (2003), Geophysical evidence for reduced melt production on the Arctic ultraslow Gakkel mid-ocean ridge, *Nature*, 423, 962–965, doi:10.1038/nature01706.

Jokat, W., J. Kollofrath, W. Geissler, and L. Jensen (2012), Crustal thickness and earthquake distribution south of the Logachev Seamount, Knipovich Ridge, *Geophys. Res. Lett.*, 39, L08302, doi:10.1029/2012GL051199.

Keen, C., and D. Barrett (1972), Seismic refraction studies in Baffin Bay: An example of a developing ocean basin, *Geophys. J. R. Astron. Soc.*, 30, 253–271, doi:10.1111/j.1365-246X.1972.tb05812.x.

Keen, C. E., K. Dickie, and S. A. Dehler (2012), The volcanic margins of the northern Labrador Sea: Insights to the rifting process, *Tectonics*, 31, TC1011, doi:10.1029/2011TC002985.

Klingelhöfer, F., L. Geli, L. Matias, N. Steinsland, and J. Mohr (2000), Crustal structure of a super-slow spreading centre: A seismic refraction study of Mohns Ridge, 72°N, *Geophys. J. Int.*, 141, 509–526, doi:10.1046/j.1365-246x.2000.00098.x.

Larsen, L. M., L. M. Heaman, R. A. Creaser, R. A. Duncan, R. Frei, and M. Hutchison (2009), Tectonomagmatic events during stretching and basin formation in the Labrador Sea and Davis Strait: Evidence from age and composition of Mesozoic to Palaeogene dyke swarms in West Greenland, *J. Geol. Soc.*, 166, 999–1012, doi:10.1144/0016-76492009-038.

Leinweber, V. T., F. Klingelhoefer, S. Neben, C. Reichert, D. Aslanian, L. Matias, I. Heyde, B. Schreckenberger, and W. Jokat (2013), The crustal structure of the Central Mozambique continental margin – wide-angle seismic, gravity and magnetic study in the Mozambique Channel, Eastern Africa, *Tectonophysics*, 599, 170–196, doi:10.1016/j.tecto.2013.04.015.

Lau, K. W. H., K. E. Loudon, T. Funck, B. E. Tucholke, W. S. Holbrook, J. R. Hopper, and H. C. Larsen (2006), Crustal structure across the Grand Banks-Newfoundland Basin continental margin – I. Results from a seismic refraction profile, *Geophys. J. Int.*, 167, 127–156, doi:10.1111/j.1365-246X.2006.02988.x

Lutter, W. J., and R. L. Nowack (1990), Inversion for crustal structure using reflections from the PASSCAL Ouachita experiment, *J. Geophys. Res.*, 95, B4, 4633–4646, doi:10.1029/JB095iB04p04633.

Müller, R., M. Sdrolias, C. Gaina, and W. Roest (2008), Age, spreading rates, and spreading asymmetry of the world's ocean crust, *Geochem. Geophys. Geosyst.*, 9 (4), Q04006, doi:10.1029/2007GC001743.

Oakey, G. N. (2005), Cenozoic evolution and lithosphere dynamics of the Baffin Bay-Nares Strait region of Arctic Canada and Greenland, PhD thesis, Vrije Universiteit, Amsterdam.

Oakey, G. N., and J. A. Chalmers (2012), A new model for the Paleogene motion of Greenland relative to North America: plate reconstructions of the Davis Strait and Nares Strait regions between Canada and Greenland, *J. Geophys. Res.*, 117, B10401, doi:10.1029/2011JB008942.

Reid, I., and H. R. Jackson (1981), Oceanic spreading rate and crustal thickness, *Mar. Geophys. Res.*, 5, 165–172.

Reid, I., and H. R. Jackson (1997), Crustal structure of the northern Baffin Bay: Seismic refraction results and tectonic implications, *J. Geophys. Res.*, 102, 523–542, doi:10.1029/96JB02656.

Roest, W. R., and S. P. Srivastava (1989), Sea-floor spreading in the Labrador Sea: a new reconstruction, *Geology*, 17, 1000–1003, doi:10.1130/0091-7613(1989)017<1000:SFSITL>2.3.CO;2.

Schindwein, V., and W. Jokat (1999), Structure and evolution of the continental crust of northern east Greenland from integrated geophysical studies, *J. Geophys. Res.*, 104, B4, 15227–15245.

Skaarup, N., H. R. Jackson and G. Oakey (2006), Margin segmentation of Baffin Bay/Davis Strait, eastern Canada based on seismic reflection and potential field data, *Mar. Petr. Geol.*, 23, 127–144, doi:10.1016/j.marpetgeo.2005.06.002.

Srivastava, S. P. (1978), Evolution of the Labrador Sea and its bearing on the early evolution of the North Atlantic, *Geophys. J. R. Astron. Soc.*, 52, 313–357, doi:10.1111/j.1365-246X.1978.tb04235.x.

Storey, M., R. A. Duncan, A. K. Pedersen, L. M. Larsen, and H.C. Larsen (1998), $^{40}\text{Ar}/^{39}\text{Ar}$ geochronology of the West Greenland Tertiary volcanic province, *Earth Planet. Sci. Lett.*, 160, 569–586, doi:10.1016/S0012-821X(98)00112-5.

Suckro, S. K., K. Gohl, T. Funck, I. Heyde, A. Ehrhardt, B. Schreckenberger, J. Gerlings, V. Damm and W. Jokat (2012), The crustal structure of southern Baffin Bay: implications from a seismic refraction experiment, *Geophys. J. Int.*, 190, 37–58, doi: 10.1111/j.1365-246X.2012.05477.x.

Suckro, S. K., K. Gohl, T. Funck, I. Heyde, B. Schreckenberger, J. Gerlings and V. Damm (2013), The Davis Strait crust - a transform margin between two oceanic basins, *Geophys. J. Int.*, 193, 78–97, doi: 10.1093/gji/ggs126.

Talwani, M., and O. Eldholm (1977), Evolution of the Norwegian-Greenland Sea, *Geol. Soc. Am. Bull.*, 88, 969–999, doi:10.1130/0016-7606(1977)88<969:EOTNS>2.0.CO;2

Van Avendonk, H. J. A., W. S. Holbrook, G. T. Nunes, D. J. Shillington, B. E. Tucholke, K. E. Loudon, H. C. Larsen, and J. R. Hopper (2006), Seismic velocity structure of the rifted margin of the eastern Grand Banks of Newfoundland, Canada, *J. Geophys. Res.*, 111, B11404, doi:10.1029/2005JB004156.

White, R. S., D. McKenzie, and R. K. O’Nions (1992), Oceanic crustal thickness from seismic measurements and rare Earth element inversion, *J. Geophys. Res.*, 97, 19, 683–19, 715, doi:10.1029/92JB01749.

White, R. S., T. A. Minshull, M. J. Bickle, and C.J. Robinson (2001), Melt generation at very slow spreading oceanic ridges: Constraints from geochemical and geophysical data, *J. Petrol.*, 42, 1171–1196, doi:10.1093/petrology/42.6.1171.

Whittaker, R. C., N. E. Hamann, and T. C. R. Pulvertaft (1997), A new frontier province offshore northern West Greenland: structure, basin development and petroleum potential of the Melville Bay area, *AAPG Bull.*, 81, 979–998

Zelt, C. A., and R. B. Smith (1992), Seismic traveltimes inversion for 2-D crustal velocity structure, *Geophys. J. Int.*, 108, 16–34, doi:10.1111/j.1365-246X.1992.tb00836.x.

5 Insights into the crustal structure of the northern transition between Nares Strait and Baffin Bay

Tabea Altenbernd*, Wilfried Jokat*, Ingo Heyde, Volkmar Damm****

***Alfred-Wegener-Institut, Helmholtz-Zentrum für Polar- und Meeresforschung, Bremerhaven**

**** Bundesanstalt für Geowissenschaften und Rohstoffe, Hannover**

5.1 Abstract

The crustal structure and continental margin between southern Nares Strait and northern Baffin Bay was studied based on seismic refraction and gravity data acquired in 2010. We present the resulting *P* wave velocity, density and geological models of the crustal structure of a profile, which extends from the Greenlandic margin of the Nares Strait into the deep basin of central northern Baffin Bay. For the first time, the crustal structure of the continent-ocean transition of the very northern part of Baffin Bay could be imaged. We divide the profile into three parts: stretched continental, thin oceanic, and transitional crust. On top of the three-layered continental crust, a low-velocity zone characterizes the lowermost layer of the three-layered Thule Supergroup underneath the Steensby Basin. The 4.3–6.3 km thick oceanic crust in the southern part of the profile can be divided into a northern and southern section, more or less separated by a fracture zone. The oceanic crust adjacent to the continent-ocean transition is composed of 3 layers and characterized by oceanic layer 3 velocities of 6.7–7.3 km/s. Toward the south only two oceanic crustal layers are necessary to model the travel time curves. Here, the lower oceanic crust has lower seismic velocities (6.4–6.8 km/s) than in the north. Rather low velocities of 7.7 km/s characterize the upper mantle underneath the oceanic crust, which we interpret as indication for the presence of upper mantle serpentinization. In the continent-ocean transition zone, the velocities are lower than in the adjacent continental and oceanic crustal units. There are no signs for massive magmatism or the existence of a transform margin in our study area.

5.2 Introduction

The Nares Strait is located north of Baffin Bay and connects it to the Arctic Ocean (Figure 5.1). Both Nares Strait and northern Baffin Bay play a key role in our understanding of the plate motion between North America and Greenland. Since decades, the origin of the area has been under discussion. Thus, constraints on the distribution of oceanic and continental crust in northern Melville Bay and southern Nares Strait are essential for reconstructing the complex geological history of the area. Based on the interpretation of seismic refraction profiles, the continental crust in southern Nares Strait and the transition between oceanic and continental crust east of Devon Island in northern Baffin Bay was examined by previous studies (Figure 5.1). However, the extent and crustal structure of the northernmost oceanic crust in Baffin Bay and the type of margin in the Smith Sound remains widely unexplored. Therefore, the interpretation of crustal structures in the Smith Sound are based

on potential field data and plate tectonic reconstructions (Hosseinpour et al., 2013, Oakey and Chalmers 2012, Figure 5.2).

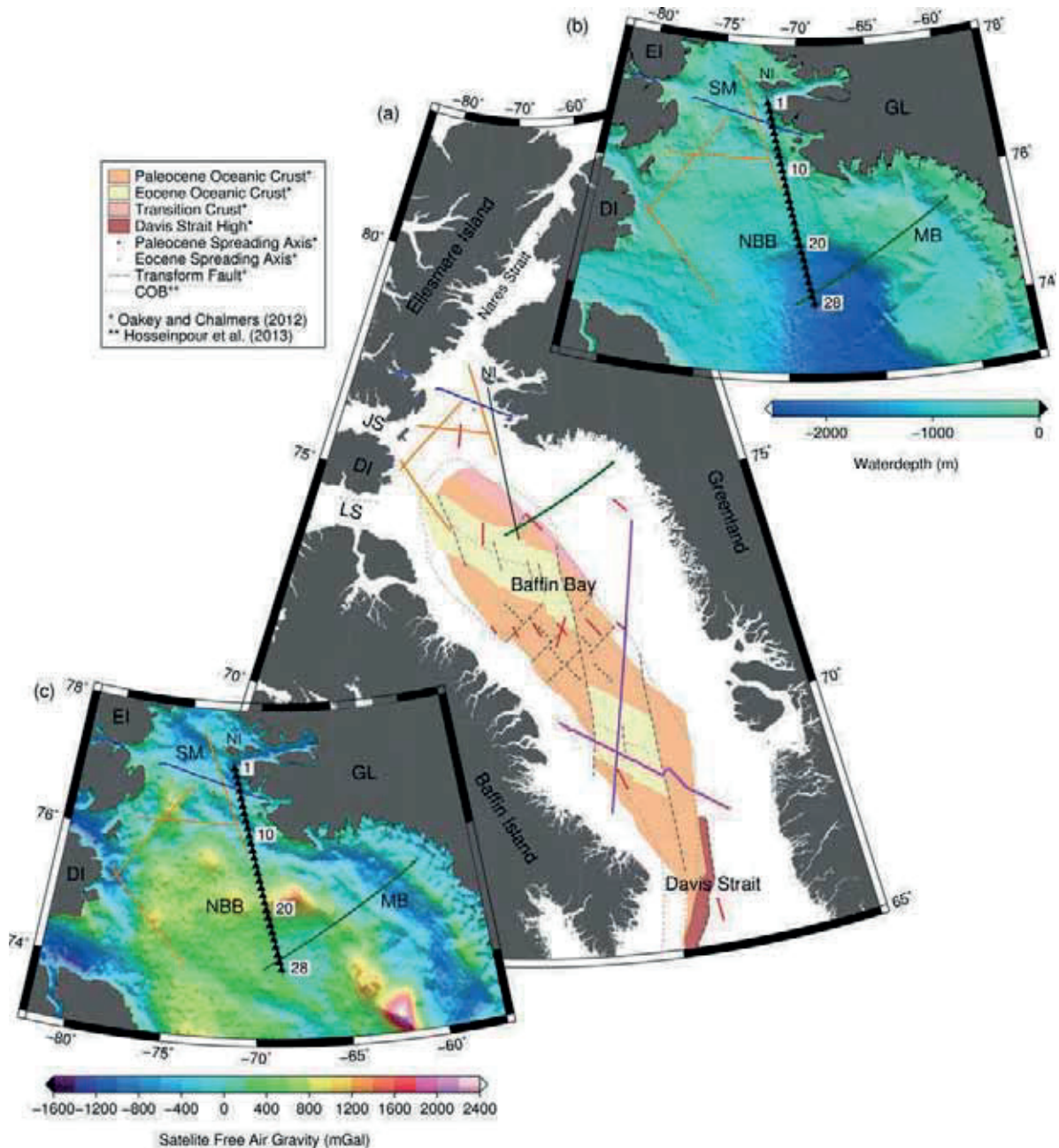


Figure 5.1: Overview, bathymetry and free-air gravity of the region of interest.

(a) Overview map of the Baffin Bay/Nares Strait region with the position of oceanic crust after Oakey and Chalmers (2012) and Hosseinpour et al. (2013) (see legend). Colored lines represent positions of seismic refraction profiles: Black line: profile AWI-20100300 (this study), green line: profile AWI-20100200 (Altenbernd et al., 2014), red lines: sonobouys (Keen and Barrett, 1972), blue line: profile line 3, (Funk et al., 2006), orange lines: profiles 91/1–91/4 (Jackson and Reid, 1994; Reid and Jackson, 1997a), purple line: profiles AWI-20100400 and AWI-20080500 (Suckro et al., 2012), pink line: profile AWI-20080600 (Funk et al., 2012).

(b) Bathymetric map (GEBCO grid 2014, version 2.0) of the area of interest, illuminated from the NE. Black triangles mark the position of the OBS (labeled with black numbers).

(c) Free-air gravity anomaly map (Sandwell et al. 2014, Version 23.1), illuminated from NE and N. Abbreviations: NI: Northumberland Island, LS: Lancaster Sound, DI: Devon Island, JS: Jones Sound, EI: Ellesmere Island, SM: Smith Sound, GL: Greenland, MB: Melville Bay, NBB: Northern Baffin Bay.

The seismic refraction profile AWI-20100300 fills this gap and extends from northern Baffin Bay into the Nares Strait. The continent-ocean transition and the type of margin in this area can be defined for the first time in this region. Since the profile crosses older seismic refraction profiles in Northern Baffin Bay and Nares Strait (Figure 5.2), the obtained P wave velocity model and its interpretation can be compared with previous models.

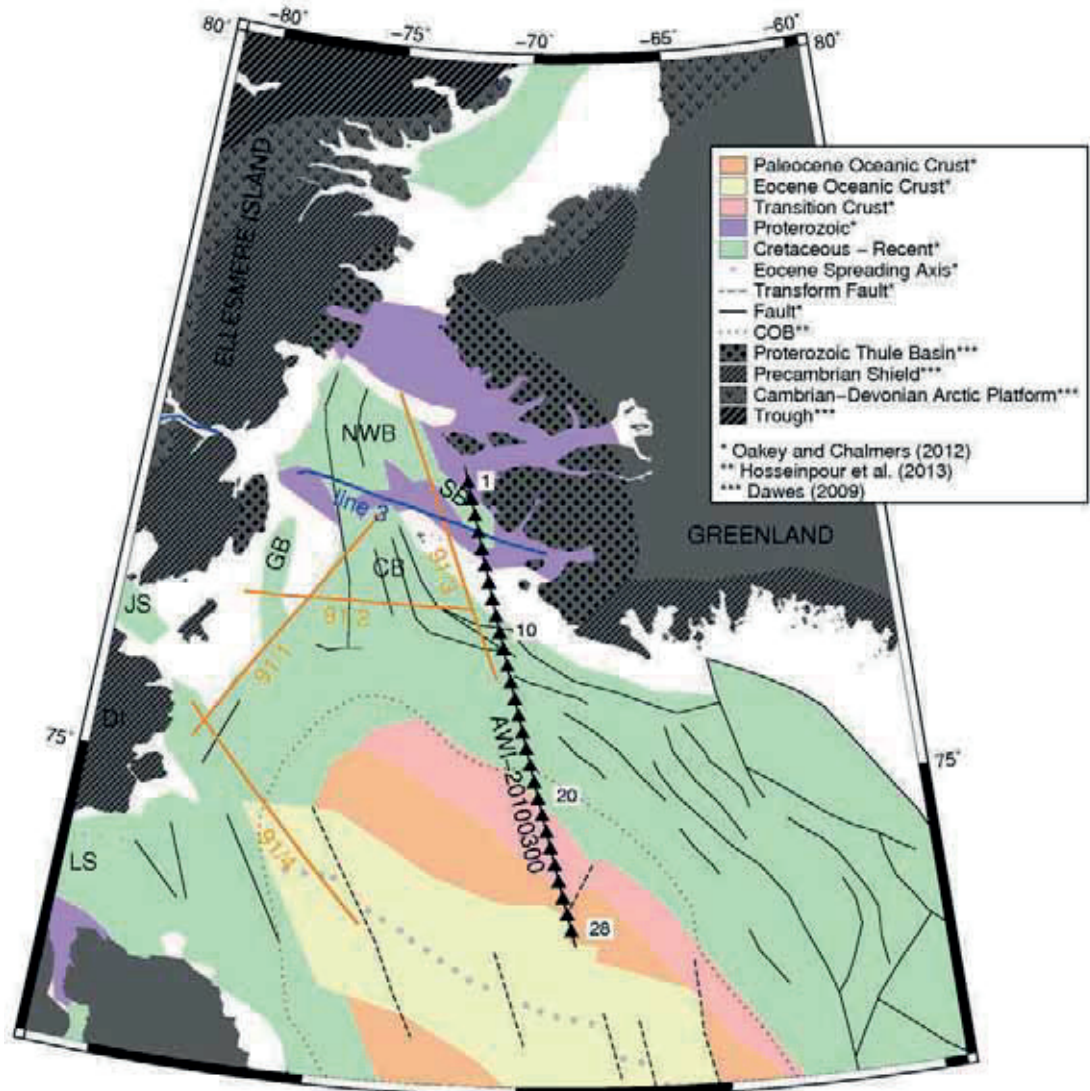


Figure 5.2: Geological provinces and offshore geology of northern Baffin Bay and southern Nares Strait. Offshore geology modified after Oakey and Chalmers (2012) and Gregersen et al. (2013), the onshore geological provinces were taken from Dawes (2009). Colored lines mark the position of seismic refraction profiles. Green line: Altenbernd et al. (2014), black line: this study, orange lines: Jackson and Reid (1994) and Reid and Jackson (1997a), blue line: Funck et al. (2006). Triangles mark the position of deployed OBS along AWI-20100300. GB: Glacier Basin, NWB: Northwater Basin, SB: Steensby Basin, CB: Carey Basin, JS: Jones Sound, LS: Lancaster Sound, DI: Devon Island.

5.3 Geological setting

The Baffin Bay is a basin, which developed during the separation of Greenland and North-America. For a long time, it has been discussed whether the Baffin Bay crust is composed of oceanic or stretched continental crust, since clear

magnetic spreading anomalies could not be identified in wide parts of the Baffin Bay. The only exceptions are weak magnetic lineations in the central part of Baffin Bay, which have been identified by Oakey and Chalmers (2012). On basis of modern seismic refraction datasets, it is now proven that southern Baffin Bay is underlain by thin to normal, 5 to 9 km thick oceanic crust (Funck et al., 2012; Suckro et al., 2012) and that northern Baffin Bay is underlain by thin, 3.5 to 6 km thick oceanic crust with partly low velocities (Altenbernd et al., 2014). Its spreading system is believed to be a prolongation of the rift system in the Labrador Sea, to which it is connected via the Davis Strait (Figure 5.1). However, due to the lack of magnetic anomalies and other dating methods, the onset of spreading in the Baffin Bay cannot be determined at present. Spreading in the adjacent Labrador Sea started in the Cretaceous (chron 33) (Roest and Srivastava, 1989) or Paleocene (chron 27N) (Chalmers and Laursen, 1995). Since the spreading system in the Baffin Bay and Labrador Sea are thought to be closely related, an accepted assumption is that spreading in the Baffin Bay started together or shortly after the spreading in the Labrador Sea. The onset of spreading between Greenland and Europe changed the plate kinematics and led to a change in the spreading direction at 55 Ma (Oakey, 2005; Roest and Srivastava, 1989). Estimates on the spreading rates in the Baffin Bay are based on kinematic considerations, which assume sea floor spreading between chron 27 and 13 (Müller et al., 2008; Oakey, 2005) or are based on assumptions on the oceanic crustal thickness like in the northern Baffin Bay (Altenbernd et al., 2014).

5.3.1 Regional geology of southern Nares Strait and Northern Baffin Bay

Since the early 1900s, it is discussed whether or not the Nares Strait represents a major plate boundary (“Wegener Fault”) between Greenland and North America. Still, no consensus has been achieved due to contradictory results (e.g., Dawes 2009, Tessensohn et al., 2006), especially in the southern Nares Strait. The complex plate motions between Greenland and North America led to the formation of extensional, transpressional and later compressional features in the Nares Strait and northern Baffin Bay. In the southern Nares Strait, rocks of the Thule Basin (Figure 5.2) and the underlying Archean shield are partly exposed onshore. The intracratonic Thule Basin contains sedimentary rocks of the Thule Supergroup, which is a sedimentary succession of Mesoproterozoic to Neoproterozoic age (1270–650 Ma), mainly composed of shallow marine sedimentary rocks and one basaltic unit (Dawes, 1997). Offshore, the Thule Supergroup can be traced across Smith Sound and has a maximum thickness of ~5 km along line 3 (Figure 5.2; Funck et al., 2006).

Other younger sediment basins offshore vary greatly in depth and orientation. The N-S trending Glacier Basin (Figure 5.2, GB) is filled with up to 6 km thick sediments (Reid and Jackson 1997a).

The NW-SE orientated Steensby Basin and the connected Northwater Basin in the center of southern Nares Strait contain sediments of unknown age having a thickness of at least 1 km along line 3 (Figure 5.2; Funck et al., 2006). Reid and Jackson (1997a) also observed that the crust underneath the Carey Basin at the very southern end of the Nares Strait is only 7 km thick and explained the thin crust with the existence of a transform plate boundary. Pull-apart basins or

flower structures in the North Water Basin (Neben et al., 2006) and flower structures west of Carey Basin (Jackson et al., 1992) are also interpreted as indicators for the presence of a transform fault/strike-slip motion in the southern Nares Strait (Reid and Jackson, 1997b; Tessensohn et al., 2006). Contrary to that, the geology on both sides of southern Nares Strait in the Smith Sound does not show any evidences for large lateral displacements (e.g., Dawes, 2009; Frisch and Dawes, 1982; Frisch and Dawes, 2014), which strongly supports the theory that southern Nares Strait and parts of Ellesmere Island are part of one geological province and have not significantly moved relative to each other. This thesis is supported by a fission-track transect across the Smith Sound, which showed no signs for thermo tectonism since the Late Paleozoic (Hansen et al., 2011). Also, an east-west trending seismic refraction transect in the southern Nares Strait did not provide any clear evidence for the presence of a transform plate boundary in the observed region (Funck et al., 2006). Because of the absence of large lateral variations in *P* wave velocities, Moho depth and Poisson's ratios along line 3, Funck et al. (2006) propose that both sides of the southern Nares Strait belong to the same geological province. However, since the western part of the model is not well constrained due to sparse data coverage, the authors also mention that the presence of a plate boundary in this region cannot be ruled out.

In the northern Baffin Bay, a two-layered, 3.5–6 km thin igneous oceanic crust is present at the western termination of AWI-20100200 (Figure 5.2; Altenbernd et al., 2014). The crust is covered by up to 6.5 km thick sedimentary rocks of unknown age, which partly show high velocities of up to 4.4 km/s (Altenbernd et al., 2014). Along the profile, the appearance of a magmatic structure and high velocities of up to 7.2 km/s in the lowermost crustal unit characterize the transition between the thin oceanic and stretched and rifted continental crust. In contrast, Reid and Jackson (1997a) interpreted thin crust with a velocity of 6.8 km/s in the eastern section of line 91/4 (Figure 5.2) to consist of serpentinized peridotites rather than oceanic layer 3. Therefore, the authors suggested that northern Baffin Bay was formed by amagmatic rifting and discussed if this margin can be considered as a transform margin.

5.4 Data acquisition and processing

5.4.1 Seismic data

Our area of investigation extends from the deep-sea area of the Baffin Bay Basin to southern Nares Strait. Seismic refraction data were acquired with an airgun array consisting of 8 G-Guns (total volume of 68.2 L). The shot interval was 60 s, the average shot distance 150 m (Damm, 2010). In total 28 ocean-bottom seismometers (OBS) were used for recording the airgun shots along profile AWI-20100300 (Figure 5.2). All OBS were equipped with a 60 sec three component broadband seismometer and a broadband hydrophone. The average spacing between the OBS positions was ~13 km.

All OBS could be recovered after the shooting. Out of 28 OBS, 21 worked without any technical problems. Unfortunately, OBS 13 failed completely and did not record any data. The hydrophone and seismometer of OBS 8 stopped working during shooting and, therefore, recorded only a small amount of data. For the other 5 OBS stations, at least one of the three seismometer components

and all hydrophone components worked properly. Due to currents, OBS often significantly surface away from their deployment position. Therefore, some OBS were relocalized if necessary. For the set-up of the P wave velocity model, the stations were later projected on a straight line.

Along the position of AWI-20100300, 2 multichannel reflection seismic profiles were acquired (Figure 5.3). Reflection seismic profile BGR10-303a covers the southern and profile BGR10-313 the northern part of AWI-20100300.

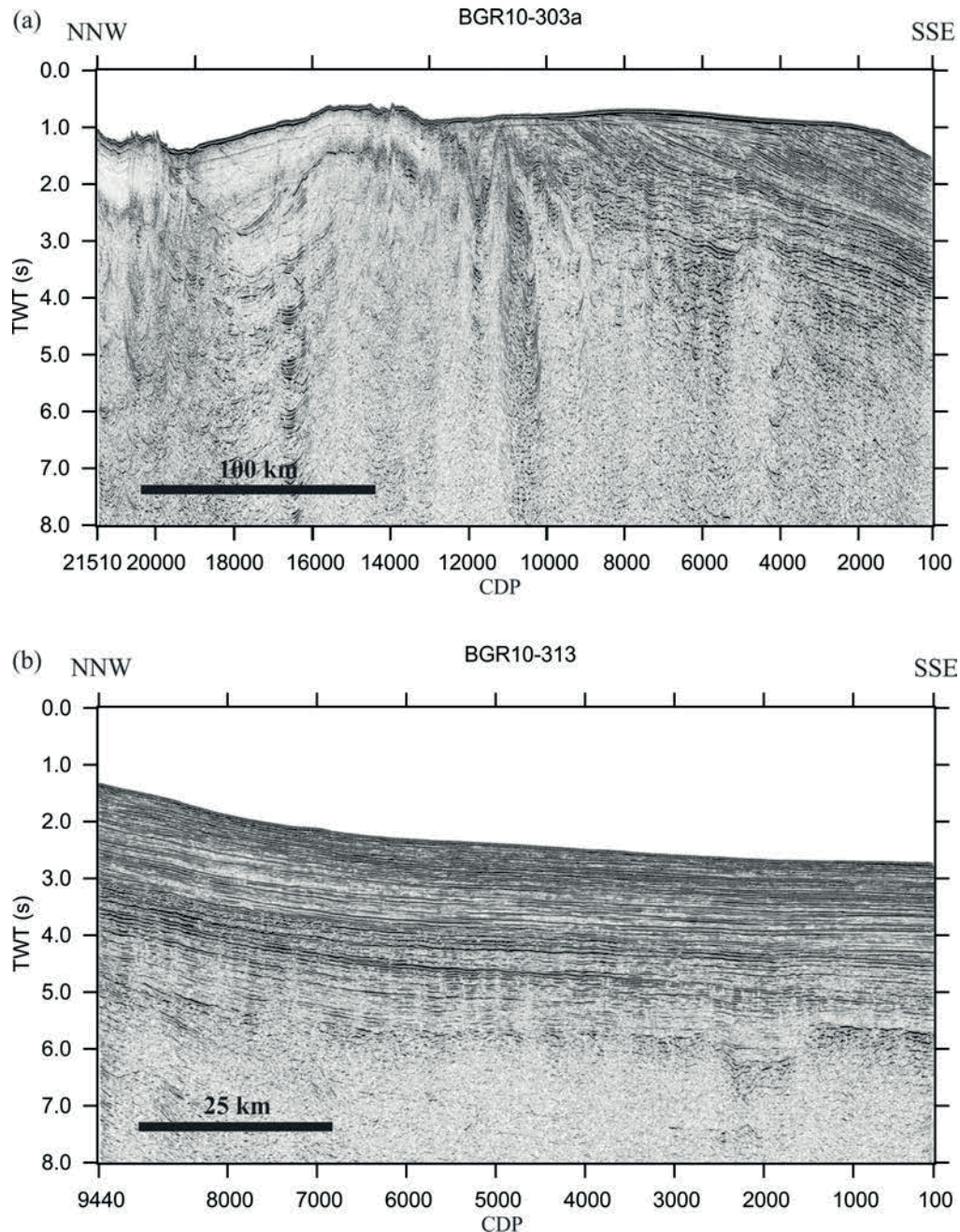


Figure 5.3: Reflection seismic data along AWI-20100300.

(a) MCS-profile BGR10-303a was acquired along the northern part of the seismic refraction profile AWI-20100300.

(b) MCS-profile BGR10-313 was acquired along the southern part of the seismic refraction profile AWI-20100300. The location of normal faults between CDP 1500 and 2500 correspond with the location of a fracture zone between OBS 26 and 27 (Figure 5.2).

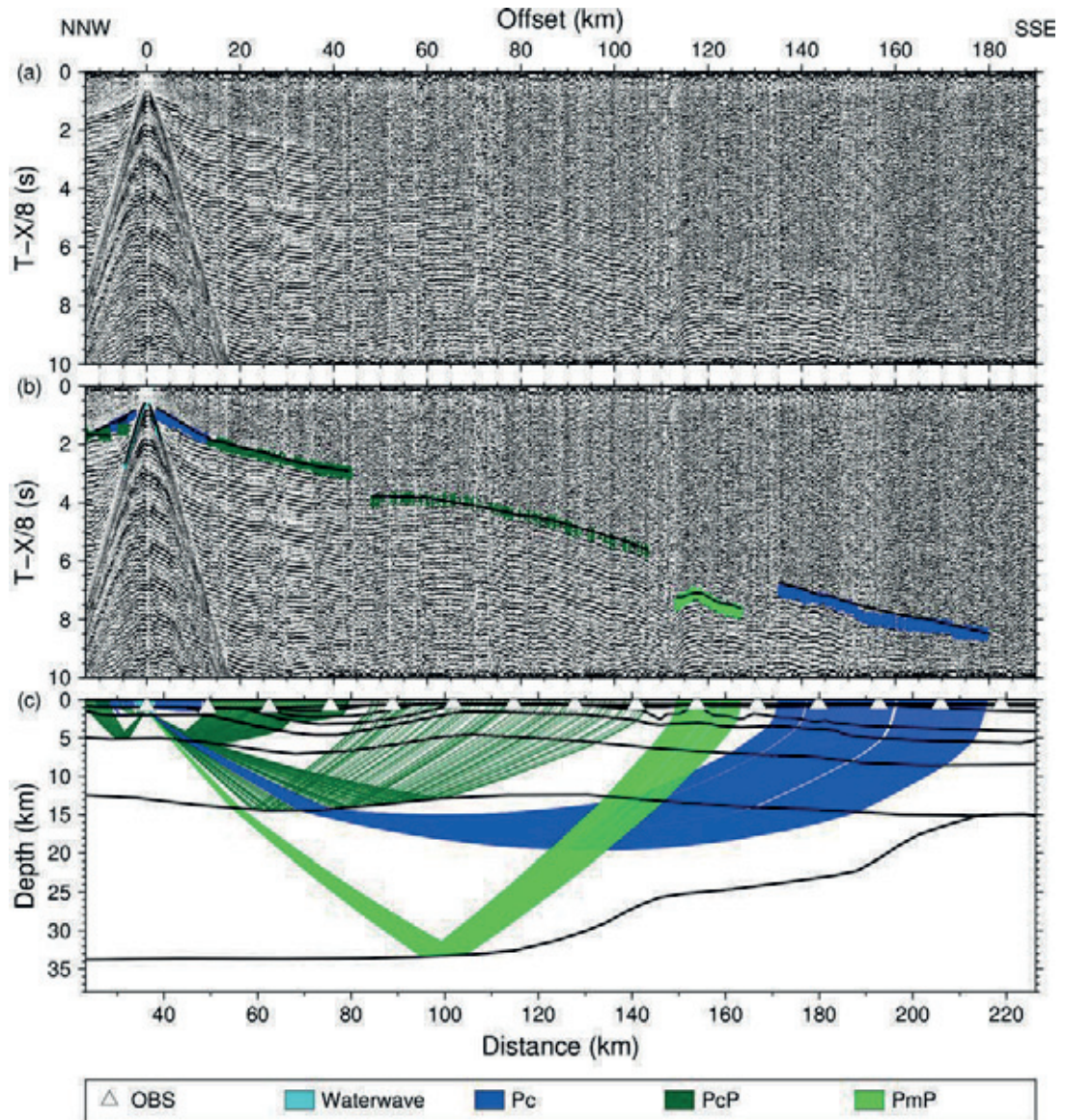


Figure 5.4: Parts of the recorded seismogram section, picked signals and modeled raypaths for OBS 1.

(a) Seismogram section of the hydrophone component, plotted with a reduction velocity of 8 km/s. A 3–14 Hz bandpass filter and an automatic gain control (AGC) is applied.

(b) Same section of the hydrophone component as seen above, but overlain by picked phases (colored vertical bars). The length of the bars represents the pick uncertainties. Black lines mark the modeled traveltimes within the *P* wave velocity model.

(c) Raypaths of the picked phases within the velocity model. Black lines mark the layer boundaries of the velocity layers.

5.4.2 Gravity data

The gravity data were acquired with the sea gravimeter system KSS31 during the entire cruise. Measurements at places with known absolute gravity values were carried out at the start- and endpoint of the cruise in Reykjavik and Bremerhaven. On basis of these measurements, the gravity data was then linked to the International Gravity Standardization Net IGSN 71. After the end of the cruise, an instrumental drift of 8.6 mGal was determined. Unfortunately, the correction of the instrumental drift increased the crossover errors and also divergence between the measured and satellite altimetry data. A slightly inaccurate scale factor of the KSS31 might be one explanation for this.

Therefore, it was decided not to correct the instrumental drift. The free-air gravity anomalies were obtained by subtraction of the normal gravity (WGS84) and the Eötvös effect.

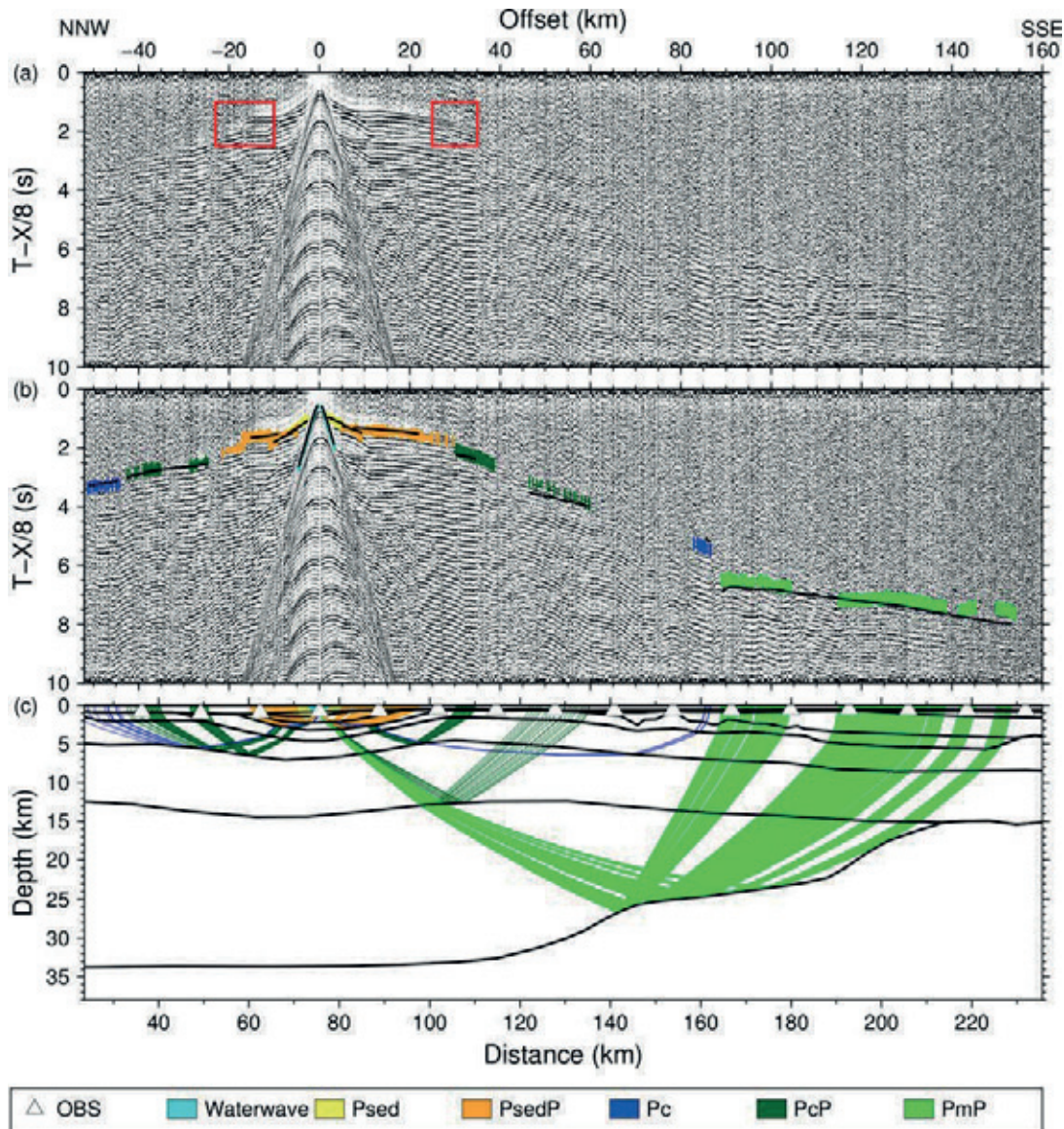


Figure 5.5: Parts of the recorded seismogram section, picked signals and modeled raypaths for OBS 4.

(a) Seismogram section of the hydrophone component, plotted with a reduction velocity of 8 km/s. A 3–14 Hz bandpass filter and an automatic gain control (AGC) is applied. Red squares mark the position of delays caused by a low velocity zone.

(b) Same section of the hydrophone component as seen above, but overlain by picked phases (colored vertical bars). The length of the bars represents the pick uncertainties. Black lines mark the modeled traveltimes within the *P* wave velocity model.

(c) Raypaths of the picked phases within the velocity model. Black lines mark the layer boundaries of the velocity layers.

5.5 Modeling of seismic refraction data

Prior to picking, a bandpass filter of 4.0–13.5 Hz and an automatic gain control (1s) was applied to the OBS data. Picking of the signals was done with the software ZP (by B. Zelt, <http://www.soest.hawaii.edu/users/bzelt/zp/zp.html>). Depending on the data quality, the hydrophone channel (OBS 1–12, 15–22, 26–

27) or the z-component channel of the seismometers (OBS 14, 23–25, 28) was used for picking refracted and reflected phases. In the following, picked refracted phases are named P_{sed1-5} (refracted phases in sediments), $P_{c1-P_{c4}}$ (refracted phases in crustal units) and P_n (refracted phases in the upper mantle). Reflected phases are named $P_{sed1P-P_{sed5}P}$ (reflections at the base of sedimentary layers) and $P_{c1P-P_{c3}P}$ (reflections from the base of crustal layers). Reflections from the crust-mantle boundary (Moho) are named P_mP .

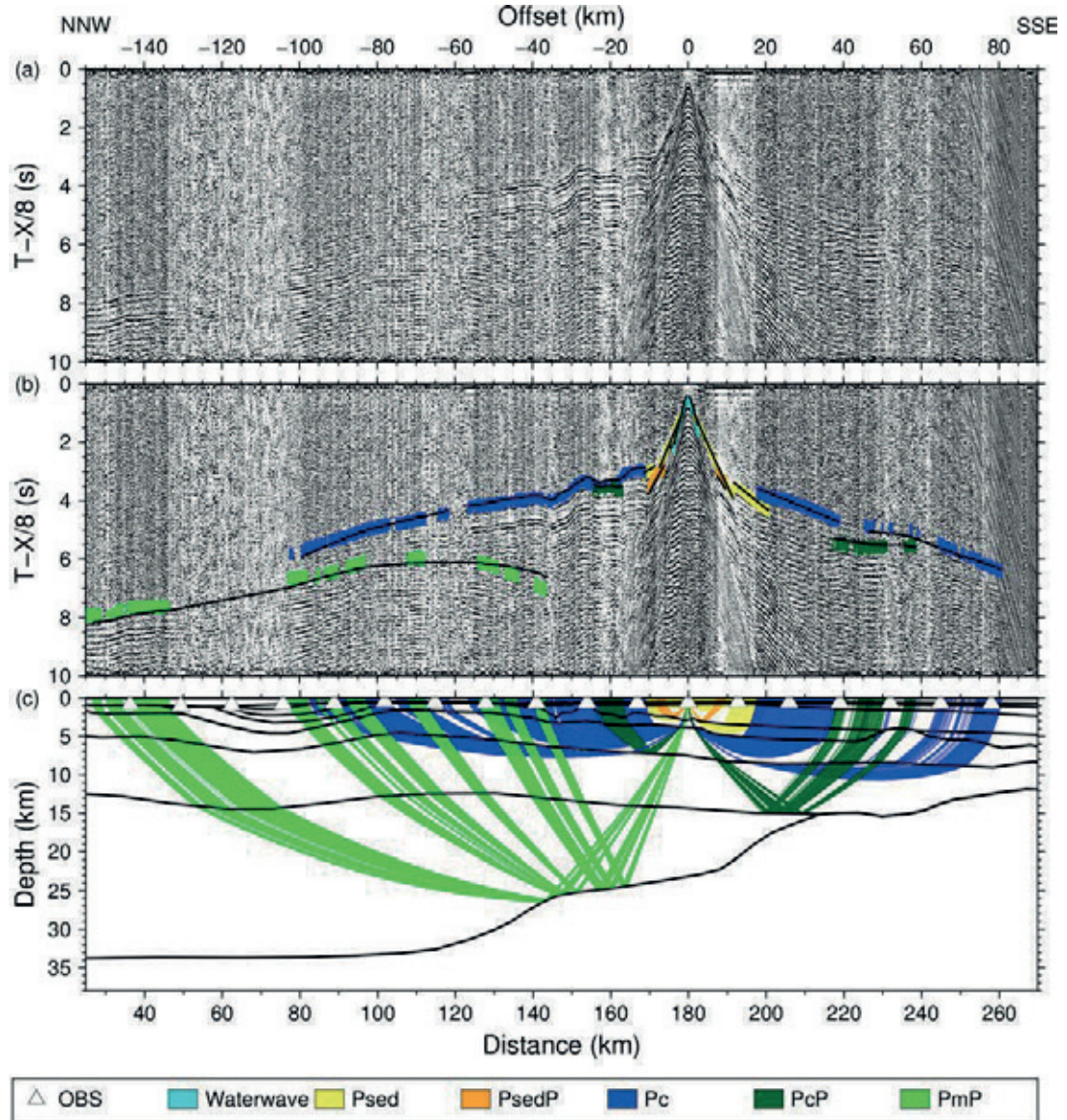


Figure 5.6: Parts of the recorded seismogram section, picked signals and modeled raypaths for OBS 12.

(a) Seismogram section of the hydrophone component, plotted with a reduction velocity of 8 km/s. A 3–14 Hz bandpass filter and an automatic gain control (AGC) is applied.

(b) Same section of the hydrophone component as seen above, but overlain by picked phases (colored vertical bars). The length of the bars represents the pick uncertainties. Black lines mark the modeled traveltimes within the P wave velocity model.

(c) Raypaths of the picked phases within the velocity model. Black lines mark the layer boundaries of the velocity layers.

Examples for seismic section, picked phases and modeled raypaths of OBS 1, 4, 12, 24 and 27 are given in Figures 5.5–5.8. A two dimensional P wave velocity model (Figure 5.9), covering 399 km between Northumberland Island and the last shotpoint of AWI-20100300, was generated by forward modeling with the rayinvr software (Zelt and Smith, 1992). Additionally, main structural elements visible as reflectors in the reflection seismic data (Figure 5.3), like the onset of oceanic basement or the position of a fault between km 370 and 385, were also included into the velocity model.

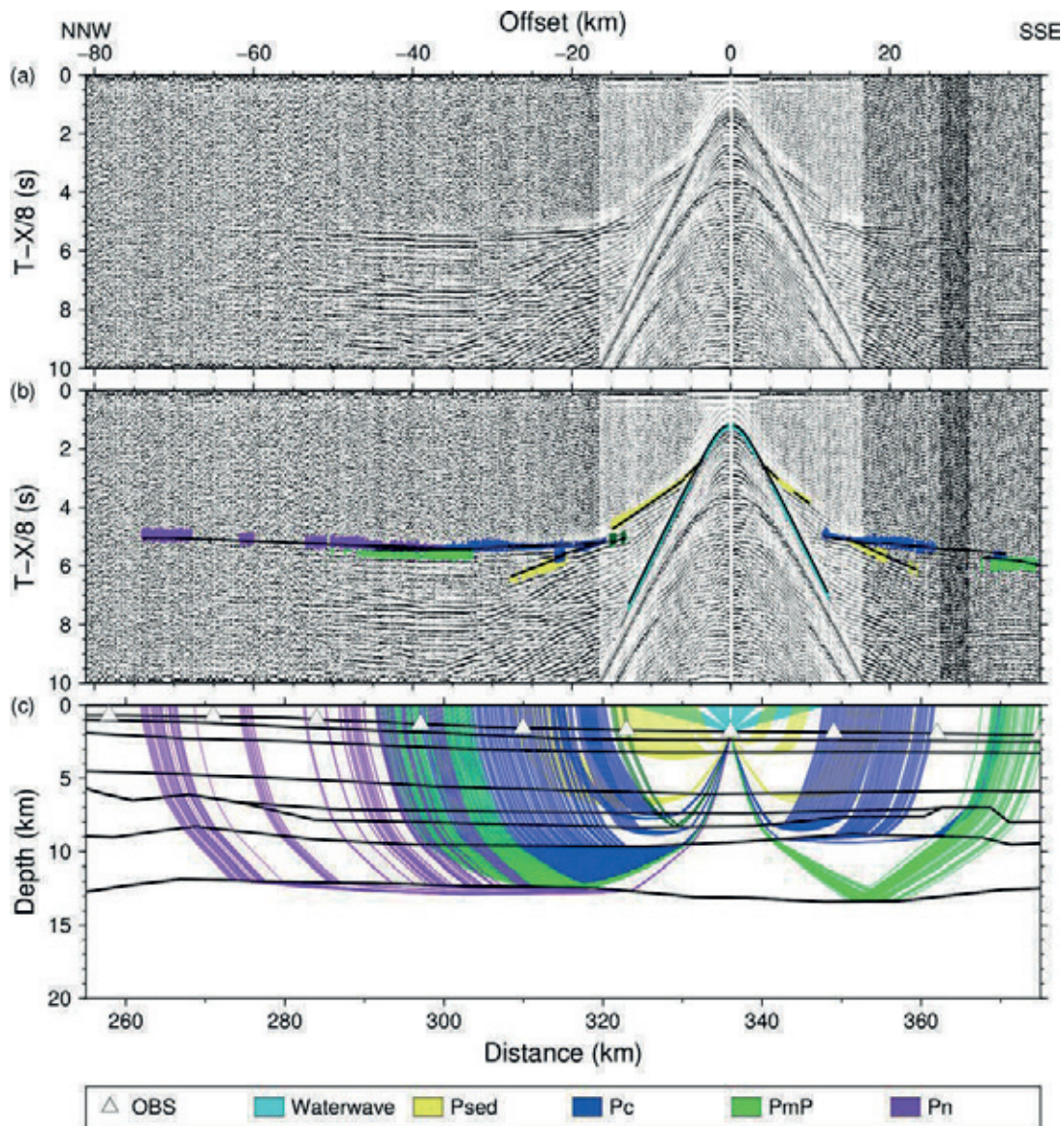


Figure 5.7: Parts of the recorded seismogram section, picked signals and modeled raypaths for OBS 24.

(a) Seismogram section of the z -component, plotted with a reduction velocity of 8 km/s. A 3–14 Hz bandpass filter and an automatic gain control (AGC) is applied.

(b) Same section of the z -component as seen above, but overlain by picked phases (colored vertical bars). The length of the bars represents the pick uncertainties. Black lines mark the modeled traveltimes within the P wave velocity model.

(c) Raypaths of the picked phases within the velocity model. Black lines mark the layer boundaries of the velocity layers.

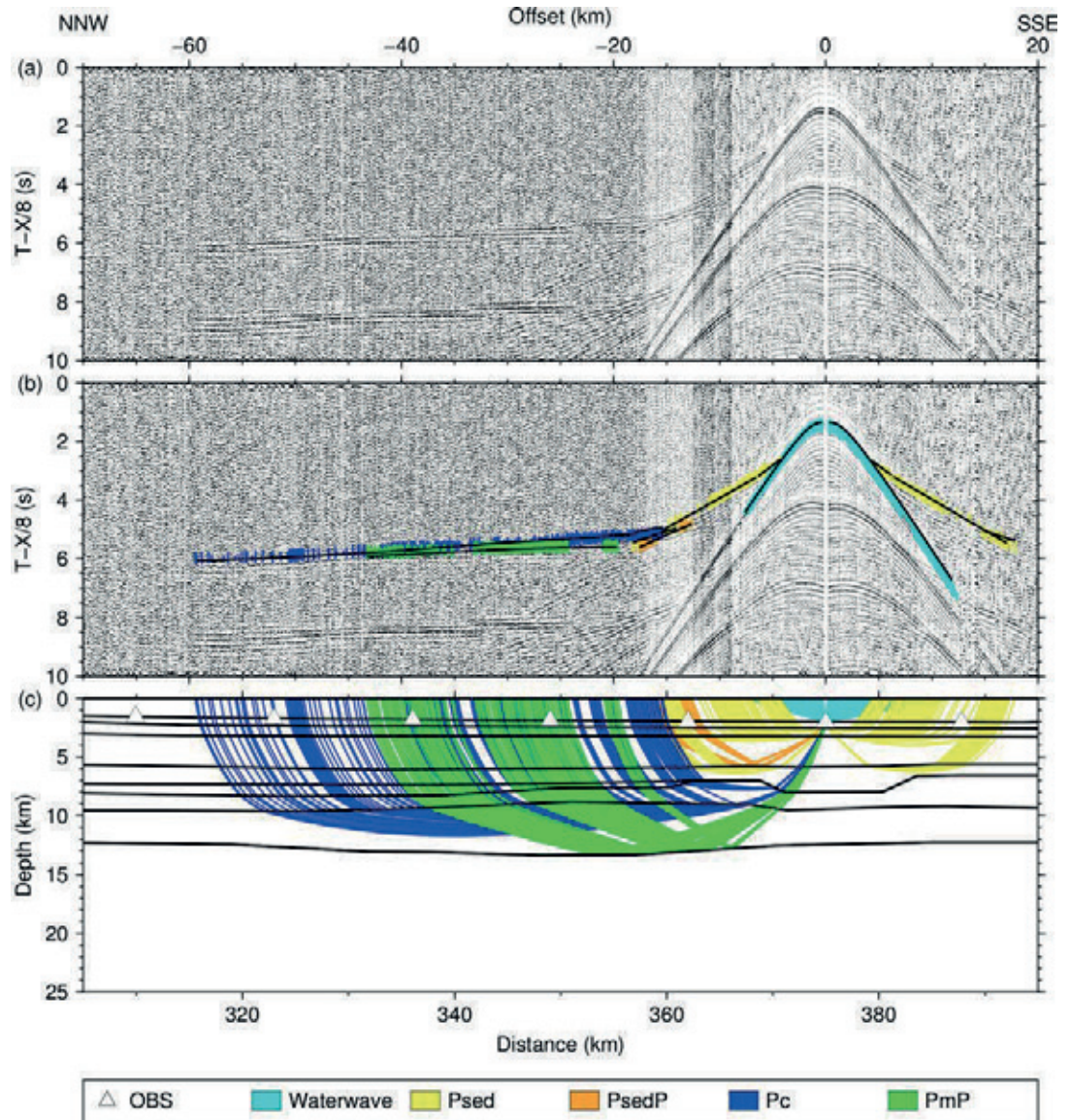


Figure 5.8: Parts of the recorded seismogram section, picked signals and modeled raypaths for OBS 27.

(a) Seismogram section of the hydrophone component, plotted with a reduction velocity of 8 km/s. A 3–14 Hz bandpass filter and an automatic gain control (AGC) is applied.

(b) Same section of the hydrophone component as seen above, but overlain by picked phases (colored vertical bars). The length of the bars represents the pick uncertainties. Black lines mark the modeled traveltimes within the *P* wave velocity model.

(c) Raypaths of the picked phases within the velocity model. Black lines mark the layer boundaries of the velocity layers.

5.5.1 Model uncertainty and error analysis

The *P* wave velocity model (Figure 5.9a) is based on 20447 picks in total. The number of picks, RMS misfits and χ^2 -values of different velocity layers are presented in Table 5.1. The used pick uncertainties range between 45 and 200 ms and are based on the signal-to-noise ratio. RMS misfits between calculated and picked travel times range between 61 and 211 ms. The average RMS misfit is 119 ms. The χ^2 -value for the model is 0.913, which is close to the perfect value of 1.

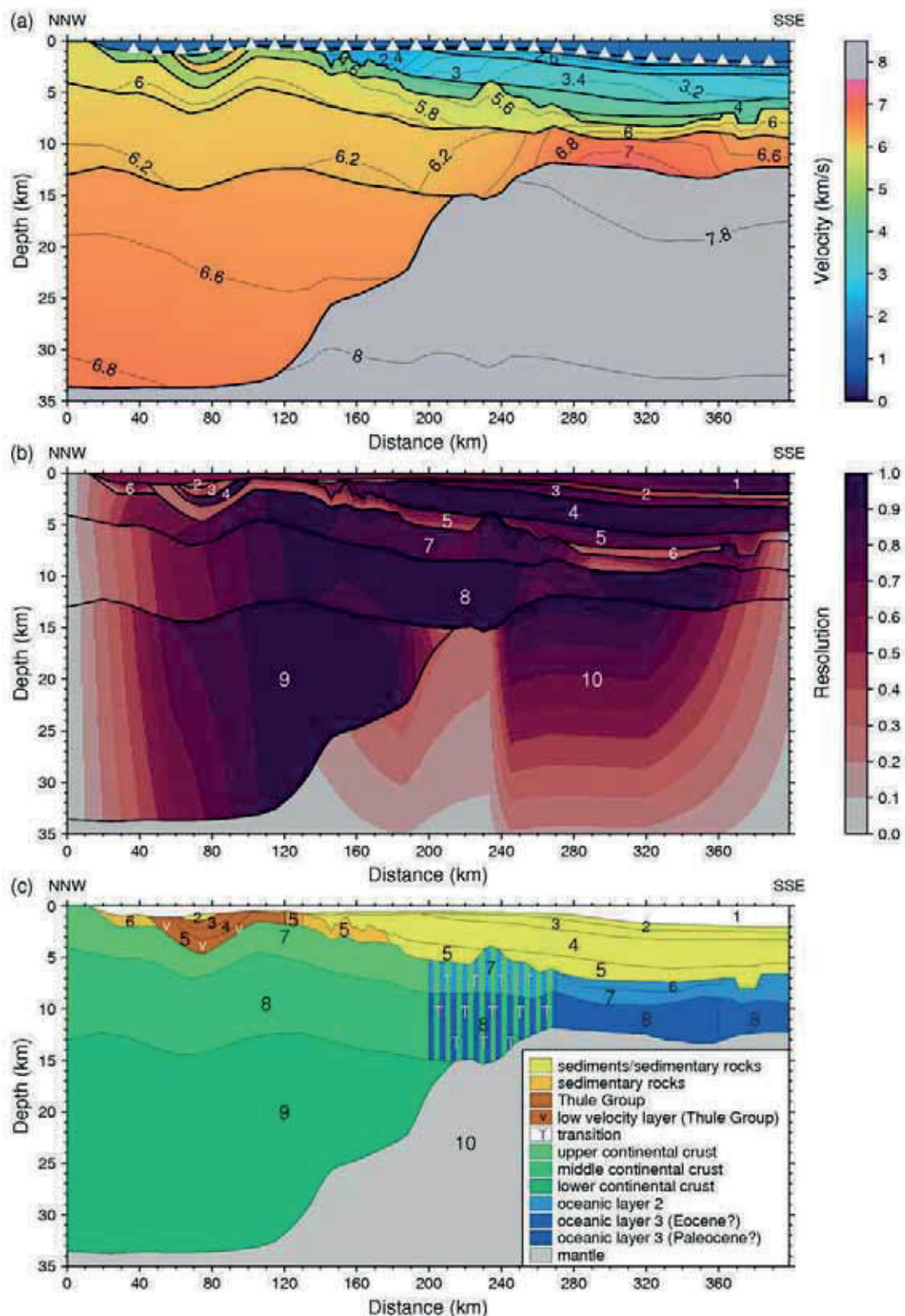


Figure 5.9: *P* wave velocity model, resolution and geological interpretation of AWI-20100300. (a) *P* wave velocity model. Intersections with profile AWI-20100200 at km 369.8 and profile line 3 at km 76.1 are labeled. Triangles mark the position of the OBS stations. (b) Diagonal values of the resolution matrix of *P* wave velocity model AWI-20100300. White numbers represent the number of the velocity layers. (c) Geological interpretation of the profile. Black numbers represent the number of the velocity layers.

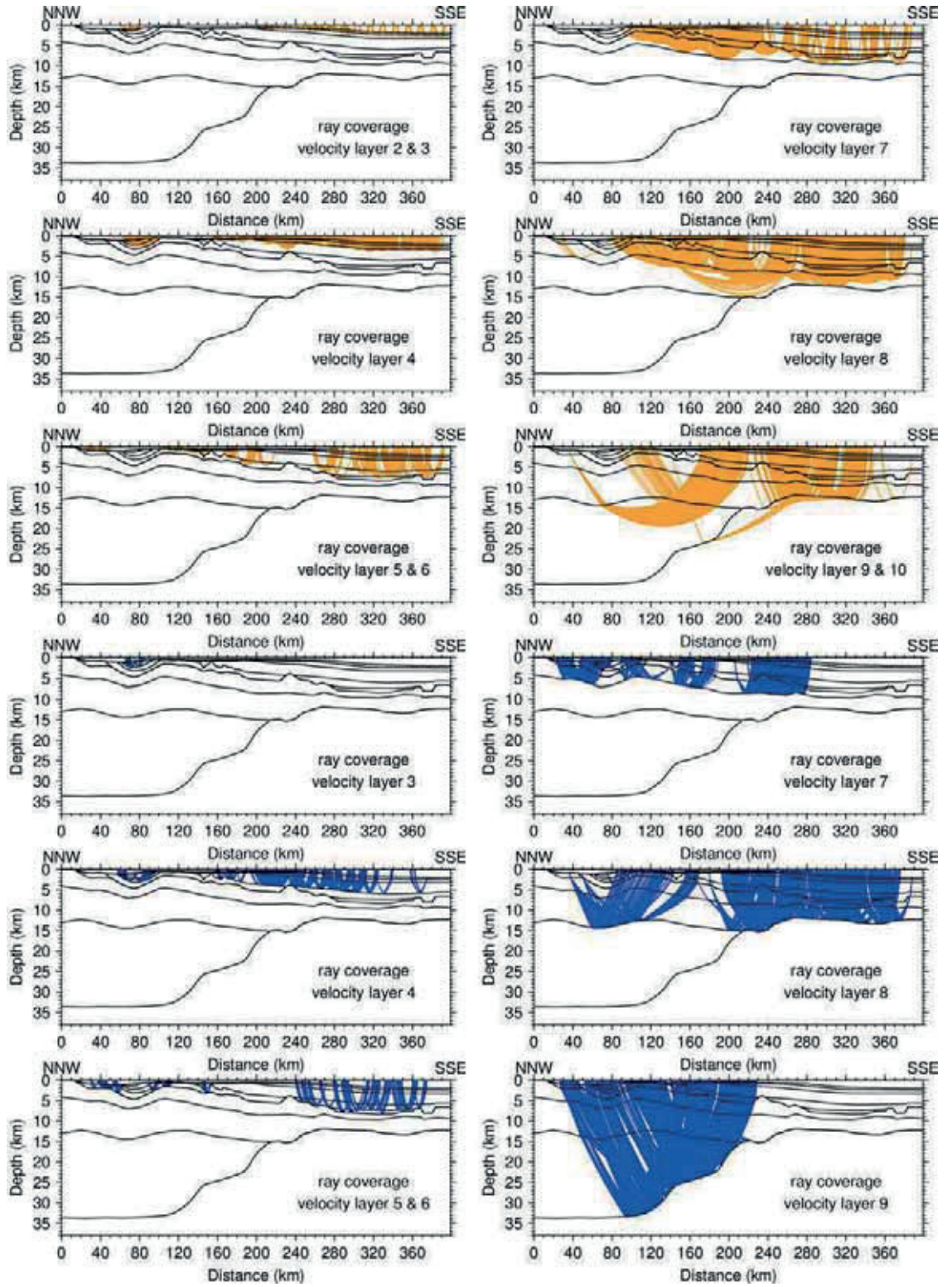


Figure 5.10: Ray coverage for different velocity layers of the *P* wave velocity model. The refracted waves are colored orange, reflected waves are colored blue.

The velocity resolution of the model, which illustrates the data constrains for the velocity nodes, is presented in Figure 5.9b. To obtain the velocity resolution, the diagonal elements of the resolution matrix diagonals were gridded. After Lutter and Nowack (1990), areas with a resolution matrix value >0.5 can be considered to be well resolved. Since the resolution depends on the ray

coverage and also on the model parameters, the ray coverage is shown in Figure 5.10.

Overall, our model is very well resolved (Figure 5.9b). A low resolution can be observed where the ray coverage is sparse (Figure 5.10), which is the case at the northern and southern termination of the model and within the eastern part of velocity layer 6. The low resolution of velocity layer 2 reflects the lack of picked arrivals for this layer. Between km 40 and 100, the low ray coverage and resolution is caused by the curved geometry of the uppermost layers and the occurrence of a low velocity layer (velocity layer 5).

Velocity and depth uncertainties have been estimated with the method of Schlindwein and Jokat (1999). The velocities of the sedimentary and crustal phases are accurate within ± 0.1 km/s. The velocity uncertainties for the upper mantle range between ± 0.15 km/s south of km 240 and are up to ± 0.2 km/s south of km 170. The upper mantle velocities north of km 170 are not constrained by any rays. The depth of the Moho can be varied up to ± 1 km, the depth of the base of velocity layer 7 up to ± 0.5 km. The base of velocity layer 6 can be changed up to ± 1.5 km between km 20 and 30, and up to ± 0.3 km between km 280 and 360. Due to the low velocities of layer 5 between km 40 and 100, the depth of its base strongly depends on the chosen velocities. To the south, the depth of the base can be varied up to ± 0.5 km. The depth uncertainties for the base of velocity layer 2, 3 and 4 are ± 0.2 km.

Table 5.1: Nomenclature of picked refracted (rfr) and reflected (rfl) phases, number of picks within the velocity layers (n), RMS misfit and χ^2 .

Velocity layer	Phases	n	RMS (s)	χ^2
1, rfl	waterwave	1909	0.121	1.516
2, rfr	P_{sed1}	22	0.079	1.781
3, rfr	P_{sed2}	613	0.067	0.664
3, rfl	$P_{sed2}P$	53	0.061	0.330
4, rfr	P_{sed3}	2026	0.073	0.532
4, rfl	$P_{sed3}P$	1362	0.081	0.512
5, rfr	P_{sed4}, P_{c1}	976	0.086	0.629
5, rfl	$P_{sed4}P, P_{c1}$	510	0.084	0.417
6, rfr	P_{c2}	190	0.104	0.794
6, rfl	P_{c2}	125	0.147	2.300
7, rfr	P_{c3}	2689	0.112	0.943
7, rfl	$P_{c3}P$	1499	0.128	0.933
8, rfr	P_{c4}	3344	0.105	0.597
8, rfl	$P_{c4}P, P_mP$	1913	0.136	0.825
9, rfr	P_{c5}	403	0.211	2.524
9, rfl	P_mP	1847	0.198	1.964
10, rfr	P_n	1033	0.070	0.188
All layers	All phases	20514	0.119	0.913

5.6 Results

5.6.1 Velocity model

Figure 5.9a shows the obtained P wave velocity model of AWI-20100300. Here, it is important to note that velocity layers do not always represent geological units. To keep the amount of velocity layers low and the velocity model simple, some geological units were combined into one velocity layer (for example velocity layer 5, Figure 5.9), even if the MCS-data showed the existence of

different structural units. For better understanding of the crustal structure, Figure 5.9c illustrates the division of velocity layers into geological units.

On basis of the *P* wave velocities, different sedimentary units and crustal types were identified. The crustal layers (velocity layer 6–9) can be divided into continental crust (km 0–200), transitional crust (km 200–270) and oceanic crust (km 270–399).

5.6.1.1 Sedimentary layers and Thule Supergroup

The thicknesses and the velocities of the sedimentary layers above the northern continental crust are highly variable. Below the up to 500 m thick sediments of the Steensby Basin at ~km 80 (Figure 5.9, velocity layer 2, 2.9–3.0 km/s), three layers with a maximum thickness of ~3.2 km are present. North and south of the Steensby Basin, these layers are partly eroded. Following the interpretation of Funck et al. (2006), the three layers represent sedimentary rocks of the Thule Supergroup. In our model, the greatest thickness of the Thule Supergroup package can be observed in the area of the Steensby Basin (~3.8 km). The uppermost two layers of the Thule Supergroup are up to 1 km thick, their velocities and thickness is well constrained by refractions and reflections (Figure 5.10). The uppermost layer has velocities of 4.5–4.9 km/s. Velocities of 6.0–6.2 km/s characterize the central layer of the Supergroup, which likely marks the basalt layer within the Thule Supergroup. Between km 57 and 102, the lowermost layer of the Thule Supergroup consists of a low velocity layer, which is indicated by a time delay between the phases visible in the recorded sections (red box, Figure 5.5). Therefore no information of the *P* wave velocity could be obtained in this region. Since the overlying layers are eroded north and south of the Steensby Basin, we were able to obtain velocities (5.0–5.3 km/s) of the lowermost Thule Supergroup layer from OBS 2, 6, and 7, and also used these velocities to model the lowermost Thule Supergroup where the velocity inversion occurs. The base of the low-velocity layer is partly well constrained by reflections (Figure 5.10).

Between km 130 and 140, the velocity of velocity layer 5 decreases significantly from 5.0–5.2 to 4.5–4.7 km/s. Due to the partial failure of OBS 8 and strong multiples in the reflection seismic data in this area (Figure 5.3a, CDP 16000–14000), it is not clear if and where a termination of the lowermost layer of the Thule Supergroup is present (see km 120–130 in Figure 5.9). Northward of km 50, velocity layer 6 has been modeled with velocities of 4.7–4.8 km/s.

Between km 130 and 399 (Figure 5.9), sediments covering the crust have been divided into four velocity layers. Here, the sediment thickness ranges between 4.5 and 6 km. Within the upper two sedimentary layers, the velocity ranges between 1.7 and 2.3 km/s (velocity layer 2), and 2.4 and 2.8 km/s (velocity layer 3). The velocity of the second sedimentary layer is well constrained by refractions, while the velocity of the first sedimentary layer is only constrained by some refracted phases picked in the seismic sections of OBS 16 and OBS 18 (Figure 5.10). A reason for this might be that the water wave (direct wave) covers the refracted arrivals of the upper sedimentary layer. Between km 137 and 399, the velocity of the third sedimentary layer (velocity layer 4) ranges between 2.2 and 3.5 km/s. The highest velocities in this layer have been modeled below the shelf edge (~3.3–3.5 km/s) and decrease toward the south. The base of the layer is well constrained by reflections, which are a result of strong velocity increase between sedimentary layer 3 and 4. The velocities of

sedimentary layer 4 (Figure 5.9, velocity layer 5) range between 4.0 and 4.3 km/s above the oceanic crust and 4.1–4.7 km/s above the transitional and continental crust. Between km ~170 and 230, a sediment basin is visible in the MCS-data. For an easier handling, we modeled the sediment basin and the adjacent older sediments with one velocity layer (velocity layer 5).

5.6.1.2 Continental crust (km 0–200)

In our model, the continental crust extends from km 0 to ~200 and is divided into an upper, middle and lower continental crust (Figure 5.9b). The maximum depth of the Moho is ~34 km and decreases toward the south in 2 steps.

The upper crust is ~2–4 km thick and has velocities of 5.7–6.1 km/s. Its base is constrained by reflections present between km 30 and 170, while the velocity of the layer is only well constrained south of km 95 (Figure 5.10). The thickness of the underlying middle crust ranges between 6.5 and 9 km. Reflections mark its base from km 58–113 while its velocity (6.1–6.2 km/s) is constrained by refractions mainly in the upper northern part. The lower continental crust is up to 21 km thick. The depth of the Moho at the base of the lower crust is documented south of km 93 (Figure 5.10). Velocities of the lower continental crust vary between 6.4 and 6.5 km/s in the south and 6.5–6.8 km/s in the north. The velocity of the upper mantle north of km 170 is not constrained by refractions and set to 8.0–8.1 km/s.

5.6.1.3 Oceanic crust (km 270–399)

In the southern part of the model between km 255 and 399 (Figure 5.9), the ~12.3–13.5 km deep Moho is well constrained by reflections. Owing to its velocity distribution and layer composition, the crust can be divided in two parts. In the northern part, the crust between km 274 and 362 is composed of three layers (velocity layer 6–8, Figure 5.9c) while the southern part is only composed of two layers.

The upper layer of the northern oceanic crust is 0.5–1 km thick. Its top and base are constrained by reflections, but the velocities of the layer (4.6–4.8 km/s) can only be derived from sparse refractions (Figure 5.10, layer 6). No signs for the existence of this layer have been observed south of km 362, though this might be a result of the sparse ray coverage at the southern end of the model. Lower crustal velocities constantly range between 5.7 and 6.2 km/s. On the contrary, the lowermost crust in the north is characterized by higher velocities (up to 6.7–7.3 km/s) than the southern lowermost crust (6.4–6.8 km/s). Underneath OBS 27, a fault, which coincides with the position of a fracture zone (Figure 5.2) is located close to the onset of lower velocities in the southern oceanic crust.

To determine the nature of this thin crust, we compare our results with the velocities and thickness of normal oceanic crust (White et al., 1992). The thickness of the crust between km 255 and 399 varies between 4.3 and 6.3 km and is therefore thinner than the average thickness of ~7.1 km for normal igneous oceanic crust (White et al., 1992).

After White et al. (1992), the velocities of oceanic layer 2 are within a range of 2.5–6.6 km/s, while layer 3 has a velocity of 6.6–7.6 km/s. Also, the velocity gradients in oceanic layer 3 are normally lower than in the overlying oceanic layer and layer 3 is about twice as thick (~5 km) as oceanic layer 2 (~2.1 km thickness).

On basis of their velocities and velocity gradients, velocity layer 7 and 8 can be classified as oceanic layer 2. In the southern part of the model, the velocities of oceanic layer 3 (>6.4 km/s) are lower than the velocities of normal oceanic layer 3. Since the same low velocities in layer 3 have also been discovered by Suckro et al. (2012) and Altenbernd et al. (2014) in central and northern Baffin Bay, the rather low velocities seem to be typical for oceanic layer 3 in the Baffin Bay. Additionally, a normal thickness proportion of 1:2 between oceanic layer 2 and 3 is only present between km 330 and 380 in our model.

We compared the crust between km 200 and 390 with velocity-depth profiles typical for 58–112 Myrs old Atlantic oceanic crust (Figure 5.11). The velocity-depth profiles between km 270 and 390 fit well and the greatest mismatch is caused by the low thickness of oceanic layer 3. This is a typical observation for abnormally thin oceanic crust, since its variations in thickness is mainly caused by thickness variations of layer 3 while layer 2 has a near-to-normal thickness (Mutter and Mutter, 1993). Therefore, we classify the crust between km 270 and 399 to consist of thin oceanic crust (km 360–399) and thin oceanic crust with a high velocity lower crust (km 270–360, Figure 5.9).

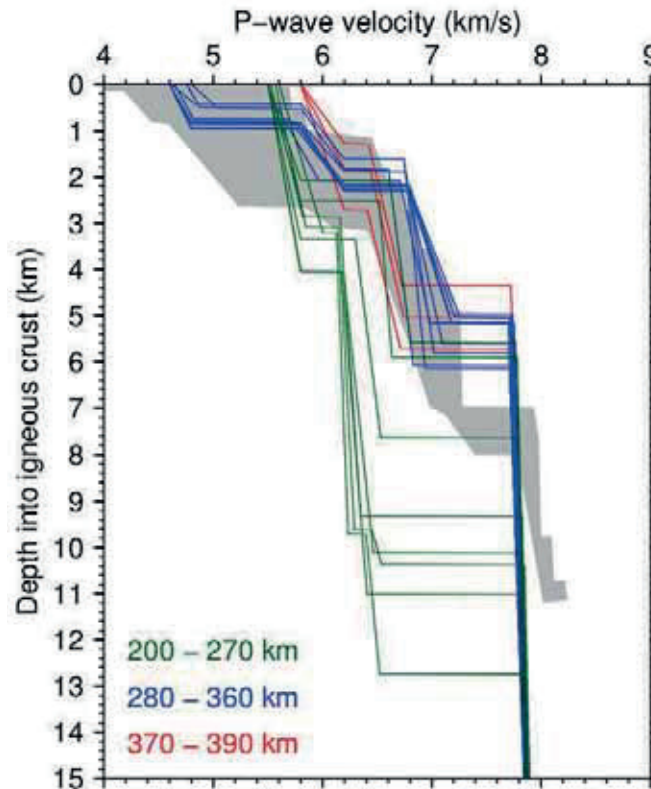


Figure 5.11: Comparison of velocity-depth-functions from AWI-20100300 with normal oceanic crust. The grey area represents velocity-depth-functions for normal, 59 - 127 Mys old Atlantic oceanic crust, taken from White et al. (1992). The velocity-depth-functions along our profile were taken every 10km in the COT (green lines), northern thin oceanic crust (blue lines), and southern thin oceanic crust (red lines).

5.6.1.4 Continent-ocean transition zone (km 200–270)

On basis of our velocity model, it is not possible to identify a clear continent-ocean boundary. However, between the crustal units we interpret to be of continental and oceanic origin, we find a continent-ocean transitional zone

(COT), which differs in its velocity structure from the adjacent crust. Within the COT, the 6–11.5 km thick crust is composed of 2 crustal layers (Figure 5.9) and the Moho depth as well as thickness and velocities of both crustal layers are well constrained by refractions and reflections (Figure 5.10). The upper crust (velocity layer 7) has a velocity of 5.5–6.0 km/s, which is lower than in the adjacent oceanic crust and lower than the adjacent upper continental crust. Within lowermost crustal layer of the COT, the velocities decrease toward the north from ~6.5–6.6 km/s to 6.1–6.2 km/s. Below the transitional crust, the upper mantle is characterized by velocities greater than 7.8 km/s. Since the mismatch between oceanic crust and crust north of km 270 increases (Figure 5.11), the onset of the COT in the south was set to km 270. In the north, we set the onset of the COT to km 200 due to the increasing velocities toward the north.

5.6.2 Density model

A 2D density model was created (Figure 5.12, starting model and modified model) by forward modeling of shipborne gravity data with the software GM-SYS (Northwest Geophysical Associates, Inc.). Layer boundaries of the seismic velocity model were taken as an input for the starting model. Also, average velocities used for *P* wave modeling were converted to densities with the velocity-density function from Barton (1986). Vertical boundaries between different density layers were inserted where strong density variations occurred within a layer.

The obtained starting model is shown in Figure 5.12a, and shows a reasonable fit between observed and calculated gravity data between km 100 and 180. In the southern part of the model, misfits between 10 and 40 mGal are present. The greatest misfits (~50 mGal) are observed in the Steensby Basin region and in the COT.

To increase the fit, the density model was partly adjusted (Figure 5.12b) and some densities were slightly changed. In contrast, the geometry of the horizontal layer boundaries (top and base of layers) derived from the velocity model remained unchanged, while the position of the introduced vertical density layer boundaries were partly adjusted, for example in the lower oceanic and transitional crust. Additionally, some density layers were divided into two or more layers with different densities to better depict density variations derived from high velocity variations within a layer. For example, a body of lower density was included into the upper crust of the COT. This resulted in a very good fit between observed and calculated gravity values. The greatest misfits could be decreased to less than 20 mGal in the Steensby Basin region and in the COT.

5.7 Discussion

In this section we compare our results to three other seismic refraction profiles, which either cross our profile (at km 76.1 and 369.8) or are located in the vicinity of AWI-20100300. By this we evaluate if our results are in agreement with previous studies on the continental and oceanic crustal structure of the region.

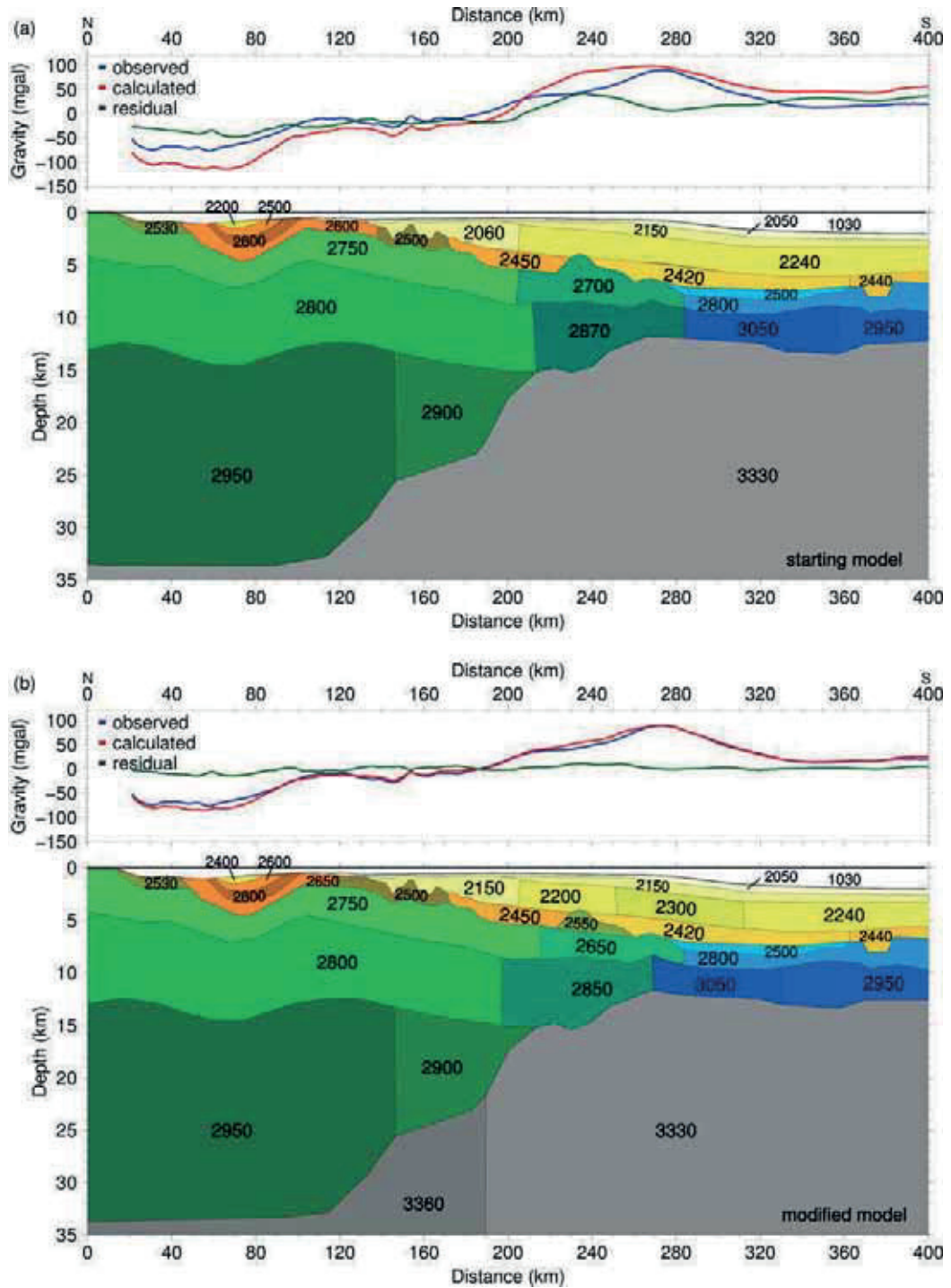


Figure 5.12: Gravity modeling along AWI-20100300.

(a) Starting model for 2D gravity modeling for AWI-20100300. The upper panel shows the observed and calculated free-air anomalies and resulting residuals. The lower panel shows the density units derived from the P wave velocity model of AWI-20100300. The densities were calculated based on the density-velocity relationship after Barton (1986) and are given in kg/m^3 .

(b) Modified model for 2D gravity modeling for AWI-20100300. The upper panel shows the observed and calculated free-air anomalies and resulting residuals. The lower panel shows the obtained density model after some adjustments (position of vertical boundaries, new inserted density units, changed densities) have been conducted.

5.7.1 Intersection with line 3 (continental crust)

Figure 5.13 shows velocity-depth profiles of the intersections between our model and the seismic refraction profiles line 3 (Funck et al., 2006). The intersection between line 3 (Funck et al., 2006) and AWI-20100300 is located in the Thule Basin within the Steensby Basin. Like Funck et al. (2006), we were able to distinguish between four sedimentary layers and divided the crust in an upper, middle and lower unit. The lowermost Thule Supergroup layer consists of a low velocity layer in both profiles. Altogether, the crustal structures of both profiles are in most instances comparable. Differences in velocities are less than ± 0.1 km/s for the central Thule Supergroup Layer and middle continental crust and up to ± 0.2 km/s for the other layers, which is within the estimated uncertainty. Major structural differences are related to variations in thickness of the lowermost Thule Supergroup Layer and the lower continental crust.

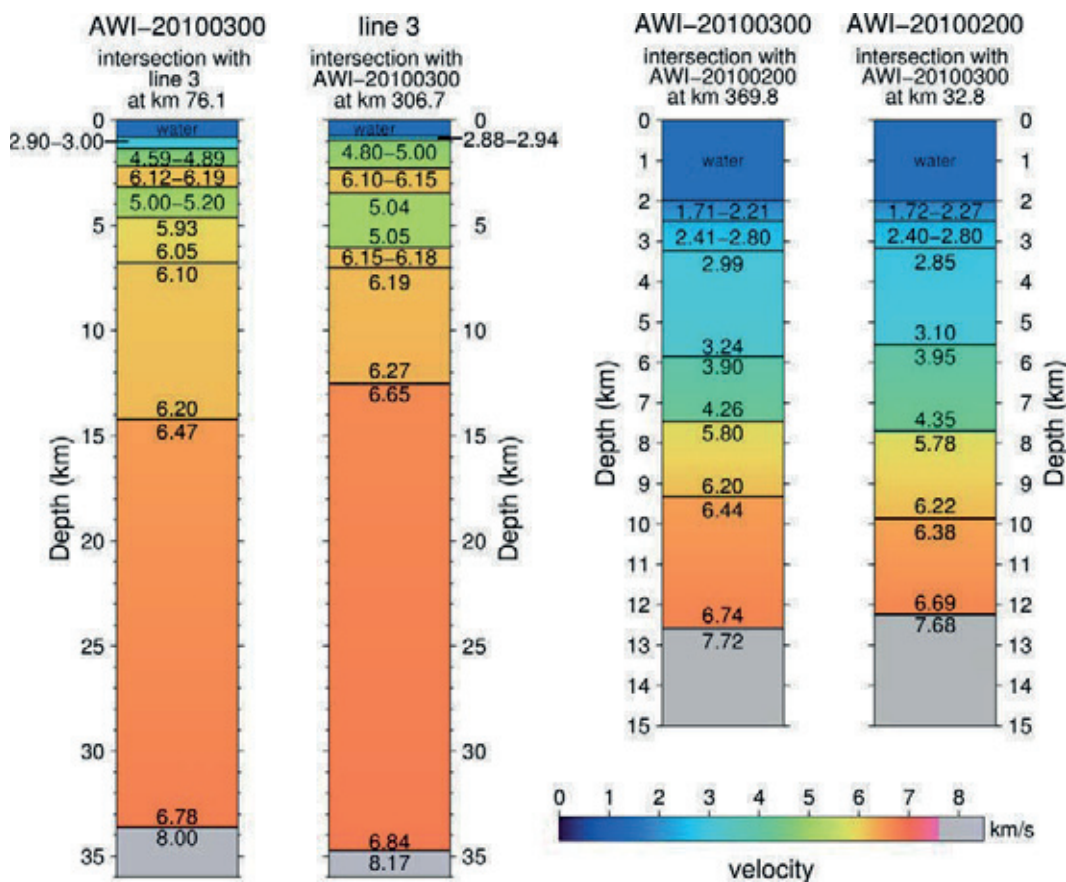


Figure 5.13: Velocity-depth profiles at the intersections between AWI-20100300 and line 3 (Funck et al., 2006) and AWI-20100200 (Altenbernd et al., 2014). Black numbers inside the columns are the P wave velocities on top and base of the layers in km/s. For location of the intersections between the profiles AWI-20100300 with line 3 and AWI-20100200 see Figures 5.2 and 5.9.

While thickness deviations of the Thule Supergroup layers are less than ~ 400 m for both upper layers, the lowermost Thule Supergroup layer is ~ 1 km thicker and characterized by a much smaller velocity gradient at line 3 than at our profile. This is probably a result of the low velocities in this layer, which cause sparse ray coverage and poor resolution. In contrast, the base of the upper continental crust is located almost at the same depth (~ 7 km) in both cross sections. At the crossing point, the base of the middle continental crust in line 3

is about 1.7 km shallower than in our model, while the velocities are only slightly higher (<0.1 km/s). In our profile, the velocity of the lower continental crust is lower and characterized by a higher gradient than in line 3. Both profiles have a good resolution (>0.7) in this area. The position of the Moho at the crossing point differs slightly (~ 1.1 km) which is almost within the estimated error for the Moho depth (± 1 km) for our profile.

5.7.2 Intersection with AWI-20100200 (oceanic crust)

The intersection between our profile and AWI-20100200 (Altenbernd et al. 2014) is located at km 369.8 in the area of the southern oceanic crust. A fracture zone (Figure 5.2) is visible in both velocity models at this intersection. Both cross-sections show a 4-layered sedimentary cover and a thin, two-layered oceanic crust (Figure 5.13). Differences in depth of layers are smaller than 1 km. The velocities differ less than 0.1 km/s with exception of third upper sedimentary layer, where the velocity at the cross point of our profile is up to 0.14 km/s greater than at the cross point of AWI-20100200.

5.7.3 Comparison with profile 91/3 of Jackson and Reid (1994)

The seismic refraction profile 91/3 (Jackson and Reid, 1994) is located almost parallel to our profile (Figure 5.2). The distance between both profiles is < 10 km in the north and < 35 km in the south. Figure 5.14 compares velocity-depth functions at the shortest distance between profile 91/3 and AWI-20100300 (red lines) and velocity-depth functions at the position of OBS 1 (AWI-20100300) and km 80 at 91/3 (blue lines, Figure 5.14).

Only five OBS were deployed along the 250 km long profile 91/3, and the number of layers used for modeling is less (two sedimentary and two continental layers) than for our profile. Jackson and Reid (1994) did not identify a low velocity layer in the sedimentary cover, and used much smaller velocities for modeling the lower continental crust (6.3–6.6 km/s), which can be a result of the lower data quality and less data coverage, as already stated by Funck et al. (2006). Nevertheless, the Moho depth in the northern part of both profiles is almost the same as in our model (Figure 5.14, blue lines, difference less than 1.5 km). At the closest point (distance ~ 10 km) between both profiles (red lines, Figure 5.14), our Moho is located ~ 2 km deeper than at 91/3. Like in our model, the depth of the Moho along 91/3 increases in a large step toward the south. The increase in Moho depth between OBS 7 and 9 (Figure 5.9) coincides with a NW-SE trending gravity low (Figure 5.1c) in southern Smith Sound.

5.7.4 Crustal structure and origin of thin oceanic crust

Altenbernd et al. (2014) showed that thin oceanic crust (3.5–6 km thick) is present in northern Baffin Bay along AWI-20100200 and suggested that slow spreading rates might be the reason for its reduced thickness. Our profile AWI-20100300 reveals that thin oceanic crust is also present in the very northern Baffin Bay. Oakey 2005 calculated spreading rates in Nares Strait based on a kinematic model: Slow spreading during the Paleocene (15 mm/a, chron 27N–25N) and Eocene (13 mm/a, chron 24N–13N) was interrupted by a short episode of faster spreading (36 mm/a) during chron 25N–24N. Like Altenbernd et al. (2014), we also identified low mantle velocities underneath thin oceanic

crust along line AWI 20100300, which is another indicator for slow spreading and likely caused by serpentinized mantle peridotites. Serpentinization of the upper mantle is a common observation beneath thin oceanic crust, and was also reported from the Boreas Basin (Hermann and Jokat, 2013) or the Mohns Ridge (Klingelhöfer et al., 2000).

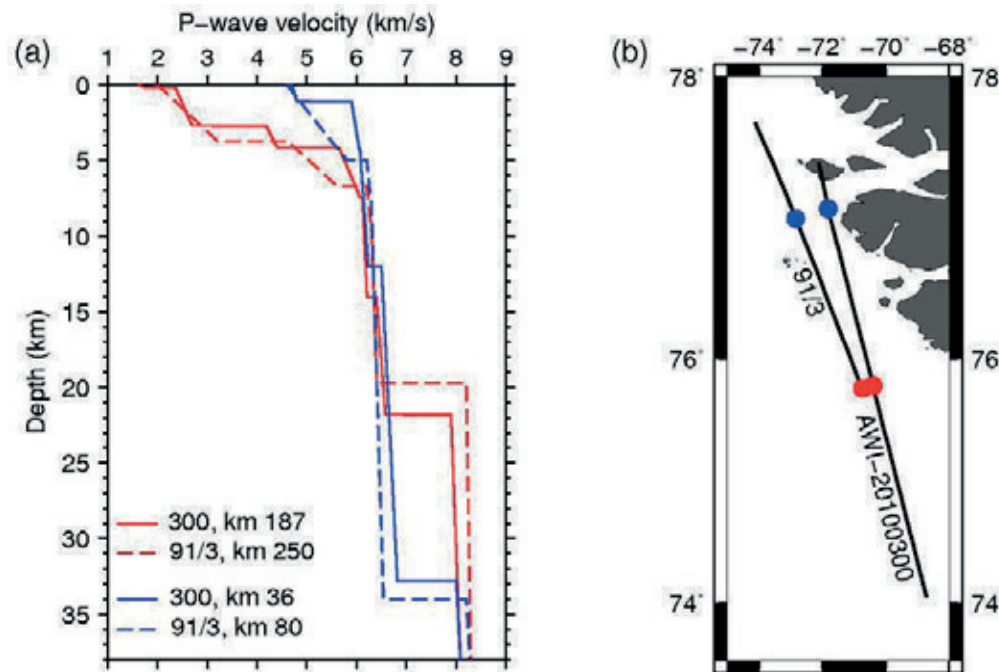


Figure 5.14: Comparison between AWI-20100300 and profile 91/3. (a) Velocity-depth-functions for AWI-20100300 (this study) and profile 91/3 (Jackson and Reid, 1994) are shown. The differences in Moho depth are less than 1.5 km at the northern point (blue lines) and ~2.5 km at the southern point (red lines). (b) Locations where the velocity-depth-functions shown in (a) were taken along the profiles. The distance between the northern locations (blue dots) is ~27 km, the distance between the southern locations (red dots) is ~10 km.

In our model, the onset of oceanic crust fits well with the position of the COT proposed by Hosseinpour et al. (2013). They calculated the COT based on crustal thicknesses and thinning factors, which were derived from potential field data and available seismic profiles. We propose that the Paleocene oceanic crust includes the “transition crust” proposed by Oakey and Chalmers (2012) (Figure 5.15): Their onset of transitional crust is almost identical with the onset of our oceanic crust. If we change their landward termination of transitional crust into the onset of oceanic crust, it almost exactly fits our findings about the extent of oceanic crust in northern Baffin Bay.

If we compare the crustal structure of the Paleocene oceanic crust from AWI-20100300 and AWI-20100200 at the crossing point, the thickness of the oceanic crust is about the same in both models (~4.5–6.5 km, Figure 5.13) and their velocity-depth functions are almost identical. But landward of the crossing point, the Paleocene oceanic crust along AWI-20100300 consists of three instead of two layers and higher velocities than along AWI-20100200 characterize oceanic layer 3. This observation is irritating since the age and origin of the three-layered, northern oceanic crust and the oceanic crust between km 30 and 80 of profile AWI-20100200 should be the same (Figure

5.2). One explanation might be that the thin uppermost oceanic layer was not identified in the seismic sections of AWI-20100200 due to its marginal thickness. Altenbernd et al. (2014) also stated that between km 50 and 80, the sedimentary layer on top of the oceanic crust may incorporate basaltic layers. Another reason for the absence of the uppermost layer found in AWI-20100300 might be a change in crustal composition north of the fracture zone (Figure 5.15).

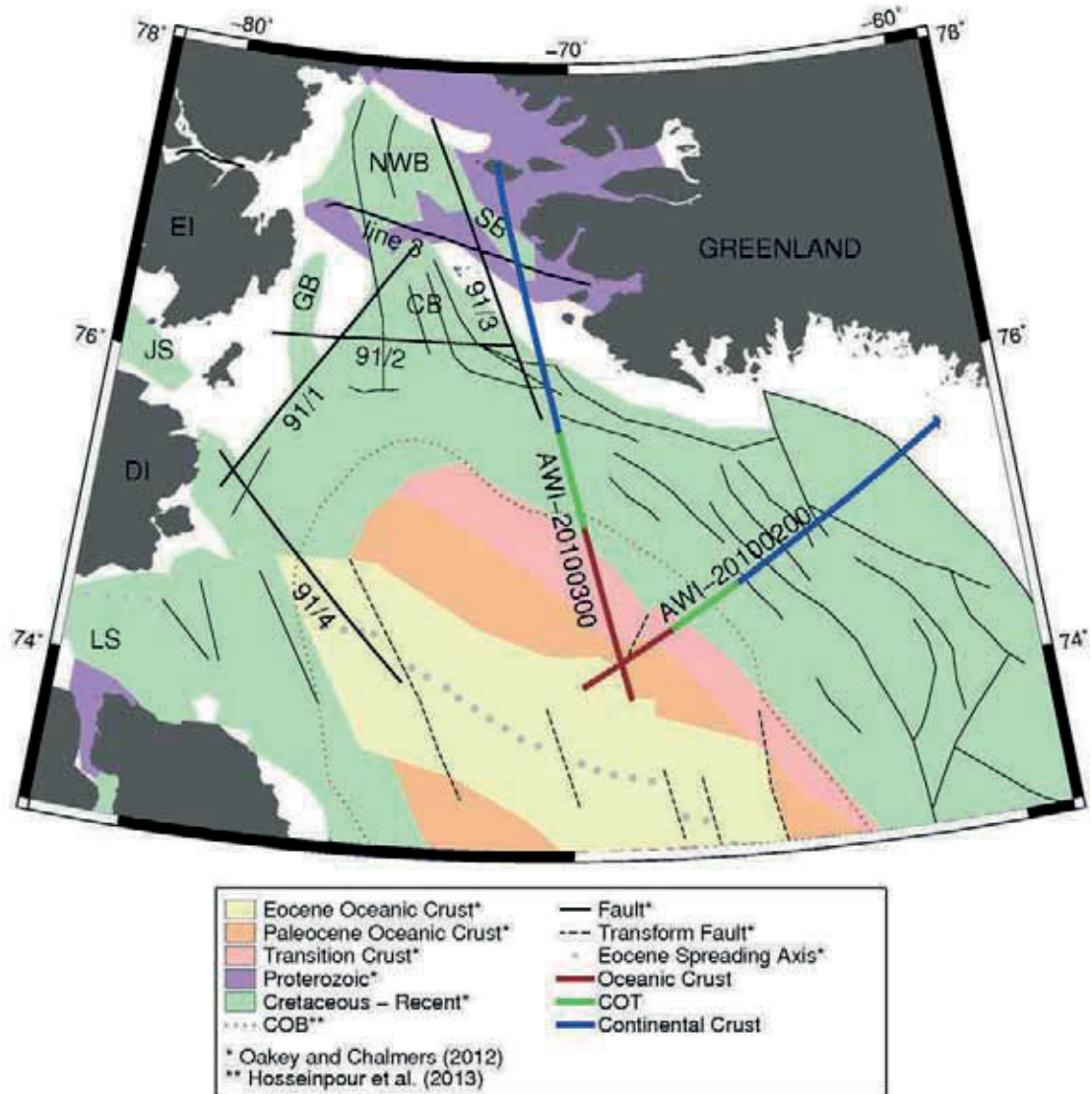


Figure 5.15: Comparison between the distribution of crustal types along AWI-20100300 (this study) and AWI-20100200 (Altenbernd et al., 2014) with offshore geology modified after Oakey and Chalmers (2012) and the COB of Hosseinpour et al. (2013). Black lines mark the position of seismic refraction profiles. AWI-20100200: Altenbernd et al. (2014), AWI-20100300: this study, 91/1 – 91/4: Jackson and Reid (1994) and Reid and Jackson (1997a), line 3: Funck et al. (2006). Abbreviations: GB: Glacier Basin, NWB: Northwater Basin, SB: Steensby Basin, CB: Carey Basin, JS: Jones Sound, LS: Lancaster Sound, DI: Devon Island.

Interestingly, in both *P* wave velocity profiles of AWI-20100200 and AWI-20100300, changes in crustal velocity of the oceanic layers occur in an area close to the proposed boundary between Paleocene and Eocene oceanic crust and also close to the location of the fracture zone (Figures 5.2 and 5.9). It has to

be kept in mind that the lower velocities within the Eocene oceanic crust in AWI-20100200 are not as reliable as along our profile, since they are only present at the very southern end of the profile where the ray coverage is sparse. Nevertheless, a change in velocities is observed in the seismic sections of OBS 26-28 of AWI-20100300. Therefore, it can be discussed if these changes are caused by different crustal composition of Eocene and Paleocene oceanic crust due to changes in magma supply along the ridge axis after the changes in spreading direction. Furthermore, this observation might be linked to the presence of the fracture zone at the southern end of the profile. Since clear magnetic spreading anomalies have not been discovered in northern Baffin Bay, the distinction between Eocene and Paleocene oceanic crust on basis of their crustal velocities and composition might be one way to map the extent of crustal units in Baffin Bay and to decipher its opening history.

To check if the changes in crustal structure and velocities can be explained with age and origin of the crust, we divide our oceanic crust in an Eocene (northern) and Paleocene (southern) segment and compare its characteristics with Paleocene and Eocene oceanic crust in southern Baffin Bay (Figure 5.1) along AWI-20080500 (Suckro et al., 2012) and AWI-20100600 (Funck et al., 2012).

Based on their findings along AWI-20080500, Suckro et al. 2012 developed a new kinematic model of the evolution of southern Baffin Bay. The resulting map of oceanic crust slightly differs from the map of Oakey and Chalmers (2012), but their extent of Eocene and Paleocene oceanic crust along profile AWI-20100500 is in accordance with the map of Oakey and Chalmers (2012) (Figure 5.1). The oceanic crust along AWI-20080500 consists of normal oceanic crust and is composed of up to three igneous layers. Thickness and velocity gradient of oceanic layer 3 are greater than along our profile. The Paleocene oceanic layer 3 along AWI-20100500 (Suckro et al., 2012) is in most instances characterized by slightly higher velocities (+0.1–0.2 km/s) than the younger Eocene oceanic crust. These velocity variations are very small and partly range within the stated velocity uncertainty of 0.1 km/s for the model.

Unfortunately, it is difficult to divide the oceanic crust along AWI-20080600 (Funck et al., 2012) in an Eocene and a Paleocene segment, since oceanic crust west of their OBS 616 is classified as Paleocene oceanic crust in the map of Oakey and Chalmers (2012) (Figure 5.1), but as Eocene oceanic crust in an older map of Chalmers and Oakey (2007). In contrast to our profile, oceanic layer 3 along AWI-20080600 (Funck et al., 2012) shows no lateral variations in velocity, but also varies in its thickness. Unlike in our profile, changes in velocity are only observed in oceanic layer 2. The thickness variations of oceanic layer 3 seem to correlate with the positions of a transform fault (Funck et al. 2012) and, like in our profile, a fracture zone.

Because there is no further data for comparison, we cannot answer if lower velocities within layer 3 are characteristic for Eocene oceanic crust in Baffin Bay or if they are a result of the fracture zone. It might even be a combination of both.

5.7.5 COT and margin

AWI-20100300 is the first seismic refraction profile, which images the COT in the northernmost part of Baffin Bay. In the southern part of the COT, the velocity of the lowermost layer changes toward the continent within a narrow

zone of ~40 km. However, we do not observe a sharp transition in velocity and thickness between oceanic and continental crust, which often occurs at transform margins. For example, this has been reported at the transform margin at the northwestern end of profile AWI-20080600 (Funck et al., 2012). A rapid change of crustal thickness within a narrow zone does not occur in the vicinity of the velocity change between oceanic and transitional crust, but ~60 km north of the onset of oceanic crust.

The COT along our profile is characterized by lower velocities than the adjacent oceanic and continental crust (Figure 5.9a). The velocities and velocity gradients of the transitional crust resemble that of the adjacent continental crust rather than velocities of the oceanic crust. Therefore, it seems reasonable that the transition is mainly composed of stretched continental crust.

Our findings of low velocities within the COT are contrary to observations made along AWI-20100200 (Altenbernd et al., 2014), where a high velocity lower crust and a magmatic structure are present in the COT. Such an influence of magmatism is not observed along AWI-20100300.

Also, no typical indications for a volcanic passive margin, like massive volcanism, SDR, or magmatic underplating, which characterize the volcanic margins of southern Baffin Bay and Davis Strait (Funck et al., 2007; Gerlings et al., 2009; Skaarup et al., 2006; Suckro et al., 2012) are present along our profile. Therefore, the margin has a non-volcanic character. But compared with the 70–80 km wide transition zone at the non-volcanic margins of southern Labrador Sea, where high gradients and velocities of 6.4–7.7 km/s of the lowermost, 4–5 km thick layer are interpreted to consist of serpentinized upper mantle (Chian et al., 1995; Chian and Loudon, 1994), we could not find indications of serpentinized upper mantle in the transition zone of AWI-20100300. This is astonishing since serpentinized upper mantle within the COT is a typical characteristic of non-volcanic margins.

5.8 Conclusions

Our findings support previous studies that the crust of southern Nares Strait is composed of a three-layered continental crust. The Moho depth along our profile steepens in two large steps toward the continent. The increase in crustal thickness between km 115 and 145 coincides with a NW-SE trending gravity low.

The continental crust is almost entirely covered by the up to ~3.8 km thick Thule Supergroup, which is partly or completely eroded north and south of the Steensby Basin. Underneath this ~0.5 km deep basin, the lowermost layer of the three-layered Thule Supergroup is characterized by a low-velocity zone.

The 70 km wide COT is characterized by lower velocities than the adjacent crustal units. The crustal velocities of the COT increase within a much narrower zone toward the ocean than toward the continent. Strong influence of magmatism, as observed at the COT of AWI-20100200, was not observed at the COT of AWI-20100300. Instead, the margin is of non-volcanic character.

On basis of its velocity structure and layer composition, we classify the 4.3–6.3 km thin crust in the northernmost area of Baffin Bay to be oceanic. Thin oceanic crust and the underlying serpentinized upper mantle with velocities of only 7.7 km/s support the theory that the Baffin Bay was formed by slow spreading.

Furthermore, the 4.3–6.3 km thick oceanic crust can be divided into two parts: The northern, likely Paleocene oceanic crust is composed of three layers and oceanic layer 3 has higher velocities than the two-layered, probably Eocene oceanic crust. Similar changes in velocity have also been observed in central Baffin Bay. Since the changes in crustal velocities occur in close vicinity to a fracture zone, we cannot make a statement whether the lower velocities are characteristic for the Eocene oceanic crust or if they are a result of the fracture zone.

5.9 Acknowledgements

We thank the DEPAS-Pool for providing the OBS for this seismic experiment. We also thank captain and crew of R/V Polarstern and the on-board seismic team, who did a great job during the acquisition of the dataset. We thank the BGR and Cairn Energy for providing the processed reflection seismic datasets of BGR10-303a and BGR10-313.

5.10 References

- Altenbernd, T., W. Jokat, I. Heyde, and V. Damm (2014), A crustal model for northern Melville Bay, Baffin Bay, *J. Geophys. Res.*, 119, 8610–8632, doi:10.1002/2014JB011559.
- Barton, P. (1986), The relationship between seismic velocity and density in continental crust—a useful constraint?, *Geophys. J. Roy. Astron. Soc.*, 87, 195–208.
- Chalmers, J. A., and K. Laursen (1995), Labrador Sea: The extent of continental and oceanic crust and the timing of the onset of seafloor spreading, *Mar. Petrol. Geol.*, 12, 205–217, doi:10.1016/0264-8172(95)92840-S.
- Chalmers, J. A., and G. N. Oakey (2007), Cretaceous–Palaeogene development of Labrador Sea and Davis Strait, *Geophys. Res. Abstr.*, 9, 01638.
- Chian, D., and K. E. Loudon (1994), The continent-ocean crustal transition across the southwest Greenland margin, *J. Geophys. Res.*, 99, 9117–9135, doi:10.1029/93JB03404.
- Chian, D., K. E. Loudon, and I. Reid (1995), Crustal structure of the Labrador Sea conjugate margin and implications for the formation of non-volcanic continental margins, *J. Geophys. Res.*, 100, 24239–24253, doi:10.1029/95JB02162.
- Damm, V. (2010), The Expedition of the Research Vessel “Polarstern” to the Arctic in 2010 (ARK-XXV/3), *Berichte zur Polar- und Meeresforschung*, 621, 234 pp., Alfred Wegener Inst. for Polar and Mar. Res., Bremerhaven, Germany.
- Dawes, P. R. (1997), The Proterozoic Thule Supergroup, Greenland and Canada: history, lithostratigraphy and development, *Geol. Greenl. Surv. Bull.*, 174, 150 pp.
- Dawes, P. R. (2009), Precambrian–Palaeozoic geology of Smith Sound, Canada and Greenland: key constraint to palaeogeographic reconstructions of northern Laurentia and the North Atlantic region, *Terra Nova* 21(1), 1–13, doi: 10.1111/j.1365-3121.2008.00845.x.
- Frisch, T., and P. R. Dawes (2014), The rotations opening the Central and Northern Atlantic Ocean: compilation, drift lines, and flow lines, *Int. J. Earth Sci.*, 103, 967–969, doi: 10.1007/s00531-013-0980-7.
- Frisch, T., and P. R. Dawes (1982), The Precambrian Shield of northernmost Baffin Bay: correlation across Nares Strait, *Medd. Grønland, Geosci.*, 8, 79–88.

Gerlings, J., T. Funck, H. Jackson, K. Loudon, and F. Klingelhöfer (2009), Seismic evidence for plume-derived volcanism during formation of the continental margin in southern Davis Strait and northern Labrador Sea, *Geophys. J. Int.*, 176, 980–994, doi:10.1111/j.1365-246X.2008.04021.x.

Gregersen, U., J. R. Hopper, and P. C. Knutz (2013), Basin seismic stratigraphy and aspects of prospectivity in the NE Baffin Bay, Northwest Greenland, *Mar. Petrol. Geol.*, 46, 1–18, doi:10.1016/j.marpetgeo.2013.05.013.

Funck, T., H. R. Jackson, S. A. Dehler, and I. D. Reid (2006), A refraction seismic transect from Greenland to Ellesmere Island, Canada: The crustal structure in southern Nares Strait, *Polarforschung*, 74, 97–112.

Funck, T., H. Jackson, K. Loudon, and F. Klingelhöfer (2007), Seismic study of the transform-rifted margin in Davis Strait between Baffin Island (Canada) and Greenland: What happens when a plume meets a transform, *J. Geophys. Res.*, 112, B04402, doi:10.1029/2006JB004308.

Funck, T., K. Gohl, V. Damm, and I. Heyde (2012), Tectonic evolution of southern Baffin Bay and Davis Strait: Results from a seismic refraction transect between Canada and Greenland, *J. Geophys. Res.*, 117, B04107, doi:10.1029/2011JB009110.

Hansen K., P. R. Dawes, T. Frisch, and P.K. Jensen (2011), A fission track transect across Nares Strait (Canada–Greenland): further evidence that the Wegener Fault is a myth, *Can. J. Earth Sci.*, 48, 819–840.

Hermann, T., and W. Jokat (2013), Crustal structures of the Boreas Basin and the Knipovich Ridge, North Atlantic, *Geophys. J. Int.*, 193, 1399–1414, doi:10.1093/gji/ggt048.

Hosseinpour, M., R. D. Müller, S. E. Williams, and J. M. Whittaker (2013), Full-fit reconstruction of the Labrador Sea and Baffin Bay, *Solid Earth*, 4, 461–479, doi:10.5194/se-4-461-2013.

Jackson, H. R., K. Dickie, and F. Marillier (1992), A seismic reflection study of northern Baffin Bay: implication for tectonic evolution, *Can. J. Earth Sci.*, 29, 2353–2369.

Jackson, H. R., and I. Reid (1994), Crustal thickness variations between the Greenland and Ellesmere Island margins determined from seismic refraction, *Can. J. Earth Sci.*, 31, 1407–1418, doi:10.1139/e94-124.

Keen, C., and D. Barrett (1972), Seismic refraction studies in Baffin Bay: An example of a developing ocean basin, *Geophys. J. Roy. Astron. Soc.*, 30, 253–271, doi:10.1111/j.1365-246X.1972.tb05812.x.

Klingelhöfer, F., L. Geli, L. Matias, N. Steinsland, and J. Mohr (2000), Crustal structure of a super-slow spreading centre: A seismic refraction study of Mohns Ridge, 72°N, *Geophys. J. Int.*, 141, 509–526, doi:10.1046/j.1365-246x.2000.00098.x.

Lutter, W. J., and R. L. Nowack (1990), Inversion for crustal structure using reflections from the PASSCAL Ouachita experiment, *J. Geophys. Res.*, 95(B4), 4633–4646, doi:10.1029/JB095iB04p04633.

Müller, R., M. Sdrolias, C. Gaina, and W. Roest (2008), Age, spreading rates, and spreading asymmetry of the world's ocean crust, *Geochem. Geophys. Geosyst.*, 9, Q04006, doi:10.1029/2007GC001743.

Mutter, C. Z., and J. C. Mutter (1993), Variations in thickness of Layer 3 dominate oceanic crustal structure, *Earth and Planet. Sci. Lett.*, 117, 295–317, doi: 10.1016/0012-821X(93)90134-U.

Neben, S., V. Damm, T. Brent, and F. Tessensohn (2006), New Multichannel seismic reflection data from North Water Bay, Nares Strait: Indications for pull-apart tectonics, *Polarforschung*, 74, 77–96.

Oakey, G. N. (2005), Cenozoic evolution and lithosphere dynamics of the Baffin Bay-Nares Strait region of Arctic Canada and Greenland, PhD thesis, Vrije Universiteit, Amsterdam.

Oakey, G. N., and J. A. Chalmers (2012), A new model for the Paleogene motion of Greenland relative to North America: Plate reconstructions of the Davis Strait and Nares Strait regions between Canada and Greenland, *J. Geophys. Res.*, 117, B10401, doi:10.1029/2011JB008942.

Reid, I., and H. R. Jackson (1997a), Crustal structure of the northern Baffin Bay: Seismic refraction results and tectonic implications, *J. Geophys. Res.*, 102, 523–542, doi:10.1029/96JB02656.

Reid, I., and H. Jackson (1997b), A review of three transform margins off eastern Canada, *Geo-Mar. Lett.*, 17(1), 87–93.

Roest, W. R., and S. P. Srivastava (1989), Sea-floor spreading in the Labrador Sea: A new reconstruction, *Geology*, 17, 1000–1003, doi:10.1130/0091-7613(1989)017<1000:SFSITL>2.3.CO;2.

Sandwell, D. T., R. D. Müller, W. H. F. Smith, E. Garcia, and R. Francis (2014), New global marine gravity model from CryoSat-2 and Jason-1 reveals buried tectonic structure, *Science*, 346, 65–67, doi: 10.1126/science.1258213.

Schlindwein, V., and W. Jokat (1999), Structure and evolution of the continental crust of northern east Greenland from integrated geophysical studies, *J. Geophys. Res.*, 104(B4), 15,227–15,245, doi:10.1029/1999JB900101.

Skaarup, N., H. R. Jackson, and G. Oakey (2006), Margin segmentation of Baffin Bay/Davis Strait, eastern Canada based on seismic reflection and potential field data, *Mar. Pet. Geol.*, 23, 127–144, doi:10.1016/j.marpetgeo.2005.06.002.

Suckro, S. K., K. Gohl, T. Funck, I. Heyde, A. Ehrhardt, B. Schreckenberger, J. Gerlings, V. Damm, and W. Jokat (2012), The crustal structure of southern Baffin Bay: Implications from a seismic refraction experiment, *Geophys. J. Int.*, 190, 37–58, doi:10.1111/j.1365-246X.2012.05477.x.

Tessensohn, F., H. R. Jackson, and I. D. Reid (2006), The Tectonic Evolution of Nares Strait: Implications of New Data, *Polarforschung*, 74, 191–198.

White, R. S., D. McKenzie, and R. K. O’Nions (1992), Oceanic crustal thickness from seismic measurements and rare Earth element inversion, *J. Geophys. Res.*, 97, 19683–19715, doi:10.1029/92JB01749.

Zelt, C. A., and R. B. Smith (1992), Seismic traveltime inversion for 2-D crustal velocity structure, *Geophys. J. Int.*, 108, 16–34, doi:10.1111/j.1365-246X.1992.tb00836.x.

6 The crustal fabric of the northeastern Baffin Bay

6.1 Abstract

The crust of the southern Melville Bay is examined based on refraction seismic and gravity data. The resulting *P* wave velocity, density, and geological models give insights into the crustal structure.

A three-layered, rifted continental crust underneath southern Melville Bay is up to 30 km thick, with crustal velocities ranging between 5.5 and 6.9 km/s. The deep Melville Bay Graben contains a 9 km thick infill with high velocities of 4 to 5.2 km/s in its lowermost part.

Along our profile, the rifted margin has been affected by magmatism. Within the ~80 km wide Continent-Ocean Transition (COT), velocities of up to 6.7 km/s mark the position of an intrusion underneath a basement high.

West of the COT, up to 5 km thick sedimentary layers cover a 4.3 to 7 km thick, two-layered oceanic crust. The upper oceanic layer 2 has velocities of 5.2 to 6.0 km/s, the oceanic layer 3 has been modeled with rather low velocities of 6.3 to 6.9 km/s. Low velocities of 7.8 km/s characterize the probably serpentinized upper mantle underneath the thin crust. The serpentinized upper mantle and low thickness of the oceanic crust are another indication for slow or ultraslow spreading during the formation of the oceanic part of the Baffin Bay.

By comparing our results on the crustal structure with other refraction seismic profiles recently published, differences in the crustal structure and sedimentary cover in northern and southern Melville Bay are revealed.

6.2 Introduction

The Melville Bay is located in the northwestern part of the Baffin Bay and characterized by deep basins filled with thick sedimentary successions. During the last years the Melville Bay was in the focus of the oil and gas industry due to assumed hydrocarbon potential in this area. Therefore, various 2D and 3D seismic reflection surveys were performed. However, the crustal structure is not well investigated and only a few refraction seismic measurements have been conducted (Figure 6.1). The crustal fabric of the Melville Bay region and the timing of the genesis remain uncertain. Statements on crustal types are in large parts based on gravity and reflection seismic data. However, investigations regarding crustal velocities, types of crust, and their extent are essential to enhance plate tectonic models and the knowledge of the genesis of the Baffin Bay.

In 2010, a research expedition was conducted in the Greenlandic part of the Baffin Bay (Damm, 2010). In this study we will present the crustal structure derived by *P* wave velocity modeling of refraction seismic data and gravity modeling of shipborne gravity data along one profile, which extends from the Baffin Bay Basin into the southern Melville Bay. The aim of the profile was to examine the crustal velocity structure, thickness, and extent of crustal units in southern Melville Bay. Moreover, the sedimentary infill within the basins in this area is examined. This information improves our knowledge about the region and provides new insights in the deep crust of the southern Melville Bay.

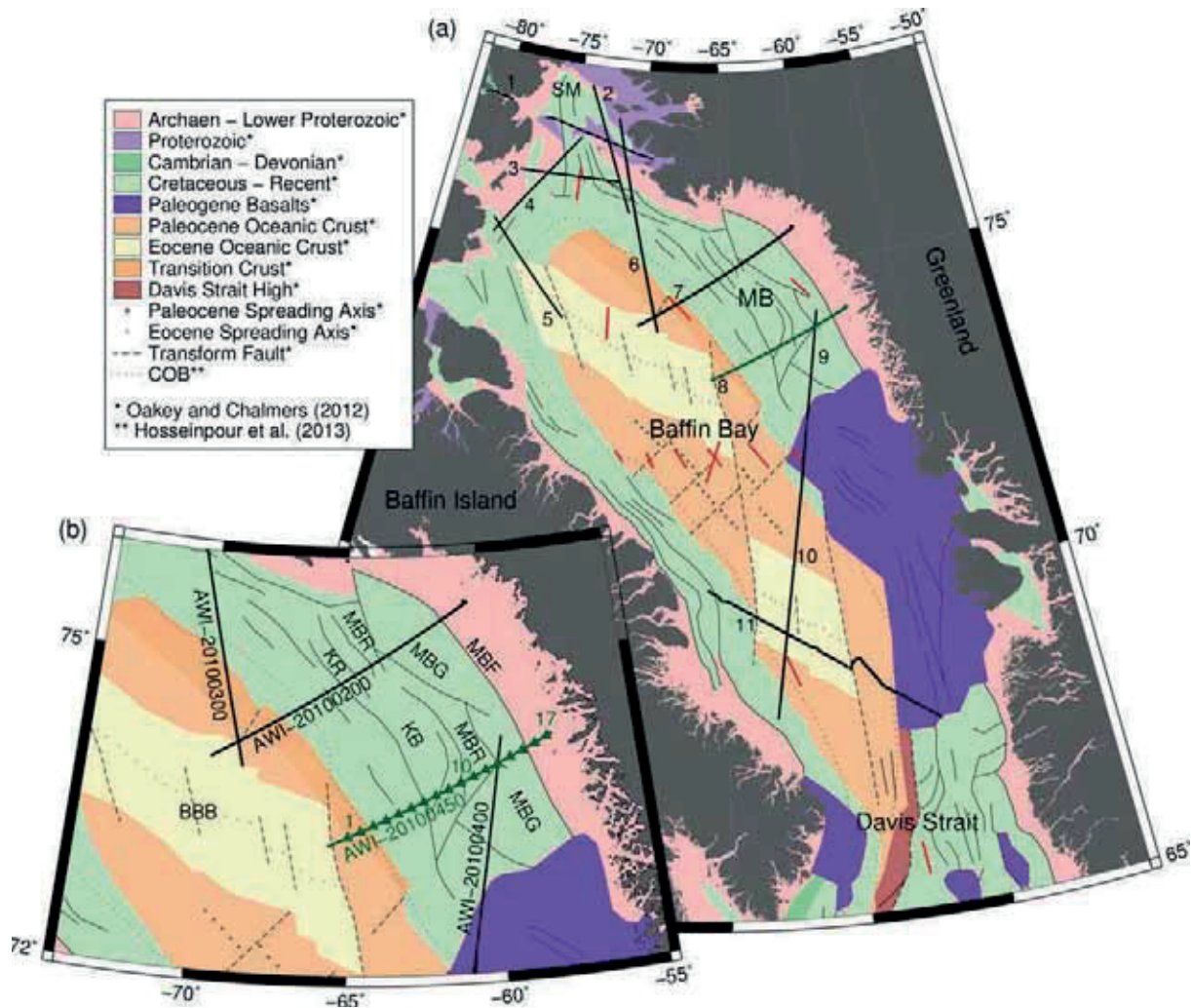


Figure 6.1: Geological map of the Baffin Bay, changed after Oakey and Chalmers (2012).

(a) Green line marks the position of profile AWI-20100450 (this study). Black lines mark the position of other modern refraction seismic profiles in the Baffin Bay. 1: line 3 (Funck et al., 2006); 2: profile 91/3 (Jackson and Reid, 1994); 3: profile 91/2 (Reid and Jackson, 1997); 4: profile 91/1 (Jackson and Reid, 1994); 5: profile 91/4 (Reid and Jackson, 1997); 6: profile AWI-20100300 (Altenbernd et al. submitted); 7: profile AWI-20100200, (Altenbernd et al., 2014); 8: profile AWI-20100450 (this study), 9: profile AWI-20100400 (Suckro et al., 2012), 10: profile AWI-20080500 (Suckro et al., 2012); 11: profile AWI-20080600 (Funck et al., 2012). Red lines mark sonobouy recordings from Keen and Barrett (1972).

(b) Close-up of the Melville Bay region. Green triangles mark the locations, green numbers the names of 17 OBS deployed along AWI-20100450. Abbreviations: KR: Kivioq Ridge, KB: Kivioq Basin, MBR: Melville Bay Ridge, MBG: Melville Bay Graben, MBF: Melville Bay Fault, BBB: Baffin Bay Basin, SM: Smith Sound, MB: Melville Bay

6.3 Geological setting of Baffin Bay and Melville Bay

The Melville Bay is part of the northwestern Baffin Bay, an oceanic basin evolved during the separation of Greenland and North America. The age of the oceanic crust and also the timing of spreading are controversial since spreading anomalies have only been discovered in the central part of the Baffin Bay (Oakey and Chalmers, 2012). In the past, the absence of clear spreading anomalies caused a discussion whether or not the Baffin Bay Basin is underlain by oceanic crust. Early refraction seismic experiments with sonobuoys revealed a ~4 km thin, two-layered oceanic crust present in the central (Keen and Barrett, 1972). Refraction seismic profiles in the very northern Baffin Bay

showed that the thin crust there probably consists of partially serpentinized upper mantle (Reid and Jackson, 1997). Modern refraction seismic datasets have revealed that the southern Baffin Bay is underlain by 6 to 9 km thick oceanic crust (Suckro et al., 2012, Funck et al., 2012). In the northwestern Baffin Bay, the crust is composed of normal to abnormally thin oceanic crust (3.5–6 km) (Altenbernd et al., 2014, Altenbernd et al., submitted). Altenbernd et al. (2014) propose that slow spreading rates might be the reason for the accretion of unusually thin oceanic crust in the Baffin Bay.

A distinct gravity low in the center of the Baffin Bay is nearly aligned in the same direction as the spreading center in the Labrador Sea and probably represents the Eocene spreading ridge (Whittaker et al., 1997). The assumed spreading center in the Baffin Bay is linked by the Ungava Fault Zone in the Davis Strait to the spreading center in the Labrador Sea (e.g., Klose et al., 1982; Chalmers and Pulvertaft, 2001). Therefore, spreading has likely begun contemporaneously in both adjacent basins. The onset of seafloor spreading in the Labrador Sea is constrained by magnetic lineations and started during the Paleocene at 60.9–61.3 Ma (Chalmers and Laursen, 1995). Geodynamic models propose that the onset of spreading coincides with the arrival of the Iceland mantle plume underneath the Greenlandic lithosphere during that time (Storey et al., 1998). The Paleocene spreading was accompanied by massive volcanism, which affected areas on- and offshore West Greenland, leaving thick basaltic successions (Storey et al., 1998) (Figure 6.1). A change in spreading direction occurred at ~55 Ma during the Eocene, caused by the onset of seafloor spreading in the North Atlantic Ocean (Srivastava, 1978; Oakey, 2005). This change in plate kinematic was accompanied by a second phase of volcanism (Storey et al., 1998). During Late Eocene or Early Oligocene, spreading ceased in the Labrador Sea and Baffin Bay (Srivastava, 1978; Oakey and Chalmers, 2012).

The lack of clear magnetic lineations in the northern and southern Baffin Bay and sparse coverage of refraction seismic measurements lead to an insufficient knowledge about the extent of crustal types in the Baffin Bay. Therefore, estimations are based on plate kinematic reconstructions, which are calculated referring to reflection seismic datasets, gravity data and a few refraction seismic datasets (Oakey and Chalmers, 2012; Suckro et al., 2012; Hosseinpour et al., 2013).

In the Melville Bay episodic rifting and sedimentation took place in several stages leaving major structural highs, deep basins and a complex fault system (Figure 6.1b). The rifting probably started in the Early-Mid Cretaceous (Whittaker et al., 1997). Since no well data is available, the exact timing remains unclear.

Ross and Henderson (1973) proposed that a negative, coast-parallel gravity anomaly present in Melville Bay is caused by a deep, sediment-filled graben (Figure 6.2). This so called Melville Bay Graben extends in a NW-SE direction and is assumed to contain up to 13 km of sediments (Whittaker et al., 1997). The Melville Bay Ridge, a pronounced basement high consisting of tilted blocks, separates the Melville Bay Graben from the parallel extending, but shallower Kivioq Basin (Figure 6.1). The Kivioq Basin widens toward the south and contains an up to 10 km thick infill (Gregersen et al., 2013). Its northwestern part is bordered by the Kivioq Ridge, which constitutes another structural high in the area. The infill of the basins is probably composed of sedimentary rocks

and may include intrusions and volcanic rocks (Gregersen et al., 2013). A pronounced positive gravity anomaly at the southern end of the Kivioq Ridge has been interpreted as a mafic intrusion (Whittaker et al., 1997) or an uncompensated sedimentary package (Oakey and Chalmers, 2012).

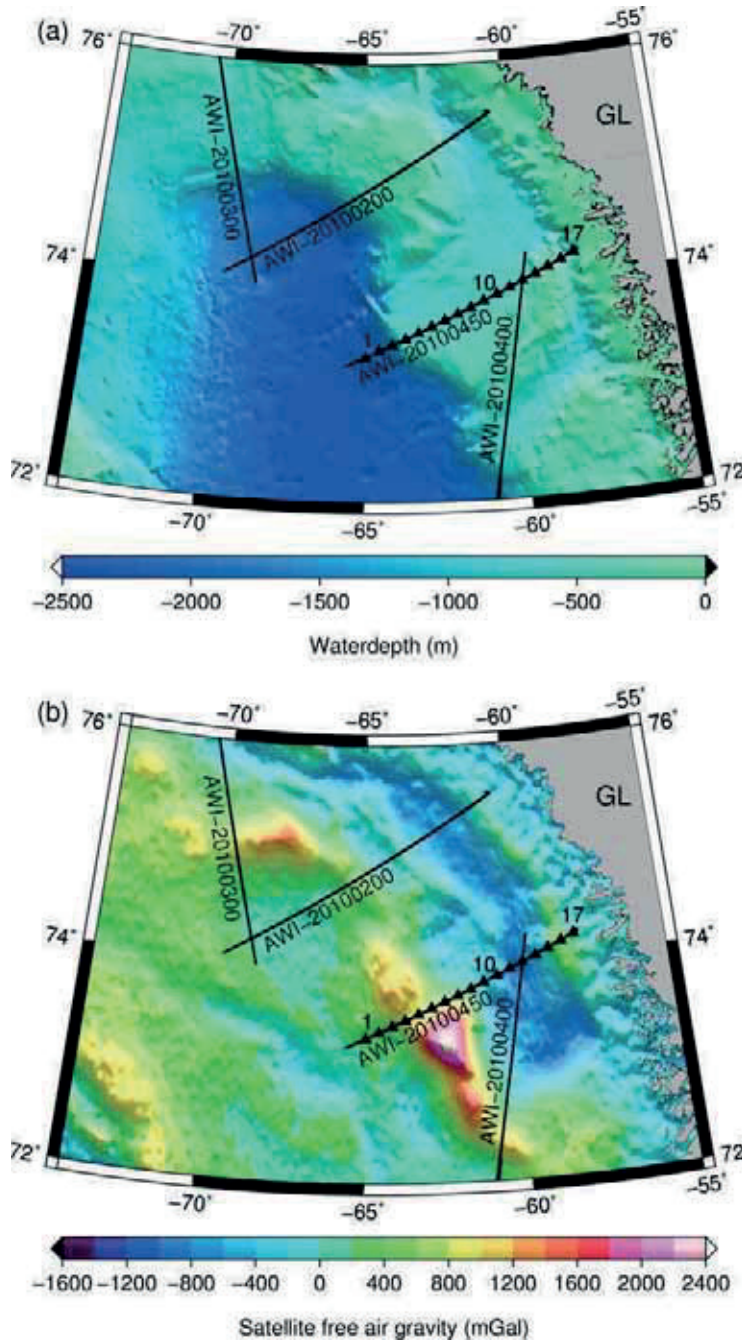


Figure 6.2: Bathymetry and free-air gravity anomalies in the Melville Bay area.
 (a) Bathymetric map (GEBCO grid of 2014, version 2.0) of the Melville Bay, illuminated from the NE. Black lines mark the position of seismic refraction profiles. Black triangles mark the position of the OBS (labeled with black numbers) along AWI-20100450.
 (b) Free-air gravity anomaly map (grid from Sandwell et al. 2014, version 23.1) of the same region as shown above, illuminated from NE and N. Abbreviation GL: Greenland.

Signs of compression and tectonic activity, like inversion structures, have been identified within the northern Melville Bay Graben and in some parts of the

Kivioq Basin (Gregersen et al., 2013; Whittaker et al., 1997), which coincide with the Eureka Orogeny in the Canadian Arctic Island (Whittaker et al., 1997). Recently, three modern deep sounding profiles examined the thickness and extent of crustal types in the Melville Bay: Refraction seismic profile AWI-20080500 covers the oceanic part of central and southern Baffin Bay, its northern prolongation AWI-20100400 terminates in the southern Melville Bay (Suckro et al., 2012). The other profile AWI-20100200 crosses the deep Baffin Bay Basin and northern Melville Bay in a SW-NE direction (Altenbernd et al., 2014). The profiles revealed transitional crust separating stretched continental crust from oceanic crust and provided first evidence of the extent and composition of crustal types in the central and northwest Baffin Bay.

The oceanic crust is abnormally thin (>3.5 km) along AWI-20100200 and normal (around 7.5 km) along AWI-20080500. Seaward dipping reflectors (SDR) cover the transitional crust of the volcanic margin in the southern Baffin Bay along AWI-20100400 and AWI-20080500 (Suckro et al., 2012). No SDR have been discovered in the transition zone along AWI-20100200, where a cone-shaped magmatic structure is the dominating feature of the COT.

Profile AWI-20100200 extends across the main crustal highs and basins in northern Melville Bay, where stretched and 14 to 25 km thick, two-layered continental crust is present (Altenbernd et al., 2014). In this area, the Melville Bay Graben contains up to 11 km thick sediments and sedimentary rocks with velocities of up to 4.9 km/s, while the infill in the smaller Kivioq Basin is only ~ 6 km thick (Altenbernd et al., 2014). The continental crust underneath the southern Melville Bay Graben is composed of three crustal units with velocities of 5.2 to 6.9 km/s (AWI-20100400, Suckro et al., 2012). The crust is buried by sedimentary rocks with a maximum thickness of ~ 6 km. Underneath, the Moho in this part of the region is located in a depth of up to 30 km (Suckro et al., 2012).

6.4 Data acquisition and processing

The presented data in this study were acquired on board of the Research Vessel "Polarstern" in 2010 during a collaborative effort between AWI (Alfred Wegener Institute Helmholtz Centre for Polar and Marine Research), and BGR (Federal Institute for Geosciences and Natural Resources). The refraction seismic profile AWI-20100450 is located in the southern Melville Bay (Figures 6.1 and 6.2). The 270 km long profile extends from the deep Baffin Bay Basin to the shelf area in a SW-NE direction. Additionally, reflection seismic data (profile BGR10-311, Figure 6.3) and shipborne gravity data were acquired along the same profile.

As seismic source, an airgun array composed of 8 G-Guns with a total volume of 68.2 l was used. The array was towed behind the ship in a depth of 10 m. A shot interval of 60 seconds resulted in a mean shot distance of 150m.

In total, 17 ocean bottom seismometers (OBS) were placed along the profile with a spacing of ~ 15 km. Every OBS was equipped with a hydrophone component and a 60 sec three component broadband seismometer. The data were recorded with a sampling rate of 250 Hz.

After acquisition, the raw data were processed in several steps. The processing of the refraction seismic data included relocation of the OBS stations and calculations of offsets between source and receiver. During deployment,

currents can shift the OBS from the initial position. We used direct arrivals to calculate the deviation in order to shift the OBS position.

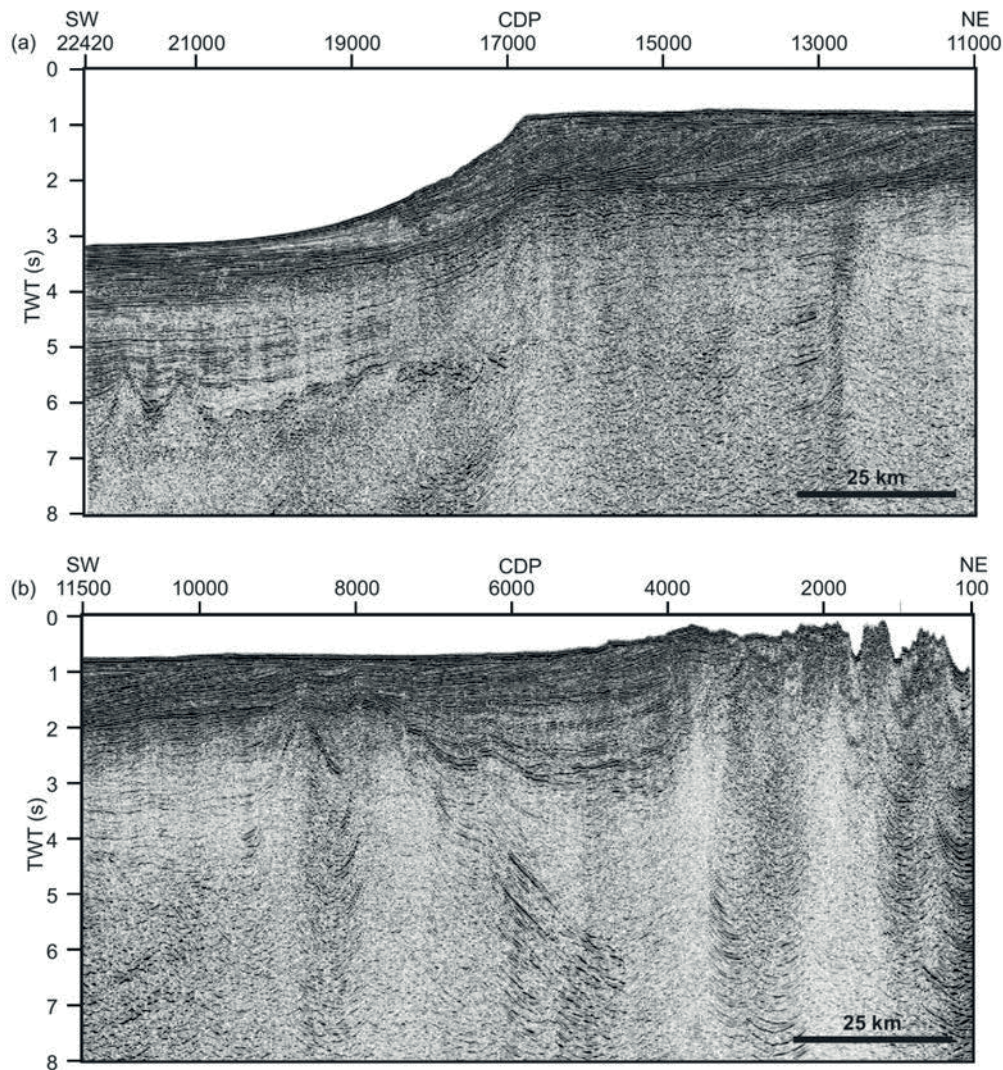


Figure 6.3: Western (a) and eastern (b) part of reflection seismic profile BGR10-311. The reflection seismic profile has been acquired along profile AWI-20100450 and was processed by BGR and Cairn Energy.

We used the software `zp` (written by Barry Zelt, see <http://www.soest.hawaii.edu/~bzelt/zp/zp.html>) for further processing and picking of refracted and reflected signals within the seismograms. Prior to picking, we filtered the data with a bandpass filter of 4.0 to 13.5 Hz and also applied an automatic gain control of 1 s to the data. The assigned pick uncertainties of 55 to 200 ms depend on the signal-to-noise ratio. Examples of picked arrivals within seismic sections of OBS 1, 2, 6, and 10–12 are shown in Figures 6.4 to 6.9.

All 17 OBS recorded data of at least 1 component, but the data quality varies greatly. For example, the data quality recorded at OBS 4 was fairly poor and signals can be observed to offsets of only ~35 km. In contrast, OBS 7, 10, and 11 recorded data with offsets of up to 150 to 160 km (Figures 6.7 and 6.8). Depending on the data-quality, seismograms of the hydrophone (OBS 1–6, 8–17) or also the z-component (OBS 7) were used for picking.

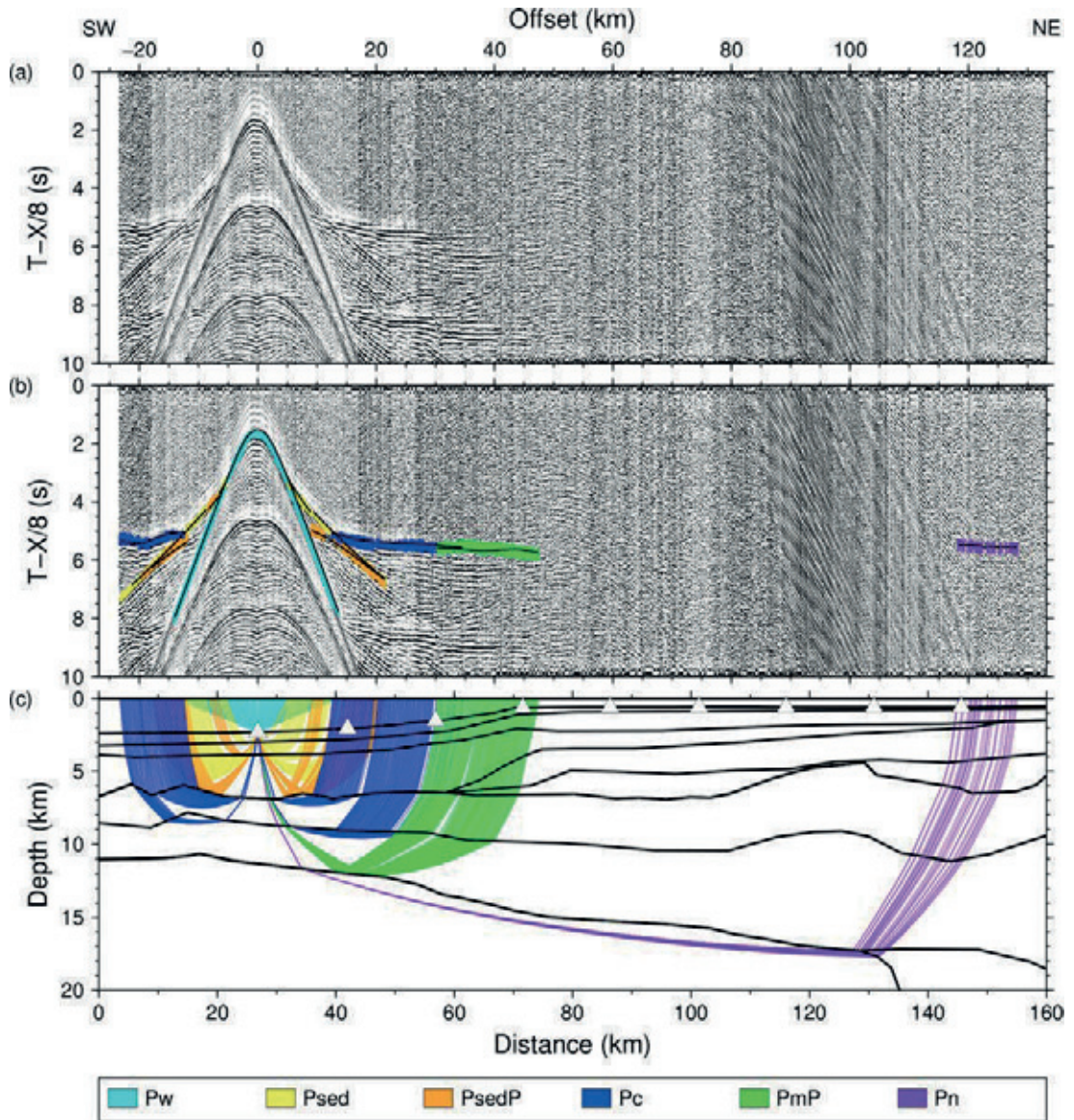


Figure 6.4: Parts of the seismic section, picked signals, and modeled raypaths for OBS 1.
 (a) Seismogram section of the hydrophone component, plotted with a reduction velocity of 8 km/s. A 4–13.5 Hz bandpass filter and an automatic gain control (AGC) with a time window of 1 s is applied.
 (b) Same section of the hydrophone component as seen above, but overlain by picked phases (colored vertical bars). The length of the bars represents the pick uncertainties. Black lines mark the modeled travel times within the P wave velocity model.
 (c) Raypaths of the picked phases within the velocity model. Black lines are the layer boundaries of the velocity layers.

Within the picked phases, we were able to identify refracted (P_{sed}) and reflected (P_{sedP}) phases within the sediments, refracted crustal phases (P_c), reflected crustal phases (P_cP), refracted phases in the upper mantle (P_n), head waves along the Moho (P_mH) and within the crust (P_cH) and reflected phases of the Moho (P_mP).

For the acquisition of seismic reflection data, we used a 3750 m long streamer. The seismic source consisted of 6 G-Guns with a total volume of 51.1 l. The shot interval was 15 s resulting in a shot distance of ~ 37.5 m. Processing of the seismic reflection data was conducted at BGR and later enhanced by Cairn Energy.

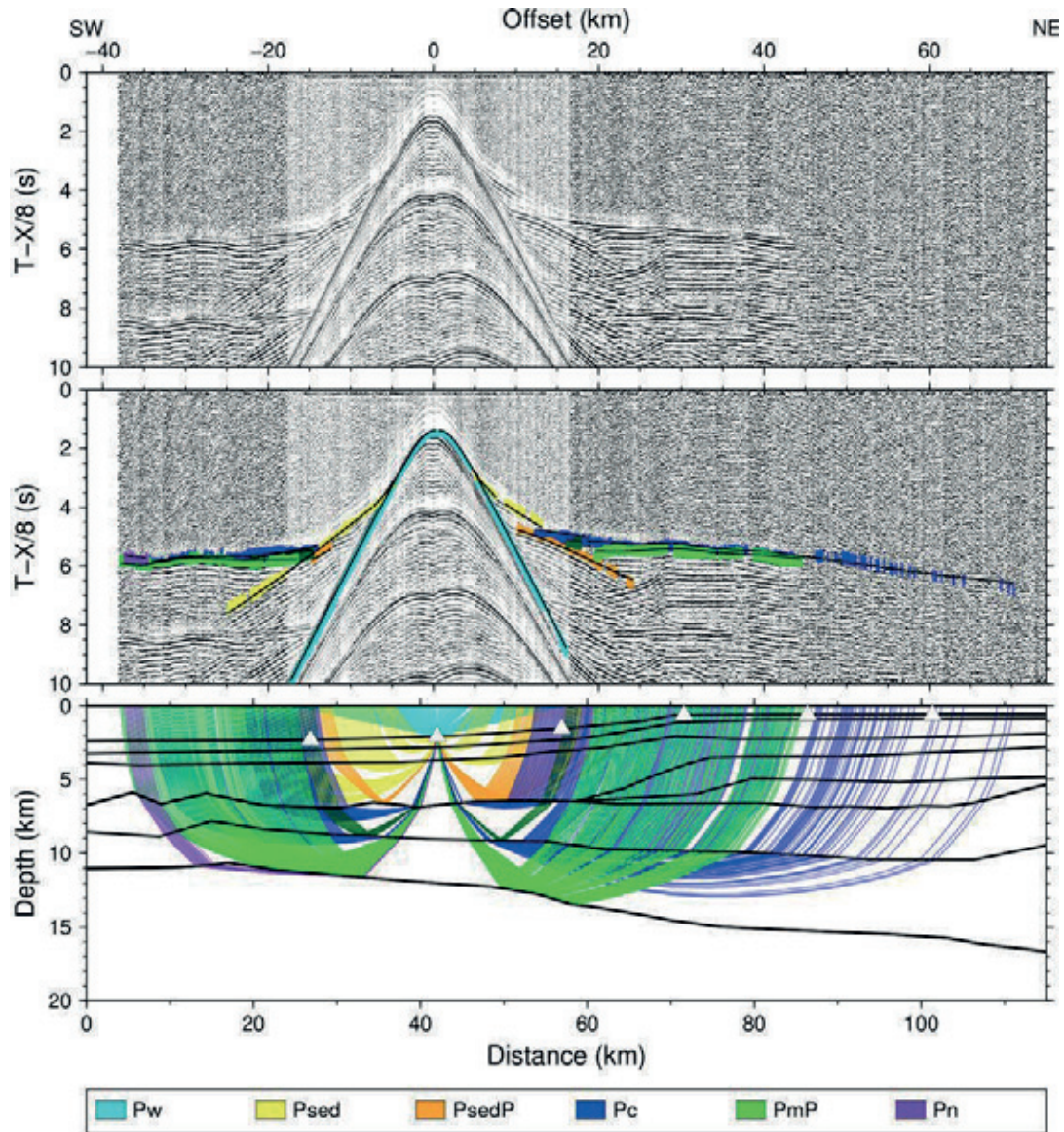


Figure 6.5: Parts of the seismic section, picked signals and modeled raypaths for OBS 2.

(a) Seismogram section of the hydrophone component, plotted with a reduction velocity of 8 km/s. A 4–13.5 Hz bandpass filter and an automatic gain control (AGC) with a time window of 1 s is applied.

(b) Same section of the hydrophone component as seen above, but overlain by picked phases (colored vertical bars). The length of the bars represents the pick uncertainties. Black lines mark the modeled travel times within the *P* wave velocity model.

(c) Raypaths of the picked phases within the velocity model. Black lines are the layer boundaries of the velocity layers.

Gravity data measurements were continuously recorded during the cruise with the sea gravimeter system KSS31 from BGR. Before and after the cruise, on-land gravity measurements in Bremerhaven and Reykjavik were conducted with a LaCoste and Romberg gravity meter. This was done to link the measured gravity data to the International Gravity Standardization Net IGSN 71 and to determine the mean instrumental drift during the cruise. Since the correction of the instrumental drift (8.6 mGal) increased the crosspoint errors between the measured on-board gravity data and satellite altimetry data, it was decided not to correct the instrumental drift. Furthermore, the normal gravity (WGS84) was subtracted from the measured gravity data and an Eötvös correction was applied to obtain the free-air gravity anomalies.

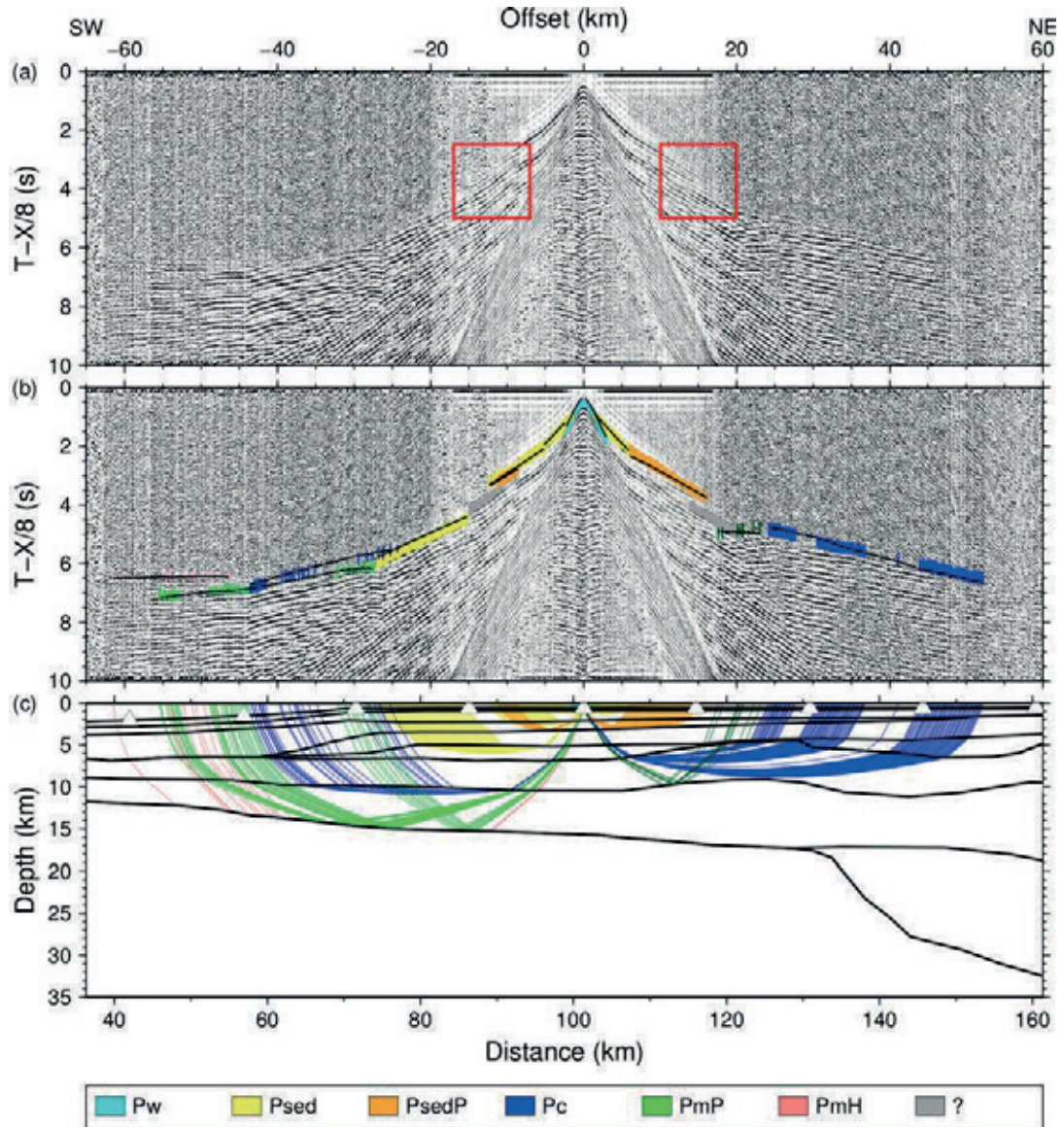


Figure 6.6: Parts of the seismic section, picked signals and modeled raypaths for OBS 6.
 (a) Seismogram section of the hydrophone component, plotted with a reduction velocity of 8 km/s. A 4–13.5 Hz bandpass filter and an automatic gain control (AGC) with a time window of 1 s is applied. The red squares mark areas indicating a low-velocity zone.
 (b) Same section of the hydrophone component as seen above, but overlain by picked phases (colored vertical bars). The length of the bars represents the pick uncertainties. Black lines mark the modeled travel times within the *P* wave velocity model.
 (c) Raypaths of the picked phases within the velocity model. Black lines are the layer boundaries of the velocity layers.

6.5 Modeling

6.5.1 *P* wave velocity model

Unfortunately, the refraction seismic profile was not shot along a great circle. For the model setup, the OBS stations were projected on a straight line between start- and endpoint of the profile, while the source-receiver distances remained unchanged. The *P* wave velocity forward modeling was conducted with the software rayinvr (Zelt and Smith, 1992). On base of the picked refracted signals, the *P* wave velocity of different layers was assigned. The picked reflected signals

were used to locate the layer-boundaries within the model. Additionally, we utilized information gained from the seismic reflection profile BGR10-311 (Figure 6.3) to verify and improve the position of the basement and the shape of geological structures, e.g., the Melville Bay Ridge. Additionally, an inversion algorithm was used to improve the fit and quality of the model.

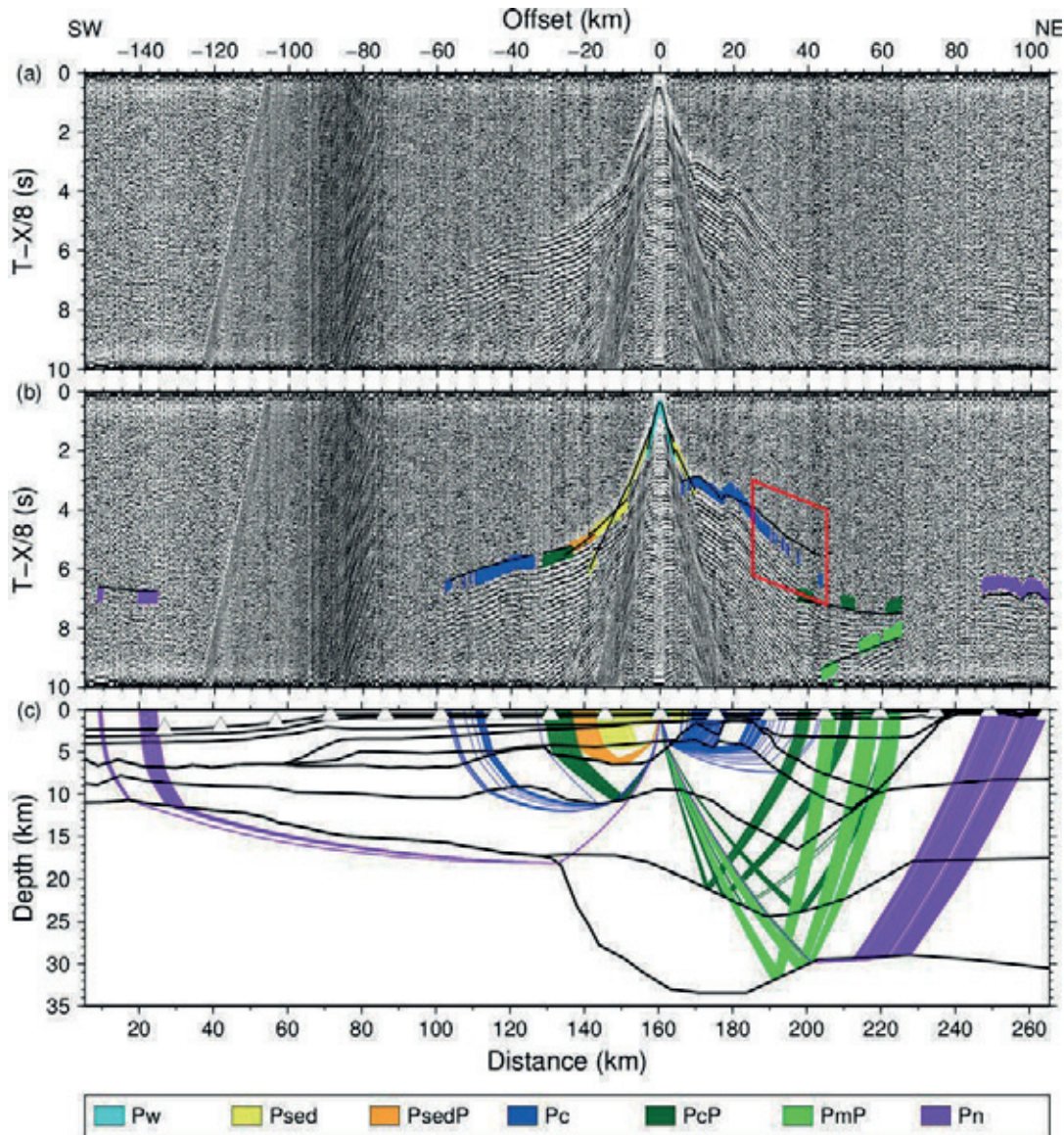


Figure 6.7: Parts of the seismic section, picked signals and modeled raypaths for OBS 10.

(a) Seismogram section of the hydrophone component, plotted with a reduction velocity of 8 km/s. A 4–13.5 Hz bandpass filter and an automatic gain control (AGC) with a time window of 1 s is applied.

(b) Same section of the hydrophone component as seen above, but overlain by picked phases (colored vertical bars). The length of the bars represents the pick uncertainties. Black lines mark the modeled travel times within the *P* wave velocity model. The red square marks the area, where a misfit between modeled raypaths and picks occurs. See text for further explanation.

(c) Raypaths of the picked phases within the velocity model. Black lines are the layer boundaries of the velocity layers.

6.5.1.1 Ray coverage, resolution and uncertainty analysis

11280 picks were traced and the resulting *P* wave velocity model is presented in Figure 6.10a. The overall travel time residual for our model is 0.154 ms. The

obtained average χ^2 value of 1.094 is only slightly higher than the ideal value 1. Table 6.1 summarizes the number of picks, χ^2 values, and average rms-misfit for every layer.

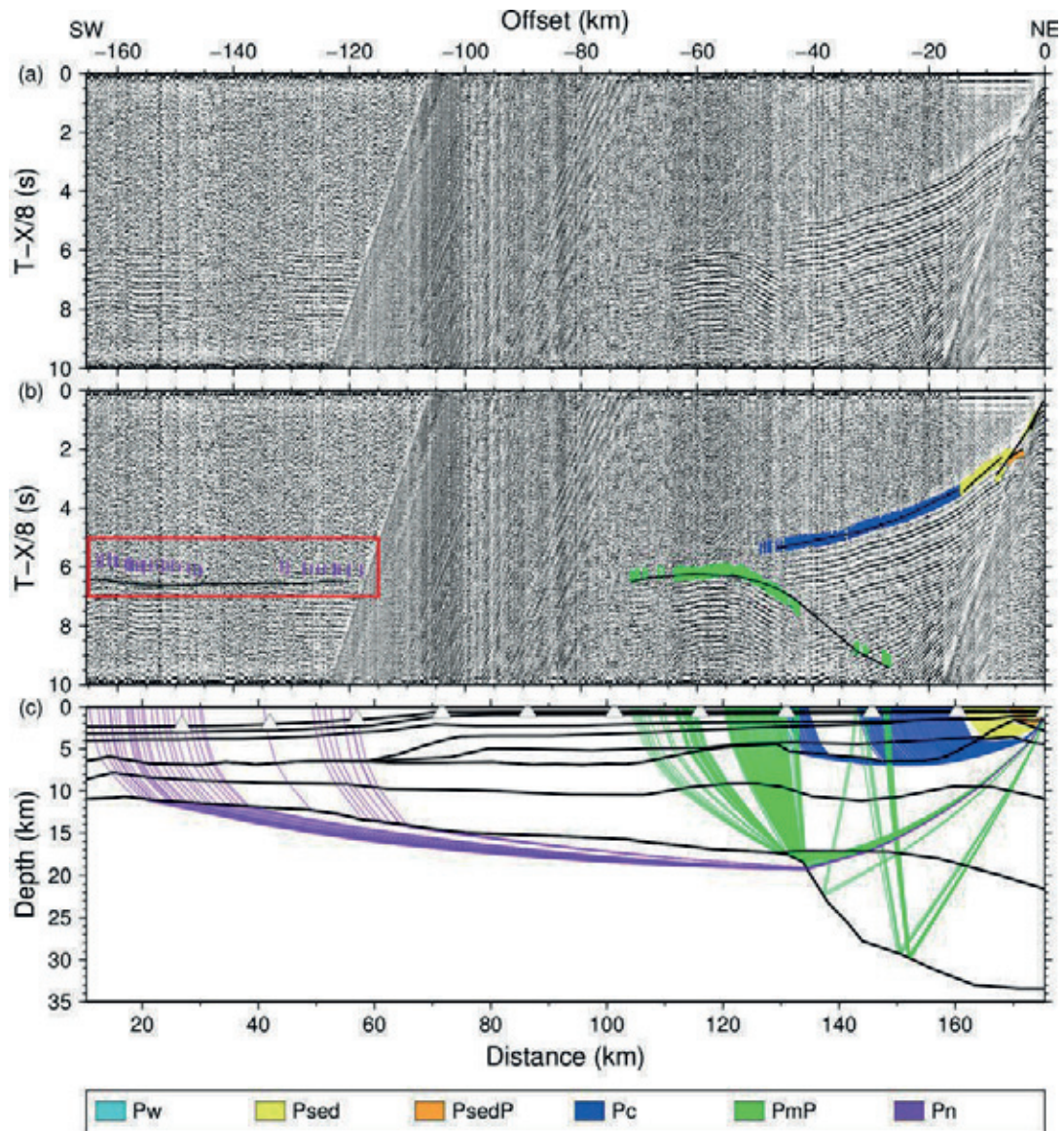


Figure 6.8: Parts of the seismic section, picked signals and modeled raypaths for OBS 11.

(a) Seismogram section of the hydrophone component, plotted with a reduction velocity of 8 km/s. A 4–13.5 Hz bandpass filter and an automatic gain control (AGC) with a time window of 1 s is applied.

(b) Same section of the hydrophone component as seen above, but overlain by picked phases (colored vertical bars). The length of the bars represents the pick uncertainties. Black lines mark the modeled travel times within the P wave velocity model. The red square marks a misfit between picked and modeled raypath of the P_n phase. See text for further information.

(c) Raypaths of the picked phases within the velocity model. Black lines are the layer boundaries of the velocity layers.

The ray coverage of different layers is shown in Figure 6.11. It illustrates how well boundaries and layers of the model are constrained by refractions (orange rays), reflections (blue rays), and head waves (green rays). For example, the depth of the Moho is very well constrained by reflections, while the ray coverage of refracted waves within the lowermost crustal layer underneath the

Melville Bay is only sparse. In areas with low ray coverage, modeling was partly challenging. These areas will be briefly described in the following.

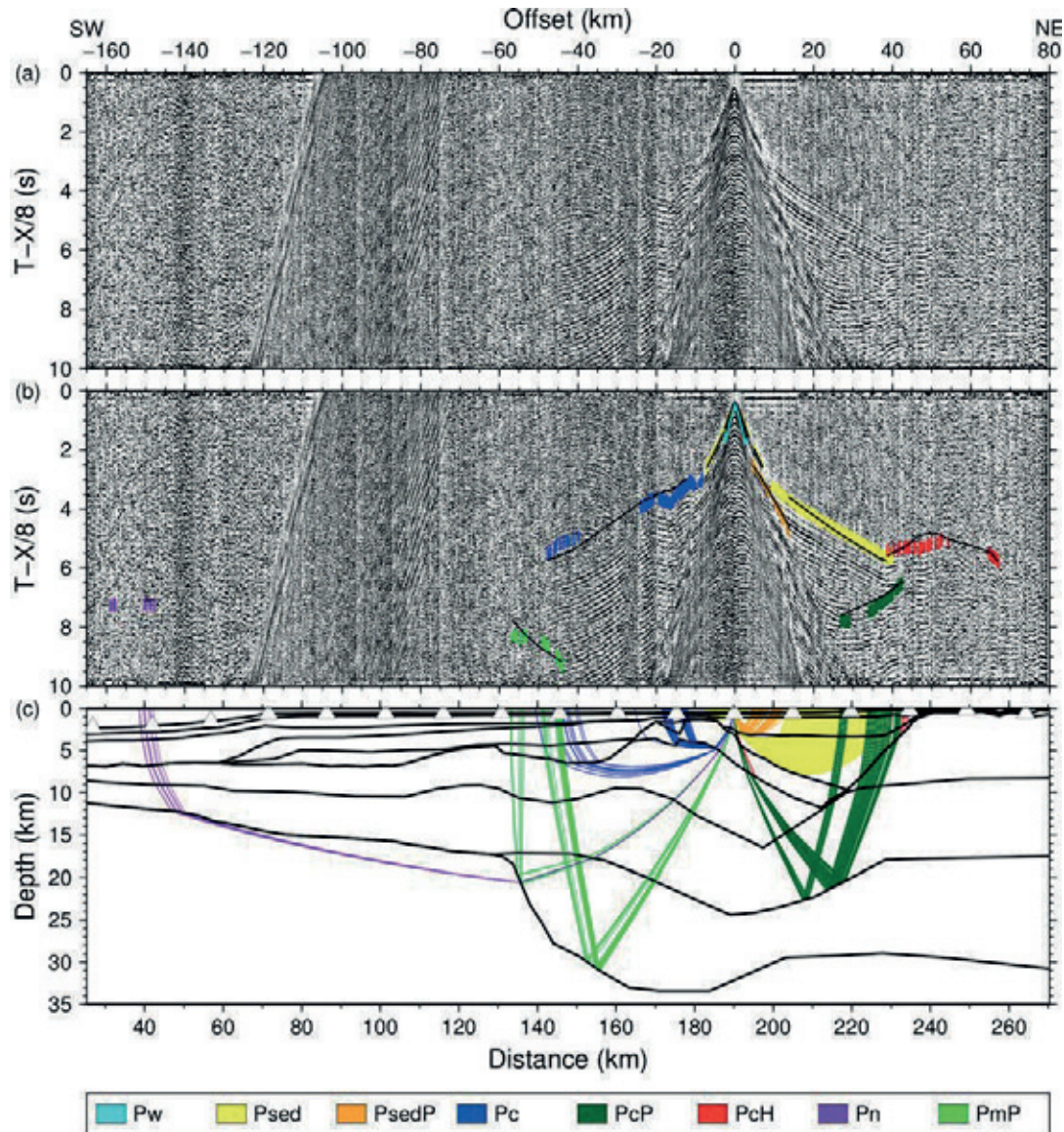


Figure 6.9: Parts of the seismic section, picked signals and modeled raypaths for OBS 12.

(a) Seismogram section of the hydrophone component, plotted with a reduction velocity of 8 km/s. A 4–13.5 Hz bandpass filter and an automatic gain control (AGC) with a time window of 1 s is applied.

(b) Same section of the hydrophone component as seen above, but overlain by picked phases (colored vertical bars). The length of the bars represents the pick uncertainties. Black lines mark the modeled travel times within the *P* wave velocity model.

(c) Raypaths of the picked phases within the velocity model. Black lines are the layer boundaries of the velocity layers.

The presence of the low-velocity zone between km 60 and 140 hampered modeling the underlying layers. Indications for a low-velocity zone can be seen in the OBS 5 to 9, where a delay in travel time arrivals occurs. An example for this is given in Figure 6.6. Additionally, we were not able to model all phases picked within the seismograms of OBS 5 and 6 (Figure 6.6), which are related to the low-velocity zone. Unfortunately, we could not use the seismic reflection data of BGR10-311 to constrain the onset and shape of the sediment layers and

basement underneath the low-velocity zone, because the quality of the seismic reflection data in this part of the model is also poor.

Table 6.1: Number of picks (n), RMS misfit, and χ^2 for different velocity layers.

Velocity layer	Phases	n	RMS (s)	χ^2
1, rfl	waterwave	968	0.118	0.936
2, rfr	P_{sed1}	77	0.065	0.512
2, rfl	$P_{sed1}P$	10	0.092	0.764
3, rfr	P_{sed2}	498	0.071	0.571
3, rfl	$P_{sed2}P$	140	0.065	0.278
4, rfr	P_{sed3}	740	0.093	0.689
4, rfl	$P_{sed3}P$	521	0.071	0.284
5, rfr	P_{sed4}	386	0.074	0.594
5, rfl	$P_{sed4}P$	247	0.170	2.681
6, rfr	P_{sed5}	890	0.144	1.049
6, rfl	$P_{sed5}P$	358	0.081	0.352
7, rfr	P_{c1}, P_{sed6}	111	0.106	0.449
7, hw	P_cH	54	0.260	3.311
8, rfr	P_{c2}	2125	0.142	0.901
8, rfl	$P_{c2}P$	577	0.207	1.859
9, rfr	P_{c3}	907	0.156	0.856
9, rfl	$P_{c3}P, P_mP$	1324	0.187	1.169
10, rfr	P_{c4}	235	0.136	0.584
10, rfl	$P_{c4}P, P_mP$	683	0.221	2.249
10, hw	P_mH	22	0.090	0.321
11, rfr	P_n	407	0.284	3.099
All layers	All phases	11280	0.154	1.094

Between km 100 and 140, we used higher velocities than in the adjacent regions to model the lowermost crustal layer (layer 9, Figure 6.10), although the ray coverage with refracted rays is sparse (layer 9, Figure 6.11). This was done because the moveout and shape of P_mP -phases indicate an increase in velocity underneath the basement high. The velocity, layer thickness, and base of the overlying crustal layer (layer 8, Figure 6.10) are very well constrained by refractions and reflections, they cannot solely account for the curvy structure of the P_mP -phases. Therefore the lowermost crust between km 100 and 140 was modeled with increased velocities of 6.1 to 6.7 km/s.

Another problem occurred during modeling a P_n phase clearly visible in the seismogram of OBS 11 (Figure 6.8). In order to reduce the misfit between picked and modeled phase, we even increased the upper mantle velocity to an unrealistic high velocity of 10 km/s, which did not significantly improved the fit. Also, changes in the geometry of the crustal layers beneath the Melville Bay High decreased the fit in all other seismograms. Therefore we decided to ignore the misfit of the P_n phase. Since OBS 11 was placed above the Melville Bay Ridge directly above a small half graben (Figures 6.8 and 6.10), we assume that its complex geometry might be the reason for the observed misfit.

Furthermore, another challenging area for modeling was the upper continental crust underneath the Melville Bay Graben. The picked crustal phases east of the Melville Bay Ridge (east of km 190) in the seismic sections of OBS 10 and 11 did not fit with modeled phases (Figure 6.7). Adjustments in velocity did not increase the fit significantly. Because shape and geometry of the eastern flank of the ridge can be confirmed by the seismic reflection data (Figure 6.3, CDP 4000–6000, TWT 4–7), we prolonged velocity layer 7 into the Melville Bay Graben.

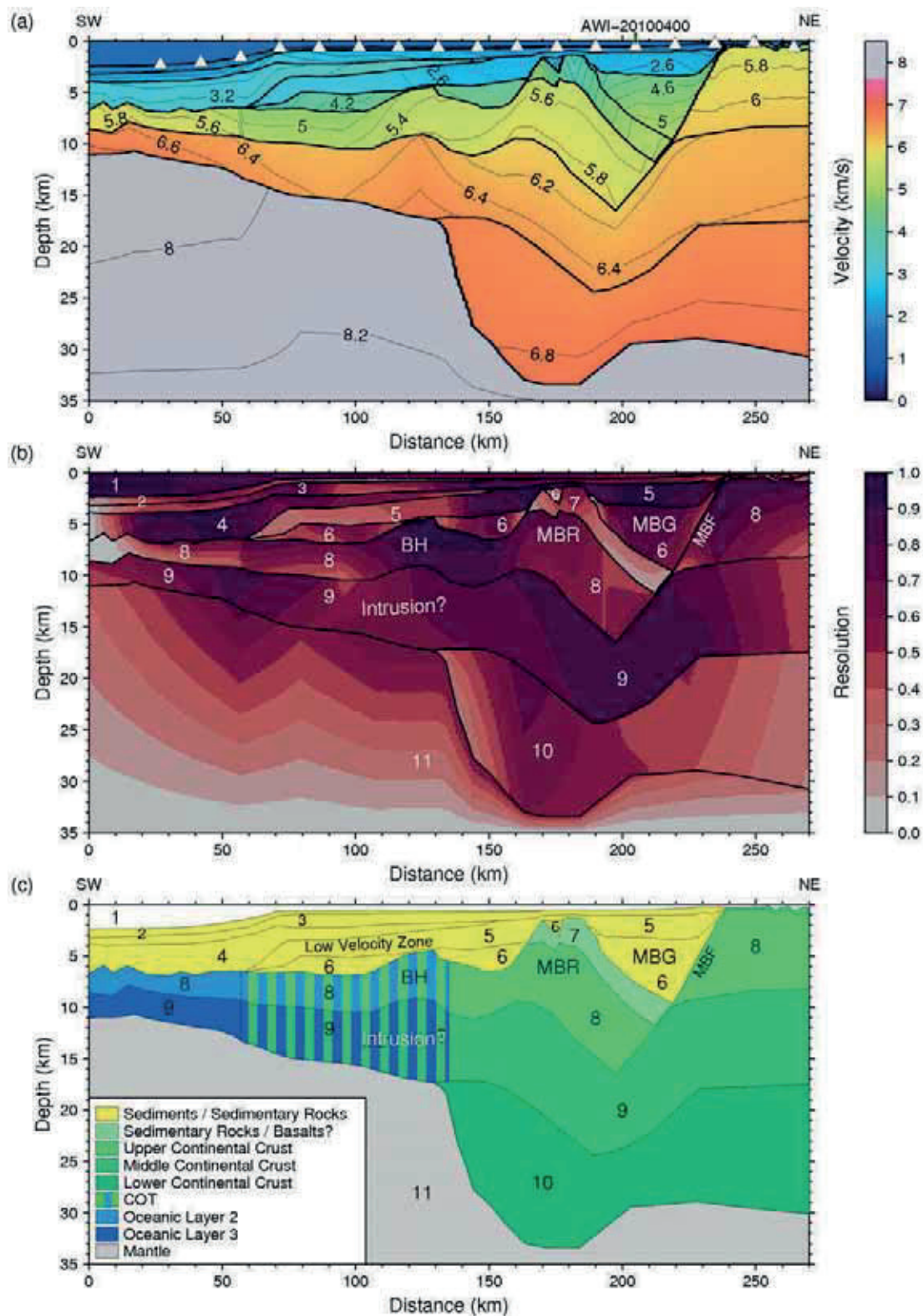


Figure 6.10: *P* wave velocity model, resolution matrix and geological interpretation of AWI-20100450.

(a) *P* wave velocity model of AWI-20100450, derived by forward modeling. White triangles mark the positions of OBS-stations along the profile. The velocity is given in km/s.

(b) Diagonal values of the resolution matrix of *P* wave velocity model AWI-20100450. White numbers represent the number of the velocity layers.

(c) Geological interpretation of the profile. Black numbers represent the number of the velocity layers.

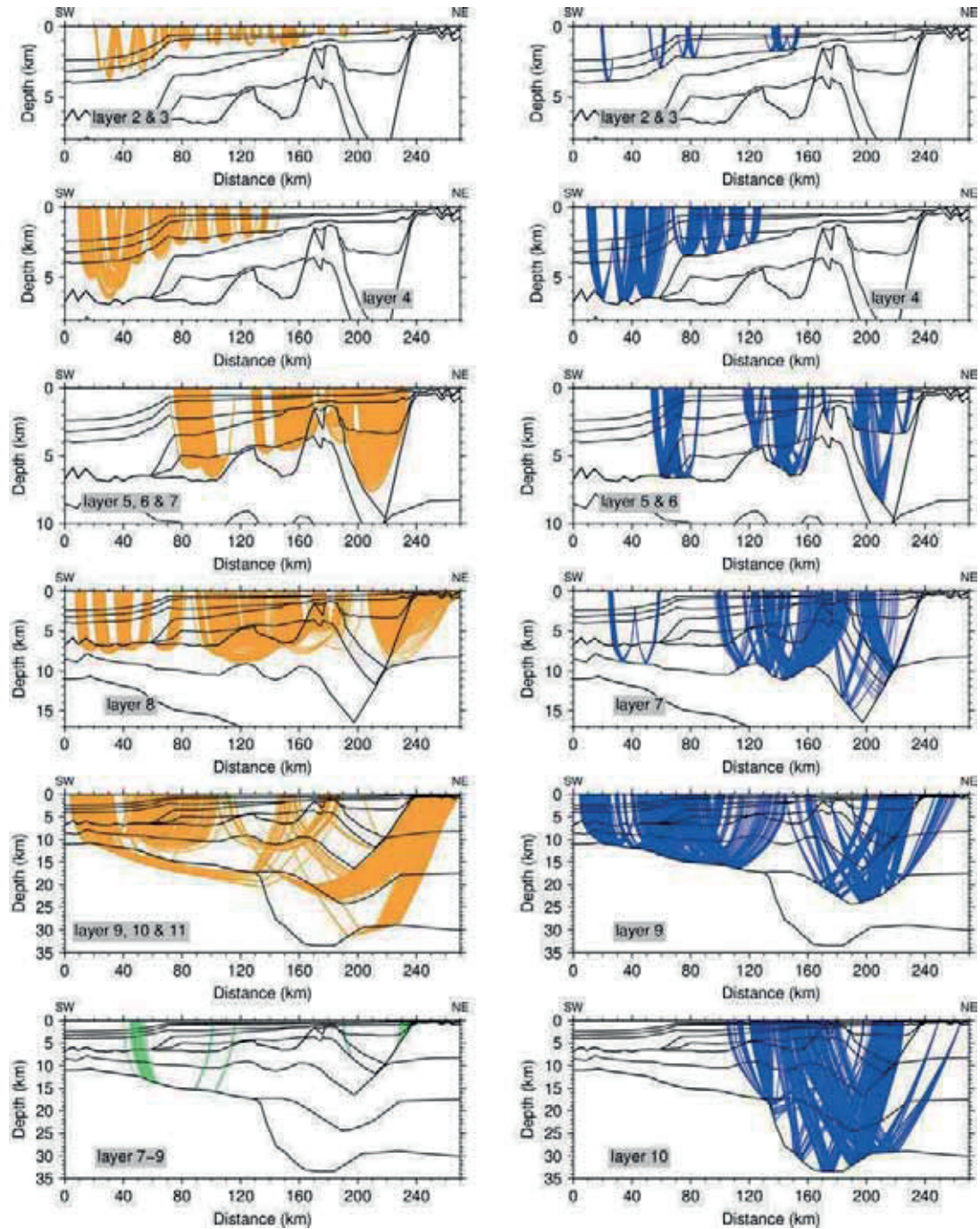


Figure 6.11: Ray coverage of the P wave velocity model. The black lines mark the layer boundaries between the velocity layers of the P wave velocity model. The ray coverage of refracted waves (orange lines), reflected waves (blue lines) and head waves (green lines) is shown for different velocity layers of the model.

Since we do not have any indications for the velocity within this part of layer 7 or the occurrence of a low-velocity zone in this region, we used velocities ranging in between the velocities of the over- and underlying layers. By this, we were able to improve the fit. In the following, we will call this part of layer 7 east of the Melville Bay Ridge “hidden layer”.

The resolution plot (Figure 6.10b) illustrates how well the velocity nodes are constrained. For this, the resolution matrix values were plotted. Areas with resolution matrix values >0.5 are well resolved (Lutter and Nowack, 1990). Areas with a low resolution are present at the eastern and western termination

of the model and in areas with low ray coverage, for example the “hidden layer” in the Melville Bay Graben or layer 5 between km 60 and 140, where the low-velocity zone is located.

In order to test the reliability of our *P* wave velocity model, we used the method of Schlindwein and Jokat (1999) to estimate depth and velocity uncertainties. With exception of the low-velocity layer, the velocities used for modeling the sedimentary layers are accurate within ± 0.1 km/s. The velocity uncertainties for the crustal phases range between ± 0.1 km/s for upper crustal phases and increase with depth to ± 0.15 km/s for the lowermost continental crust. Due to missing information, the velocity uncertainty within the “hidden layer” and the low-velocity layer can be greater than ± 0.2 km/s. Depth uncertainties increase with depth ranging from ± 0.2 km for the base of sedimentary layers to up to 2 km for the depth of the Moho underneath the Melville Bay Graben.

6.5.2 Density model

Based on the gravity data acquired along AWI-20100450 and the results of the *P* wave velocity model, a 2D density model was created (Figure 6.12). To set up the geometry of the starting model, we transferred the layer boundaries obtained by the velocity model into the density model. The average *P* wave velocities of each layer were converted into densities using the values after Barton (1986). Layers with great lateral velocity changes, for example the crustal layers, were divided into blocks with different densities. The resulting starting model and the observed and calculated gravity data are shown in Figure 6.12a.

Altogether, a reasonable fit was obtained. But in certain areas, it was necessary to enhance the fit between observed and calculated gravity data: in the Melville Bay Graben, the measured gravity low does not coincide with the deepest region of the Graben, which resulted in a maximum misfit of 21 mGal. Other misfits are observed at the western (<13 mGal) and eastern (<19 mGal) borders of the model, and west of the Melville Bay Ridge (<11 mGal) (Figure 6.12a).

To enhance the fit, some adjustments were conducted. In Figure 6.12b, all changed density blocks of the modified density model are colored grey. The density values of density blocks within the Melville Bay Graben and at the western end of the model were adjusted. Additionally, the eastern boundary of three density blocks were partly changed (km 120–160, crustal units) and one density block in the Melville Bay Graben was divided into two (Figure 6.12b). The geometry of the remaining boundaries remained unchanged. By this, the fit between observed and calculated gravity data is enhanced and the misfits are reduced to <6 mGal at the western end of the model, <13 mGal at the eastern end of the model and <8 mGal west of the Melville Bay Ridge. Also, the misfit in the Melville Bay Graben is reduced to 13 mGal, but the position of the measured gravity low is still located ~ 10 km westward of the calculated gravity data.

6.6 Results and interpretation

We divided the velocity model into three parts: the western part (km 0–57) consists of thin oceanic crust, whereas the eastern part (km 135–170) is composed of stretched and faulted, up to 32 km thick continental crust. In transitional crust connects the oceanic and continental crust (km 57–135). All three crustal units will be briefly characterized in the following.

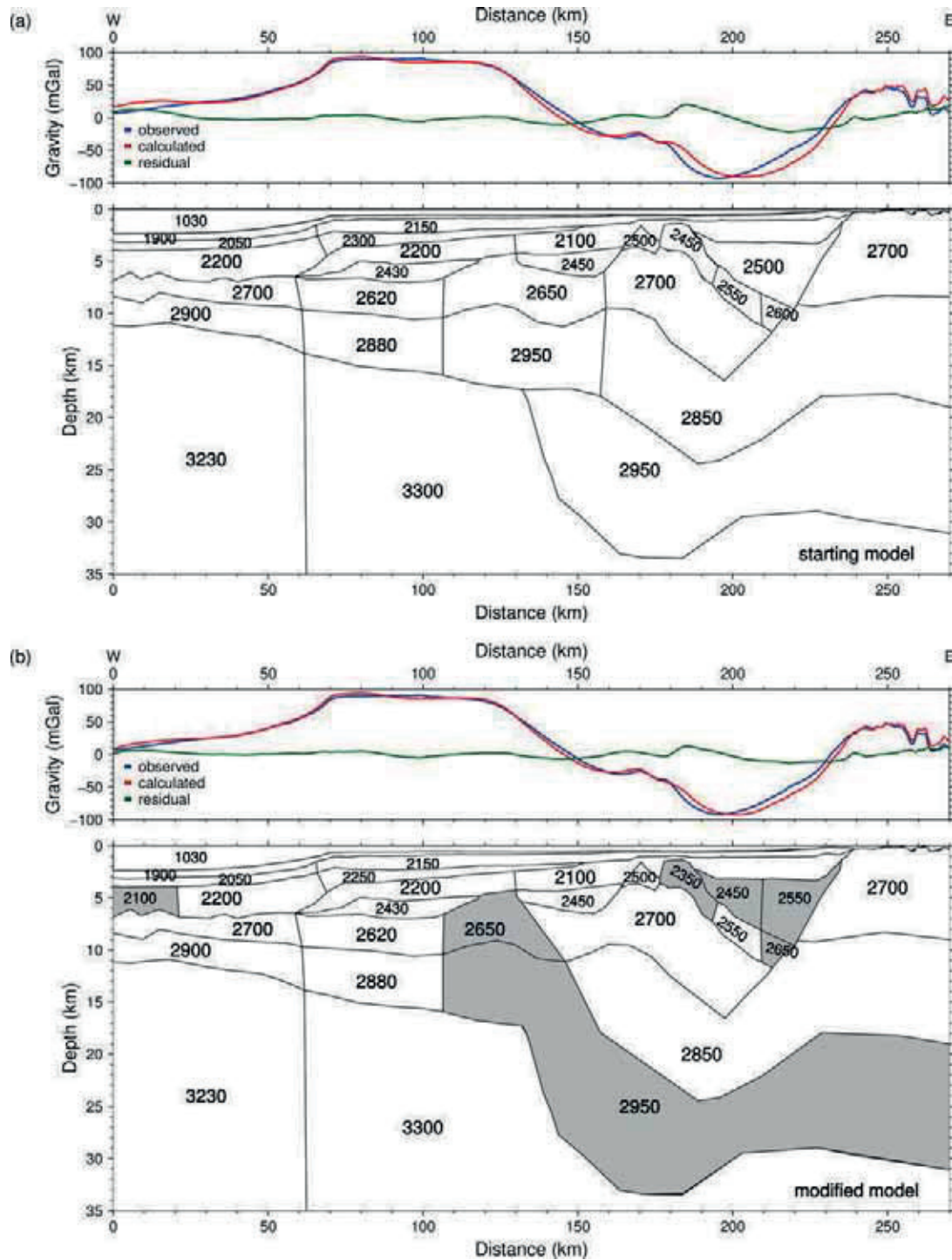


Figure 6.12: Density model of AWI-20100450.

(a) Starting model for 2D gravity modeling. The upper panel shows the observed and calculated free-air anomalies and the resulting residuals. The shown density units in the lower panel were calculated on basis of the density-velocity relationship after Barton (1986) and are given in kg/m^3 .

(b) Modified model for 2D gravity modeling. The upper panel shows the observed and calculated free-air anomalies and the resulting residuals. The lower panel shows the modified density model. Units with changed densities and/or boundaries are colored grey.

6.6.1 Oceanic crust (km 0–57)

In the western part of the profile up to 5 km thick sediments cover the igneous crust. We modeled three sedimentary layers with velocities of 1.7 to 2.1 km/s,

2.2 to 2.7 km/s, and 2.9 to 3.3 km/s (Figure 6.10a). The top of the underlying, partly hummocky igneous basement is constrained by reflections in both the reflection and refraction seismic data (Figures 6.3–6.5, Figure 6.11). Underneath the thin crust, the upper mantle has velocities of >7.8 km/s, which is well constrained by refractions (Figure 6.11). The depth of the Moho ranges between 11.5 and 13.5 km.

The 4.3 to 7 km thick igneous crust is divided into two layers: The upper layer ranges in thickness between 1.8 and 2.8 km, and has velocities of 5.2 to 6.0 km/s, while the slightly thicker lowermost crust has a thickness of 2 to 4 km and velocities of 6.3 to 6.9 km/s. We interpret this as oceanic crust. Oceanic crust is typically composed of two layers: the oceanic layer 2 is composed of pillow basalts and sheeted dikes while the underlying oceanic layer 3 consists of gabbros. After White et al. (1992), normal oceanic layer 2 has velocities of 2.5 to 6.6 km/s and a thickness of ~ 2.1 km, while oceanic layer 3 has a thickness of ~ 5 km thick, a low velocity gradient and velocities ranging from 6.6 to 7.6 km/s.

The velocities of both crustal layers increase toward the west, but it has to be kept in mind that the ray coverage and the resolution at the western end of the model is sparse (Figure 6.10b and Figure 6.11). The depth of the Moho ranges between 11.5 and 13.5 km.

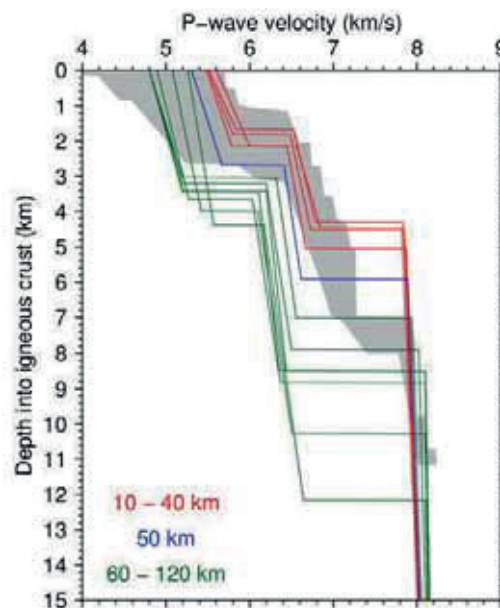


Figure 6.13: Comparison of velocity-depth functions from AWI-20100450 with typical Atlantic oceanic crust. The grey area outlines velocity-depth-functions typical for normal, 59 to 127 Myrs old Atlantic oceanic crust (White et al., 1992). The colored lines are velocity-depth profiles. The velocity-depth profiles were taken every 10 km between km 10 and 120 of profile AWI-20100450.

We compared velocity-depth profiles taken every 10 km between km 10 and 120 to normal Atlantic oceanic crust with an age of 59 to 127 Myrs (White et al., 1992) (Figure 6.13). Between km 0 and 50, the 4.3 to 7 km thick igneous crust is partly much thinner than normal oceanic crust (~ 7.1 km thickness, White et al., 1992), and its lowermost layer has lower velocities (6.4 to 6.9 km/s) than typical for oceanic layer 3. But with exception of the low crustal thickness, the crust between km 0 and 40 fits into the area typical for oceanic crust (Figure

6.13). At km 50, the velocity-depth profile is outside this area because of rather low velocities in the lowermost crustal layer. Nevertheless, due to a clear decrease in velocity in the uppermost crustal layer east of km 57, which indicates a change in crustal composition, we classify the crust between km 0 and 57 as thin, two-layered oceanic crust with a partly slow oceanic layer 3.

6.6.2 COT (km 57–135)

The COT extends from km 57 across the shelf edge to a sudden increase in crustal thickness at km 135. Especially in its eastern part, the termination of the transitional crust is not easy to determine and might be located further east, since the velocity changes are very smooth in this part of the model.

The sedimentary cover above the crust consists of five sedimentary layers with velocities between 1.6 and 4.4 km/s and up to 6.2 km thickness (Figure 6.10). The ray coverage and resolution of the uppermost sedimentary layer is sparse (Figure 6.10b and Figure 6.11), its thickness and velocities (1.6–2.5 km/s) increase seaward. The velocities of the second sedimentary layer decrease landward of the shelf edge from 2.8 to 3.0 km/s to 2.0 to 2.2 km/s. Its ray coverage is excellent and its base is constrained by reflections (Figure 6.11). The third, wedge-shaped sedimentary layer starts west of km 153 and has velocities of 3.1 to 3.6 km/s. Underneath, the underlying layer 4 is characterized by velocities of 2.5 to 3.0 km/s, and therefore represents a low-velocity zone, which does not produce refracted phases in this part of the model. However, further to the coast at km 140–170, the velocity of the upper layer decreases and layer 4 does no longer represent a velocity inversion. The velocity is constrained by refracted phases. Between km 60 and 140 we used slightly higher velocities, since the layer depth increases and the increased overburden leads to more compaction and higher velocities. Due to the great impedance contrast, the top of the low-velocity zone is very well constrained by reflections (Figure 6.11), while reflections on its base are sparse. The maximum thickness of the layer is 2.5 km, but its resolution is poor.

Underneath the low-velocity zone, a basement high at km 130 divides the lowermost sedimentary layer. Sediments west of the basement high have been modeled with velocities of 3.9 to 4.3 km/s, while the layer east of the basement high has faster velocities of 4.2 to 4.4 km/s. The onset of the basement, especially between the basement high and the Melville Bay Ridge, is constrained by reflections (Figure 6.11).

The crust in the transition zone underneath the sediments has a crustal thickness of 7 to 13 km. It can be divided into two layers: the upper layer (velocity layer 8) varies in its thickness between 4 and 5 km. The basement high at km 110–160 is the best resolved structure of this layer. The upper crust west of the basement high has a constant velocity of 4.8 to 5.2 km/s. The velocity of this layer increases toward the Melville Bay Ridge, ranging between 5.0 and 5.7 km/s.

The velocity of the underlying, second crustal layer (6.2–7.6 km/s) is only constrained by a few refractions (Figure 6.11), but its base, which represents the Moho between km 56 and 128, is well constrained by reflections and head waves in the mantle.

The upper mantle velocities underneath the transitional crust are slightly faster than underneath the oceanic crust (>7.8 km/s) and have been modeled with a velocity of >8.0 km/s based on refractions and head waves (Figure 6.11).

The velocity-depth profiles of this part of the model are not typical of oceanic crust (Figure 6.13). The change from a two-layered to a three-layered crust and a dramatic increase of crustal thickness is a strong indication for the eastern termination of the COT. Therefore, we classify the two-layered crust between km 57 and 135 to be of “transitional” character.

The origin of the crust along the COT along our profile is difficult to determine. The velocities of the lower crust are similar to the velocities of the middle continental crust; they are only slightly higher in the area of the intrusion and have a lower gradient west of it. The velocities of upper crust within the COT are lower than in the adjacent oceanic and continental units and range between 5.0 and 5.7 km/s in the area of the basement high and 4.8 to 5.2 km/s west of it. Since the velocities of the basement high differ only slightly from the velocities of the adjacent upper continental crust and show a smooth decrease, we favor that the lower crust and the upper crust in the area of the basement high is mainly composed of highly thinned and stretched continental crust. In contrast, the rather low velocities of the upper crust west of the basement high could also be the result of magmatic layers covering crystalline crust. Therefore, we cannot rule out that basalts or magmatic material cover the region west of the basement high.

6.6.3 Continental crust (km 135–270)

The eastern part of our model consists of a three-layered, stretched and faulted continental crust. Sediments cover the faulted Melville Bay Ridge and are deposited in the more than 9 km deep Melville Bay Graben. East of km 240 the basement is exposed at the seafloor.

The uppermost sedimentary layer with velocities of 1.8 to 2.2 km/s is constrained by only some refractions (Figure 6.11, layer 3). The thickest part of the second sedimentary layer is deposited within the Melville Bay Graben (~ 2.2 km), where the velocities vary between 2.3 and 2.8 km/s. The underlying sedimentary wedge is up to 6.2 km thick and has velocities of 4.0 to 5.1 km/s. An example for a refracted phase indicating the high velocities of this sedimentary layer is given in Figure 6.9. The shape of the layer strongly points to a synrift origin. Due to the high velocities, the sedimentary rocks may also contain basaltic layers.

The upper part of the Melville Bay Ridge and the base of the Melville Bay Graben have been modeled with one layer (layer 7, Figure 6.10). Between km 160 and 190, the velocity of the layer is constrained by refractions (3.5–4.9 km/s). The eastern part of the layer has been modeled with velocities between 4.5 and 5.2 km/s; the velocities are not constrained by any refractions (“hidden layer”, see chapter 6.5.1.1.). Because of the strong reflections visible in the seismic reflection data (Figure 6.3, CDP 4500–7000), the “hidden layer” may represent highly compacted or metamorphosed sedimentary rocks and may also contain basalts.

The continental crust is divided in 3 crustal layers based on reflections at the base of every layer (Figure 6.11). The Melville Bay Fault divides the upper

continental crust in two parts, which have velocities of 5.5 to 5.9 km/s west of, and 5.7 to 6.1 km/s east of the Melville Bay Fault.

The geometry of the fault influences the whole crust, from the upper- to lowermost layer causing a detachment in downward continuation of the fault plane and an increased crustal thickness underneath the Melville Bay Ridge. The mid-crustal layer with a thickness between 7.5 and 10.5 km has been modeled with velocities of 6.0 to 6.5 km/s, its base underneath the Melville Bay Graben is very well constrained by reflections. The lowermost crustal layer has velocities of 6.6 to 6.9 km/s and a thickness of up to 14 km underneath the Melville Bay Ridge. Further east below the Melville Bay Graben, the depth of the Moho decreases and the lower continental crust is only ~6 km thick.

Underneath the prominent Melville Bay Graben, the upper mantle has been modeled with velocities of 8.1 km/s based on refractions. To the east and west, no P_n refractions were identified.

6.7 Discussion

In the following, we will compare our results with other seismic datasets acquired in the Baffin Bay. The presented model intersects profile AWI-20100400 in the Melville Bay Graben (Suckro et al., 2012). The velocity-depth functions at the intersection of both profiles are in good agreement. Additionally, our profile extends parallel to the profile AWI-20100200, which also crosses the Melville Bay in a SW-NE direction (Altenbernd et al., 2014). Thus, we can compare the structural inventory of the Melville Bay in its northern and southern part. Furthermore, we set the structure of oceanic crust in the western part of our model side by side with oceanic crust in the northern and southern Baffin Bay and also discuss which kind of margin is present in the northeastern Baffin Bay. Based on a compilation of results from the refraction seismic profile AWI-20100200, AWI-20100300, and our study, we discuss which type of margin is present in the Baffin Bay and map the extent of crustal units in this region.

6.7.1 Intersection with profile AWI-20100400

Our profile crosses the refraction seismic profile AWI-20100400 (Suckro et al., 2012) in its northern part in the Melville Bay Graben (profile km 210, Figure 6.10a). OBS 1 of profile AWI-20100400 and OBS 13 of profile AWI-20100450 were deployed at the same position above the Melville Bay Graben.

The velocities modeled for the upper sedimentary successions in the Melville Bay Graben (0.5 to 8 km depth) are almost identical at the intersection between both profiles, although AWI-20100400 has been modeled with more layers than our profile (Figure 6.14). The top of the sediments with the unusually high velocities greater than 4.3 km/s is at almost the same depth in both profiles (~3.2 km depth). However, Suckro et al. (2012) modeled the layers between 3 and 8 km depth with two units. Their upper layer with velocities of 4.3 to 4.4 km/s is of sedimentary composition, while their lower layer (4.8–5.1 km/s) is of indistinct composition: either sediments or basalts. We used one layer for modeling the depth range of 3 to 8 km, and interpret the sediments to consist of highly compacted sediments or sedimentary rocks and/or basalts with velocities of 4.3 to 5.0 km/s.

Suckro et al. (2012) also divided their continental crust in three distinct layers. Due to the absence of a layer with velocities of 5.06 to 5.11 km/s (“hidden layer” in our profile) in profile AWI-20100400, the top of upper, middle and lower continental crust is shallower (1.7–3.5 km difference), but the thickness of all three crustal layers in both profiles is comparable. We inserted the “hidden layer” because of indications for its presence in the reflection seismic data and misfits in the *P* wave velocity modeling in this particular region (see chapter 6.5.1.1). Since we did not find any reflections at its base or refractions, its thickness and velocity is not well resolved and ambiguous.

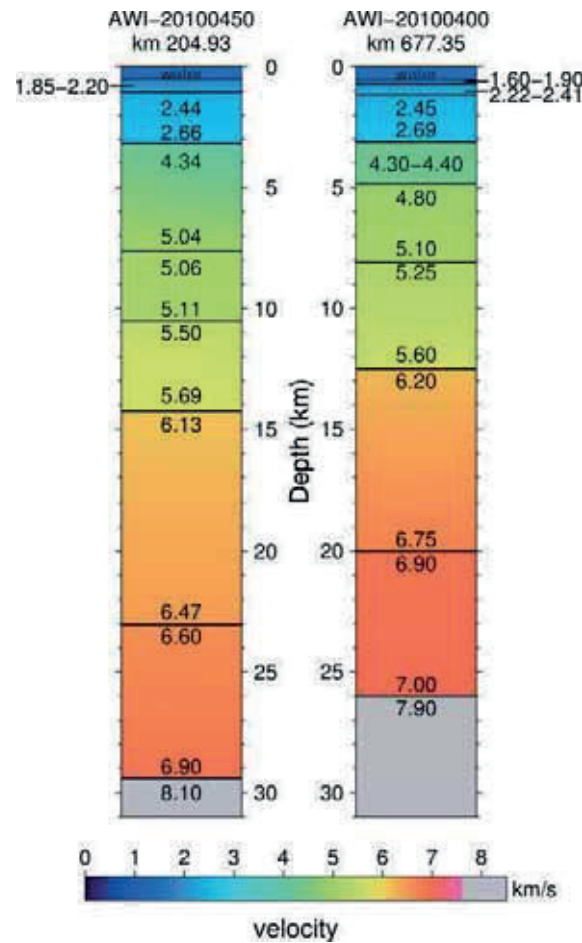


Figure 6.14: Velocity-depth-profiles at the intersection between AWI-20100450 (this study) and AWI-20100400 (Suckro et al., 2012). The velocities are given in km/s. For location see Figure 6.10a.

For the stretched continental crust, Suckro et al. (2012) used higher velocities (difference of 0.1–0.3 km/s) to model the mid- and lower continental crust. Also, the depth of the Moho at the intersection of both profiles differs by 3.4 km. Deviations in crustal velocities of upper, middle, and lower continental crust and differences in Moho depth can be explained by the ray coverage, which is slightly better along our profile. Sparse refracted rays verify the velocities of continental crustal units in our profile (Figure 6.11), but no refracted signals occur in this part of profile AWI-20100400. Also, the intersection between both profiles is located at the eastern end of AWI-20100400, therefore the resolution of crustal layers is below 0.5 (see Figure 4 in Suckro et al., 2012).

6.7.2 Comparison with the northern Melville Bay (AWI-20100200)

Although the parallel profiles AWI-20100450 and AWI-20100200 cross the Melville Bay in a SW-NE direction and are only ~160 km apart from each other (Figure 6.2), they show some major differences.

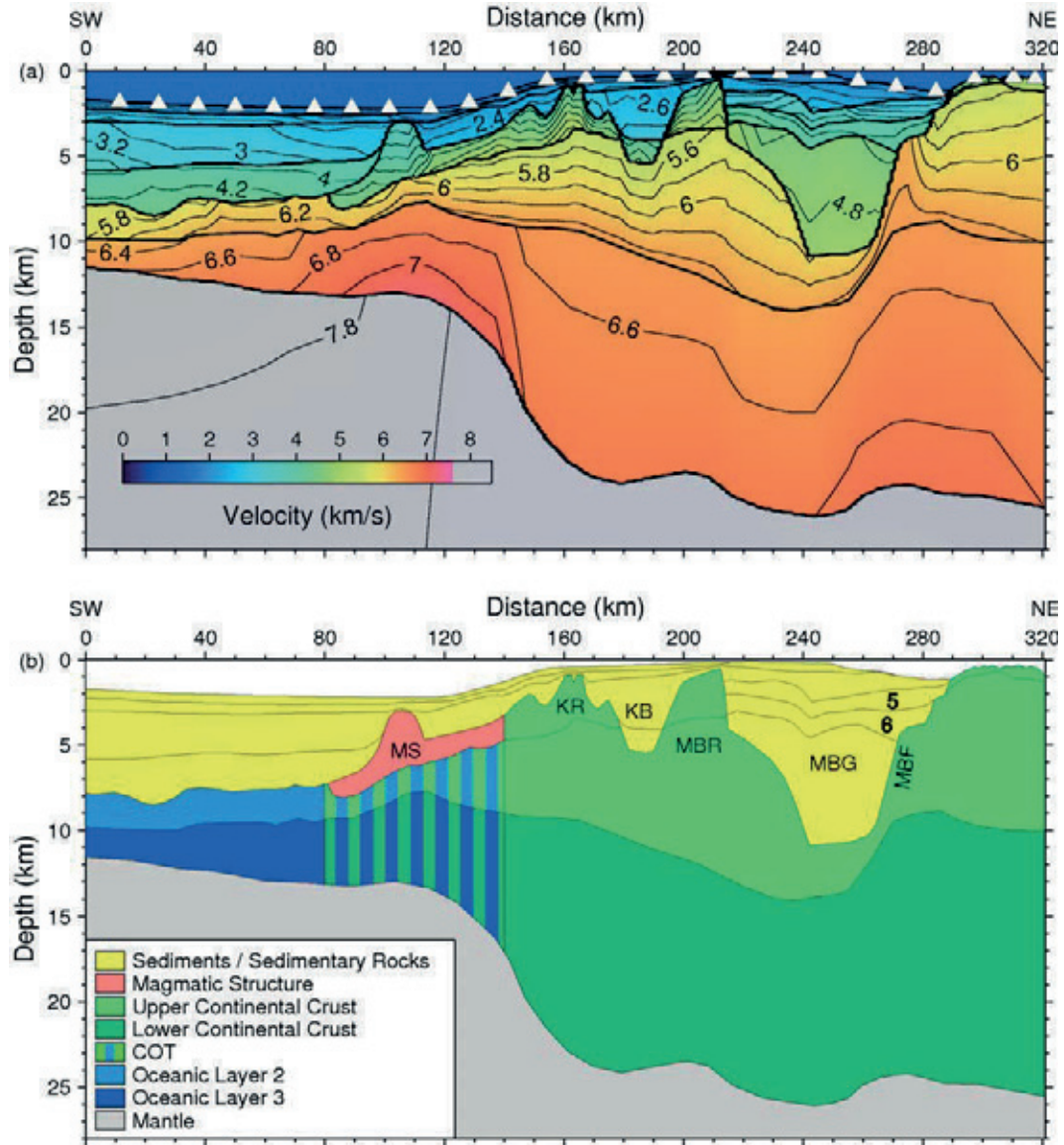


Figure 6.15: Refraction seismic profile AWI-20100200.

(a) *P* wave velocity model of AWI-20100200, taken from Altenbernd et al. (2014).

(b) Geological interpretation of AWI-20100200, changed after Altenbernd et al. (2014). Bold black numbers are the numbers of velocity layers. Abbreviations: MS: magmatic structure, KR: Kivioq Ridge, KB: Kivioq Basin, MBR: Melville Bay Ridge, MBG: Melville Bay Graben, MBF: Melville Bay Fault.

The northern profile AWI-20100200 (Figure 6.15a) reveals a highly compacted sedimentary layer with rather high velocities of 3.9 to 4.4 km/s overlying the oceanic crust. In contrast, these sediments are either absent or too thin to be detected at AWI-20100450 (Figure 6.10). Both explanations are reasonable, since Keen and Barrett (1972) interpreted consolidated sediments with velocities of 3.9 to 4.2 km/s in the central Baffin Bay and Suckro et al. (2012)

modeled sediments with velocities of up to 4.1 km/s in southern but not in the northern part along profile AWI-20080500.

Another difference between both profiles is the low-velocity layer above the transitional crust in profile AWI-20100450. There are no indications for a low-velocity layer in the seismograms of AWI-20100200 and the change in the sedimentary structure indicates a change in the sedimentation process or composition.

The continental crust along AWI-20100450 is composed of three continental crustal layers. In contrast, the crust underneath AWI-20100200 has been modeled with only two layers (Figure 6.15b). The reason for that are sparse intra-crustal reflections at AWI-20100450 (Altenbernd et al., 2014). Therefore, the boundary between upper and lower continental crust are in most parts only based on changes in the velocity gradient and the crust underneath AWI-20100200 might also be composed of 3 layers.

The origin and age of the infill within the basins in the Melville Bay can only be discussed based on reflection seismic data and very few refraction seismic datasets derived from sonobuoy recordings (Figure 6.1) since no well data are available for this area. The refraction seismic profiles AWI-20100200, AWI-20100400 and AWI-20100450 are the only reliable and modern data of *P* wave velocities measured in the area.

Gregersen et al. (2013) interpreted the infill of the Melville Bay Graben based on reflection seismic data and interval velocities derived from migration velocity analysis. Their G1-horizon probably corresponds to the base of lowermost layer of sedimentary rocks and/or basalts in our model (base of velocity layer 6, Figure 6.10).

However, the velocities of the lowermost sedimentary layer deviate. Gregersen et al. (2013) calculated apparent velocities slower than 4 km/s and suggested a jump in velocities, possibly even higher than >5 km/s below the G1-horizon. In contrast, we observed significantly faster velocities of 5.1 km/s in the lowermost sediments (velocity layer 6) and a clear jump in velocity at the top of layer 6 and not at its base. All refraction seismic profiles across the Melville Bay show high seismic velocities in the lowermost infill of the graben: 4.5 to 4.9 km/s at AWI-20100200 (Altenbernd et al., 2014), 4.3 to 5.1 km/s at AWI-20100400 (Suckro et al., 2012), and 4.0 to 5.2 km/s at AWI-20100450 (this study). Especially along our profile, the base of layer 6 is well constrained by reflections and the high velocities by refractions, even in the lowermost part of the wedge-shaped layer. The underlying “hidden layer” in AWI-20100450 (Figures 6.10b and 6.10c) seems to correspond to unit G of Gregersen et al. (2013), which is interpreted by the authors to consist of metamorphosed sedimentary rocks, which may also include intrusions. This is in agreement with our interpretation of highly compacted sediments and possibly basalts within the “hidden layer”.

In the Melville Bay Graben, two sedimentary layers with velocities ranging between 2.8 and 4.1 km/s cover the lowermost infill with high velocities in northern Melville Bay along profile AWI-20100200 (Figure 6.15, layer 5 and 6). Sediments with comparable velocities have neither been identified in the Melville Bay Graben along our profile nor along profile AWI-20100400 (Suckro et al., 2012). Therefore, the layers are either too thin to be detected or were not deposited in this area, since no indications of erosion are present within the infill of the Melville Bay Graben in the seismic reflection data (Figure 6.3).

The depth of the Moho and the crustal thickness in the Melville Bay vary, but the thickest crystalline crust is consistently located below the ridges and east of the Melville Bay Fault in both profiles (AWI-20100450 and AWI-20100200). However, the depth of the Moho decreases underneath the Melville Bay Graben along AWI-20100450 (Figure 6.10), but increases along AWI-20100200 (Figure 6.15).

Therefore, Moho depressions in northern and southern Melville Bay are located underneath different structures. This might be a result of the changing geometry of the Melville Bay Graben, which is a graben in the north, and a half graben in its central part (Whittaker et al., 1997). Statements about the depth of this graben are often based on gravity anomalies (e.g., Whittaker et al., 1997). Our data show that the local minimum of the gravity anomalies does not necessarily coincide with the deepest point of the graben (Figure 6.12). As a consequence, gravity modeling only may be misleading, and the negative gravity anomalies can be caused by the Moho topography. Interestingly, the geometry and direction of the westward limiting fault of the Melville Bay Graben changes directly south of our profile (Figure 6.1b) and close to the point, where the gravity misfit is observed. Therefore, the change in geometry of the Melville Bay Graben and a resulting 3D-effect might be the reason why the gravity low does not coincide with the deepest point of the Melville Bay Graben.

6.7.3 COT

The width and velocity structure of the COT vary along the continental margin. The COT in the southern Baffin Bay along our profile is wider (~80 km) than in the north (60 km, AWI-20100200, Altenbernd et al., 2014). The transitional crust along AWI-20100200 is characterized by a magmatic structure covering the underlying crust and velocities of up to 7.2 km/s in the lowermost crustal layer (Figure 6.15). In contrast to AWI-20100200, there are no obvious indications for extrusive volcanism in the COT along our profile. However, the COT along AWI-20100450 is affected by intrusive magmatism: a local velocity increase in the lower crust (up to 6.2–6.7 km/s) and the overlying basement high indicates an intrusion at the eastern termination of the COT (Figure 6.10). The western area of the COT is not affected by magmatism.

A strong positive gravity anomaly south of our profile has been interpreted as mafic or ultramafic intrusion resulting from late Paleocene magmatism (Figure 6.2, Whittaker et al., 1997). Whittaker et al. (1997) also presented an ultramafic intrusion marked in a simplified line-drawing of seismic reflection data acquired in the Baffin Bay, but unfortunately no location of the profile is given. In contrast, Oakey and Chalmers (2012) proposed that the gravity anomaly could also be caused by a sequence of uncompensated sediments. Based on the increased velocities at the COT along AWI-20100450, we propose that the gravity anomaly south of our profile is caused by a large mafic intrusion, which northernmost part is revealed in our profile.

6.7.4 Margin of the northeastern Melville Bay

There are two types of passive continental margins: volcanic and non-volcanic margins.

At non-volcanic margins, a high velocity lower crust (7.2–7.7 km/s) is composed of serpentinites (Chian et al., 1999). Moho reflections are absent or weak

because of serpentinized upper mantle peridotites (Dean et al., 2000). Highly stretched continental crust and rotated fault blocks landward of the COT are also characteristic. Peridotite ridges are a common feature along non-volcanic margins, for example in the Iberia Abyssal Plain (Dean et al., 2000).

Volcanic margins are passive continental rifted margins characterized by massive volcanism. The crust at volcanic margins is often characterized by seaward dipping reflectors (SDR) and high velocities in the lower crust (7.2–7.6 km/s), interpreted as magmatic underplating and mafic intrusions (White and McKenzie, 1989; Eldholm et al., 1987; Mutter et al., 1984). Volcanic margins are present, for example, at the South Atlantic margins (Elliott et al., 2009), the North Atlantic margins (Mjelde et al., 2005) or in the northern Labrador Sea (Gerlings et al., 2009).

The proposed arrival of the Iceland plume at ~62 Ma is suspected to let to the formation of volcanic margins in the Davis Strait and the adjacent regions. Clear indications for a volcanic margin, like SDR and/or thick igneous crust and underplating, have been discovered in the northern Labrador Sea (Chalmers, 1997), Davis Strait (Skaarup et al., 2006; Gerlings et al., 2009, Funck et al., 2007), and southern Baffin Bay (Suckro et al., 2012, Funck et al., 2012). The crust in the Davis Strait and Labrador Sea first underwent non-volcanic rifting and was later overprinted by volcanics possibly related to the Iceland mantle plume (Funck et al., 2007; Gerlings et al., 2009; Chalmers and Pulvertaft, 2001). During that time, the Ungava Fault Zone, which connects the spreading systems in the Baffin Bay and Labrador Sea, acted as a leaky transform fault (Storey et al., 1998, Funck et al., 2007).

In contrast, the COT of the southern Labrador Sea is of non-volcanic character and was not affected by plume-related magmatism. Here, the two-layered crust has low velocities of 4-5 km/s in its upper part, underlain by serpentinized mantle with velocities of 6.4 to 7.7 km/s (Chian et al., 2005). As a consequence, the influence of the Iceland mantle plume seems to decrease with increasing distance from the Davis Strait area. Therefore, the change from a volcanic to a non-volcanic margin must be located in the central or northern Baffin Bay (Funck et al., 2012).

Indications for mafic intrusions within the lower crust of the COT are also present along our profile and along the northern profile AWI-20100200. However, there are no indications for SDRs or massive underplating as clear indications for volcanic passive margins in these areas. The influence of magmatism seems to decrease toward the north: along the northern profile AWI-20100300, the COT is composed of a two-layered crust with velocities of 5.5 to 6.6 km/s, showing no indications for a large magmatic influence (Altenbernd et al., submitted). Due to missing magmatic influence, the margin along AWI-20100300 was classified as non-volcanic (Altenbernd et al., submitted). However, typical indications for a non-volcanic margin like a serpentinite ridge or weak or no clear Moho reflections are absent along the COT of AWI-20100450, AWI-20100200, and AWI-20100300; serpentinized upper mantle is only present underneath the thin, oceanic crust of these profiles. In contrast, signs for amagmatic rifting have been discovered in the northern Baffin Bay off the Canadian margin. Here, thin crust underneath profile 91/4 (Figure 6.1) is probably composed of serpentinized upper mantle (Reid and Jackson, 1997).

Because of missing clear indicators, we cannot classify the margin in west of the Melville Bay area as a typical volcanic or non-volcanic passive margin. It could be best described as rifted margin with decreasing signs for magmatic activity toward the north and no signs for serpentinization in its lowermost layer.

We, therefore, propose that rifting in the Baffin Bay was amagmatic until the arrival of the Iceland mantle plume at ~ 62 Ma. Like in the northern Labrador Sea, plume material was channeled underneath the lithosphere (Gerlings et al. 2009) and transported along major faults, like the UFZ, toward the north. The plume material interacted with the thinned lithosphere and led to magmatic activity in form of local intrusive and extrusive magmatism in the northeastern Baffin Bay.

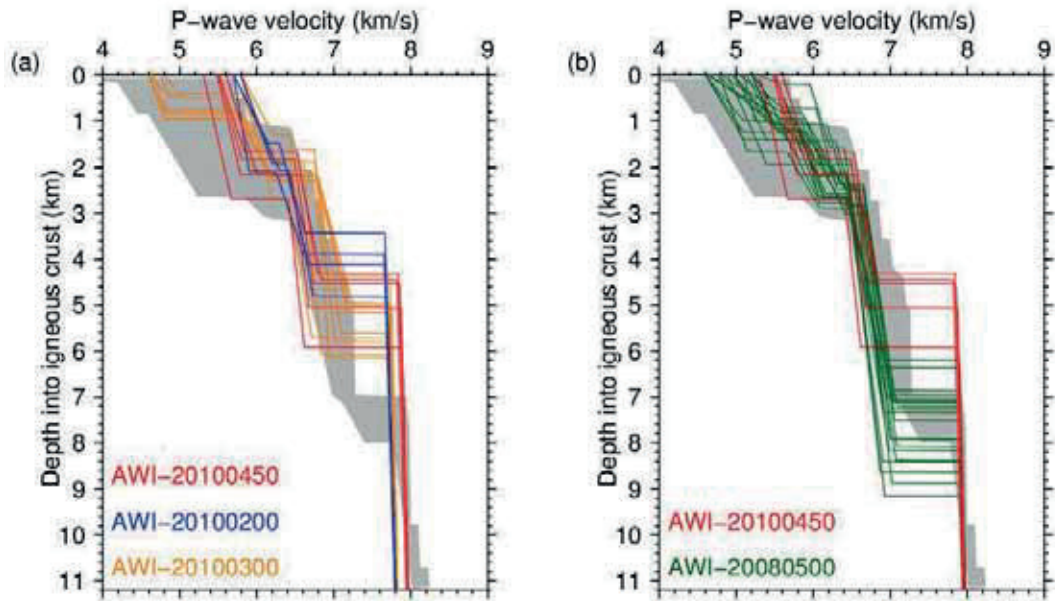


Figure 6.16: Comparison of oceanic crust from AWI-20100450 with oceanic crust in northern (a) and southern (b) Baffin Bay. The grey area marks velocity-depth-functions typical for normal Atlantic oceanic crust with an age of 59 to 127 Myrs (White et al., 1992).

(a) Comparison of velocity-depth functions of oceanic crust, taken every 10 km along AWI-20100450 (this study), AWI-20100200 (Altenbernd et al. 2014) and AWI-20100300 (Altenbernd et al., submitted).

(b) Comparison of velocity-depth functions of oceanic crust, taken every 10 km along AWI-20100450 (this study) and AWI-20080500 (Suckro et al. 2012).

6.7.5 Oceanic crust and upper mantle

Sonobuoy recordings of Keen and Barrett (1972) first indicated thin oceanic crust in the central Baffin Bay. The thin oceanic crust along our profile is mainly caused by a reduced thickness of layer 3. After White et al. (1992), the average thickness of oceanic layer 3 is ~ 5 km. In contrast, our layer 3 is only 2 to 4 km thick and has been modeled with velocities of 6.3 to 6.9 km/s. A thin oceanic layer 3 with velocities lower than the average of 6.6 to 7.6 km/s (White et al., 1992) has also been observed in the northern Baffin Bay along AWI-20100200 (6.2–7.0 km/s, Altenbernd et al., 2014) and in the southern part of AWI-20100300 (6.4–6.8 km/s, Altenbernd et al., submitted). With the exception of lower crustal velocities in oceanic layer 2, the velocity-depth functions and thickness of the crust in our profile fit well to the thin oceanic crust found in the

northern part of the Baffin Bay, especially to the parallel extending profile AWI-20100200 (Figure 6.16a).

In contrast to the northern Baffin Bay, southern Baffin Bay is underlain by normal to thick oceanic crust. Compared with the normal oceanic crust along AWI-20080500 (Suckro et al., 2012), our oceanic layer 3 is thinner (Figure 6.16b). The velocities of oceanic layer 3 along AWI-20080500 (6.2–7.2 km/s) are partly faster than along our profile and show a higher gradient than along any other profile in the Baffin Bay.

Funck et al. (2012) found 6 to 9 km thick oceanic crust underneath the southern Baffin Bay Basin (AWI-20080600, Figure 6.1a). The authors explain the increased thickness with additional magma supply related to the Iceland mantle plume and thinner crustal units with the occurrence of a fracture zone and a transform fault. Also, a thick sequence of ~20 km thick igneous crust is present within the Ungava Fault Zone along AWI-20080600, which acted as a leaky transform fault in the southern Baffin Bay and Davis Strait (Funck et al., 2007).

Altenbernd et al. (2014) proposed that the thin crust in the northern Baffin Bay can be explained by formation during ultraslow to slow spreading and variations in its crustal thickness might be the result of changing magma supply. Thin oceanic crust is often observed in regions with slow to ultraslow spreading, e.g., the Gakkel Ridge (Jokat et al. 2003) or the Mohns Ridge (Klingelhöfer et al., 2000). Furthermore, the low upper mantle velocities observed in our profile support low spreading rates. Low mantle velocities are common at the ultraslow spreading Knipovich Ridge, Gakkel Ridge or Mohns Ridge (Ljones et al., 2004; Klingelhöfer et al., 2000; Jokat and Schmidt-Aursch, 2007; Hermann and Jokat, 2013), and have also been observed along AWI-20100200 and AWI-20100300.

Table 6.2: Velocity and thickness ranges of oceanic layer 2 and oceanic layer 3 along the profiles AWI-20100300 (Altenbernd et al., submitted), AWI-20100200 (Altenbernd et al., 2014), AWI-20100450 (this study), AWI-20080500 (Suckro et al., 2012), and AWI-20080600 (Funck et al., 2012).

Profile	Layer 2		Layer 3	
	Thickness (km)	Velocity (km/s)	Thickness (km)	Velocity (km/s)
AWI-20100300	<1 (only north)	4.6–4.8	2.8–5.5 (north)	6.7–7.3 (north)
	1–3	5.7–6.2	3–4 (south)	6.4–6.8 (south)
AWI-20100200	1.5–2	5.6–6.4	1.8–3.9	6.2–7.0
AWI-20100450	1.8–2.8	5.2–6.0	2–4	6.3–6.9
AWI-20080500	0.7–2	4.6–5.6	3.5–6	6.2–7.2
	<2	5.7–6.5		
AWI-20080600	2–4 (borders)	5.5–6.0	5–9	6.8–7.2
	2–2.5 (center)	6.1–6.5		

Table 6.2 summarizes information about crustal thickness and *P* wave velocities of oceanic crust along all modern refraction seismic profiles in the Baffin Bay from the north to the south and reveals a high variability in its crustal structure. To sum up, a general trend of normal and thicker crust in the southern Baffin Bay and partly abnormal thin crust in the northern Baffin Bay is visible. Following the interpretation of Funck et al. (2012), the greater crustal thickness in the south can be explained by ample magma supply provided by material of Iceland mantle plume. Toward the north, the influence of the Plume decreased

and slow or even ultraslow spreading rates created a highly variable and thin oceanic crust.

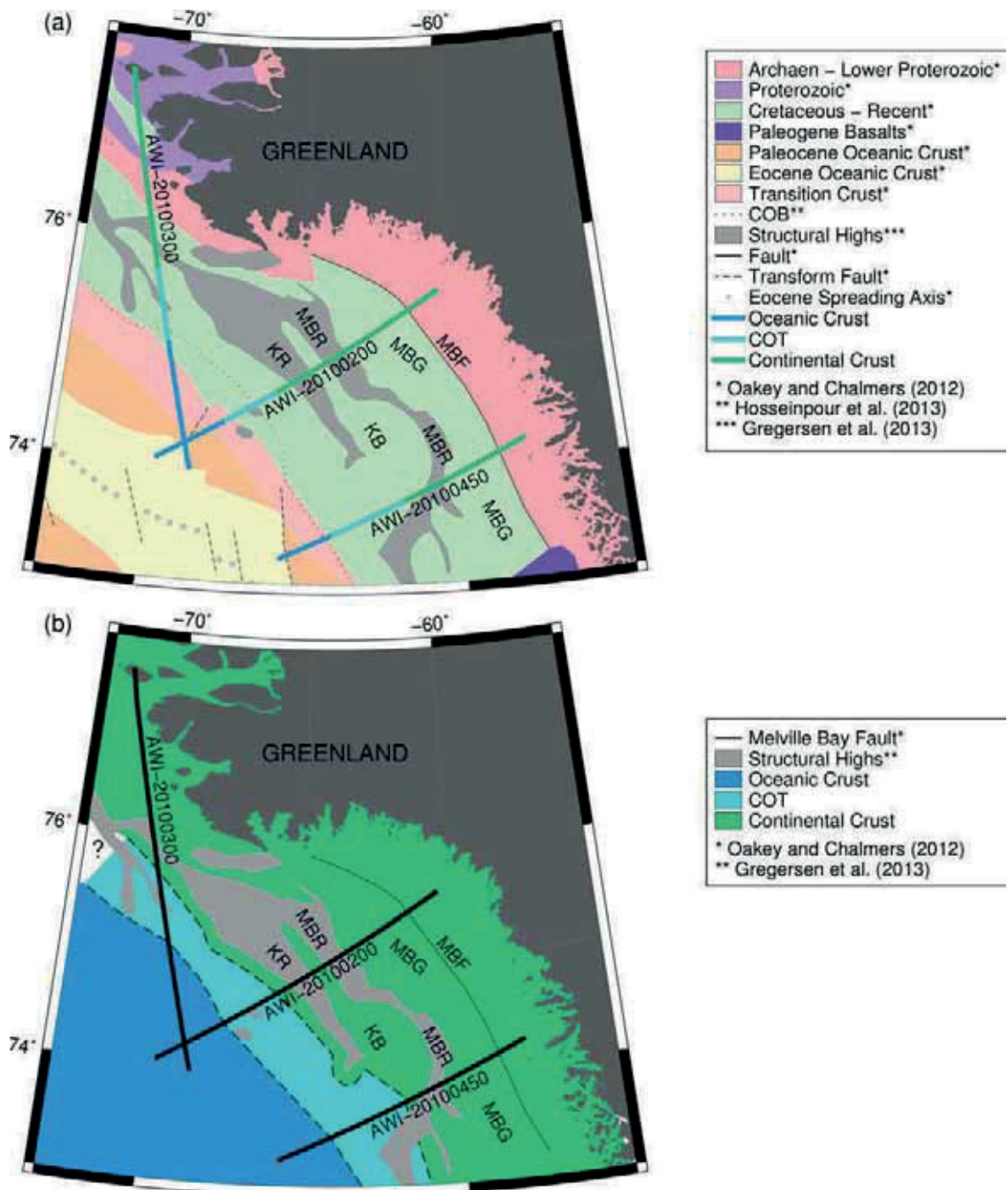


Figure 6.17: Distribution of crustal types in Baffin Bay.

(a) Comparison of crustal types in Baffin Bay from Oakey and Chalmers (2012) and Hosseinpour et al. (2013) with results derived from *P* wave modeling of modern refraction seismic data in the Melville Bay and northern Baffin Bay. The distribution of oceanic, transitional and continental crust is indicated by different colors along the profiles. The extend of crustal types along the profiles is taken from Altenbernd et al. (2014) (AWI-20100200), Altenbernd et al. (submitted) (AWI-20100300) and this study (AWI-20100450).

(b) Distribution of crustal types in the area of interest, based on results of refraction seismic profiles seen above. Between the profiles, the border between oceanic crust and the COT is geared to the landward termination of the transitional zone of Oakey and Chalmers (2012). The landward termination of the COT is geared to the Kivioq Ridge at its northern part and to a prominent gravity high (see Figure 6.2) in its southern part. Abbreviations: KR: Kivioq Ridge, KB: Kivioq Basin, MBR: Melville Bay Ridge, MBG: Melville Bay Graben, MBF: Melville Bay Fault

6.7.6 Crustal units in the northeastern Baffin Bay

We specify the extent of transitional and continental crust in the Baffin Bay based on the refraction seismic profiles AWI-20100300, AWI-20100450 and AWI-20100200. Figure 6.17a shows the geological map of Oakey and Chalmers (2012), and the proposed position of the COT in the northeastern Baffin Bay (Hosseinpour et al., 2013). The onset of oceanic crust differs between our results and Oakey and Chalmers (2012), and Hosseinpour et al. (2013). The oceanic crust constrained by the new refraction lines includes the “transitional crust” of Oakey and Chalmers (2012). In the north along the profiles AWI-20100300 and AWI-20100200, the onset of oceanic crust is located further west than the Continent-Ocean Boundary (COB) of Hosseinpour et al. (2013), while the position of the COB almost exactly fits our results along AWI-20100450.

Figure 6.17b shows the extent of crustal units in northeastern Melville Bay defined by the *P* wave velocity models of Altenbernd et al. (2014) and Altenbernd et al. (submitted). Since the extent of crustal units is only verified along the profiles, we interpolated the eastern boundary of oceanic crust along the onset of transitional crust after Oakey and Chalmers (2012). The seaward onset of continental crust is interpolated along the Kivioq Ridge at its northern part and includes the gravity high in its southern part (see Figure 6.2b). Based on the refraction seismic data, the COT covers the western part of the Melville Bay area and is located further east than postulated by previous studies.

6.8 Conclusion

We presented the *P* wave velocity model and a density model along refraction seismic profile AWI-20100450 and detected stretched continental and thin oceanic crust separated by a COT. Compilation of our results with previous refraction seismic profiles show, that the COT and, in some parts, the oceanic crust cover a much larger area toward the continent than previously postulated. Along our profile, the two-layered COT is characterized by lower velocities in its uppermost layer than in the adjacent continental and oceanic crust. The COT is likely composed of stretched continental crust and may also include magmatic layers in its upper crust west of a basement high. In the east, the lowermost layer of the COT incorporates an intrusion beneath the basement high. The intrusion may be the northern part of a much larger, late Paleocene intrusion indicated by a positive gravity anomaly south of the profile.

The type of margin in the Melville Bay area can be best described as rifted margin with decreasing signs for magmatic activity toward the north. Typical indications for a non-volcanic margin, like serpentinized upper mantle in the COT, are missing.

The sedimentary cover in the COT hosts a low-velocity zone. This low-velocity zone has not been observed along the northern profile AWI-20100200 and indicates a change in sedimentary composition from the north to the south.

The stretched continental crust underneath southern Melville Bay is composed of a three-layered, up to 30 km thick crust, covered by sediments. Sediments and sedimentary rocks within the Melville Bay Graben are up to 9 km thick. The lowermost, synrift infill has unusually high velocities of 4 to 5.2 km/s, but are very well constrained by refractions. The greatest Moho depth (~33 km) is present below the Melville Bay Ridge and decreases to ~24 km underneath the Melville Bay Graben. This is contrary to the parallel extending, northern profile

AWI-20100200, where the Moho underneath the Melville Bay Graben and the Kivioq Ridge is located at greater depth than underneath the Melville Bay Ridge. The Melville Bay Graben is a graben in the north and a half graben in the south. This change in geometry might cause the change in Moho topography and the different location of the deepest Moho with relation to the Melville Bay Graben. Also, the sedimentary infill changes from the north to the south, since sediments with velocities of 2.8 and 4.1 km/s present in the northern Melville Bay Graben have not been identified along our profile.

Up to 5 km thick sediments cover the oceanic crust in the western part of the model. In contrast to the northern Baffin Bay, no compacted sediments with high velocities of 3.9 to 4.4 km/s overly the oceanic crust. The 4.3 to 7 km thick oceanic crust is composed of 2 igneous layers. The upper oceanic layer 2 has velocities of 5.2 to 6.0 km/s, oceanic layer 3 has unusually low velocities of 6.3 to 6.9 km/s. The partly unusually thin oceanic crust and low upper mantle velocities of >7.8 km/s underneath indicate slow or ultraslow spreading in the Baffin Bay.

6.9 Acknowledgements

We thank captain and the crew of RV Polarstern and also the onboard OBS-crew for their excellent work during the research expedition in the Baffin Bay 2010. We thank the Deutsche Geräte-Pool für amphibische Seismologie (DEPAS pool) for providing the OBS for the experiment. We thank the BGR for providing the processed seismic reflection data and Cairn Energy for providing the reprocessed seismic reflection data of BGR10-311.

The new refraction seismic datasets used for this publication are available upon request at Alfred Wegener Institute Helmholtz Centre for Polar and Marine Research in Bremerhaven, Germany. The seismic sections of profile BGR10-311 are available upon request at the Federal Institute for Geosciences and Natural Resources in Hanover, Germany.

6.10 References

- Altenbernd, T., W. Jokat, I. Heyde, and V. Damm (2014), A crustal model for northern Melville Bay, Baffin Bay, *J. Geophys. Res.*, 119, 8610–8632, doi:10.1002/2014JB011559.
- Altenbernd, T., W. Jokat, I. Heyde, and V. Damm, submitted, Insights in the crustal structure of the transition between Nares Strait and Baffin Bay, submitted to *Tectonophysics* in June 2015.
- Barton, P. (1986), The relationship between seismic velocity and density in continental crust—a useful constraint?, *Geophys. J. Roy. Astron. Soc.*, 87, 195–208.
- Chalmers, J. A. (1997), The continental margin off southern Greenland: Along-strike transition from an amagmatic to a volcanic margin, *J. Geol. Soc. London*, 154, 571–576, doi:10.1144/gsjgs.154.3.0571.
- Chalmers, J. A., and K. Laursen (1995), Labrador Sea: The extent of continental and oceanic crust and the timing of the onset of seafloor spreading, *Mar. Petrol. Geol.*, 12, 205–217, doi:10.1016/0264-8172(95)92840-S.
- Chalmers, J. A., and T. C. R. Pulvertaft (2001), Development of the continental margins of the Labrador Sea: A review, in *Non-Volcanic Rifting of Continental Margins: A Comparison of Evidence From Land and Sea*, *Geol. Soc. Spec. Publ.*, vol. 187, edited by R. C. L. Wilson et al., pp. 77–105, doi:10.1144/GSL.SP.2001.187.01.05.

Chian, D., K. E. Loudon, and I. Reid (1995), Crustal structure of the Labrador Sea conjugate margin and implications for the formation of non-volcanic continental margins, *J. Geophys. Res.*, 100, 24,239–24,253, doi:10.1029/95JB02162.

Chian, D., K. E. Loudon, T. A. Minshull, and R. B. Whitmarsh (1999), Deep structure of the ocean–continent transition in the southern Iberia Abyssal Plain from seismic refraction profiles: Ocean Drilling Program (Legs 149 and 173) transect, *J. Geophys. Res.*, 104, 7443–7462.

Damm, V. (2010), The Expedition of the Research Vessel “Polarstern” to the Arctic in 2010 (ARK-XXV/3), *Berichte zur Polar- und Meeresforschung*, 621, 234 pp., Alfred Wegener Inst. for Polar and Mar. Res., Bremerhaven, Germany.

Dean, S. M., T. A. Minshull, R. B. Whitmarsh, and K. E. Loudon (2000), Deep structure of the ocean–continent transition in the southern Iberia Abyssal Plain from seismic refraction profiles: The IAM-9 transect at 40°20'N, *J. Geophys. Res.*, 105, 5859–5886.

Eldholm, O., J. Thiede, and E. Taylor (1987), Evolution of the Norwegian continental margin: Background and objectives, *Proc. Ocean Drill. Program Initial Rep. part A*, 104, 5–25.

Elliott, G. M., C. Berndt, and L. M. Parson (2009), The SW African volcanic rifted margin and the initiation of the Walvis Ridge, South Atlantic, *Marine Geophys. Res.*, 30(3), 207–214, doi 10.1007/s11001-009-9077-x.

Funck, T., H. R. Jackson, S. A. Dehler, and I. D. Reid (2006), A refraction seismic transect from Greenland to Ellesmere Island, Canada: The crustal structure in southern Nares Strait, *Polarforschung*, 74, 97–112.

Funck, T., H. Jackson, K. Loudon, and F. Klingelhöfer (2007), Seismic study of the transform–rifted margin in Davis Strait between Baffin Island (Canada) and Greenland: What happens when a plume meets a transform, *J. Geophys. Res.*, 112, B04402, doi:10.1029/2006JB004308.

Funck, T., K. Gohl, V. Damm, and I. Heyde (2012), Tectonic evolution of southern Baffin Bay and Davis Strait: Results from a seismic refraction transect between Canada and Greenland, *J. Geophys. Res.*, 117, B04107, doi:10.1029/2011JB009110.

Gerlings, J., T. Funck, H. Jackson, K. Loudon, and F. Klingelhöfer (2009), Seismic evidence for plume-derived volcanism during formation of the continental margin in southern Davis Strait and northern Labrador Sea, *Geophys. J. Int.*, 176, 980–994, doi:10.1111/j.1365-246X.2008.04021.x.

Gregersen, U., J. R. Hopper, and P. C. Knutz (2013), Basin seismic stratigraphy and aspects of prospectivity in the NE Baffin Bay, Northwest Greenland, *Mar. Petrol. Geol.*, 46, 1–18, doi:10.1016/j.marpetgeo.2013.05.013.

Hermann, T. and Jokat, W. (2013), Crustal structure of the Boreas Basin and the Knipovich Ridge at 76° N in the North Atlantic, *Geophysical Journal International*, 193(3), 1399–1414, doi: 10.1093/gji/ggt048.

Hosseinpour, M., R. D. Müller, S. E. Williams, and J. M. Whittaker (2013), Full-fit reconstruction of the Labrador Sea and Baffin Bay, *Solid Earth*, 4, 461–479, doi:10.5194/se-4-461-2013.

Jackson, H. R., and I. Reid (1994), Crustal thickness variations between the Greenland and Ellesmere Island margins determined from seismic refraction, *Can. J. Earth Sci.*, 31, 1407–1418, doi:10.1139/e94-124.

Jokat, W., and M. C. Schmidt-Aursch (2007), Geophysical characteristics of the ultraslow spreading Gakkel Ridge, Arctic Ocean, *Geophys. J. Int.*, 168, 983–998 doi: 10.1111/j.1365-246X.2006.03278.x.

- Jokat, W., O. Ritzmann, M. C. Schmidt-Aursch, S. Drachev, S. Gauger, and J. Snow (2003), Geophysical evidence for reduced melt production on the Arctic ultraslow Gakkel mid ocean ridge, *Nature*, 423, 962–965, doi:10.1038/nature01706.
- Keen, C., and D. Barrett (1972), Seismic refraction studies in Baffin Bay: An example of a developing ocean basin, *Geophys. J. Roy. Astron. Soc.*, 30, 253–271, doi:10.1111/j.1365-246X.1972.tb05812.x.
- Klingelhöfer, F., L. Geli, L. Matias, N. Steinsland, and J. Mohr (2000), Crustal structure of a super-slow spreading centre: A seismic refraction study of Mohns Ridge, 72°N, *Geophys. J. Int.*, 141, 509–526, doi:10.1046/j.1365-246x.2000.00098.x.
- Klose, G. W., E. Malterre, N. J. McMillan, and C. G. Zinkan (1982), Petroleum exploration offshore southern Baffin Island, northern Labrador Sea, Canada, in *Arctic Geology and Geophysics*, edited by A. F. Embry, and H. R. Balkwill, *Mem. Can. Soc. Pet. Geol.*, 8, 233–244.
- Ljones, F., A. Kuwano, R. Mjelde, A. Breivik, H. Shimamura, Y. Murai, and Y. Nishimura (2004), Crustal transect from the North Atlantic Knipovich Ridge to the Svalbard Margin west of Hornsund, *Tectonophysics*, 378, 17–41.
- Lutter, W. J., and R. L. Nowack (1990), Inversion for crustal structure using reflections from the PASSCAL Ouachita experiment, *J. Geophys. Res.*, 95(B4), 4633–4646, doi:10.1029/JB095iB04p04633.
- Mjelde, R., T. Raum, B. Myhren, H. Shimamura, Y. Murai, T. Takanami, R. Karpuz, and U. Næss (2005), Continent-ocean transition on the Vøring Plateau, NE Atlantic, derived from densely sampled ocean bottom seismometer data, *J. Geophys. Res.*, 110, B05101, doi:10.1029/2004JB003026.
- Mutter, J. C., M. Talwani, and P. L. Stoffa (1984), Evidence for a thick oceanic crust adjacent to the Norwegian margin, *J. Geophys. Res.*, 89, 483–502.
- Oakey, G. N. (2005), Cenozoic evolution and lithosphere dynamics of the Baffin Bay-Nares Strait region of Arctic Canada and Greenland, PhD thesis, Vrije Universiteit, Amsterdam.
- Oakey, G. N., and J. A. Chalmers (2012), A new model for the Paleogene motion of Greenland relative to North America: Plate reconstructions of the Davis Strait and Nares Strait regions between Canada and Greenland, *J. Geophys. Res.*, 117, B10401, doi:10.1029/2011JB008942.
- Reid, I., and H. R. Jackson (1997), Crustal structure of the northern Baffin Bay: Seismic refraction results and tectonic implications, *J. Geophys. Res.*, 102, 523–542, doi:10.1029/96JB02656.
- Ross, D. I., and G. Henderson (1973), New geophysical data on the continental shelf of central and northern west Greenland, *Can. J. Earth Sci.*, 10, 485–497.
- Sandwell, D. T., R. D. Müller, W. H. F. Smith, E. Garcia, and R. Francis (2014), New global marine gravity model from CryoSat-2 and Jason-1 reveals buried tectonic structure, *Science*, 346, 65–67, doi: 10.1126/science.1258213.
- Schlindwein, V., and W. Jokat (1999), Structure and evolution of the continental crust of northern east Greenland from integrated geophysical studies, *J. Geophys. Res.*, 104(B4), 15,227–15,245, doi:10.1029/1999JB900101.
- Skaarup, N., H. R. Jackson, and G. Oakey (2006), Margin segmentation of Baffin Bay/Davis Strait, eastern Canada based on seismic reflection and potential field data, *Mar. Pet. Geol.*, 23, 127–144, doi:10.1016/j.marpetgeo.2005.06.002.
- Srivastava, S. P. (1978), Evolution of the Labrador Sea and its bearing on the early evolution of the North Atlantic, *Geophysical Journal of the Royal Astronomical Society*, 52, 313–357, doi:10.1111/j.1365-246X.1978.tb04235.x.

Storey, M., R. A. Duncan, A. K. Pedersen, L. M. Larsen, and H. C. Larsen (1998), $^{40}\text{Ar}/^{39}\text{Ar}$ geochronology of the West Greenland Tertiary volcanic province, *Earth Planet. Sci. Lett.*, 160, 569–586, doi:10.1016/S0012-821X(98)00112-5.

Suckro, S. K., K. Gohl, T. Funck, I. Heyde, A. Ehrhardt, B. Schreckenberger, J. Gerlings, V. Damm, and W. Jokat (2012), The crustal structure of southern Baffin Bay: Implications from a seismic refraction experiment, *Geophys. J. Int.*, 190, 37–58, doi:10.1111/j.1365-246X.2012.05477.x.

White, R. and D. McKenzie (1989), Magmatism at rift zones: the generation of volcanic continental margins and flood basalts, *J. Geophys. Res.*, 94, 7685–7729.

White, R. S., D. McKenzie, and R. K. O’Nions (1992), Oceanic crustal thickness from seismic measurements and rare Earth element inversion, *J. Geophys. Res.*, 97, 19,683–19,715, doi:10.1029/92JB01749.

Whittaker, R. C., N. E. Hamann, and T. C. R. Pulvertaft (1997), A new frontier province offshore northern West Greenland: Structure, basin development and petroleum potential of the Melville Bay area, *AAPG Bull.*, 81, 979–998.

Zelt, C. A., and R. B. Smith (1992), Seismic traveltimes inversion for 2-D crustal velocity structure, *Geophys. J. Int.*, 108, 16–34, doi:10.1111/j.1365-246X.1992.tb00836.x.

7 Conclusion

This thesis provided detailed new insights into the crustal structure of Baffin Bay and southern Nares Strait. A summary of the major results of the three publications is provided in this chapter. All research questions listed in chapter 1.4 will be answered.

What kind of crust is present in the Melville Bay area? How is the crustal structure composed? How thick is the crust?

The two parallel refraction seismic profiles AWI-20100200 (north) and AWI-20100450 (south) revealed that the crust in the Melville Bay area consists of stretched and rifted, up to three-layered continental crust, which is separated from the oceanic crust in central Baffin Bay by a 60 to 80 km wide COT.

The crystalline continental crust is up to 30 km thick and the crustal velocities range between 5.5 and 6.9 km/s. The maximum depth of the Moho is 26 km in the northern and 33 km in the southern part of the Melville Bay.

How is the infill of the basins within Melville Bay characterized? Can we detect major differences between the crustal structure of northern and southern Melville Bay?

Deep basins and steep faults are present within the crust of the Melville Bay. The deepest basin along both profiles in the Melville Bay area is the Melville Bay Graben, which has a depth of up to 11 km. It contains an infill composed of sediments, sedimentary rocks, and presumably also basalts. The lowermost infill of the Melville Bay Graben is characterized by unusual high velocities of up to 5.2 km/s in southern and up to 4.9 km/s in northern Baffin Bay. The high velocities can be the result of compacted and already metamorphosed sediments and/or basaltic layers. The infill of the shallower Kivioq Basin west of the Melville Bay Ridge has been modeled with velocities of 1.6 to 4.7 km/s along AWI-20100200.

The crustal geometry and the sedimentary composition in the Melville Bay area changes from the north to the south: In the Melville Bay, the greatest Moho depth is present under different structures: along profile AWI-20100450 in southern Melville Bay, the greatest Moho depth is present below the Melville Bay Ridge. Along the northern profile AWI-20100200, the Moho underneath the Melville Bay Graben and the Kivioq Ridge is located at greater depth than underneath the Melville Bay Ridge. Additionally, some sediment layers which are present in northern Melville Bay Graben are absent in southern Melville Bay Graben or are too thin to be detected. Further, a low velocity zone is present in the sedimentary cover of the southern COT, which has not been observed in our northern profile AWI-20100200. Therefore, the genesis of northern and southern Melville Bay area differs in terms of basin development and sedimentary deposition.

What type of margin is present in the Melville Bay area? How is the transition between assumed oceanic and continental crust in the Smith Sound characterized? What type of margin is present?

The COT at the Melville Bay margin has been affected by magmatism, which is extrusive along the northern profile and intrusive along the southern profile.

The magmatic influence decreases towards the north, since no signs of magmatism have been identified at the COT in the Smith Sound area. Clear indications for a volcanic margin, like SDRs or magmatic underplating, are absent. However, typical characteristics of a non-volcanic margin, like a lower crust composed of serpentized upper mantle in the COT, or weak or absent Moho reflections, have not been observed. A certain division in a volcanic- and non-volcanic style margin is therefore not possible and the margin can be described best as rifted margin with decreasing influence of magmatism towards the north.

Is oceanic crust present in central northern Baffin Bay? If so, how is it characterized? Does the crustal structure provide indications for the genesis of the region?

My models confirm that a partly abnormally thin, oceanic crust is present in northern and central Baffin Bay. Its velocity structure and thickness (3.5 to 7 km thick) is highly variable and differs from “normal” Atlantic oceanic crust of White et al. (1992). Especially oceanic layer 3 is in great parts thinner and characterized by much lower velocities than average Atlantic oceanic crust.

The unusually thin, oceanic crust and the underlying serpentized upper mantle with velocities of >7.6 km/s are an indication for slow to ultraslow spreading rates during the formation of the oceanic crust. Since no clear spreading anomalies and therefore no explicit dating of the oceanic crust is possible in the Baffin Bay, this observation contributes to the understanding of the formation of the oceanic crust and genesis of the region.

The fact that the working area in northern Baffin Bay is underlain by thinner oceanic crust than southern Baffin Bay can be explained by a decreased magma supply with increasing distance to the proposed Iceland mantle plume.

In the velocity models of profiles of AWI-20100200 and AWI-20100300, changes in crustal velocity within the lowermost oceanic crust occur close to the proposed boundary between Paleocene and Eocene oceanic crust after the map of Oakey and Chalmers (2012). Unfortunately I could neither confirm nor disprove that these changes in the crustal structure are characteristic for Paleocene or Eocene oceanic crust, since a fracture zone present in this area can also cause these changes.

What is the extent of different crustal types in Northeastern Baffin Bay? Do my results confirm previous models about the extent of crustal types in Baffin Bay?

Based on the three refraction seismic profiles, the extent of the different crustal types was investigated. In comparison with previous studies, the extent of oceanic crust towards the east was either underestimated (Oakey and Chalmers, 2012) or partly overestimated (Hosseinpour et al., 2013). Also, the COT covers a much larger area than postulated by Oakey and Chalmers (2012). The results of this study can now be taken as basis for future plate tectonic models.

8 Outlook

After summarizing the new insights I gained during my thesis, I would like to focus on the still remaining and newly aroused research questions for the Baffin Bay and Nares Strait and how they could be addressed in the future.

The main uncertainties in the geological setting of the Baffin Bay are the lack of dated oceanic crust and sedimentary sequences, as well as the lack of insight into the crustal structure of the Canadian part of the Baffin Bay.

Due to missing clear spreading anomalies in northern Baffin Bay, drilling is the only possibility to determine of the age of the oceanic crust, the onset of spreading and thereby the spreading rates. Additionally, deep drilling of sediments within the northern and southern Melville Bay Graben would reveal the age and composition of the infill and provide new insights into the timing of basin development. But because of the rough weather conditions in the arctic region and the high costs for drilling operations, scientific drilling in the Baffin Bay will probably not take place within the next years. Since the oil industry is exploring the Melville Bay area, acquisition of well data within the sedimentary successions is more likely to be achieved than drilling the oceanic crust in northern Baffin Bay within the next years.

However, other aspects than the age determination can be investigated in the Baffin Bay. Unfortunately, the Canadian part of central Baffin Bay has not yet been examined by modern refraction seismic data. Therefore, further research work should concentrate on this area. I propose to acquire 4 new refraction and reflection seismic profiles together with gravity data in the Canadian part of Baffin Bay.

Extent of crustal types in the Canadian part of Baffin Bay

My results show that the extent of oceanic crust and especially of the COT is underestimated in many plate tectonic models of the Baffin Bay. However, I did not calculate a new plate tectonic model for the Baffin Bay, since the extent of crustal types at the central part of the conjugate Canadian continental margin has never been examined with refraction seismic data. However, knowledge about the extent of crustal types in the Canadian Baffin Bay is essential for reliable plate tectonic modeling. The onset of crustal types in the Canadian part of central Baffin Bay can be studied with profiles C and D, which examine the conjugate margins of the Melville Bay area, where profile AWI-20100200 and AWI-20100450 are located. Profile A additionally provides insights into the crustal types of the northern Baffin Bay.

Position of the Paleocene Spreading Axis

Another important aspect for new kinematic modeling is the location of the Paleocene spreading ridge, which position is in contrast to the Eocene spreading ridge not indicated by gravity data. Therefore the underestimated extent of oceanic and transitional crust in the Greenlandic part of the Baffin Bay could also be the result of a wrong position of the spreading center, which would cause a misidentification of oceanic crust. The profiles C and D are nearly aligned perpendicular to the assumed Paleocene spreading axis and therefore perfect to study this subject.

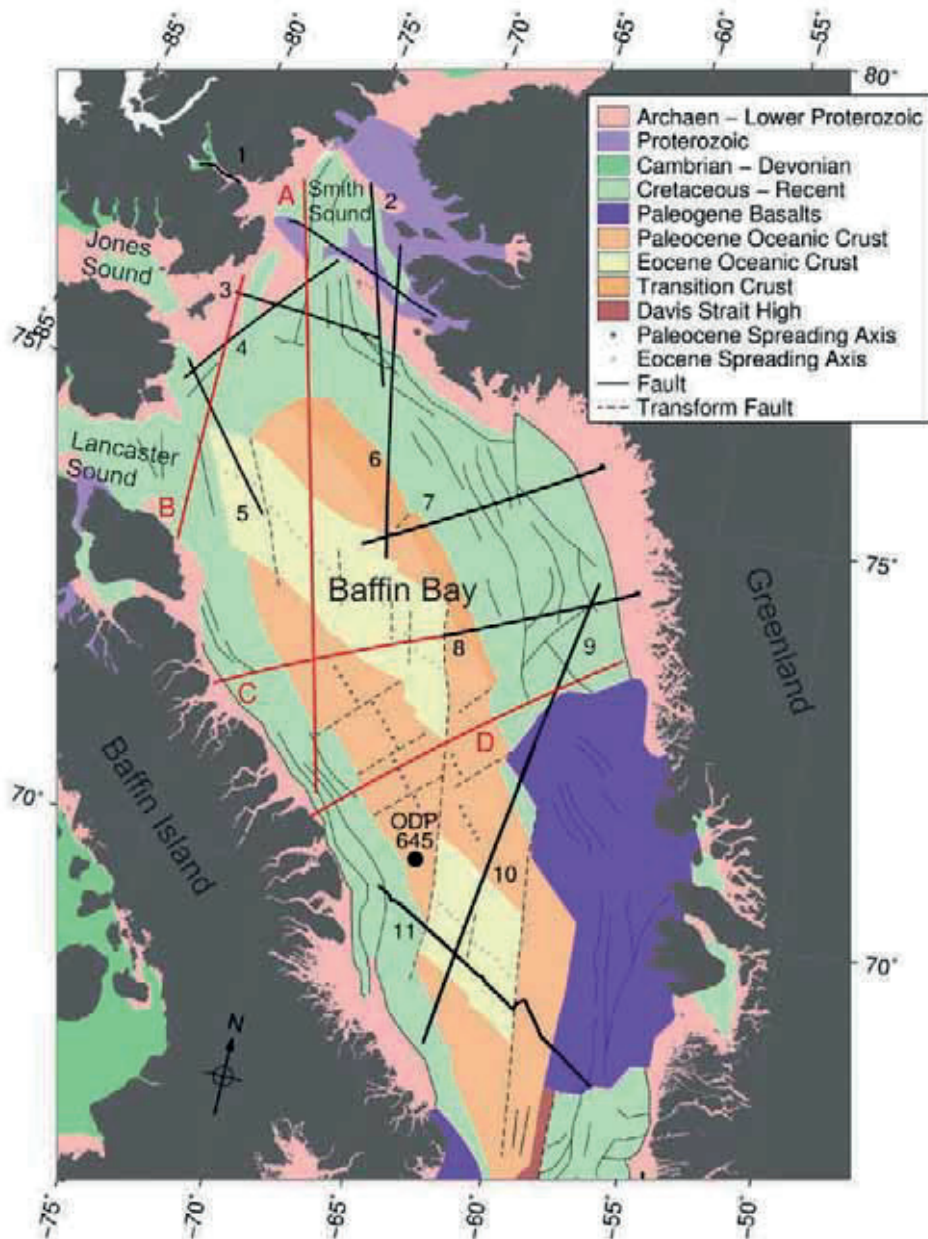


Figure 8.1: Geological map, modified after Oakey and Chalmers (2012), with proposed location of new refraction seismic profiles (red lines). Black lines with numbers mark the position of refraction seismic profiles: 1: line 3 (Funck et al., 2006); 2: profile 91/3 (Jackson and Reid, 1994); 3: profile 91/2 (Reid and Jackson, 1997); 4: profile 91/1 (Jackson and Reid, 1994); 5: profile 91/4 (Reid and Jackson, 1997); 6: profile AWI-20100300 (this thesis); 7: profile AWI-20100200, (this thesis); 8: AWI_20100450 (this thesis); 9: profile AWI-20100400 (Suckro et al., 2012); 10: profile AWI-20080500 (Suckro et al., 2012); 11: profile AWI-20080600 (Funck et al., 2012). Profile A extends in a NNW-SSE-direction. It starts in the southern Nares Strait, where it intersects three older refraction seismic profiles in its northern part and the proposed Profile C in the southern part. It crosses the Eocene oceanic crust perpendicular to the proposed spreading axis and ends at the Canadian margin. Profile B covers the area east of the Lancaster Sound and Smith Sound and extents in a N-S direction. Profile C is a prolongation the profile AWI-20100450. Together with the older profile, it provides a complete transect from the Canadian to the Greenlandic shelf. Profile D also provides a SW-NE transect through Baffin Bay.

Type of margin east of Baffin Island

Another aspect for further research should be the type of margin along western Baffin Bay. The margin at the Melville Bay area does not show characteristics typical for volcanic or non-volcanic margins. Are clear indications for the type of margin also missing at the conjugate margins east of Baffin Island? The profiles C and D cover the conjugate margins of profiles AWI-20100200 and AWI-20100450 and are therefore an ideal location to investigate similarities and differences. This can provide further insight into the initial separation between Canada and Greenland.

Differences between Eocene and Paleocene oceanic crust

My studies indicate differences in the crustal structure of Paleocene and Eocene oceanic crust. However, it is unclear if these differences are caused by a different genesis or composition of the oceanic crust or by nearby fracture zones. Since the profiles only cover the outer part of the oceanic crust, which is probably to a great amount composed of Paleocene oceanic crust, further attention should be drawn to the crustal fabric of Eocene oceanic crust in Baffin Bay. Profile A extends perpendicular to the assumed Eocene oceanic crust and located far away from assumed transform faults. It is therefore perfect to study the fabric of Eocene crust and also crosses the older, Paleocene crust. Profiles C and D will also provide insights in the crustal structure of Paleocene and Eocene oceanic crust.

Location of extinct spreading ridge axis and the Wegener Fault

After the map of Oakey and Chalmers (2012) (Figure 8.1), the northernmost part of the extinct Eocene spreading axis might be present in the Lancaster Sound. Tessensohn et al. (2006) propose that a connection between the spreading center in the Baffin Bay and a possible landward continuation of the Wegener Fault Zone might be located in the Smith Sound east of Grise fjord (Figure 1.6). Profile B is located east and close to the onset of the Lancaster Sound and Jones Sound. Based on this profile the position of extinct spreading centers and deep faults, which may be present in this area, can be determined. These findings would help us to better understand the motion of Greenland relative to North America and would contribute to solve the mystery of the Wegener Fault.

Bibliography

Altenbernd, T., W. Jokat, I. Heyde, and V. Damm (2014), A crustal model for northern Melville Bay, Baffin Bay, *J. Geophys. Res.*, 119, 8610–8632, doi:10.1002/2014JB011559.

Altenbernd, T., W. Jokat, I. Heyde, and V. Damm, submitted, Insights in the crustal structure of the transition between Nares Strait and Baffin Bay, submitted to *Tectonophysics* in June 2015.

Barton, P. (1986), The relationship between seismic velocity and density in continental crust—a useful constraint?, *Geophys. J. Roy. Astron. Soc.*, 87, 195–208.

Bown, J.W., and White, R. S. (1994), Variation with spreading rate of oceanic crustal thickness and geochemistry, *Earth Planet. Sci. Lett.*, 121, 435–449, doi:10.1016/0012-821X(94)90082-5.

Chalmers, J. A. (1997), The continental margin off southern Greenland: Along-strike transition from an amagmatic to a volcanic margin, *J. Geol. Soc. London*, 154, 571–576, doi:10.1144/gsjgs.154.3.0571.

Chalmers, J. A., and K. Laursen (1995), Labrador Sea: the extent of continental and oceanic crust and the timing of the onset of seafloor spreading, *Mar. Petrol. Geol.*, 12, 205–217, doi:10.1016/0264-8172(95)92840-S.

Chalmers, J. A., and G. N. Oakey (2007), Cretaceous-Palaeogene development of Labrador Sea and Davis Strait, *Geophys. Res. Abstr.*, 9, 01638.

Chalmers, J. A., and T. C. R. Pulvertaft (2001), Development of the continental margins of the Labrador Sea: A review, in *Non-Volcanic Rifting of Continental Margins: A Comparison of Evidence From Land and Sea*, edited by R. C. L. Wilson et al., *Geol. Soc. Spec. Publ.*, 187, 77–105, doi:10.1144/GSL.SP.2001.187.01.05.

Chalmers, J. A., T. C. R. Pulvertaft, F. G. Christiansen, H. C. Larsen, K. H. Laursen and T.G. Ottesen (1993), The southern West Greenland continental margin: rifting history, basin development, and petroleum potential. In: Parker, J.R. (ed), *Petroleum Geology of Northwest Europe: Proceedings of the 4th Conference*, *Geol. Soc. London*, 915–931.

Chen, Y. (1992), Oceanic crustal thickness versus spreading rate, *Geophys. Res. Lett.*, 19, 743–756, doi:10.1029/92GL00161.

Chian, D., and K. Loudon (1992), The structure of Archean-Ketilidian crust along the continental shelf of southwestern Greenland from a seismic refraction profile, *Can. J. Earth Sci.*, 29, 301–313.

Chian, D., and K. E. Loudon (1994), The continent-ocean crustal transition across the southwest Greenland margin, *J. Geophys. Res.*, 99, 9117–9135, doi:10.1029/93JB03404.

Chian, D., K. E. Loudon, and I. Reid (1995a), Crustal structure of the Labrador Sea conjugate margin and implications for the formation of non-volcanic continental margins, *J. Geophys. Res.*, 100, 239–24, 253, doi:10.1029/95JB02162.

Chian, D., K. E. Loudon, and I. Reid (1995b), Crustal structure of the Labrador Sea conjugate margin and implications for the formation of nonvolcanic continental margins, *J. Geophys. Res.*, 100, 24239–24253.

Chian, D., K. E. Loudon, T. A. Minshall, and R. B. Whitmarsh (1999), Deep structure of the ocean-continent transition in the southern Iberia Abyssal Plain from seismic refraction profiles: Ocean Drilling Program (Legs 149 and 173) transect, *J. Geophys. Res.*, 104, 7443–7462.

Damm, V. (2010), The Expedition of the Research Vessel "Polarstern" to the Arctic in 2010 (ARK-XXV/3), *Berichte zur Polar- und Meeresforschung*, 621, 234 pp., Alfred Wegener Inst. for Polar and Mar. Res., Bremerhaven, Germany.

Dawes, P. R. (1997), The Proterozoic Thule Supergroup, Greenland and Canada: history, lithostratigraphy and development, *Geol. Greenl. Surv. Bull.*, 174, 150 pp.

Dawes, P. R. (2009), Precambrian–Palaeozoic geology of Smith Sound, Canada and Greenland: key constraint to palaeogeographic reconstructions of northern Laurentia and the North Atlantic region, *Terra Nova* 21(1), 1–13, doi: 10.1111/j.1365-3121.2008.00845.x.

Dean, S. M., T. A. Minshull, R. B. Whitmarsh, and K. E. Loudon (2000), Deep structure of the ocean-continent transition in the southern Iberia Abyssal Plain from seismic refraction profiles: The IAM-9 transect at 40°20'N, *J. Geophys. Res.*, 105, 5859–5886.

Ehlers, B. M., and W. Jokat (2009), Subsidence and crustal roughness of ultra-slow spreading ridges in the northern North Atlantic and the Arctic Ocean, *Geophys. J. Int.*, 177, 451–462, doi:10.1111/j.1365-246X.2009.04078.x.

Eldholm, O., J. Thiede, and E. Taylor (1987), Evolution of the Norwegian continental margin: Background and objectives, *Proc. Ocean Drill. Program Initial Rep. part A*, 104, 5–25.

Elliott, G. M., C. Berndt, and L. M. Parson (2009), The SW African volcanic rifted margin and the initiation of the Walvis Ridge, South Atlantic, *Marine Geophys. Res.*, 30(3), 207–214, doi 10.1007/s11001-009-9077-x.

Frisch, T., and P. R. Dawes (1982), The Precambrian Shield of northernmost Baffin Bay: correlation across Nares Strait, *Medd. Grønland, Geosci.*, 8, 79–88.

Frisch, T., and P. R. Dawes (2014), The rotations opening the Central and Northern Atlantic Ocean: compilation, drift lines, and flow lines, *Int. J. Earth Sci.*, 103, 967–969, doi: 10.1007/s00531-013-0980-7.

Funck, T., and K. E. Loudon (1999), Wide-angle seismic transect across the Torngat Orogen, northern Labrador: Evidence for a Proterozoic crustal root, *J. Geophys. Res.*, 104, 7463–7480, doi:10.1029/1999JB900010.

Funck, T., J. R. Hopper, H. C. Larsen, K. E. Loudon, B. E. Tucholke, and W. S. Holbrook (2003), Crustal structure of the ocean-continent transition at Flemish Cap: Seismic refraction results, *J. Geophys. Res.*, 108, B11, 2531, doi:10.1029/2003JB002434.

Funck, T., H. R. Jackson, S. A. Dehler, and I. D. Reid (2006), A refraction seismic transect from Greenland to Ellesmere Island, Canada: The crustal structure in southern Nares Strait, *Polarforschung*, 74, 97–112.

Funck, T., H. Jackson, K. Loudon, and F. Klingelhöfer (2007), Seismic study of the transform-rifted margin in Davis Strait between Baffin Island (Canada) and Greenland: what happens when a plume meets a transform, *J. Geophys. Res.*, 112, B04402, doi:10.1029/2006JB004308.

Funck, T., K. Gohl, V. Damm, and I. Heyde (2012), Tectonic evolution of southern Baffin Bay and Davis Strait: Results from a seismic refraction transect between Canada and Greenland, *J. Geophys. Res.*, 117, B04107, doi:10.1029/2011JB009110.

Gerlings, J., T. Funck, H. Jackson, K. Loudon, and F. Klingelhöfer (2009), Seismic evidence for plume-derived volcanism during formation of the continental margin in southern Davis Strait and northern Labrador Sea, *Geophys. J. Int.*, 176, 980–994, doi:10.1111/j.1365-246X.2008.04021.x.

Gladchenko, T. P., J. Skogseid, and O. Eldholm (1998), Namibia volcanic margin, *Mar. Geophys. Res.*, 20, 313–341, doi:10.1023/A:1004746101320.

Gregersen, U., J. R. Hopper, and P. C. Knutz (2013), Basin seismic stratigraphy and aspects of prospectivity in the NE Baffin Bay, Northwest Greenland, *Mar. Pet. Geol.*, 46, 1–18, doi:10.1016/j.marpetgeo.2013.05.013.

Hansen, K., P. R. Dawes, T. Frisch, and P.K. Jensen (2011), A fission track transect across Nares Strait (Canada–Greenland): further evidence that the Wegener Fault is a myth, *Can. J. Earth Sci.*, 48, 819–840.

Harrison, J. C. (2006), In search of the Wegener Fault: re-evaluation of the strike-slip displacements along and bordering Nares Strait, *Polarforschung*, 74, 129–160.

Hermann, T. and Jokat, W. (2013), Crustal structure of the Boreas Basin and the Knipovich Ridge at 76° N in the North Atlantic, *Geophysical Journal International*, 193(3), 1399–1414, doi:10.1093/gji/ggt048.

Horen, H., M. Zamora, and G. Dubuisson (1996), Seismic waves velocities and anisotropy in serpentinized peridotites from Xigaze ophiolite: abundance of serpentine in slow spreading ridge, *Geophys. Res. Lett.*, 23(1), 9–12, doi:10.1029/95GL03594.

Hosseinpour, M., R. D. Müller, S. E. Williams and J. M. Whittaker (2013), Full-fit reconstruction of the Labrador Sea and Baffin Bay, *Solid Earth*, 4, 461–479, doi:10.5194/se-4-461-2013.

Jackson, H. R., K. Dickie, and F. Marillier (1992), A seismic reflection study of northern Baffin Bay: implication for tectonic evolution, *Can. J. Earth Sci.*, 29, 2353–2369.

Jackson, H. R., and I. Reid (1994), Crustal thickness variations between the Greenland and Ellesmere Island margins determined from seismic refraction, *Can. J. Earth Sci.*, 31, 1407–1418, doi:10.1139/e94-124.

Johnson, G. L., and Srivastava, S. P. (1982), The case for major displacement along Nares Strait, *Medd. Grønland, Geosci.*, 8, 365–368.

Jokat, W., and M. C. Schmidt-Aursch (2007), Geophysical characteristics of the ultra-slow spreading Gakkel Ridge, Arctic Ocean, *Geophys. J. Int.*, 168, 983–998, doi:10.1111/j.1365-246X.2006.03278.x.

Jokat, W., O. Ritzmann, M. C. Schmidt-Aursch, S. Drachev, S. Gauger, and J. Snow (2003), Geophysical evidence for reduced melt production on the Arctic ultraslow Gakkel mid-ocean ridge, *Nature*, 423, 962–965, doi:10.1038/nature01706.

Jokat, W., J. Kollofrath, W. Geissler, and L. Jensen (2012), Crustal thickness and earthquake distribution south of the Logachev Seamount, Knipovich Ridge, *Geophys. Res. Lett.*, 39, L08302, doi:10.1029/2012GL051199.

Keen, C., and D. Barrett (1972), Seismic refraction studies in Baffin Bay: An example of a developing ocean basin, *Geophys. J. R. Astron. Soc.*, 30, 253–271, doi:10.1111/j.1365-246X.1972.tb05812.x.

Keen, C. E., K. Dickie, and S. A. Dehler (2012), The volcanic margins of the northern Labrador Sea: Insights to the rifting process, *Tectonics*, 31, TC1011, doi:10.1029/2011TC002985.

Kerr, J. W. (1967), Nares submarine rift valley and the relative rotation of north Greenland, *Bull. Can. Petrol. Geol.*, 15, 483–520.

Klingelhöfer, F., L. Geli, L. Matias, N. Steinsland, and J. Mohr (2000), Crustal structure of a super-slow spreading centre: A seismic refraction study of Mohns Ridge, 72°N, *Geophys. J. Int.*, 141, 509–526, doi:10.1046/j.1365-246x.2000.00098.x.

Klose, G. W., E. Malterre, N. J. McMillan, and C. G. Zinkan (1982), Petroleum exploration offshore southern Baffin Island, northern Labrador Sea, Canada, in *Arctic Geology and Geophysics*, edited by A. F. Embry, and H. R. Balkwill, *Mem. Can. Soc. Pet. Geol.*, 8, 233–244.

Larsen, L. M., L. M. Heaman, R. A. Creaser, R. A. Duncan, R. Frei, and M. Hutchison (2009), Tectonommagmatic events during stretching and basin formation in the Labrador Sea and Davis Strait: Evidence from age and composition of Mesozoic to Palaeogene dyke swarms in West Greenland, *J. Geol. Soc.*, 166, 999–1012, doi:10.1144/0016-76492009-038.

Lau, K. W. H., K. E. Loudon, T. Funck, B. E. Tucholke, W. S. Holbrook, J. R. Hopper, and H. C. Larsen (2006), Crustal structure across the Grand Banks-Newfoundland Basin continental margin – I. Results from a seismic refraction profile, *Geophys. J. Int.*, 167, 127–156, doi:10.1111/j.1365-246X.2006.02988.x

Leinweber, V. T. (2011), *Geophysical study of the conjugate East African and East Antarctic margins*, PhD thesis, Universität Bremen.

Leinweber, V. T., F. Klingelhoefer, S. Neben, C. Reichert, D. Aslanian, L. Matias, I. Heyde, B. Schreckenberger, and W. Jokat (2013), The crustal structure of the Central Mozambique continental margin – wide-angle seismic, gravity and magnetic study in the Mozambique Channel, Eastern Africa, *Tectonophysics*, 599, 170–196, doi:10.1016/j.tecto.2013.04.015.

Ljones, F., A. Kuwano, R. Mjelde, A. Breivik, H. Shimamura, Y. Murai, and Y. Nishimura (2004), Crustal transect from the North Atlantic Knipovich Ridge to the Svalbard Margin west of Hornsund, *Tectonophysics*, 378, 17–41.

Lutter, W. J., and R. L. Nowack (1990), Inversion for crustal structure using reflections from the PASSCAL Ouachita experiment, *J. Geophys. Res.*, 95, B4, 4633–4646, doi:10.1029/JB095iB04p04633.

Mjelde, R., T. Raum, B. Myhren, H. Shimamura, Y. Murai, T. Takanami, R. Karpuz, and U. Næss (2005), Continent-ocean transition on the Vøring Plateau, NE Atlantic, derived from densely sampled ocean bottom seismometer data, *J. Geophys. Res.*, 110, B05101, doi:10.1029/2004JB003026.

Müller, R., M. Sdrolias, C. Gaina, and W. Roest (2008), Age, spreading rates, and spreading asymmetry of the world's ocean crust, *Geochem. Geophys. Geosyst.*, 9 (4), Q04006, doi:10.1029/2007GC001743.

Mutter, C. Z., and J. C. Mutter (1993), Variations in thickness of Layer 3 dominate oceanic crustal structure, *Earth and Planet. Sci. Lett.*, 117, 295–317, doi: 10.1016/0012-821X(93)90134-U.

Mutter, J. C., M. Talwani, and P. L. Stoffa (1984), Evidence for a thick oceanic crust adjacent to the Norwegian margin, *J. Geophys. Res.*, 89, 483–502.

Neben, S., V. Damm, T. Brent, and F. Tessensohn (2006), New Multichannel seismic reflection data from North Water Bay, Nares Strait: Indications for pull-apart tectonics, *Polarforschung*, 74, 77–96.

Oakey, G. N. (2005), *Cenozoic evolution and lithosphere dynamics of the Baffin Bay-Nares Strait region of Arctic Canada and Greenland*, PhD thesis, Vrije Universiteit, Amsterdam.

Oakey, G. N., and J. A. Chalmers (2012), A new model for the Paleogene motion of Greenland relative to North America: plate reconstructions of the Davis Strait and Nares Strait regions between Canada and Greenland, *J. Geophys. Res.*, 117, B10401, doi:10.1029/2011JB008942.

Reid, I., and H. R. Jackson (1997a), Crustal structure of the northern Baffin Bay: Seismic refraction results and tectonic implications, *J. Geophys. Res.*, 102, 523–542, doi:10.1029/96JB02656.

Reid, I., and H. Jackson (1997b), A review of three transform margins off eastern Canada, *Geo-Mar. Lett.*, 17(1), 87–93.

Reid, I., and H. R. Jackson (1981), Oceanic spreading rate and crustal thickness, *Mar. Geophys. Res.*, 5, 165–172.

Roest, W. R., and S. P. Srivastava (1989), Sea-floor spreading in the Labrador Sea: a new reconstruction, *Geology*, 17, 1000–1003, doi:10.1130/0091-7613(1989)017<1000:SFSITL>2.3.CO;2.

Ross, D. I., and G. Henderson (1973), New geophysical data on the continental shelf of central and northern west Greenland, *Can. J. Earth Sci.*, 10, 485–497.

Sandwell, D. T., R. D. Müller, W. H. F. Smith, E. Garcia, and R. Francis (2014), New global marine gravity model from CryoSat-2 and Jason-1 reveals buried tectonic structure, *Science*, 346, 65–67, doi: 10.1126/science.1258213.

Schindwein, V., and W. Jokat (1999), Structure and evolution of the continental crust of northern east Greenland from integrated geophysical studies, *J. Geophys. Res.*, 104(B4), 15,227–15,245, doi:10.1029/1999JB900101.

Skaarup, N., H. R. Jackson, and G. Oakey (2006), Margin segmentation of Baffin Bay/Davis Strait, eastern Canada based on seismic reflection and potential field data, *Mar. Petr. Geol.*, 23, 127–144, doi:10.1016/j.marpetgeo.2005.06.002.

Srivastava, S. P. (1978), Evolution of the Labrador Sea and its bearing on the early evolution of the North Atlantic, *Geophys. J. R. Astron. Soc.*, 52, 313–357, doi:10.1111/j.1365-246X.1978.tb04235.x.

Srivastava, S. P. (1985), Evolution of the Eurasian Basin and its implications to the motion of Greenland along Nares Strait, *Tectonophysics*, 114, 29–53.

Srivastava, S. P., and R. K. H. Falconer (1982), Nares Strait: a conflict between plate tectonic predictions and geological interpretation, *Medd. Grønland, Geosci.*, 8, 339–354.

Srivastava, S. P., and C. R. Tapscott (1986), Plate kinematics of the North Atlantic, in: *The Geology of North America, The Western North Atlantic Region*, Geological Society of America, M, 379–404.

Storey, M., R. A. Duncan, A. K. Pedersen, L. M. Larsen, and H.C. Larsen (1998), ⁴⁰Ar/³⁹Ar geochronology of the West Greenland Tertiary volcanic province, *Earth Planet. Sci. Lett.*, 160, 569–586, doi:10.1016/S0012-821X(98)00112-5.

Suckro, S. K., K. Gohl, T. Funck, I. Heyde, A. Ehrhardt, B. Schreckenberger, J. Gerlings, V. Damm and W. Jokat (2012), The crustal structure of southern Baffin Bay: implications from a seismic refraction experiment, *Geophys. J. Int.*, 190, 37–58, doi: 10.1111/j.1365-246X.2012.05477.x.

Suckro, S. K., K. Gohl, T. Funck, I. Heyde, B. Schreckenberger, J. Gerlings and V. Damm (2013), The Davis Strait crust - a transform margin between two oceanic basins, *Geophys. J. Int.*, 193, 78–97, doi: 10.1093/gji/ggs126.

Talwani, M., and O. Eldholm (1977), Evolution of the Norwegian-Greenland Sea, *Geol. Soc. Am. Bull.*, 88, 969–999, doi:10.1130/0016-7606(1977)88<969:EOTNS>2.0.CO;2

Taylor, F. B. (1910), Bearing on the Tertiary mountain belt on the origin of the earth's plan, *Bull. Geol. Soc. Amer.*, 21, 179–226.

Tessensohn, F., H. R. Jackson, and I. D. Reid (2006), The Tectonic Evolution of Nares Strait: Implications of New Data, *Polarforschung*, 74, 191–198.

Van Avendonk, H. J. A., W. S. Holbrook, G. T. Nunes, D. J. Shillington, B. E. Tucholke, K. E. Loudon, H. C. Larsen, and J. R. Hopper (2006), Seismic velocity structure of the rifted margin of the eastern Grand Banks of Newfoundland, Canada, *J. Geophys. Res.*, 111, B11404, doi:10.1029/2005JB004156.

Wegener, A. L. (1912), Die Entstehung der Kontinente, *Geol. Rundschau*, 3, 276–292.

Wegener, A. (1915), Die Entstehung der Kontinente und Ozeane, Friedrich Vieweg und Sohn, Braunschweig, 1–94.

White, R. and D. McKenzie (1989), Magmatism at rift zones: the generation of volcanic continental margins and flood basalts, *J. Geophys. Res.*, 94, 7685–7729.

White, R. S., D. McKenzie, and R. K. O’Nions (1992), Oceanic crustal thickness from seismic measurements and rare Earth element inversion, *J. Geophys. Res.*, 97, 19, 683–19, 715, doi:10.1029/92JB01749.

White, R. S., T. A. Minshull, M. J. Bickle, and C.J. Robinson (2001), Melt generation at very slow spreading oceanic ridges: Constraints from geochemical and geophysical data, *J. Petrol.*, 42, 1171–1196, doi:10.1093/petrology/42.6.1171.

Whittaker, R. C., N. E. Hamann, and T. C. R. Pulvertaft (1997), A new frontier province offshore northern West Greenland: structure, basin development and petroleum potential of the Melville Bay area, *AAPG Bull.*, 81, 979–998

Wilson, J. T. (1963), Hypothesis of Earth’s behavior, *Nature*, 198, 925–929, doi:10.1038/198925a0.

Zelt, C. A., and R. B. Smith (1992), Seismic travelttime inversion for 2-D crustal velocity structure, *Geophys. J. Int.*, 108, 16–34, doi:10.1111/j.1365-246X.1992.tb00836.x.

Appendix

Seismic sections, profile AWI-20100200

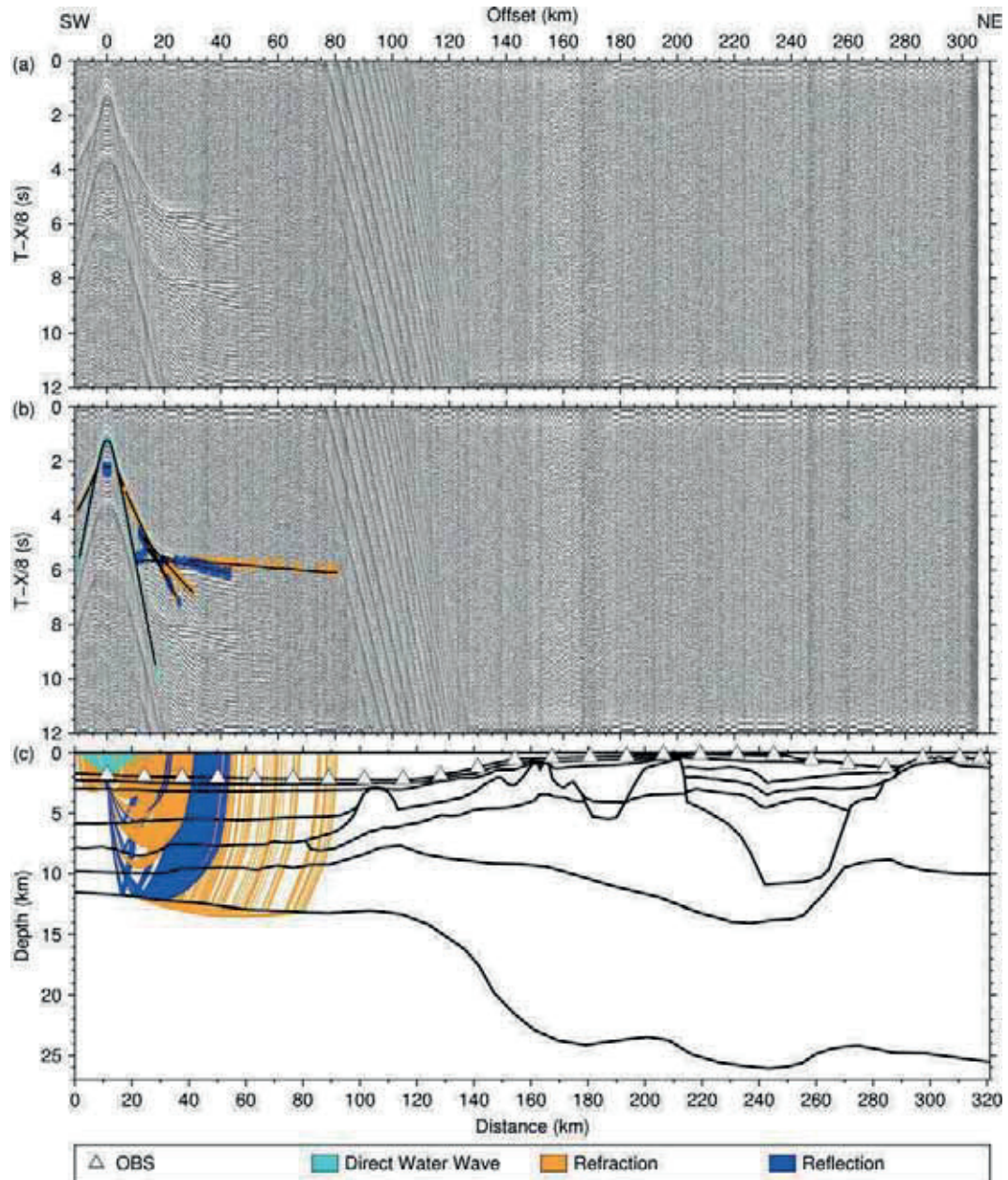


Figure A.1: Seismic section, picks and modeled raypaths of OBS 1 (AWI-20100200)

(a) Seismic section of the hydrophone component with a reduction velocity of 8 km/s.

(b) The colored lines mark the picked phases within the seismic section. The vertical lengths of the picks correspond to the assigned pick uncertainties. The black lines are the calculated travel times.

(c) The black lines are the boundaries between different velocity layers of the *P* wave velocity model. The colored lines mark the modeled raypaths of the corresponding picked phases shown in the panel above.

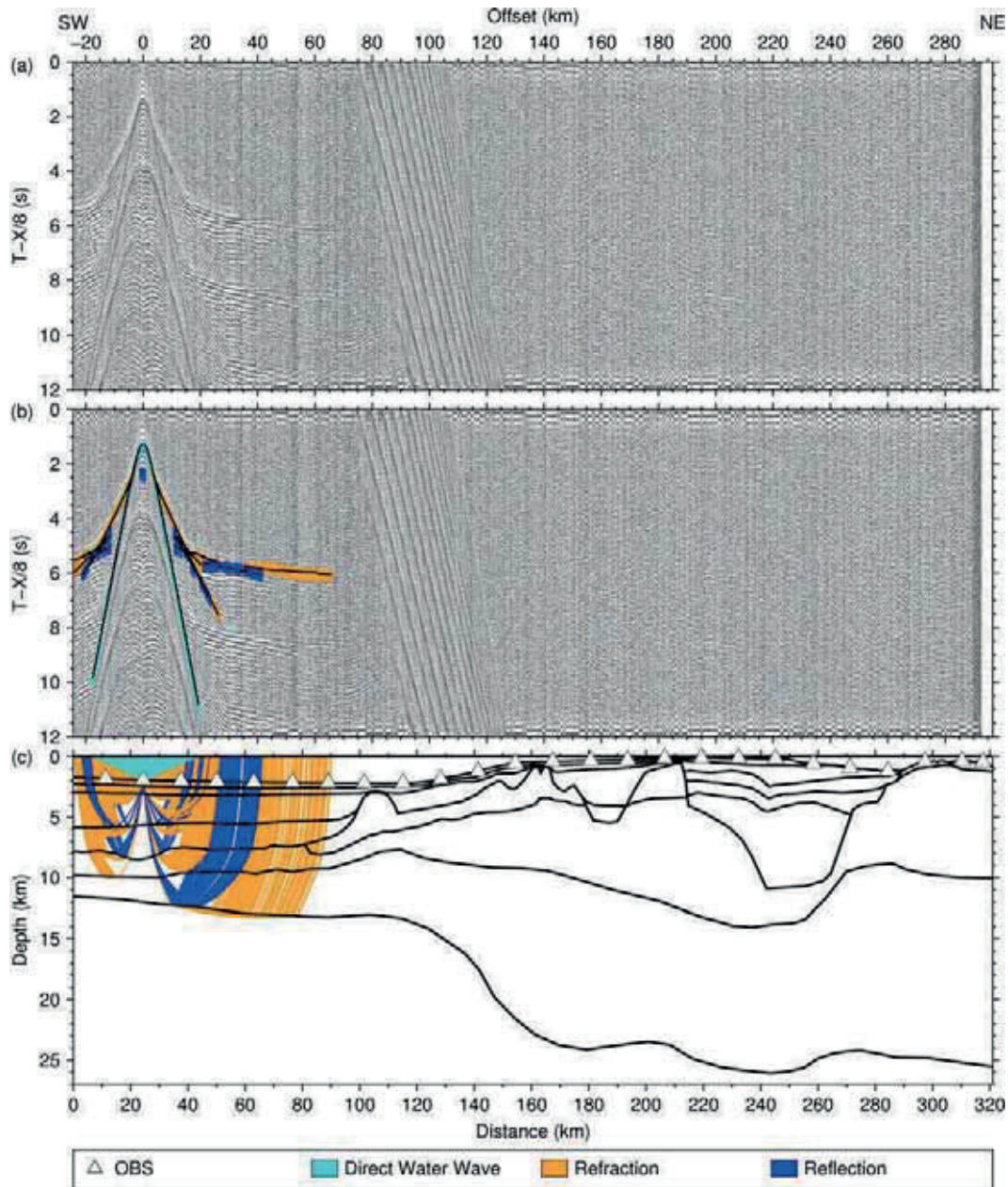


Figure A.2: Seismic section, picks and modeled raypaths of OBS 2 (AWI-20100200)

(a) Seismic section of the hydrophone component with a reduction velocity of 8 km/s.

(b) The colored lines mark the picked phases within the seismic section. The vertical lengths of the picks correspond to the assigned pick uncertainties. The black lines are the calculated travel times.

(c) The black lines are the boundaries between different velocity layers of the *P* wave velocity model. The colored lines mark the modeled raypaths of the corresponding picked phases shown in the panel above.

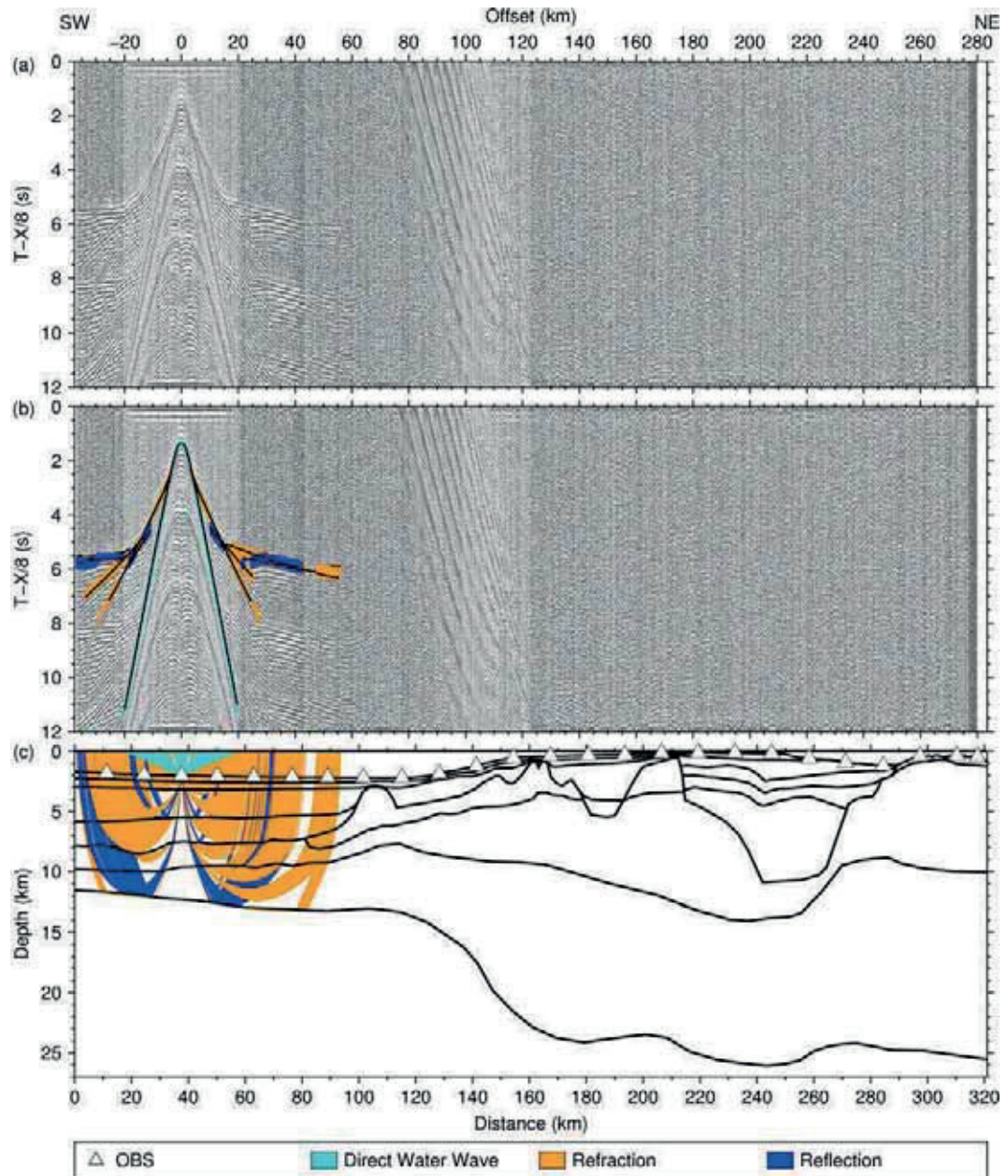


Figure A.3: Seismic section, picks and modeled raypaths of OBS 3 (AWI-20100200)
 (a) Seismic section of the hydrophone component with a reduction velocity of 8 km/s.
 (b) The colored lines mark the picked phases within the seismic section. The vertical lengths of the picks correspond to the assigned pick uncertainties. The black lines are the calculated travel times.
 (c) The black lines are the boundaries between different velocity layers of the *P* wave velocity model. The colored lines mark the modeled raypaths of the corresponding picked phases shown in the panel above.

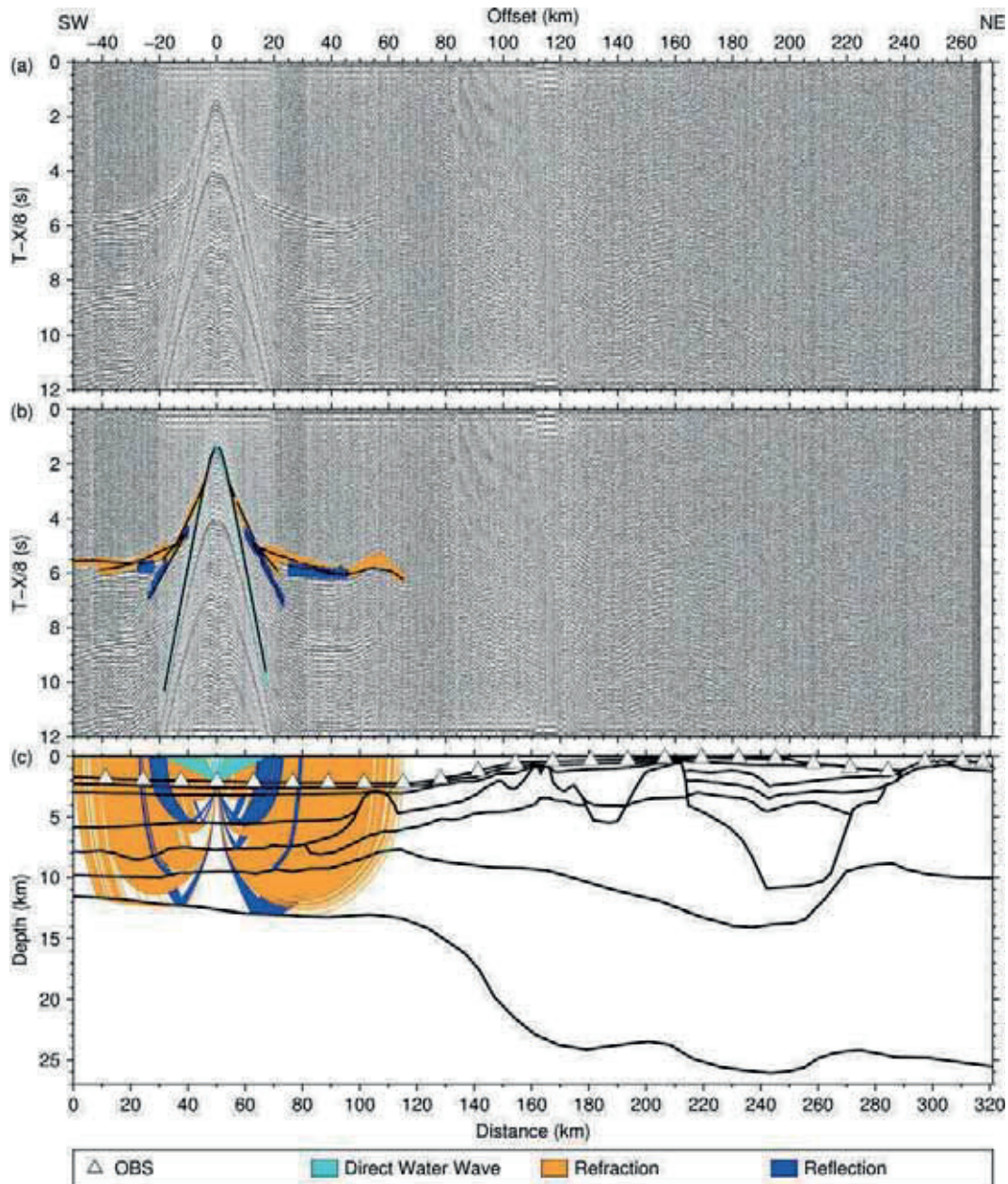


Figure A.4: Seismic section, picks and modeled raypaths of OBS 4 (AWI-20100200)

(a) Seismic section of the hydrophone component with a reduction velocity of 8 km/s.

(b) The colored lines mark the picked phases within the seismic section. The vertical lengths of the picks correspond to the assigned pick uncertainties. The black lines are the calculated travel times.

(c) The black lines are the boundaries between different velocity layers of the *P* wave velocity model. The colored lines mark the modeled raypaths of the corresponding picked phases shown in the panel above.

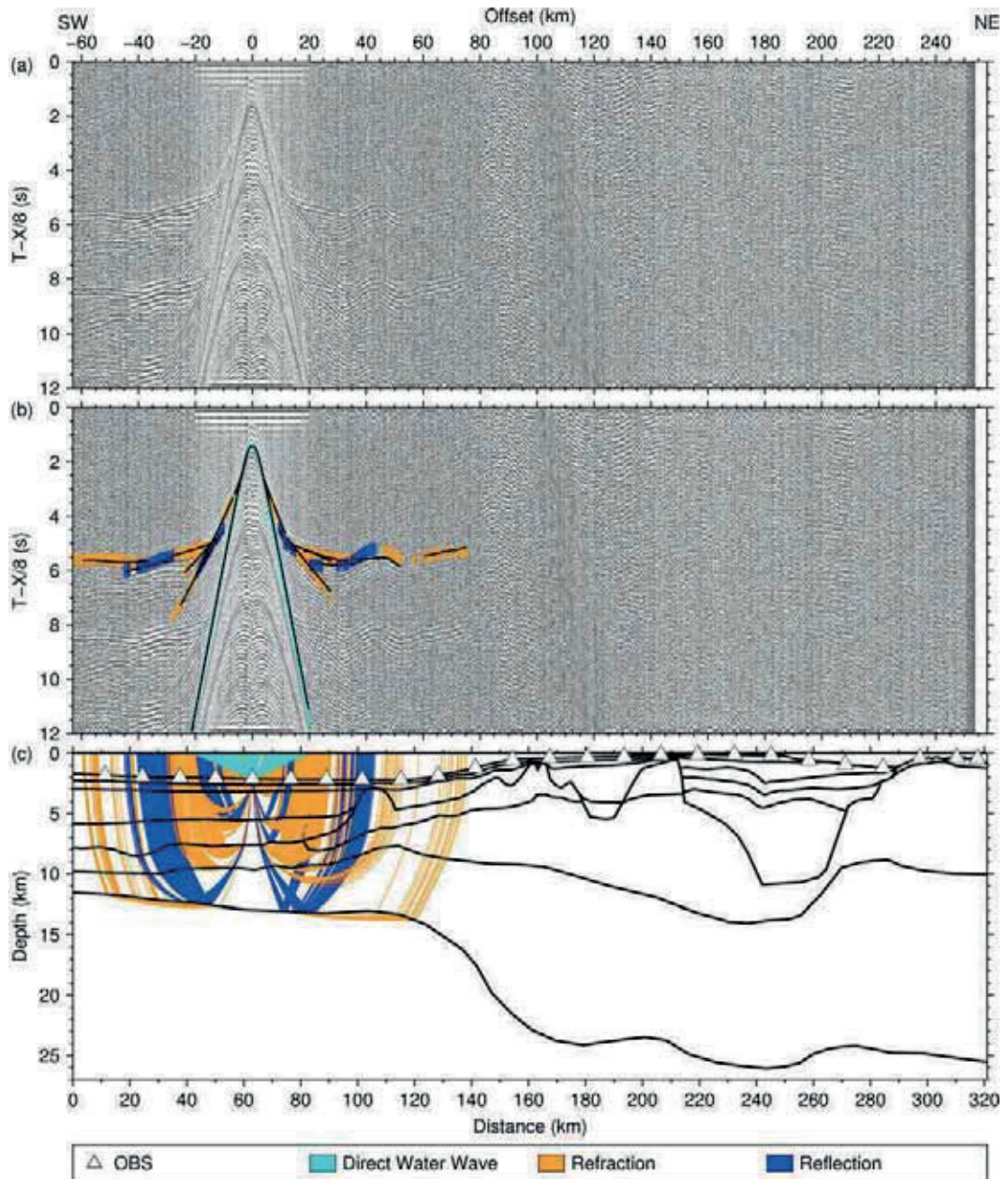


Figure A.5: Seismic section, picks and modeled raypaths of OBS 5 (AWI-20100200)
 (a) Seismic section of the hydrophone component with a reduction velocity of 8 km/s.
 (b) The colored lines mark the picked phases within the seismic section. The vertical lengths of the picks correspond to the assigned pick uncertainties. The black lines are the calculated travel times.
 (c) The black lines are the boundaries between different velocity layers of the *P* wave velocity model. The colored lines mark the modeled raypaths of the corresponding picked phases shown in the panel above.

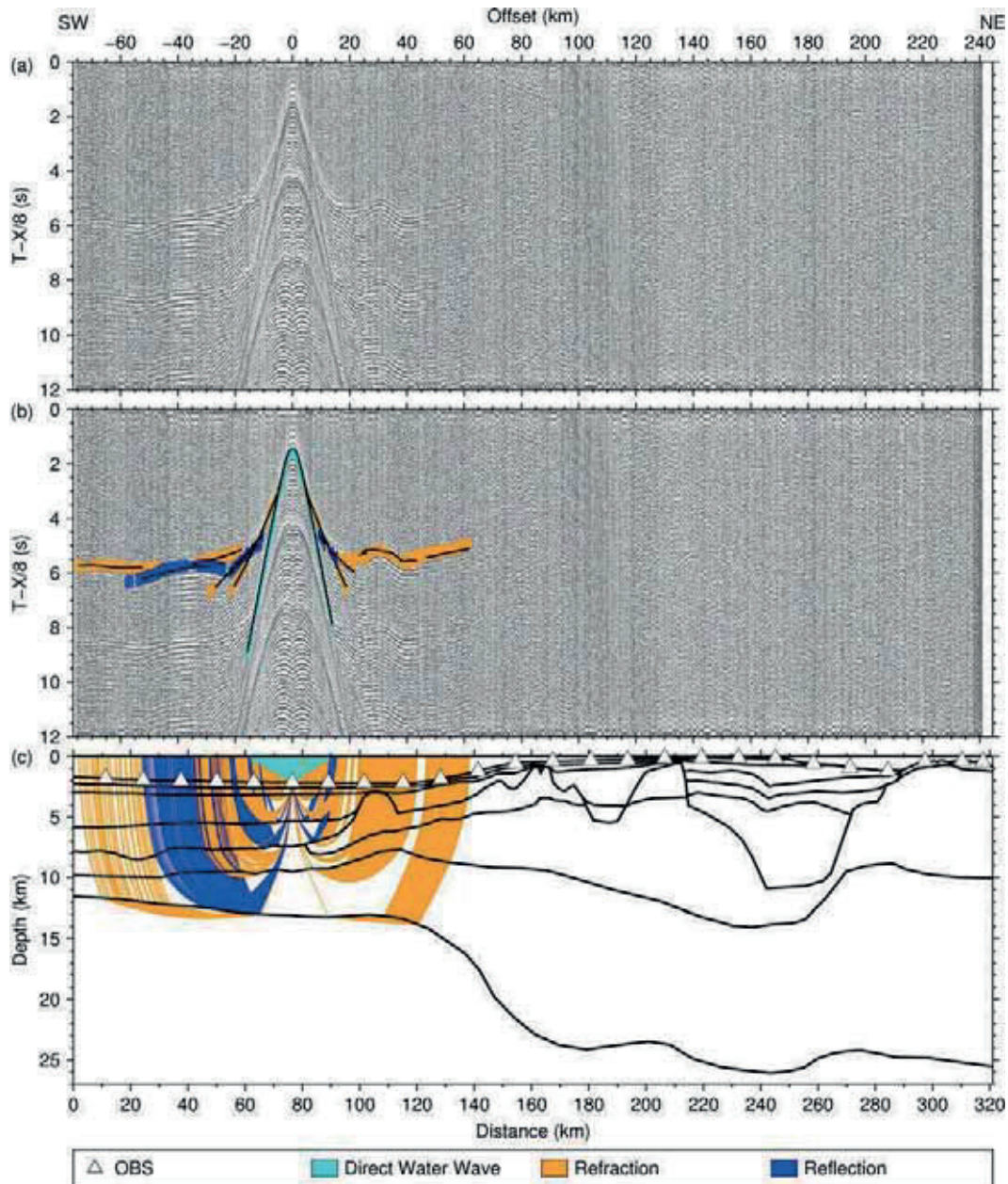


Figure A.6: Seismic section, picks and modeled raypaths of OBS 6 (AWI-20100200)

(a) Seismic section of the hydrophone component with a reduction velocity of 8 km/s.

(b) The colored lines mark the picked phases within the seismic section. The vertical lengths of the picks correspond to the assigned pick uncertainties. The black lines are the calculated travel times.

(c) The black lines are the boundaries between different velocity layers of the *P* wave velocity model. The colored lines mark the modeled raypaths of the corresponding picked phases shown in the panel above.

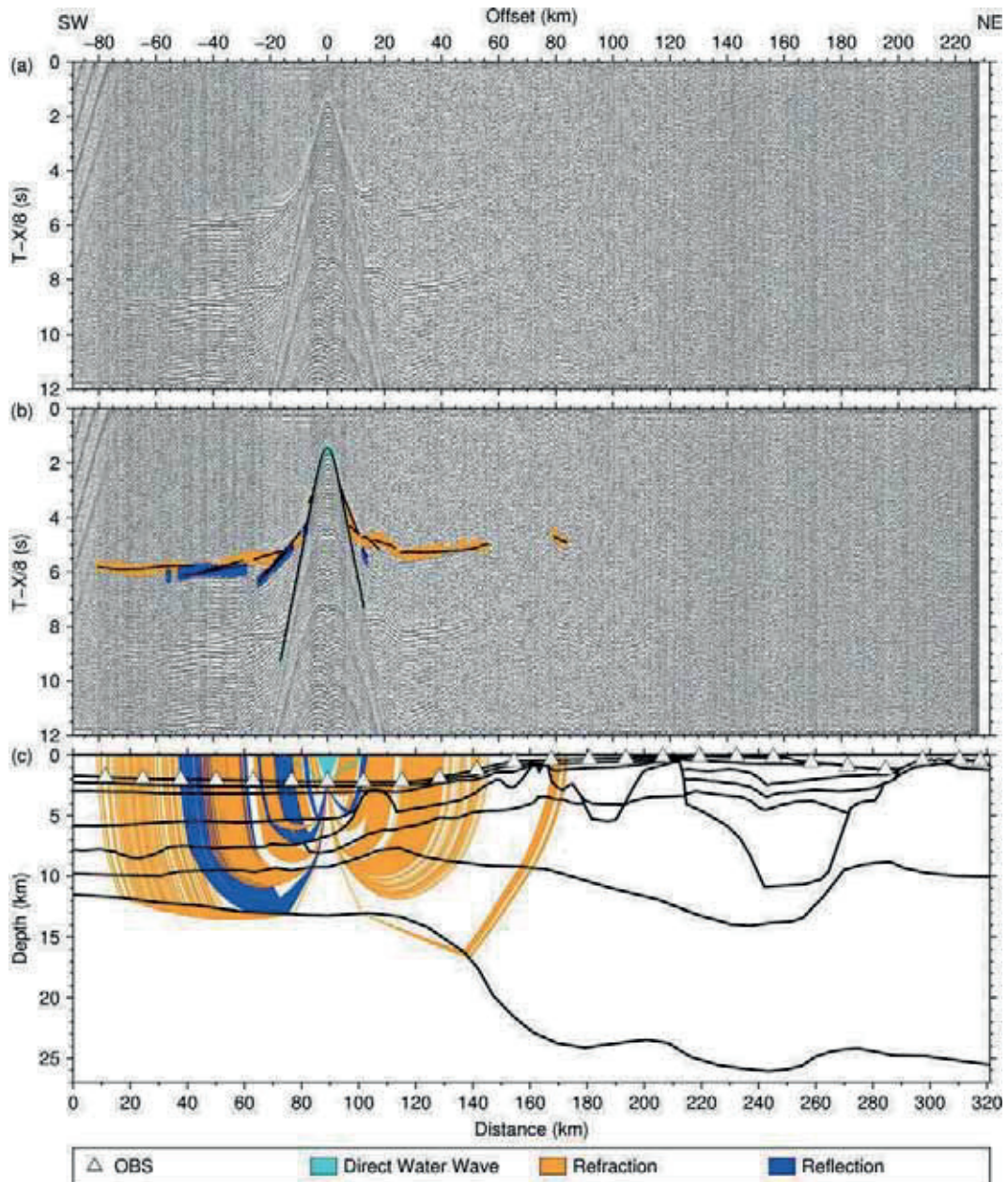


Figure A.7: Seismic section, picks and modeled raypaths of OBS 7 (AWI-20100200)

(a) Seismic section of the hydrophone component with a reduction velocity of 8 km/s.

(b) The colored lines mark the picked phases within the seismic section. The vertical lengths of the picks correspond to the assigned pick uncertainties. The black lines are the calculated travel times.

(c) The black lines are the boundaries between different velocity layers of the *P* wave velocity model. The colored lines mark the modeled raypaths of the corresponding picked phases shown in the panel above.

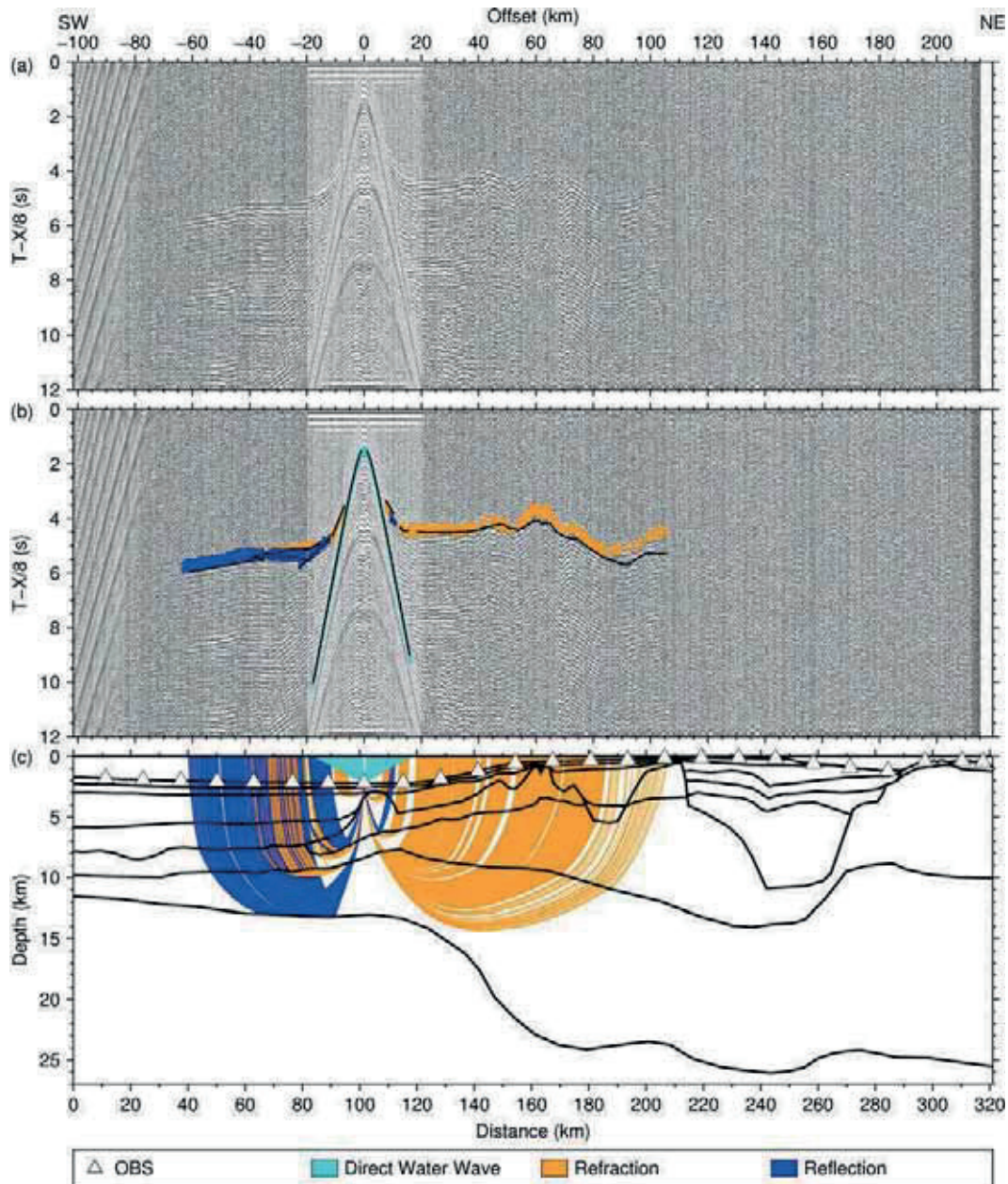


Figure A.8: Seismic section, picks and modeled raypaths of OBS 8 (AWI-20100200)

(a) Seismic section of the hydrophone component with a reduction velocity of 8 km/s.

(b) The colored lines mark the picked phases within the seismic section. The vertical lengths of the picks correspond to the assigned pick uncertainties. The black lines are the calculated travel times.

(c) The black lines are the boundaries between different velocity layers of the *P* wave velocity model. The colored lines mark the modeled raypaths of the corresponding picked phases shown in the panel above.

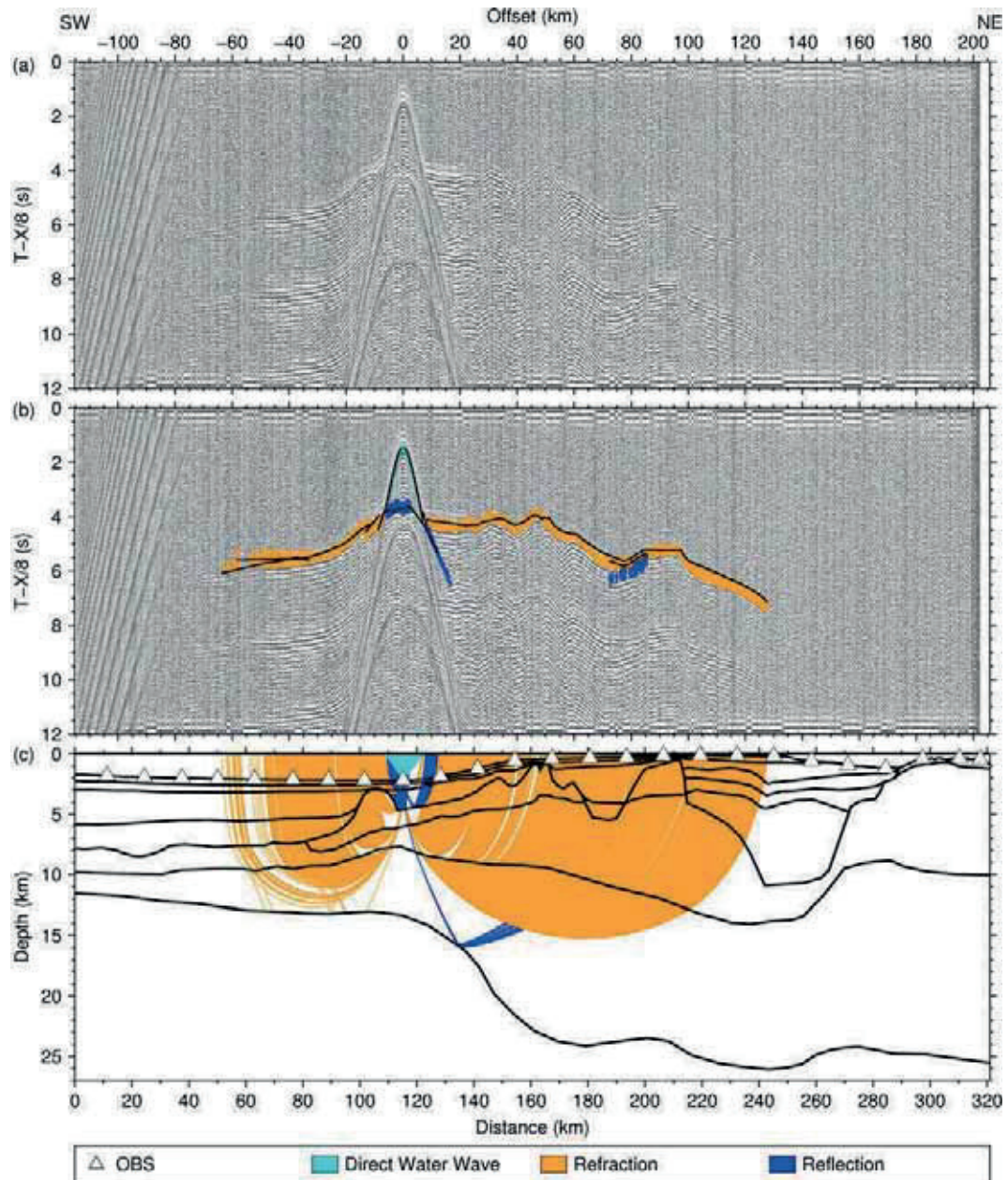


Figure A.9: Seismic section, picks and modeled raypaths of OBS 9 (AWI-20100200)
 (a) Seismic section of the hydrophone component with a reduction velocity of 8 km/s.
 (b) The colored lines mark the picked phases within the seismic section. The vertical lengths of the picks correspond to the assigned pick uncertainties. The black lines are the calculated travel times.
 (c) The black lines are the boundaries between different velocity layers of the *P* wave velocity model. The colored lines mark the modeled raypaths of the corresponding picked phases shown in the panel above.

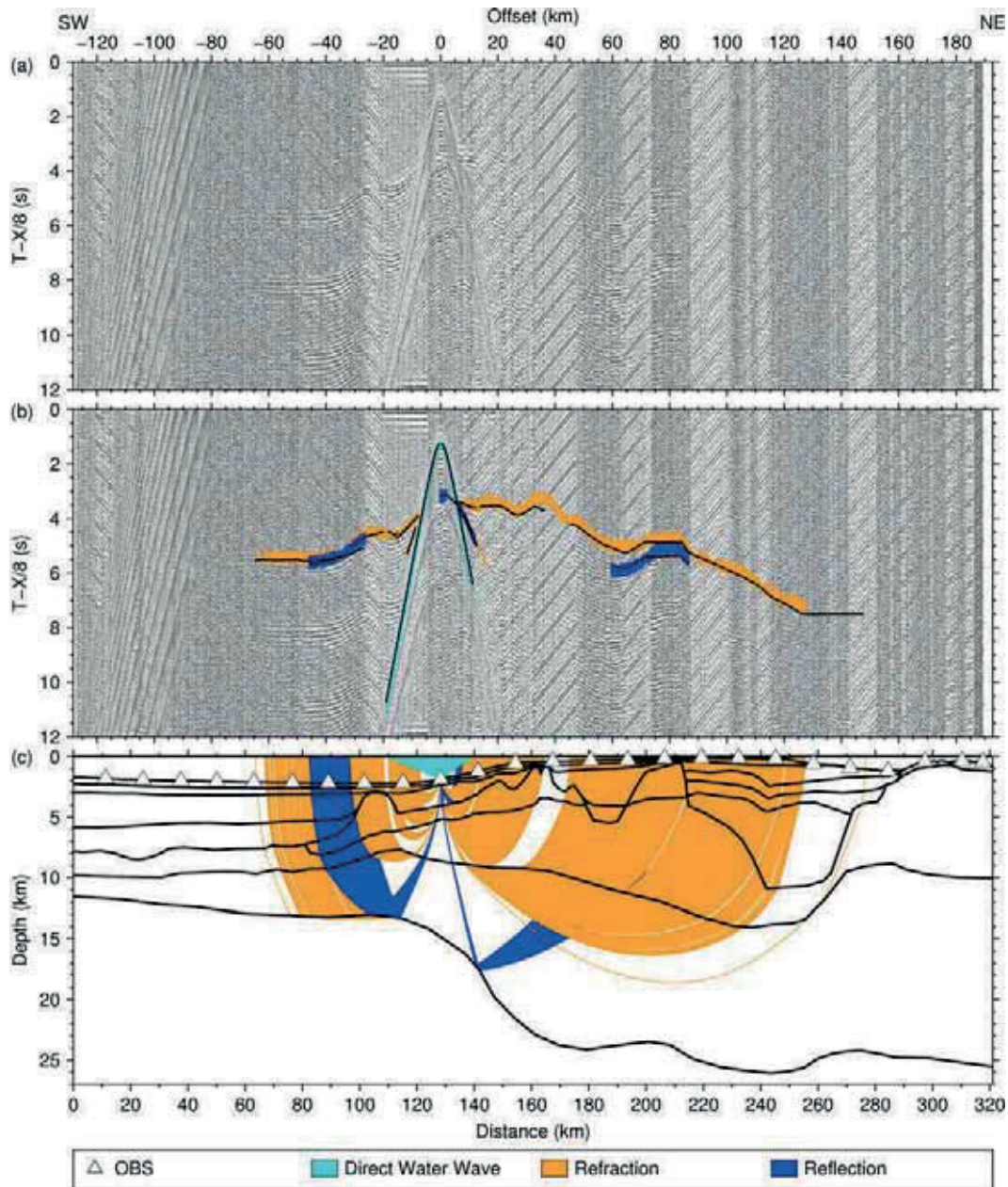


Figure A.10: Seismic section, picks and modeled raypaths of OBS 10 (AWI-20100200)

(a) Seismic section of the hydrophone component with a reduction velocity of 8 km/s.

(b) The colored lines mark the picked phases within the seismic section. The vertical lengths of the picks correspond to the assigned pick uncertainties. The black lines are the calculated travel times.

(c) The black lines are the boundaries between different velocity layers of the *P* wave velocity model. The colored lines mark the modeled raypaths of the corresponding picked phases shown in the panel above.

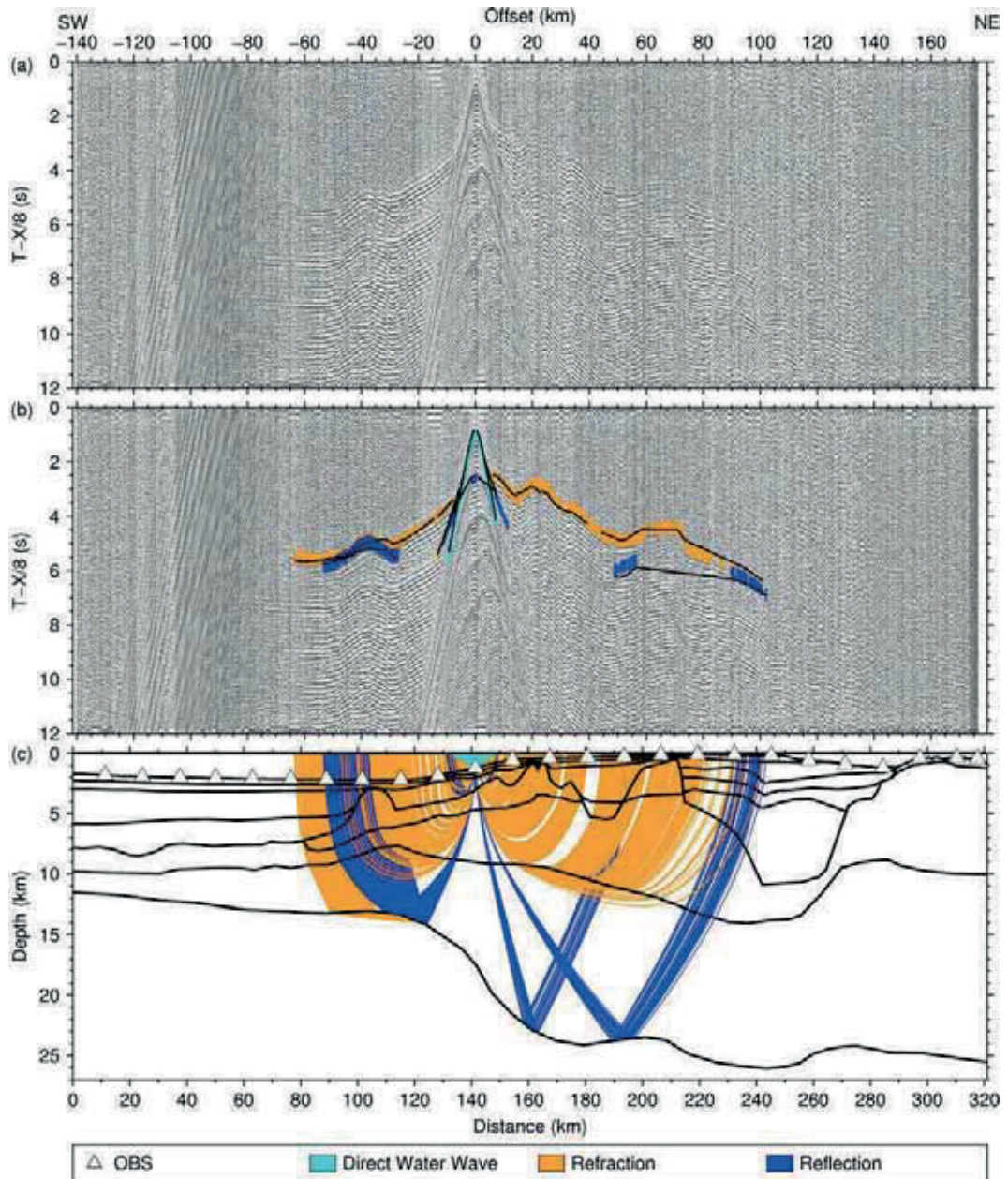


Figure A.11: Seismic section, picks and modeled raypaths of OBS 11 (AWI-20100200)

(a) Seismic section of the hydrophone component with a reduction velocity of 8 km/s.

(b) The colored lines mark the picked phases within the seismic section. The vertical lengths of the picks correspond to the assigned pick uncertainties. The black lines are the calculated travel times.

(c) The black lines are the boundaries between different velocity layers of the *P* wave velocity model. The colored lines mark the modeled raypaths of the corresponding picked phases shown in the panel above.

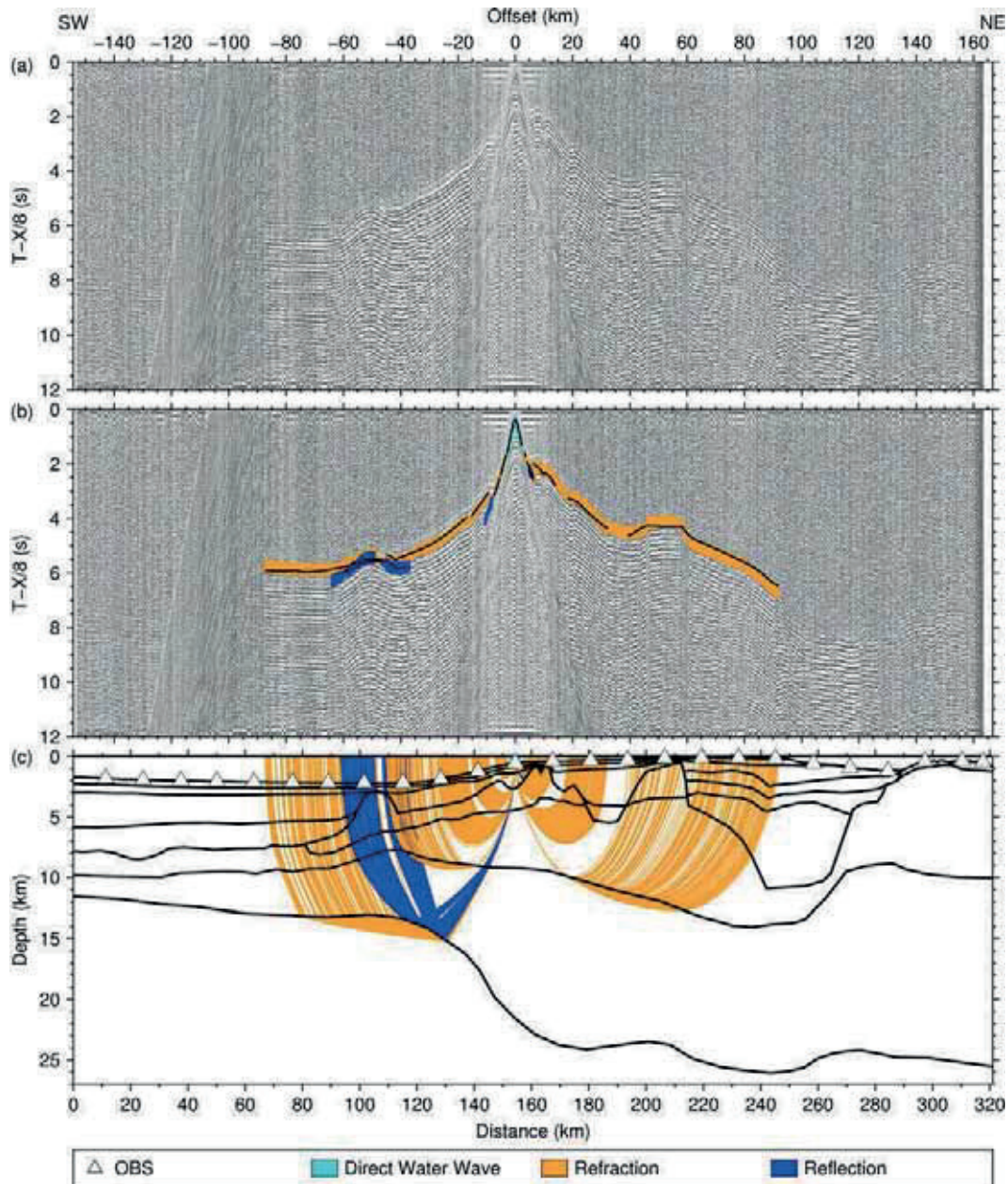


Figure A.12: Seismic section, picks and modeled raypaths of OBS 12 (AWI-20100200)
 (a) Seismic section of the hydrophone component with a reduction velocity of 8 km/s.
 (b) The colored lines mark the picked phases within the seismic section. The vertical lengths of the picks correspond to the assigned pick uncertainties. The black lines are the calculated travel times.
 (c) The black lines are the boundaries between different velocity layers of the *P* wave velocity model. The colored lines mark the modeled raypaths of the corresponding picked phases shown in the panel above.

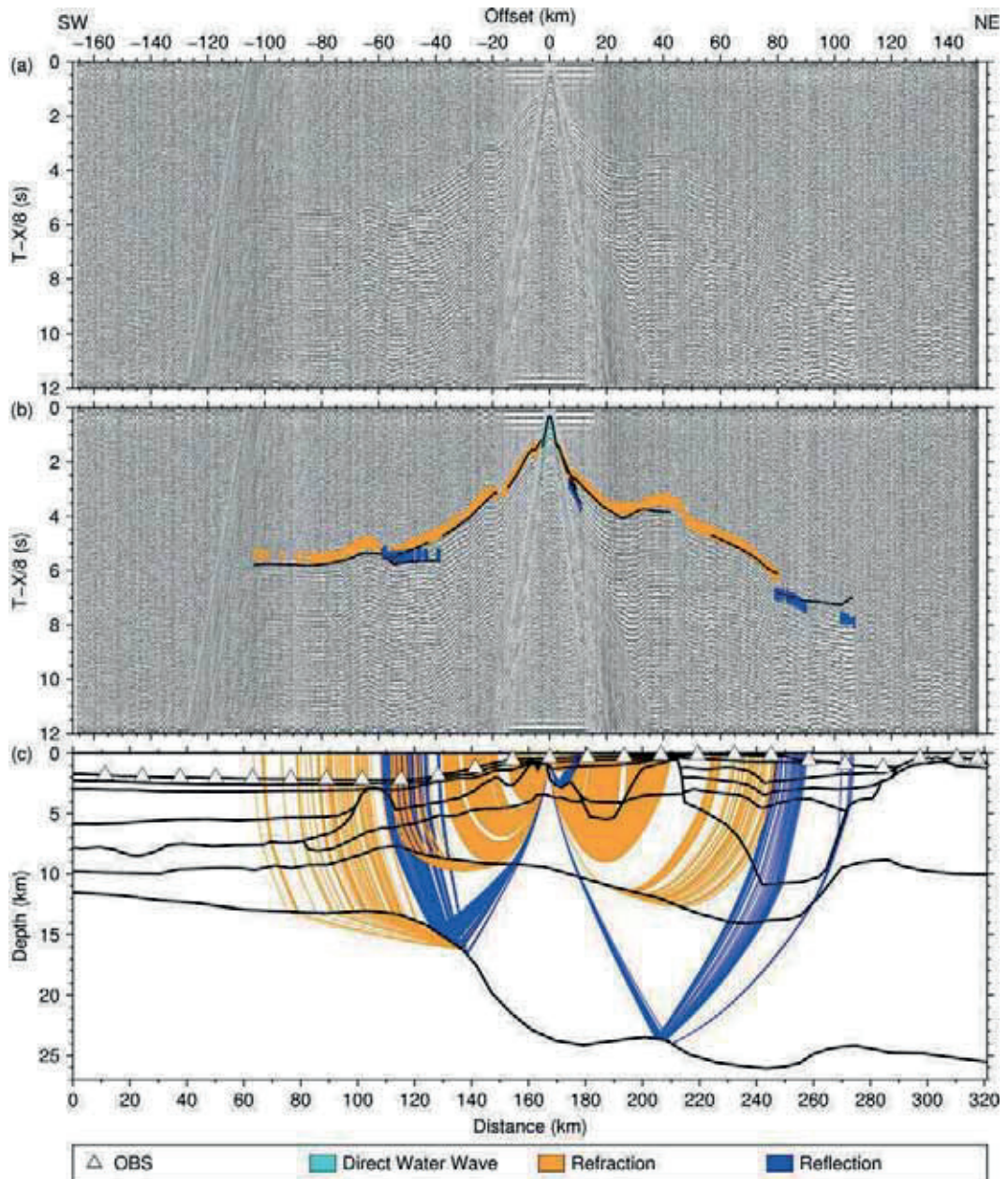


Figure A.13: Seismic section, picks and modeled raypaths of OBS 13 (AWI-20100200)

(a) Seismic section of the hydrophone component with a reduction velocity of 8 km/s.

(b) The colored lines mark the picked phases within the seismic section. The vertical lengths of the picks correspond to the assigned pick uncertainties. The black lines are the calculated travel times.

(c) The black lines are the boundaries between different velocity layers of the *P* wave velocity model. The colored lines mark the modeled raypaths of the corresponding picked phases shown in the panel above.

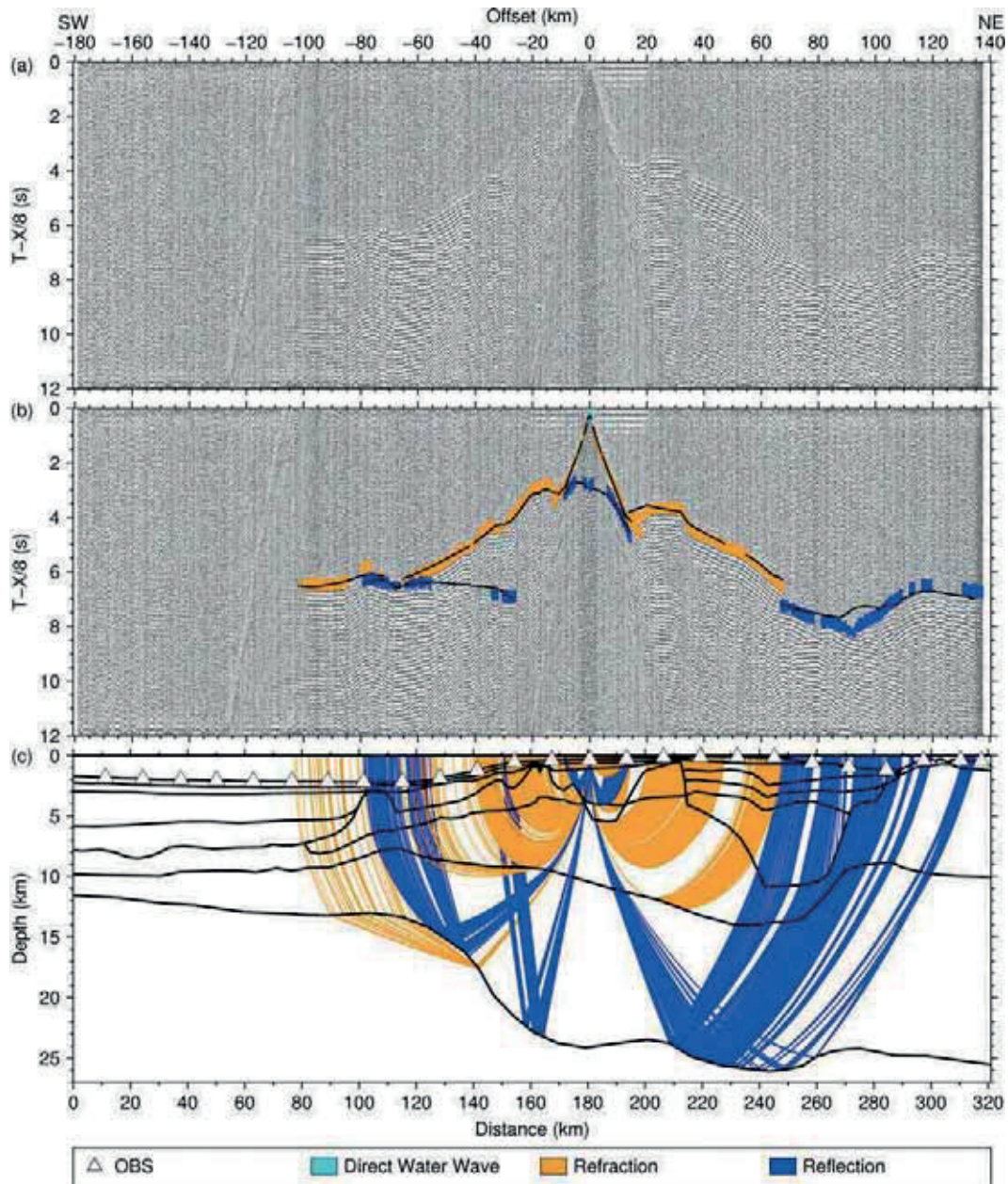


Figure A.14: Seismic section, picks and modeled raypaths of OBS 14 (AWI-20100200)

(a) Seismic section of the hydrophone component with a reduction velocity of 8 km/s.

(b) The colored lines mark the picked phases within the seismic section. The vertical lengths of the picks correspond to the assigned pick uncertainties. The black lines are the calculated travel times.

(c) The black lines are the boundaries between different velocity layers of the *P* wave velocity model. The colored lines mark the modeled raypaths of the corresponding picked phases shown in the panel above.

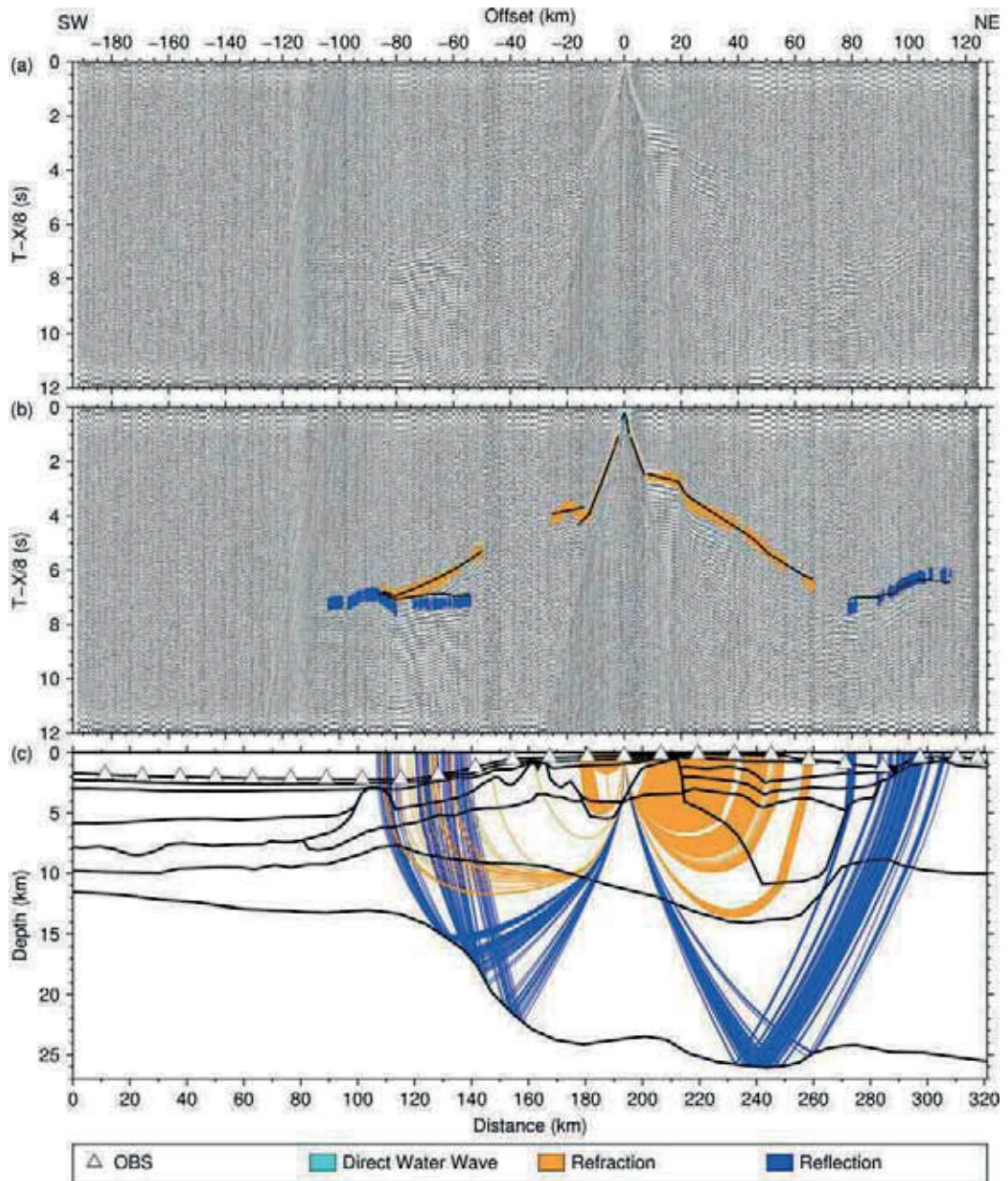


Figure A.15: Seismic section, picks and modeled raypaths of OBS 15 (AWI-20100200)

(a) Seismic section of the hydrophone component with a reduction velocity of 8 km/s.

(b) The colored lines mark the picked phases within the seismic section. The vertical lengths of the picks correspond to the assigned pick uncertainties. The black lines are the calculated travel times.

(c) The black lines are the boundaries between different velocity layers of the *P* wave velocity model. The colored lines mark the modeled raypaths of the corresponding picked phases shown in the panel above.

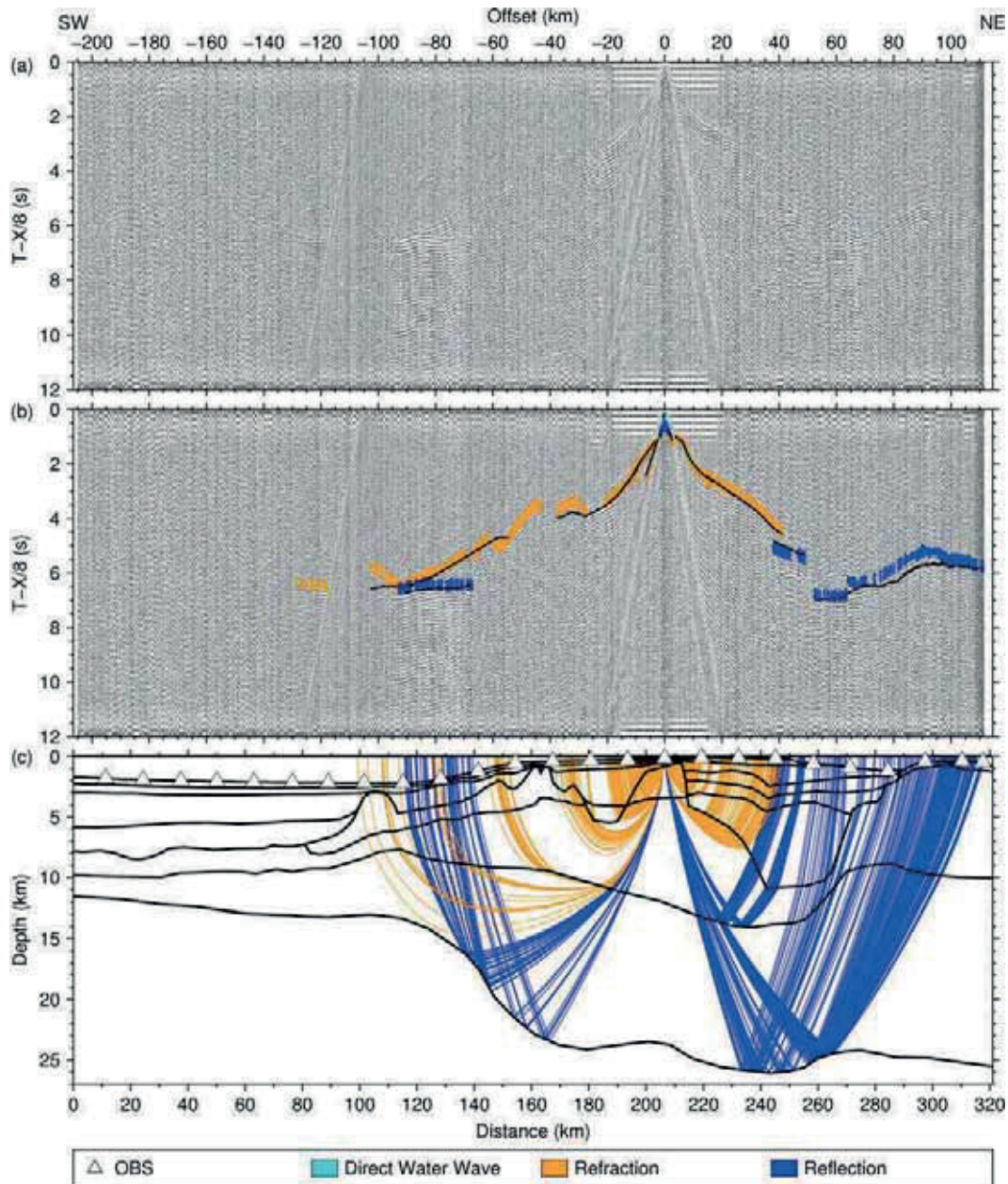


Figure A.16: Seismic section, picks and modeled raypaths of OBS 16 (AWI-20100200)

(a) Seismic section of the hydrophone component with a reduction velocity of 8 km/s.

(b) The colored lines mark the picked phases within the seismic section. The vertical lengths of the picks correspond to the assigned pick uncertainties. The black lines are the calculated travel times.

(c) The black lines are the boundaries between different velocity layers of the *P* wave velocity model. The colored lines mark the modeled raypaths of the corresponding picked phases shown in the panel above.

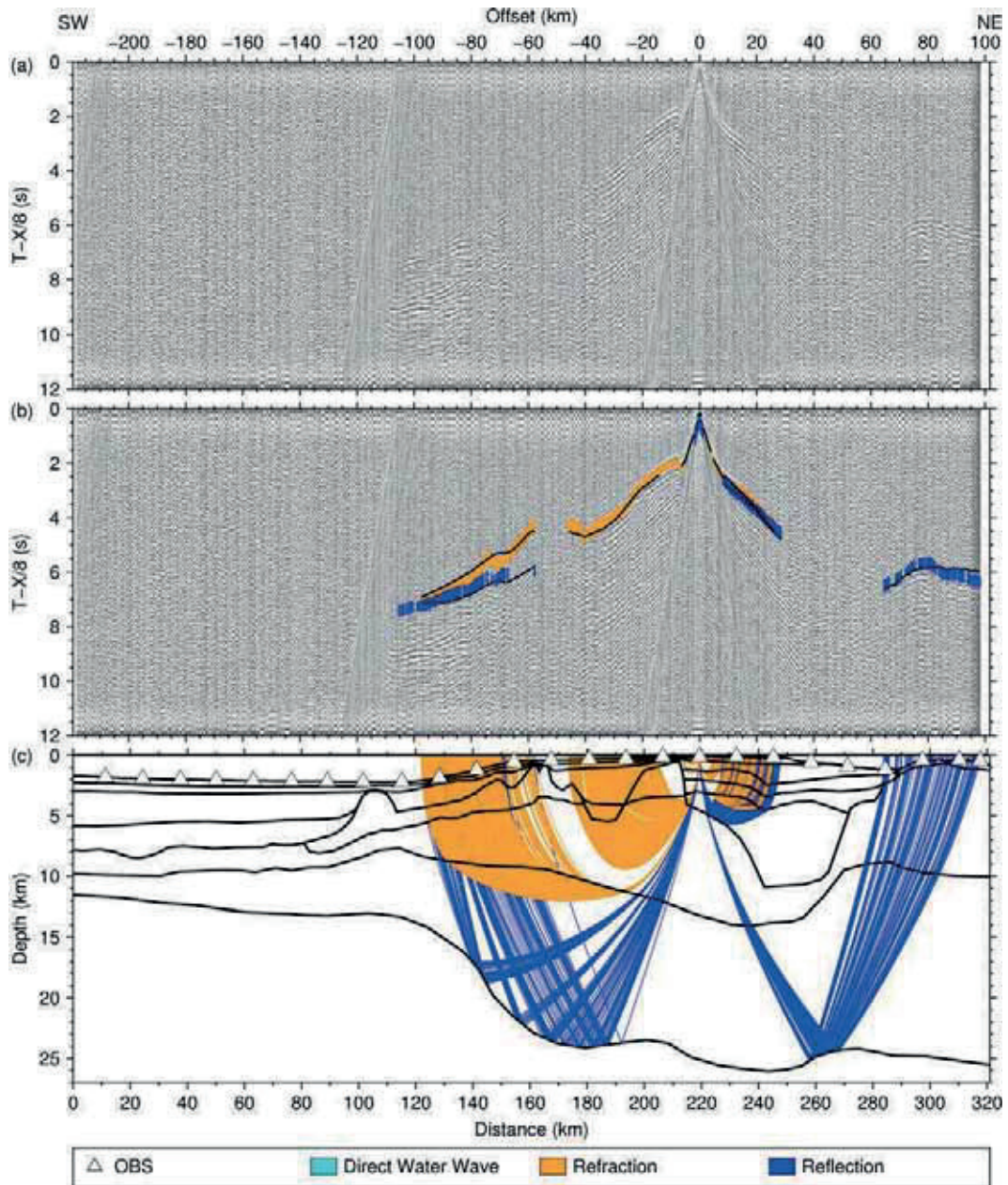


Figure A. 17: Seismic section, picks and modeled raypaths of OBS 17 (AWI-20100200)

(a) Seismic section of the hydrophone component with a reduction velocity of 8 km/s.

(b) The colored lines mark the picked phases within the seismic section. The vertical lengths of the picks correspond to the assigned pick uncertainties. The black lines are the calculated travel times.

(c) The black lines are the boundaries between different velocity layers of the *P* wave velocity model. The colored lines mark the modeled raypaths of the corresponding picked phases shown in the panel above.

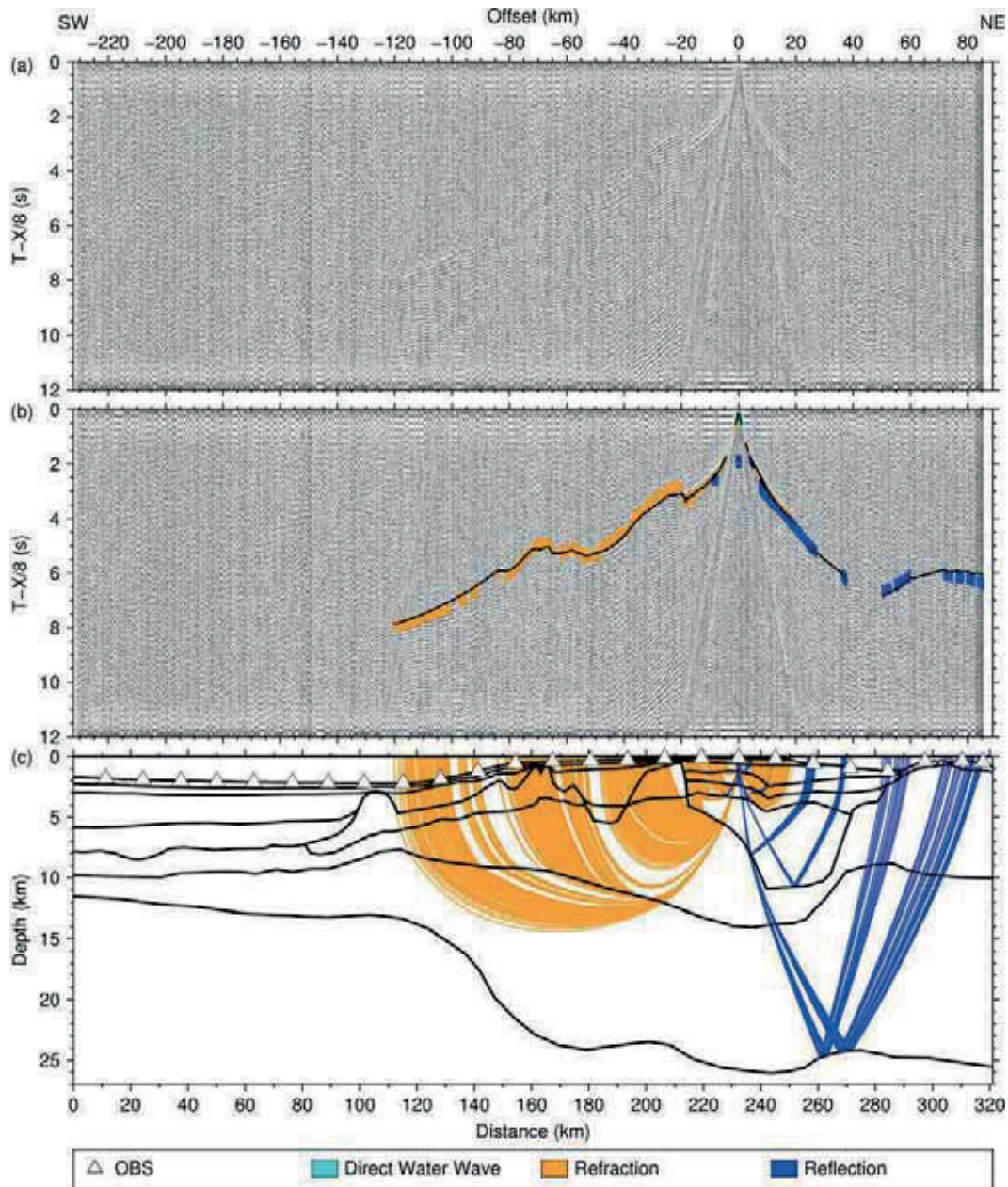


Figure A.18: Seismic section, picks and modeled raypaths of OBS 18 (AWI-20100200)

(a) Seismic section of the hydrophone component with a reduction velocity of 8 km/s.

(b) The colored lines mark the picked phases within the seismic section. The vertical lengths of the picks correspond to the assigned pick uncertainties. The black lines are the calculated travel times.

(c) The black lines are the boundaries between different velocity layers of the *P* wave velocity model. The colored lines mark the modeled raypaths of the corresponding picked phases shown in the panel above.

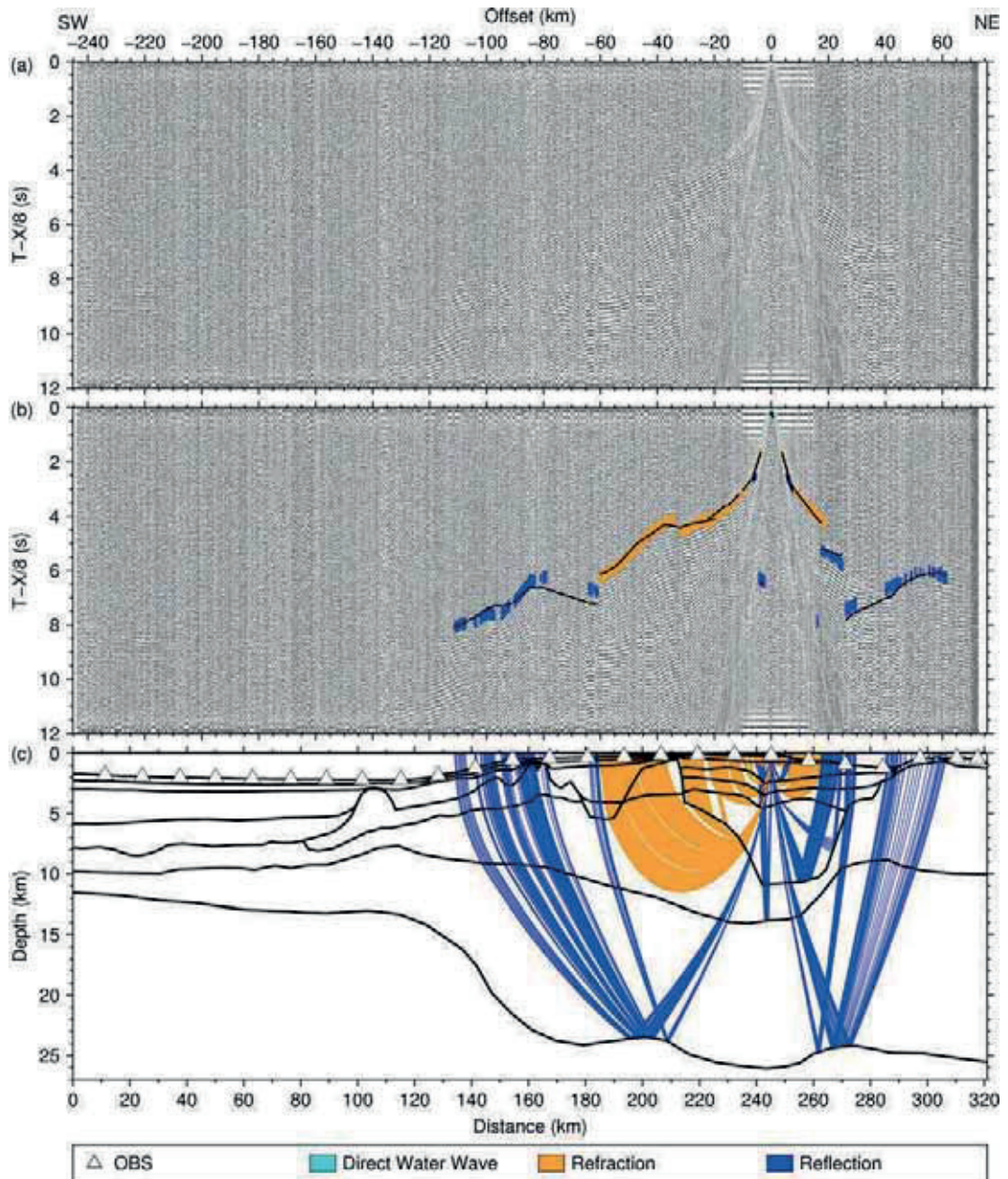


Figure A.19: Seismic section, picks and modeled raypaths of OBS 19 (AWI-20100200)

(a) Seismic section of the hydrophone component with a reduction velocity of 8 km/s.

(b) The colored lines mark the picked phases within the seismic section. The vertical lengths of the picks correspond to the assigned pick uncertainties. The black lines are the calculated travel times.

(c) The black lines are the boundaries between different velocity layers of the *P* wave velocity model. The colored lines mark the modeled raypaths of the corresponding picked phases shown in the panel above.

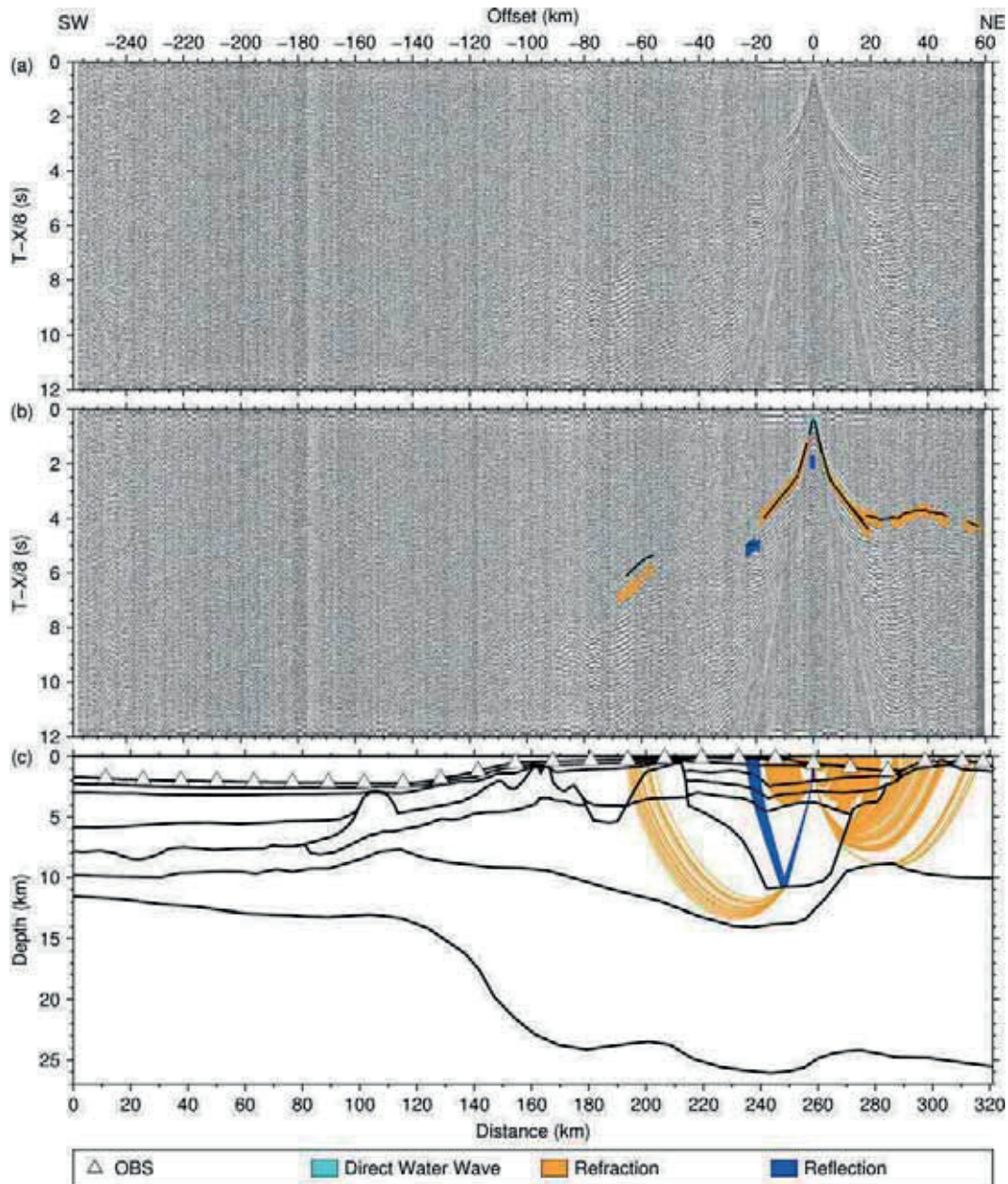


Figure A.20: Seismic section, picks and modeled raypaths of OBS 20 (AWI-20100200)

(a) Seismic section of the hydrophone component with a reduction velocity of 8 km/s.

(b) The colored lines mark the picked phases within the seismic section. The vertical lengths of the picks correspond to the assigned pick uncertainties. The black lines are the calculated travel times.

(c) The black lines are the boundaries between different velocity layers of the *P* wave velocity model. The colored lines mark the modeled raypaths of the corresponding picked phases shown in the panel above.

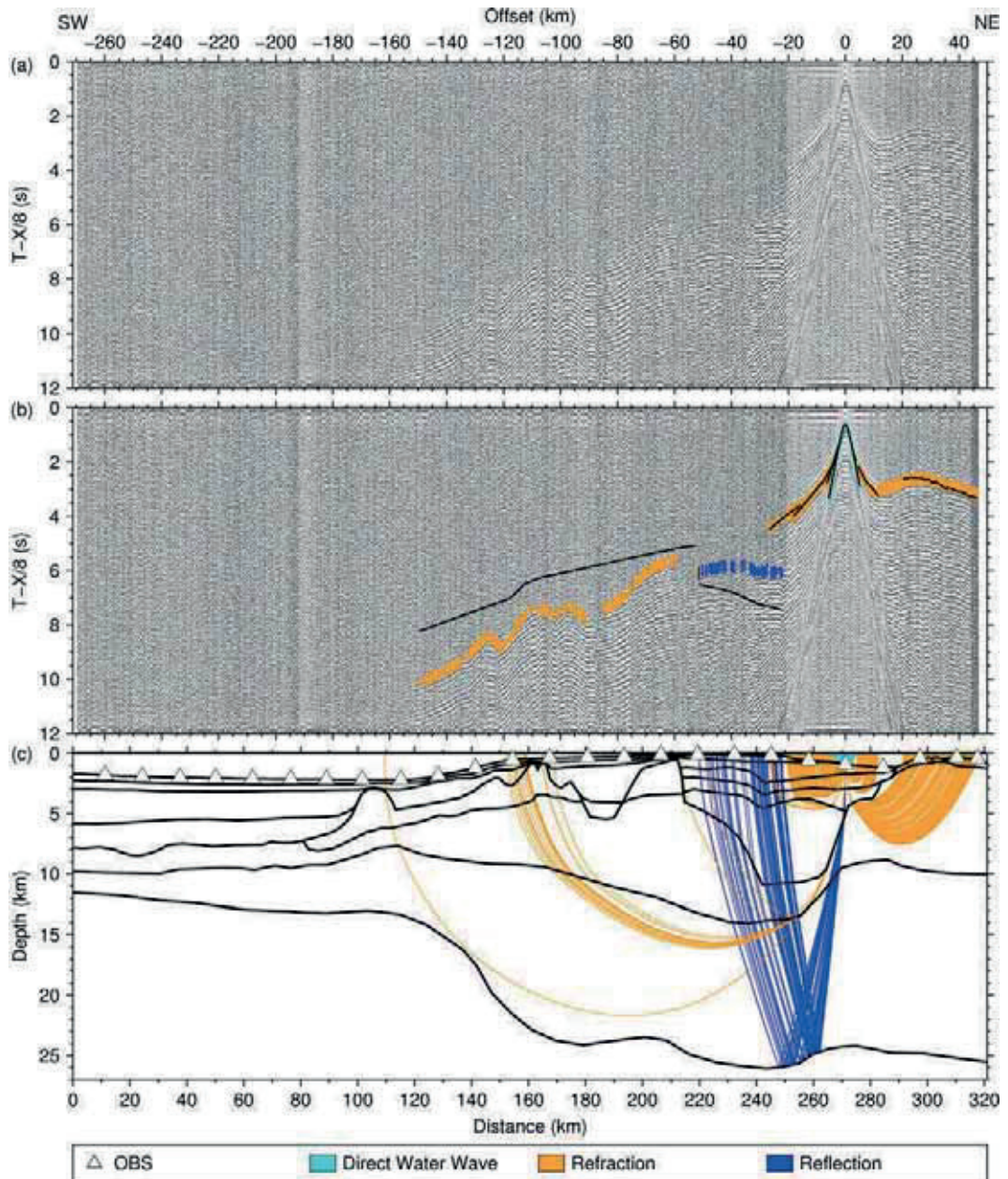


Figure A.21: Seismic section, picks and modeled raypaths of OBS 21 (AWI-20100200)

(a) Seismic section of the hydrophone component with a reduction velocity of 8 km/s.

(b) The colored lines mark the picked phases within the seismic section. The vertical lengths of the picks correspond to the assigned pick uncertainties. The black lines are the calculated travel times.

(c) The black lines are the boundaries between different velocity layers of the P wave velocity model. The colored lines mark the modeled raypaths of the corresponding picked phases shown in the panel above.

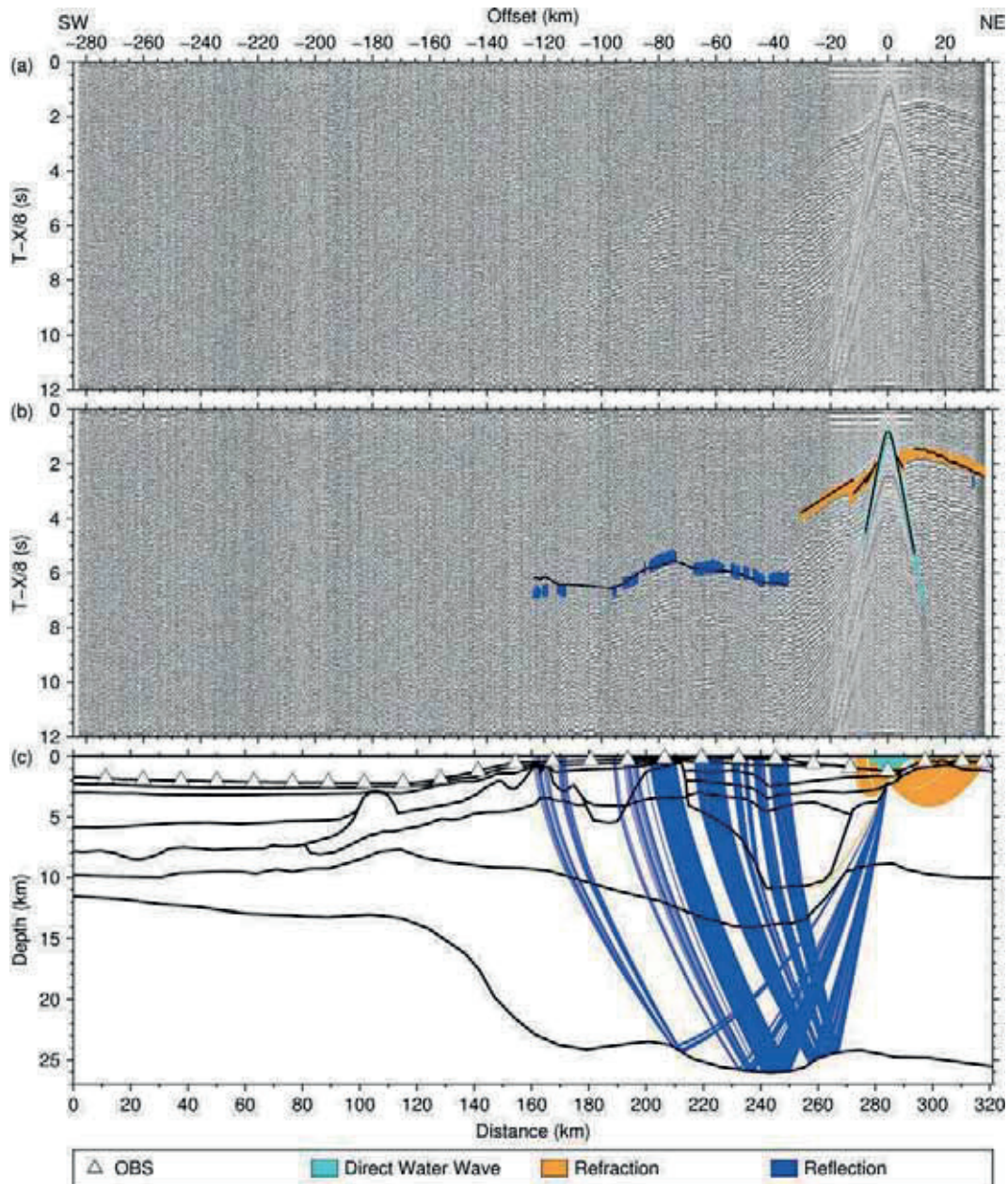


Figure A.22: Seismic section, picks and modeled raypaths of OBS 22 (AWI-20100200)

(a) Seismic section of the hydrophone component with a reduction velocity of 8 km/s.

(b) The colored lines mark the picked phases within the seismic section. The vertical lengths of the picks correspond to the assigned pick uncertainties. The black lines are the calculated travel times.

(c) The black lines are the boundaries between different velocity layers of the *P* wave velocity model. The colored lines mark the modeled raypaths of the corresponding picked phases shown in the panel above.

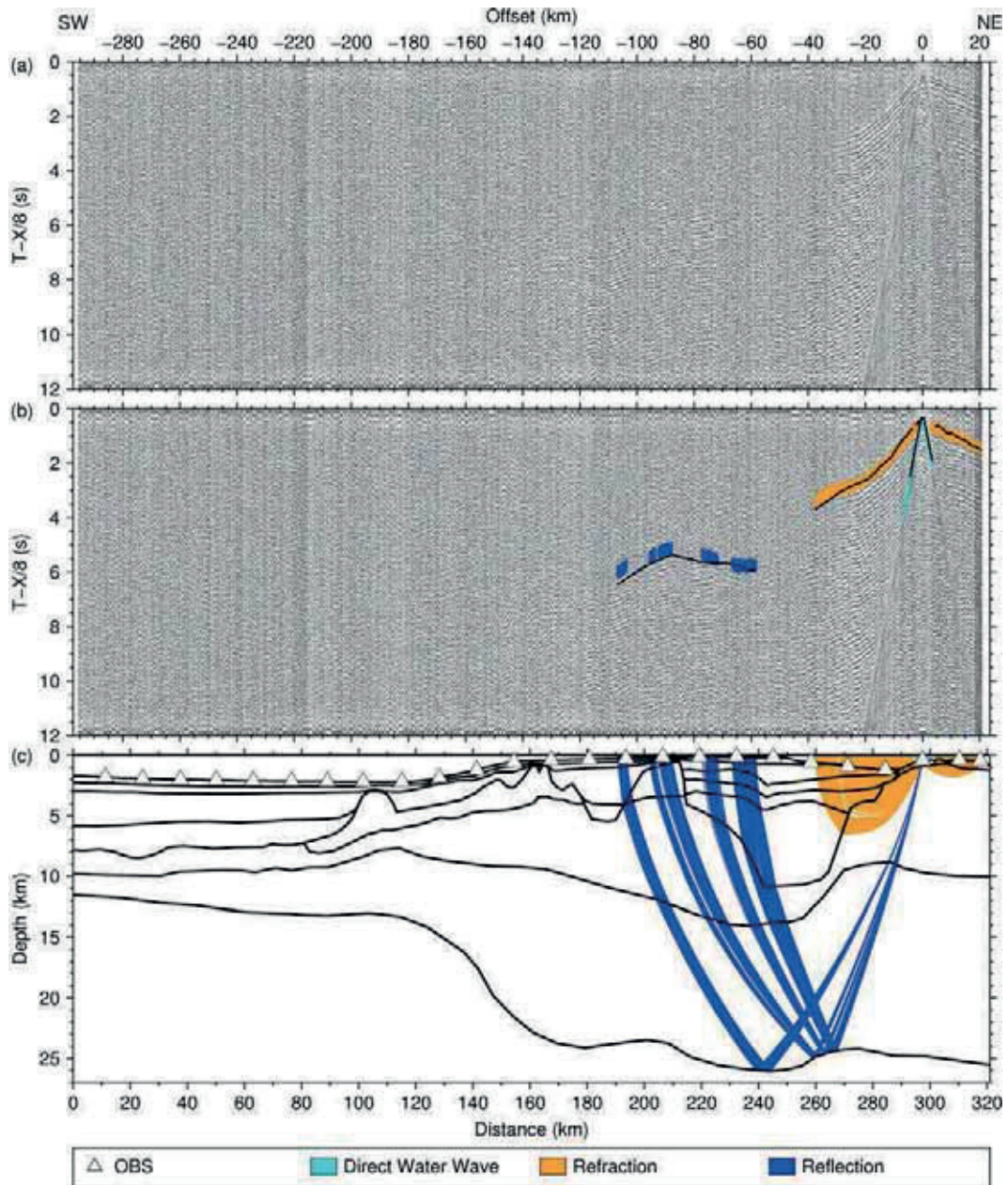


Figure A.23: Seismic section, picks and modeled raypaths of OBS 23 (AWI-20100200)

(a) Seismic section of the hydrophone component with a reduction velocity of 8 km/s.

(b) The colored lines mark the picked phases within the seismic section. The vertical lengths of the picks correspond to the assigned pick uncertainties. The black lines are the calculated travel times.

(c) The black lines are the boundaries between different velocity layers of the *P* wave velocity model. The colored lines mark the modeled raypaths of the corresponding picked phases shown in the panel above.

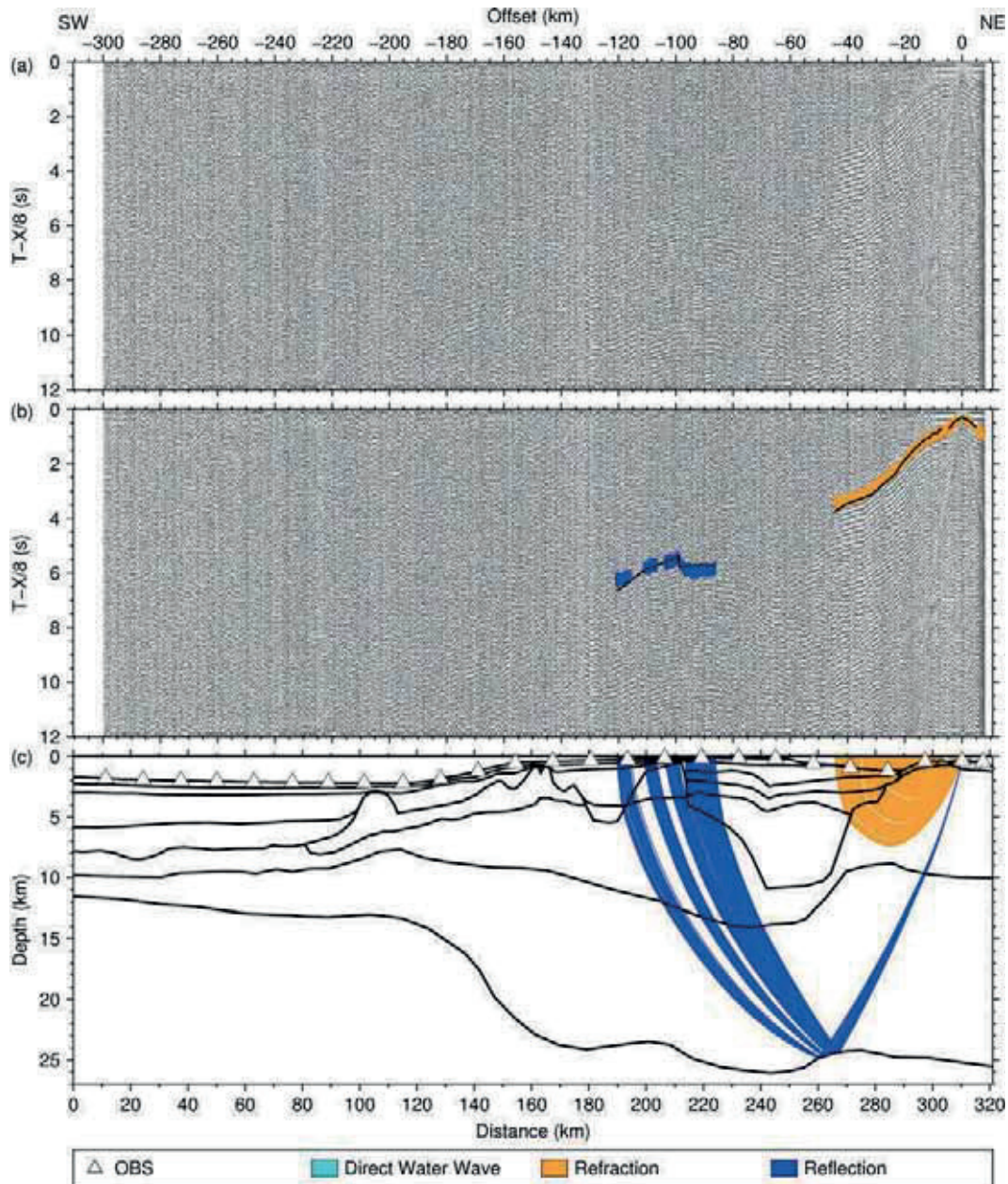


Figure A.24: Seismic section, picks and modeled raypaths of OBS 24 (AWI-20100200)

(a) Seismic section of the hydrophone component with a reduction velocity of 8 km/s.

(b) The colored lines mark the picked phases within the seismic section. The vertical lengths of the picks correspond to the assigned pick uncertainties. The black lines are the calculated travel times.

(c) The black lines are the boundaries between different velocity layers of the *P* wave velocity model. The colored lines mark the modeled raypaths of the corresponding picked phases shown in the panel above.

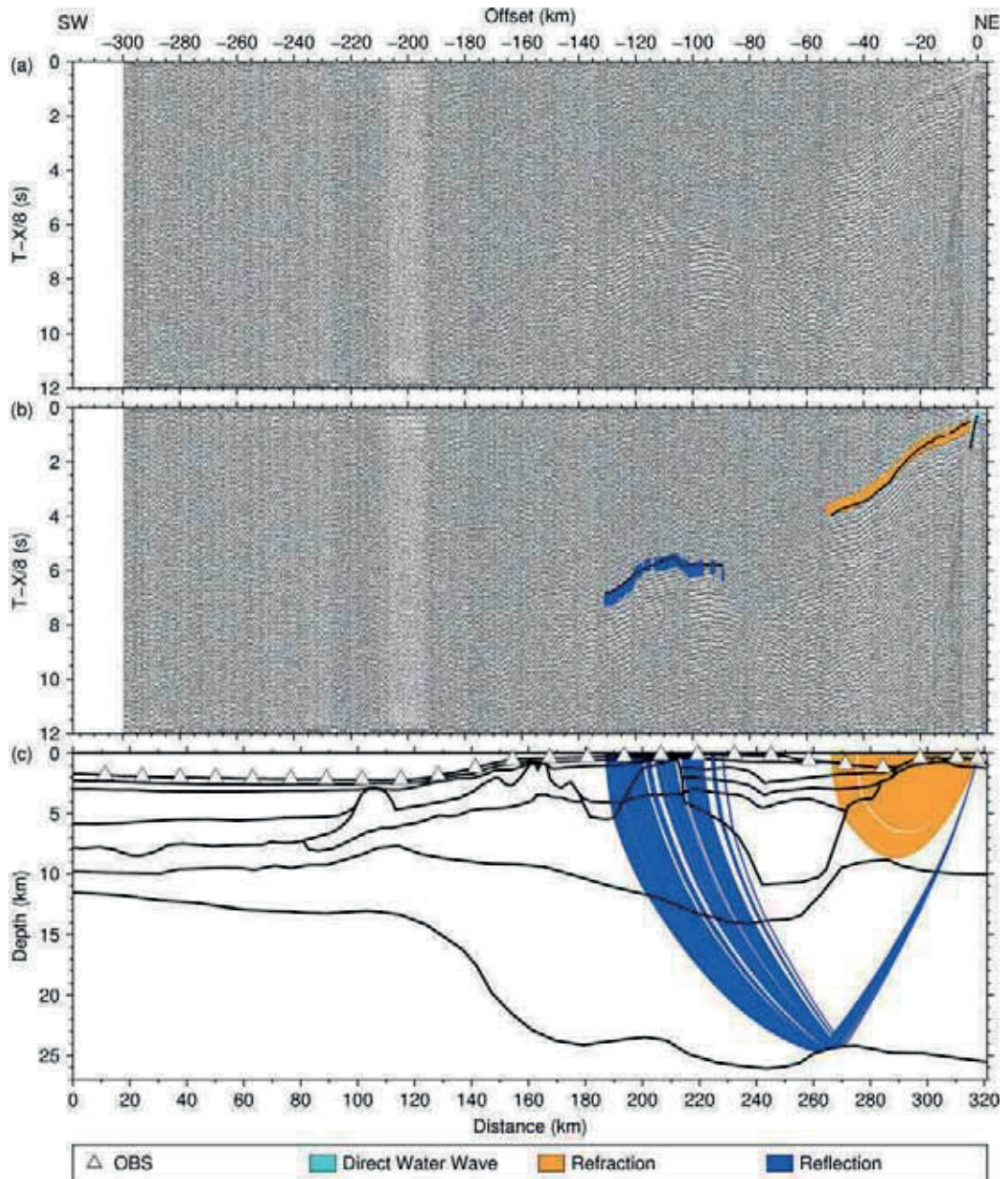


Figure A.25: Seismic section, picks and modeled raypaths of OBS 25 (AWI-20100200)

(a) Seismic section of the hydrophone component with a reduction velocity of 8 km/s.

(b) The colored lines mark the picked phases within the seismic section. The vertical lengths of the picks correspond to the assigned pick uncertainties. The black lines are the calculated travel times.

(c) The black lines are the boundaries between different velocity layers of the *P* wave velocity model. The colored lines mark the modeled raypaths of the corresponding picked phases shown in the panel above.

Seismic sections, profile AWI-20100300

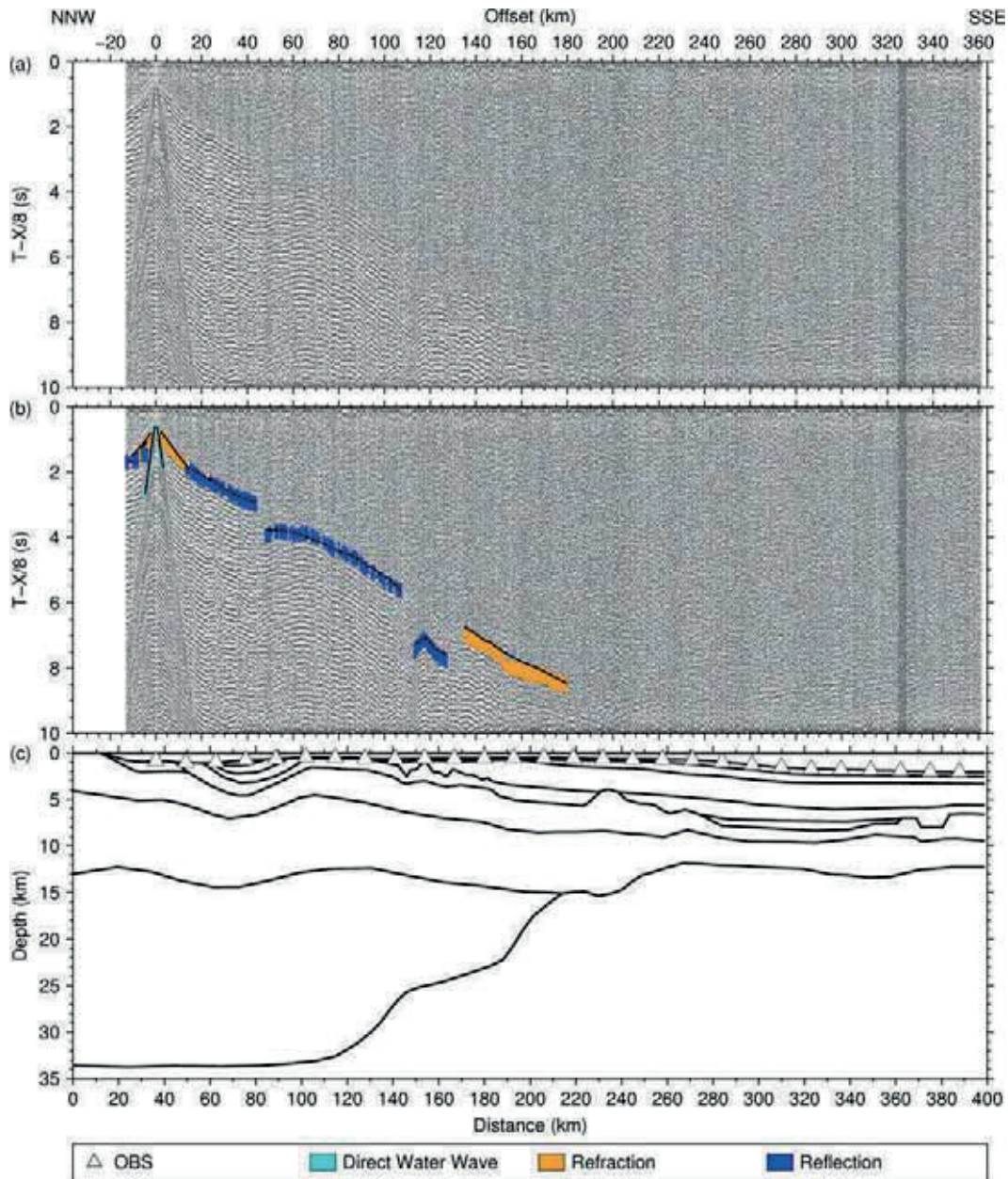


Figure B.1: Seismic section, picks and modeled raypaths of OBS 1 (AWI-20100300)

(a) Seismic section of the hydrophone component with a reduction velocity of 8 km/s.

(b) The colored lines mark the picked phases within the seismic section. The vertical lengths of the picks correspond to the assigned pick uncertainties. The black lines are the calculated travel times.

(c) The black lines are the boundaries between different velocity layers of the *P* wave velocity model. The colored lines mark the modeled raypaths of the corresponding picked phases shown in the panel above.

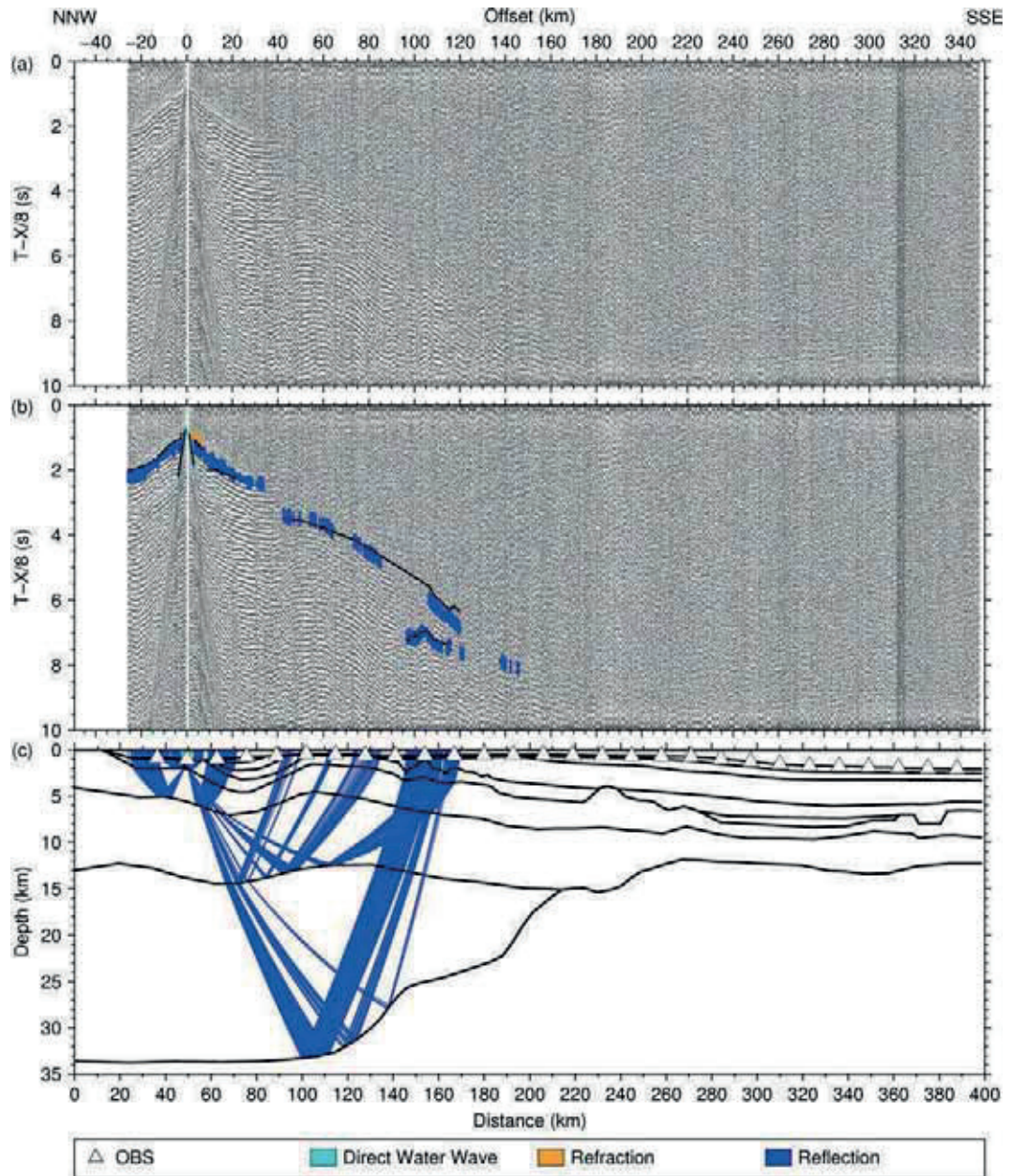


Figure B.2: Seismic section, picks and modeled raypaths of OBS 2 (AWI-20100300)

(a) Seismic section of the hydrophone component with a reduction velocity of 8 km/s.

(b) The colored lines mark the picked phases within the seismic section. The vertical lengths of the picks correspond to the assigned pick uncertainties. The black lines are the calculated travel times.

(c) The black lines are the boundaries between different velocity layers of the *P* wave velocity model. The colored lines mark the modeled raypaths of the corresponding picked phases shown in the panel above.

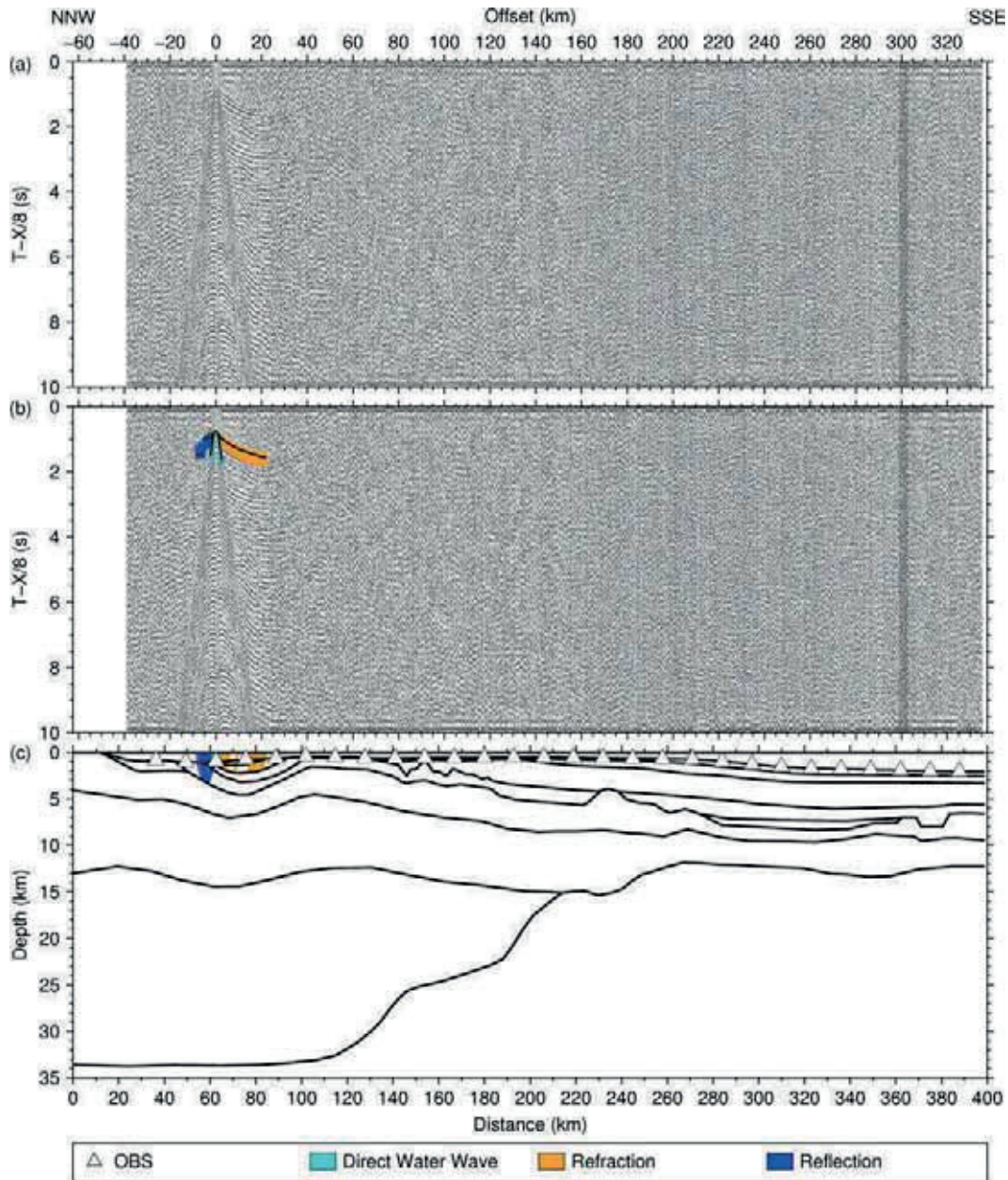


Figure B.3: Seismic section, picks and modeled raypaths of OBS 3 (AWI-20100300)
 (a) Seismic section of the hydrophone component with a reduction velocity of 8 km/s.
 (b) The colored lines mark the picked phases within the seismic section. The vertical lengths of the picks correspond to the assigned pick uncertainties. The black lines are the calculated travel times.
 (c) The black lines are the boundaries between different velocity layers of the P wave velocity model. The colored lines mark the modeled raypaths of the corresponding picked phases shown in the panel above.

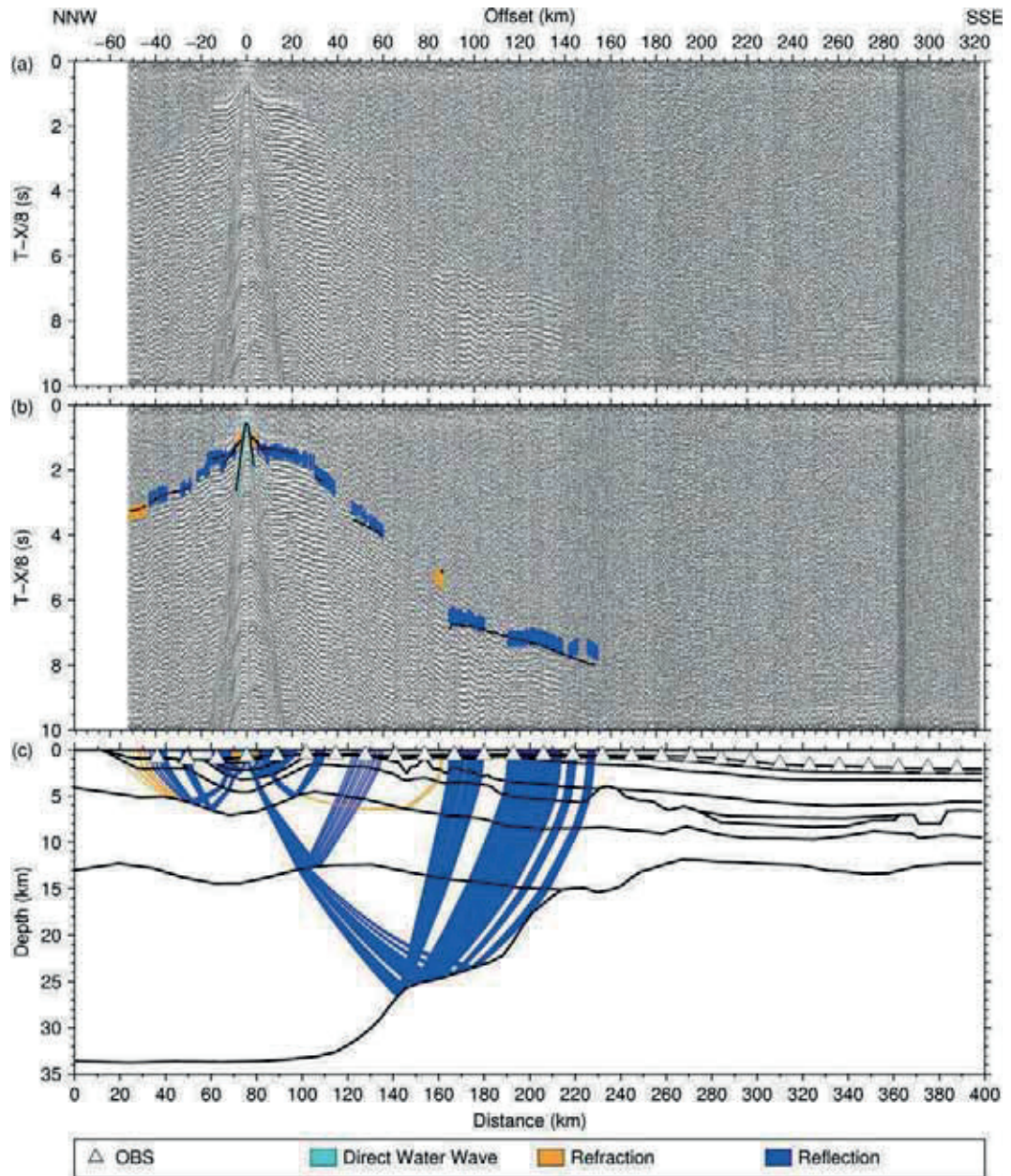


Figure B.4: Seismic section, picks and modeled raypaths of OBS 4 (AWI-20100300)

(a) Seismic section of the hydrophone component with a reduction velocity of 8 km/s.

(b) The colored lines mark the picked phases within the seismic section. The vertical lengths of the picks correspond to the assigned pick uncertainties. The black lines are the calculated travel times.

(c) The black lines are the boundaries between different velocity layers of the *P* wave velocity model. The colored lines mark the modeled raypaths of the corresponding picked phases shown in the panel above.

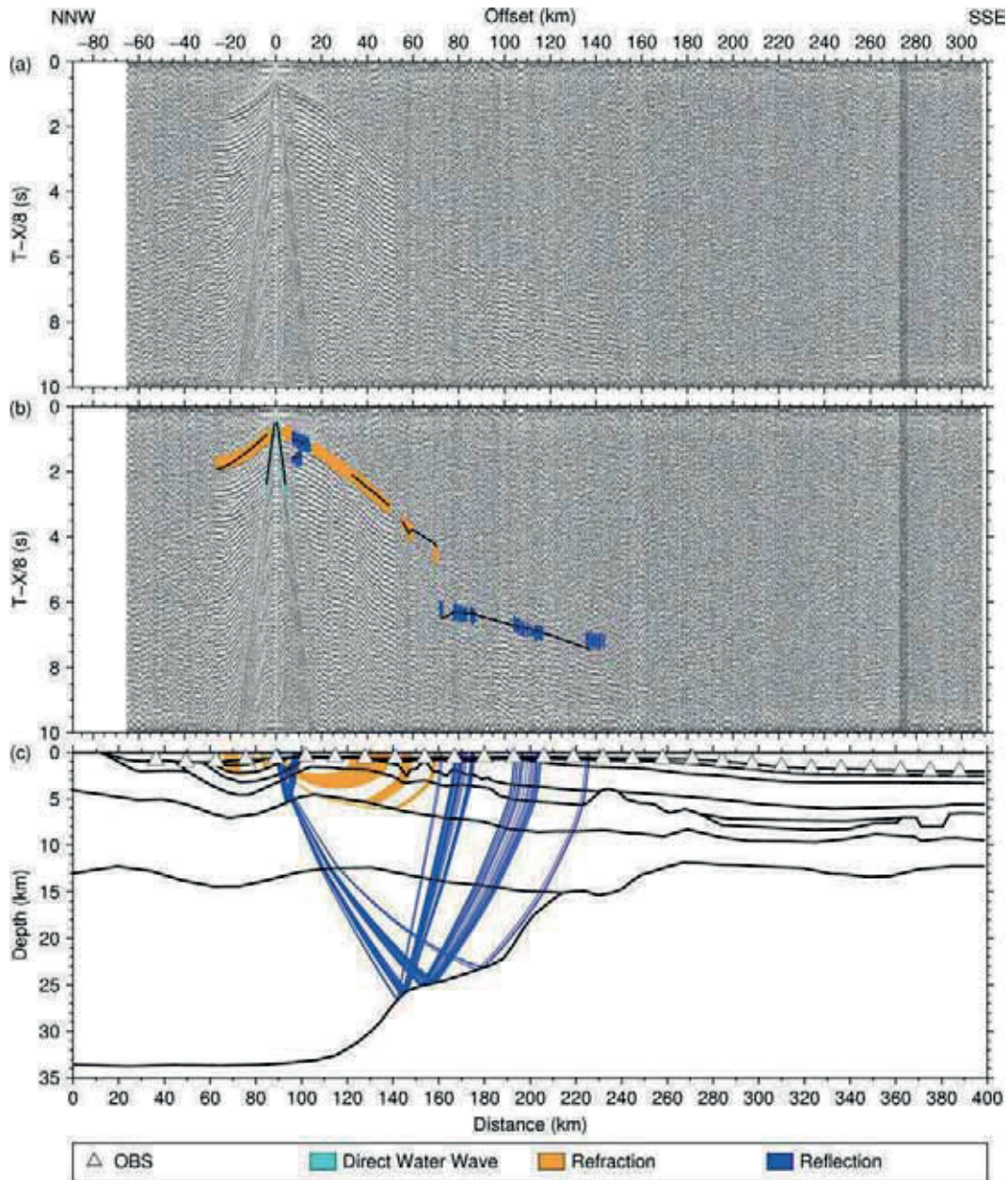


Figure B.5: Seismic section, picks and modeled raypaths of OBS 5 (AWI-20100300)
 (a) Seismic section of the hydrophone component with a reduction velocity of 8 km/s.
 (b) The colored lines mark the picked phases within the seismic section. The vertical lengths of the picks correspond to the assigned pick uncertainties. The black lines are the calculated travel times.
 (c) The black lines are the boundaries between different velocity layers of the *P* wave velocity model. The colored lines mark the modeled raypaths of the corresponding picked phases shown in the panel above.

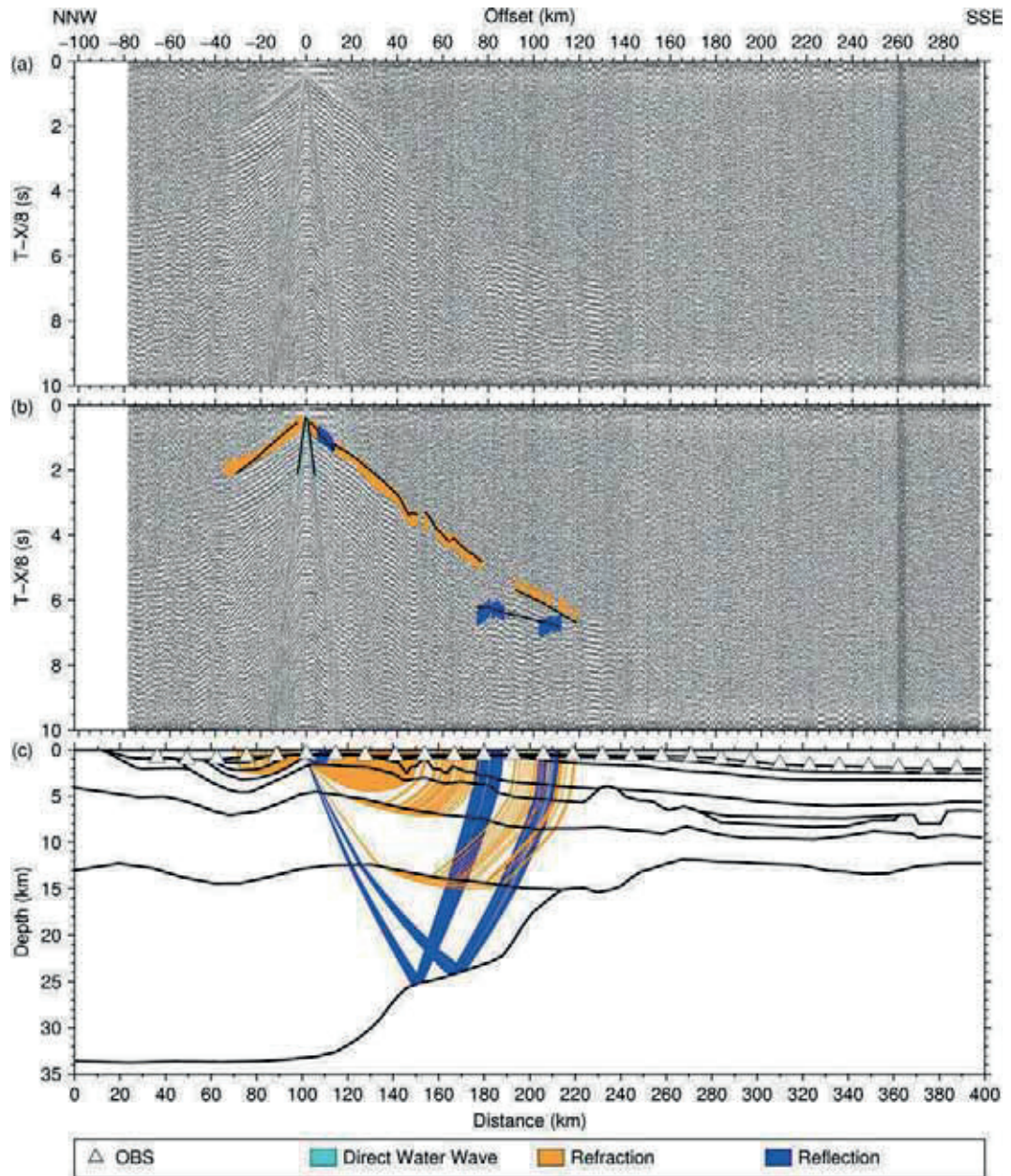


Figure B.6: Seismic section, picks and modeled raypaths of OBS 6 (AWI-20100300)
 (a) Seismic section of the hydrophone component with a reduction velocity of 8 km/s.
 (b) The colored lines mark the picked phases within the seismic section. The vertical lengths of the picks correspond to the assigned pick uncertainties. The black lines are the calculated travel times.
 (c) The black lines are the boundaries between different velocity layers of the *P* wave velocity model. The colored lines mark the modeled raypaths of the corresponding picked phases shown in the panel above.

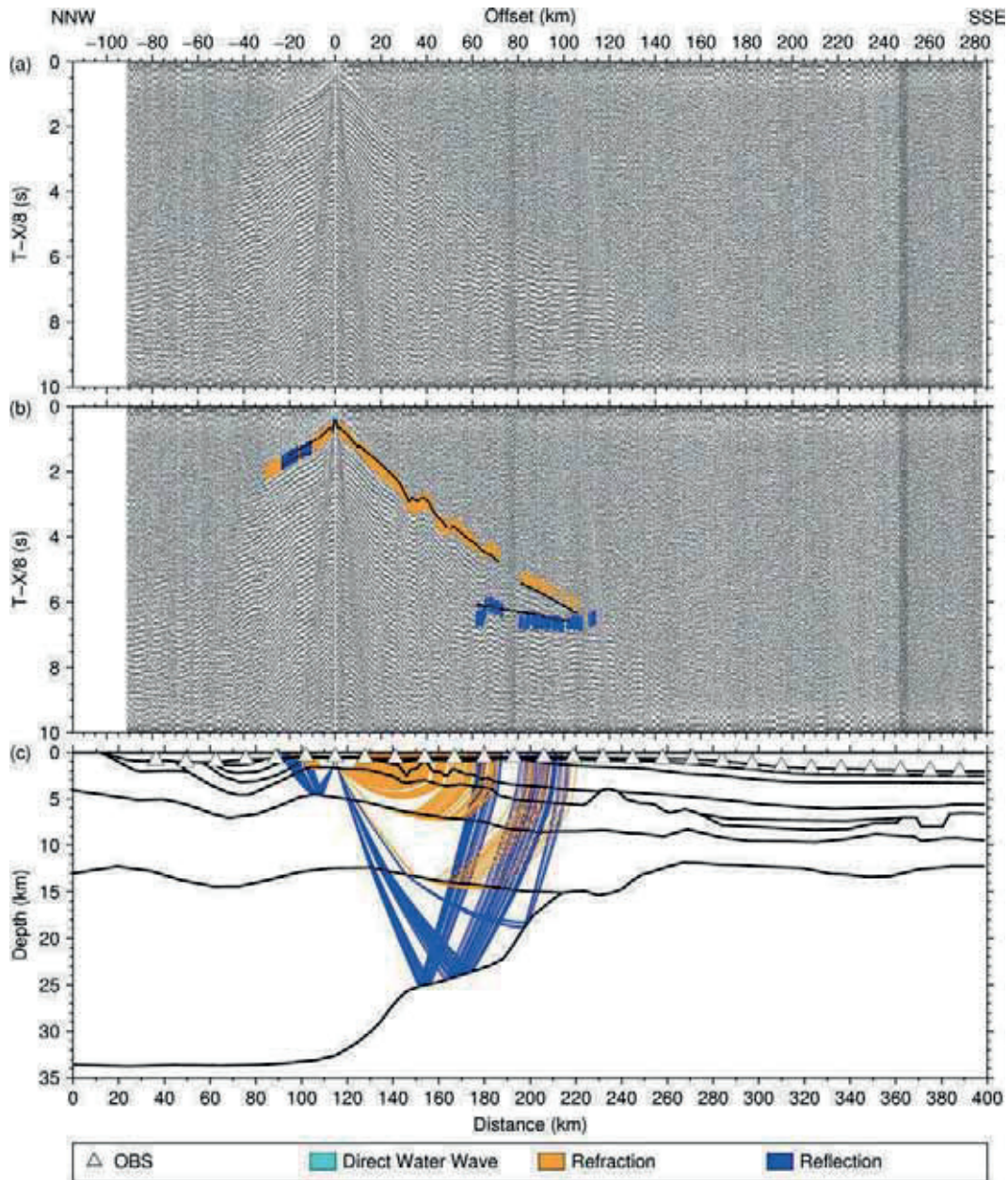


Figure B.7: Seismic section, picks and modeled raypaths of OBS 7 (AWI-20100300)
 (a) Seismic section of the hydrophone component with a reduction velocity of 8 km/s.
 (b) The colored lines mark the picked phases within the seismic section. The vertical lengths of the picks correspond to the assigned pick uncertainties. The black lines are the calculated travel times.
 (c) The black lines are the boundaries between different velocity layers of the P wave velocity model. The colored lines mark the modeled raypaths of the corresponding picked phases shown in the panel above.

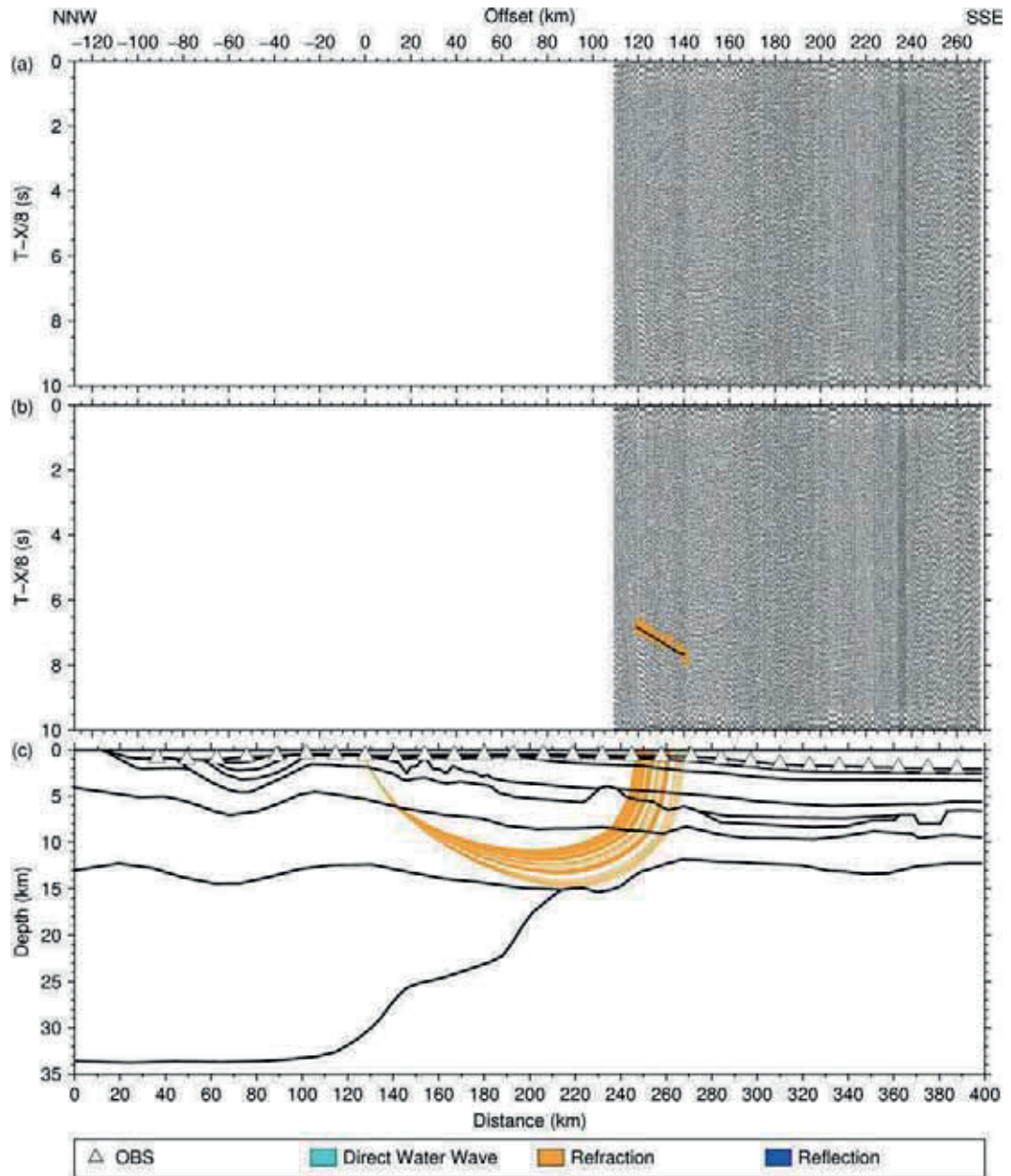


Figure B.8: Seismic section, picks and modeled raypaths of OBS 8 (AWI-20100300)

(a) Seismic section of the hydrophone component with a reduction velocity of 8 km/s.

Because of an OBS-failure, only a small amount of data was recorded.

(b) The colored lines mark the picked phases within the seismic section. The vertical lengths of the picks correspond to the assigned pick uncertainties. The black lines are the calculated travel times.

(c) The black lines are the boundaries between different velocity layers of the *P* wave velocity model. The colored lines mark the modeled raypaths of the corresponding picked phases shown in the panel above.

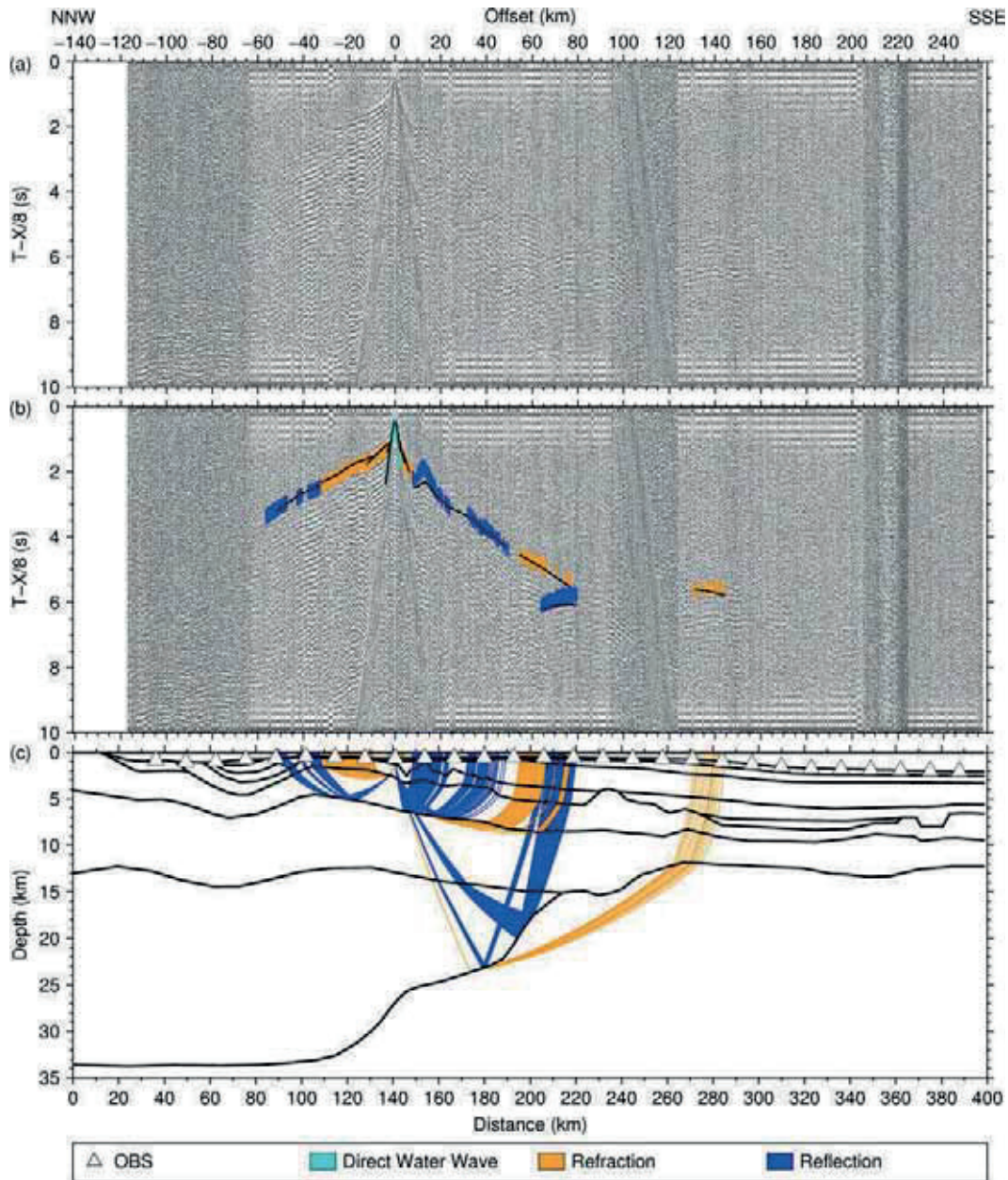


Figure B.9: Seismic section, picks and modeled raypaths of OBS 9 (AWI-20100300)
 (a) Seismic section of the hydrophone component with a reduction velocity of 8 km/s.
 (b) The colored lines mark the picked phases within the seismic section. The vertical lengths of the picks correspond to the assigned pick uncertainties. The black lines are the calculated travel times.
 (c) The black lines are the boundaries between different velocity layers of the *P* wave velocity model. The colored lines mark the modeled raypaths of the corresponding picked phases shown in the panel above.

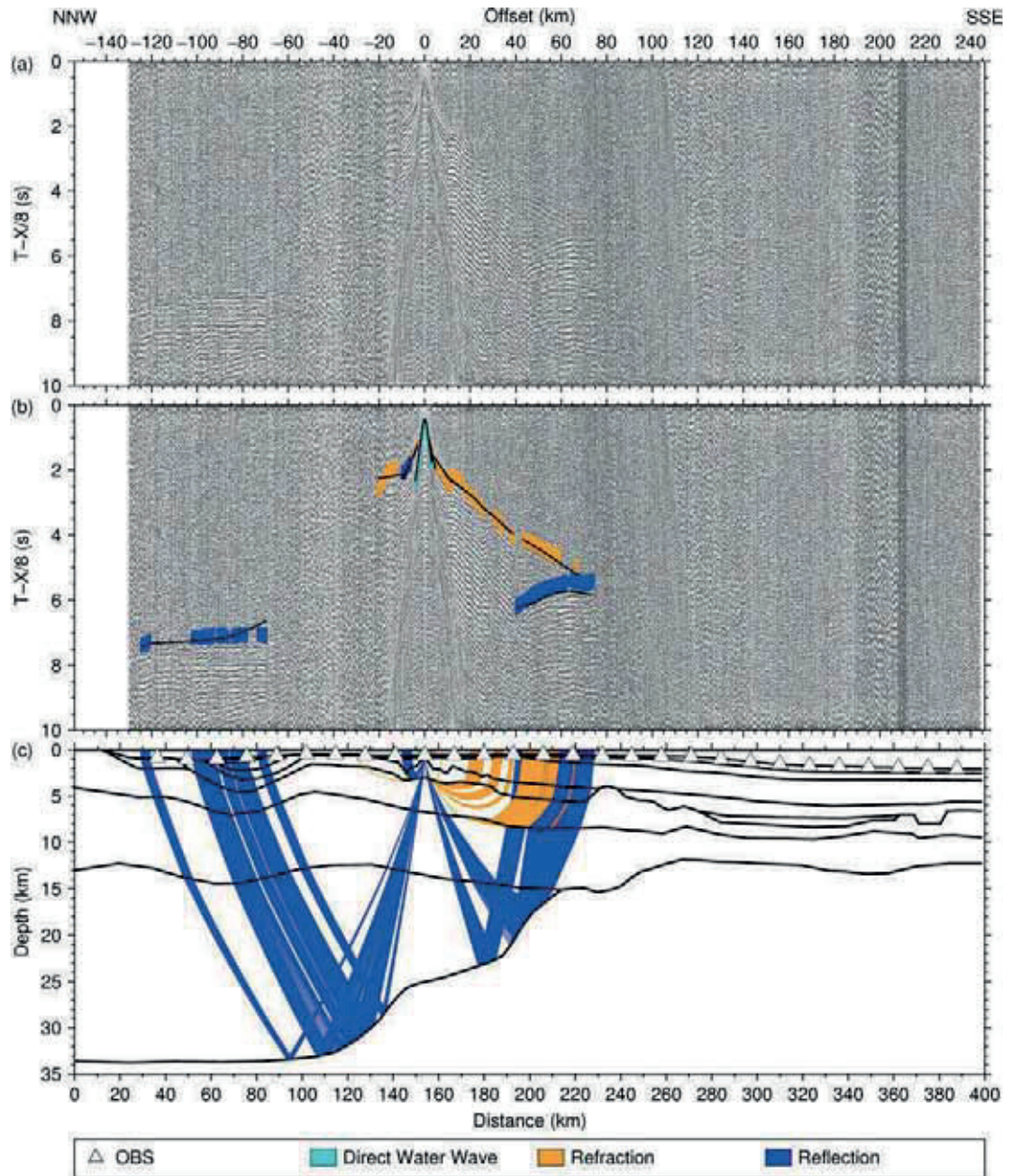


Figure B.10: Seismic section, picks and modeled raypaths of OBS 10 (AWI-20100300)

(a) Seismic section of the hydrophone component with a reduction velocity of 8 km/s.

(b) The colored lines mark the picked phases within the seismic section. The vertical lengths of the picks correspond to the assigned pick uncertainties. The black lines are the calculated travel times.

(c) The black lines are the boundaries between different velocity layers of the P wave velocity model. The colored lines mark the modeled raypaths of the corresponding picked phases shown in the panel above.

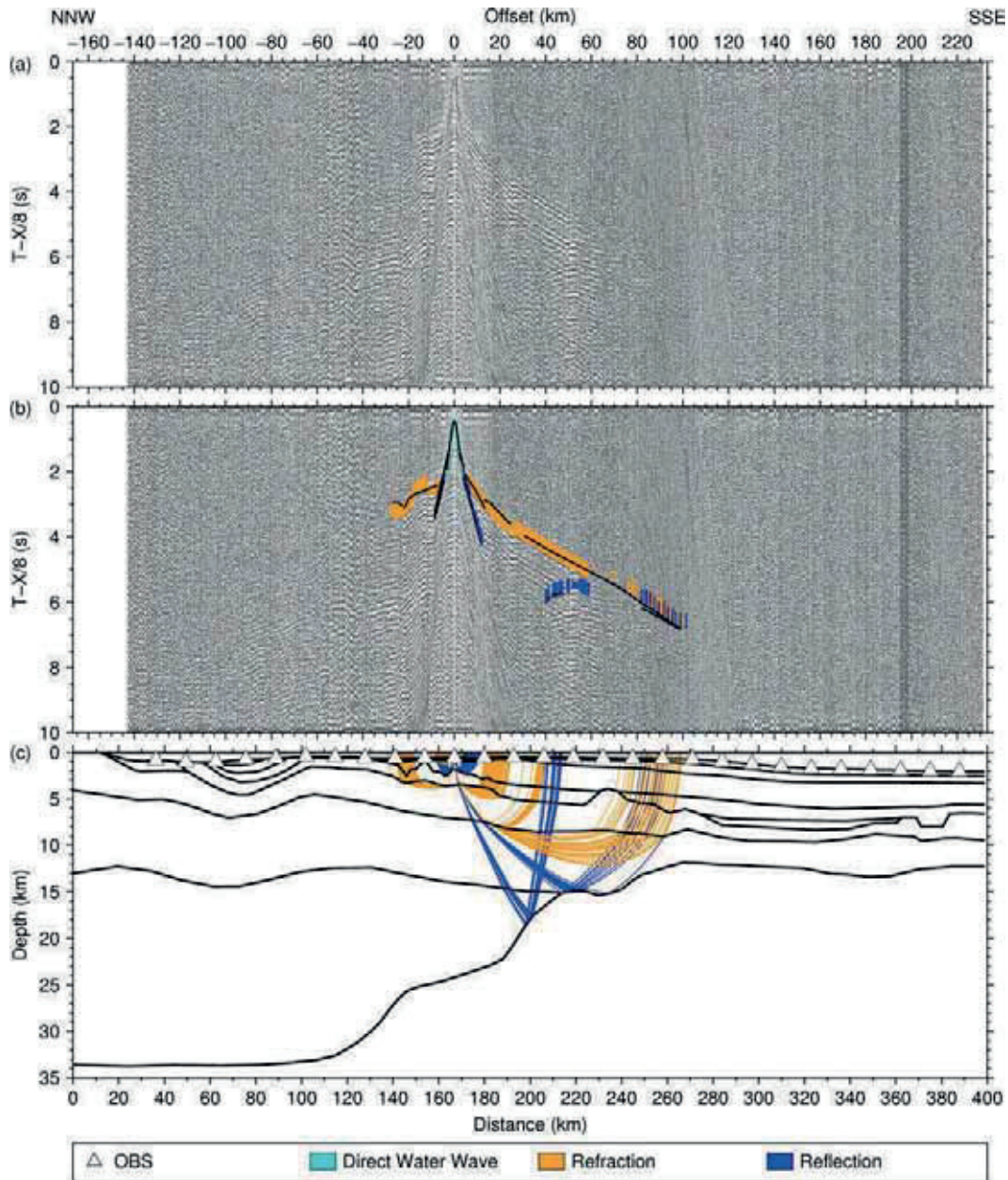


Figure B.11: Seismic section, picks and modeled raypaths of OBS 11 (AWI-20100300)
 (a) Seismic section of the hydrophone component with a reduction velocity of 8 km/s.
 (b) The colored lines mark the picked phases within the seismic section. The vertical lengths of the picks correspond to the assigned pick uncertainties. The black lines are the calculated travel times.
 (c) The black lines are the boundaries between different velocity layers of the *P* wave velocity model. The colored lines mark the modeled raypaths of the corresponding picked phases shown in the panel above.

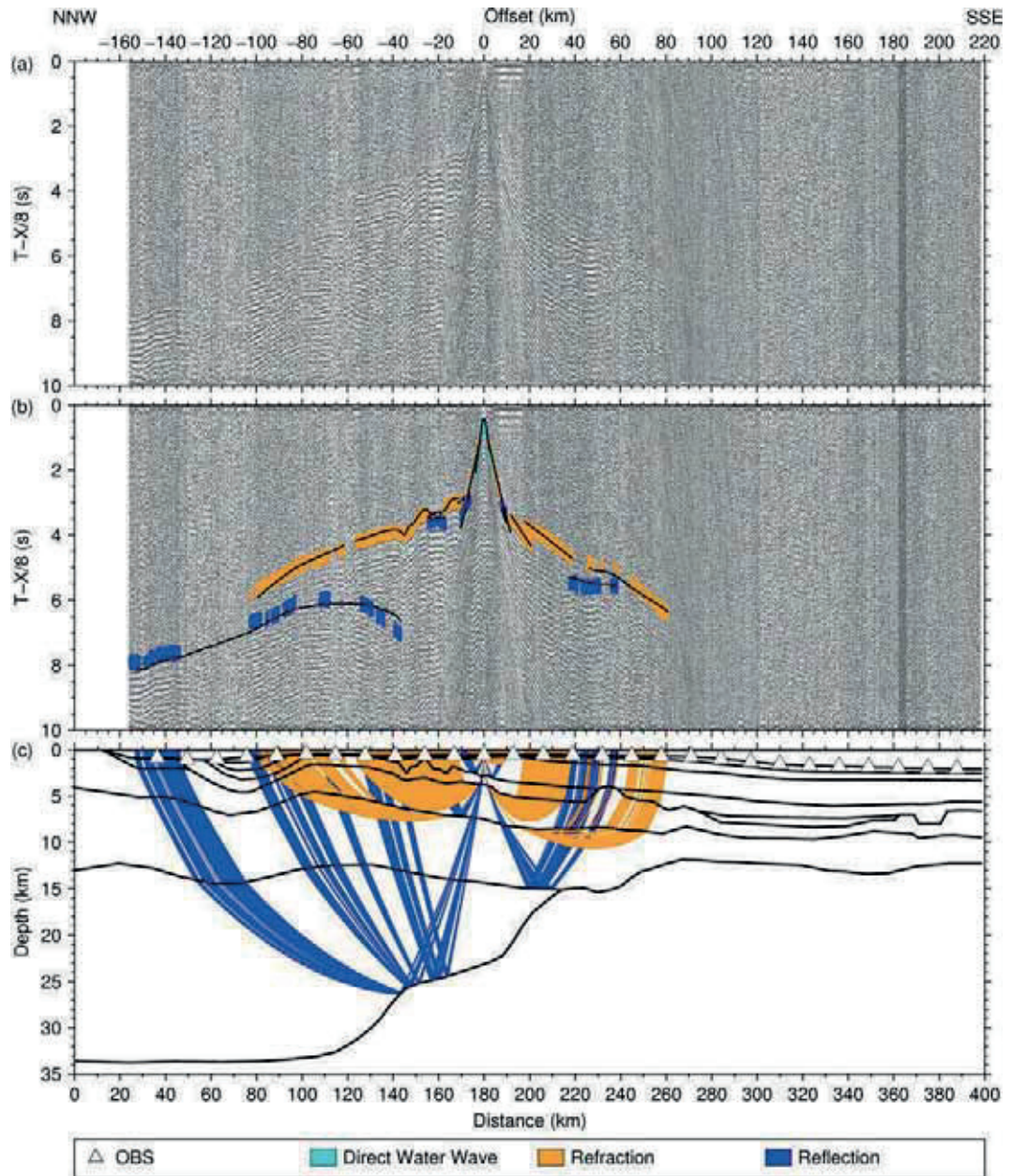


Figure B.12: Seismic section, picks and modeled raypaths of OBS 12 (AWI-20100300)

(a) Seismic section of the hydrophone component with a reduction velocity of 8 km/s.

(b) The colored lines mark the picked phases within the seismic section. The vertical lengths of the picks correspond to the assigned pick uncertainties. The black lines are the calculated travel times.

(c) The black lines are the boundaries between different velocity layers of the *P* wave velocity model. The colored lines mark the modeled raypaths of the corresponding picked phases shown in the panel above.

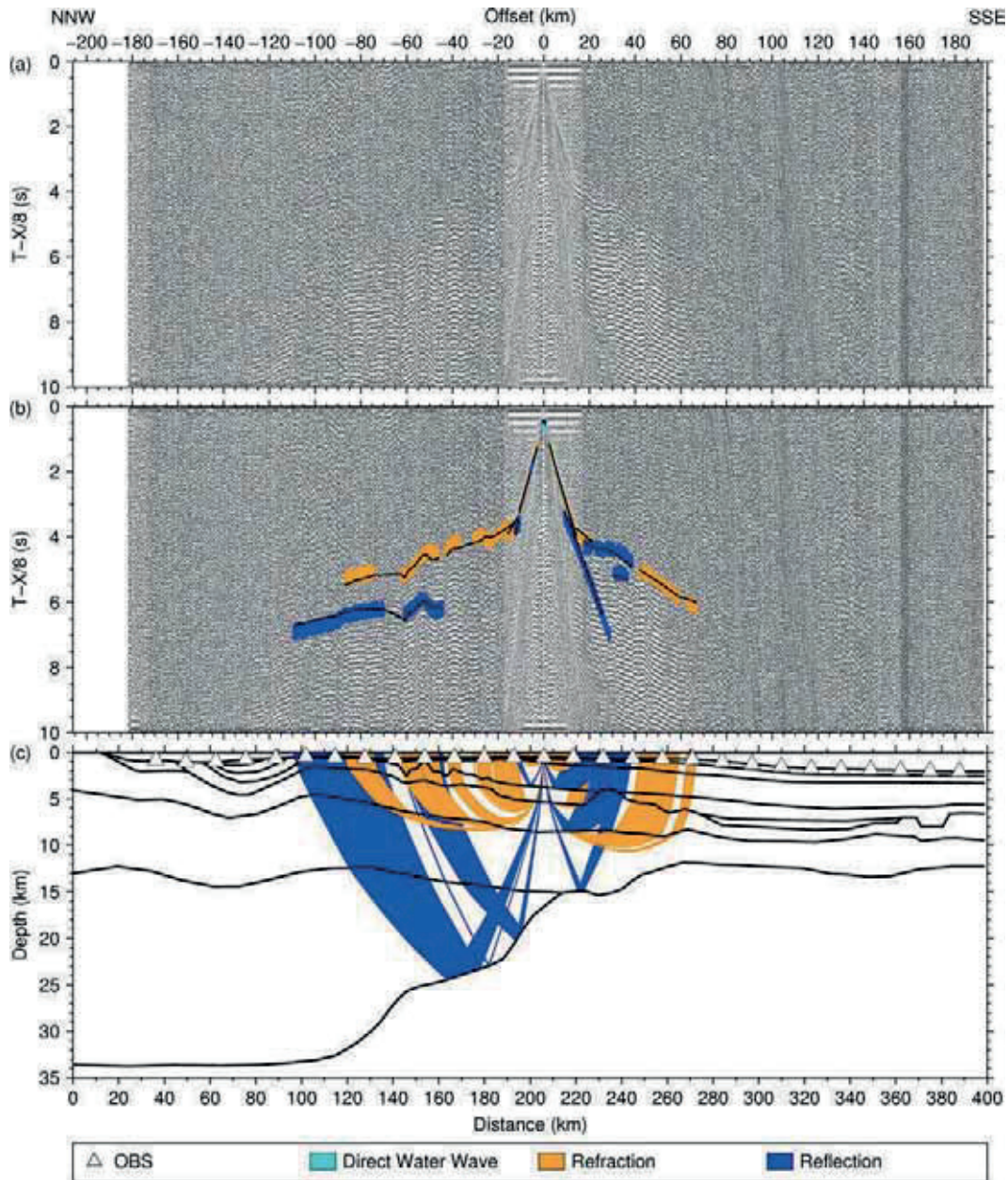


Figure B.13: Seismic section, picks and modeled raypaths of OBS 14 (AWI-20100300)
 (a) Seismic section of the z-component (seismometer) with a reduction velocity of 8 km/s.
 (b) The colored lines mark the picked phases within the seismic section. The vertical lengths of the picks correspond to the assigned pick uncertainties. The black lines are the calculated travel times.
 (c) The black lines are the boundaries between different velocity layers of the *P* wave velocity model. The colored lines mark the modeled raypaths of the corresponding picked phases shown in the panel above.

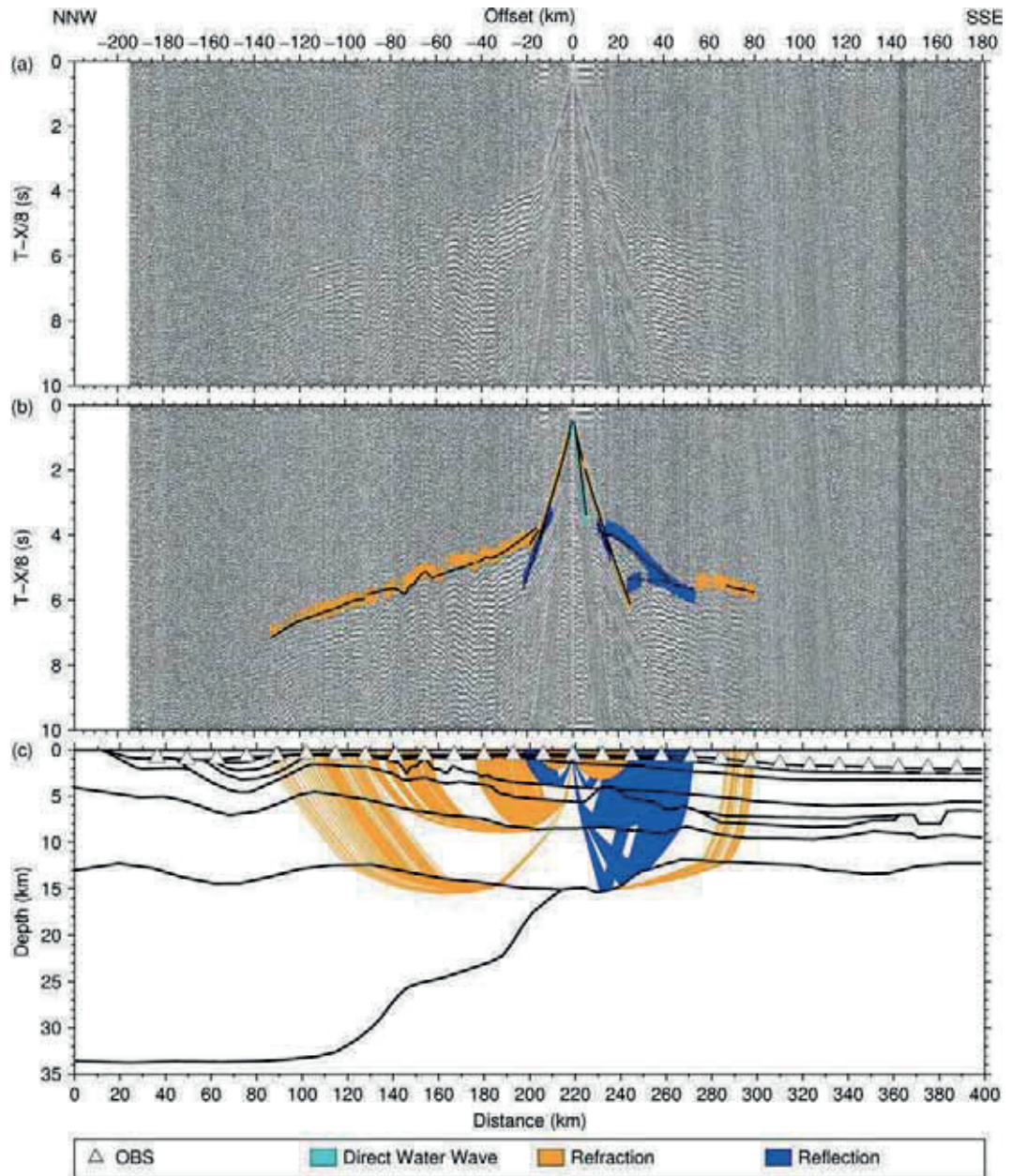


Figure B.14: Seismic section, picks and modeled raypaths of OBS 15 (AWI-20100300)

(a) Seismic section of the hydrophone component with a reduction velocity of 8 km/s.

(b) The colored lines mark the picked phases within the seismic section. The vertical lengths of the picks correspond to the assigned pick uncertainties. The black lines are the calculated travel times.

(c) The black lines are the boundaries between different velocity layers of the *P* wave velocity model. The colored lines mark the modeled raypaths of the corresponding picked phases shown in the panel above.

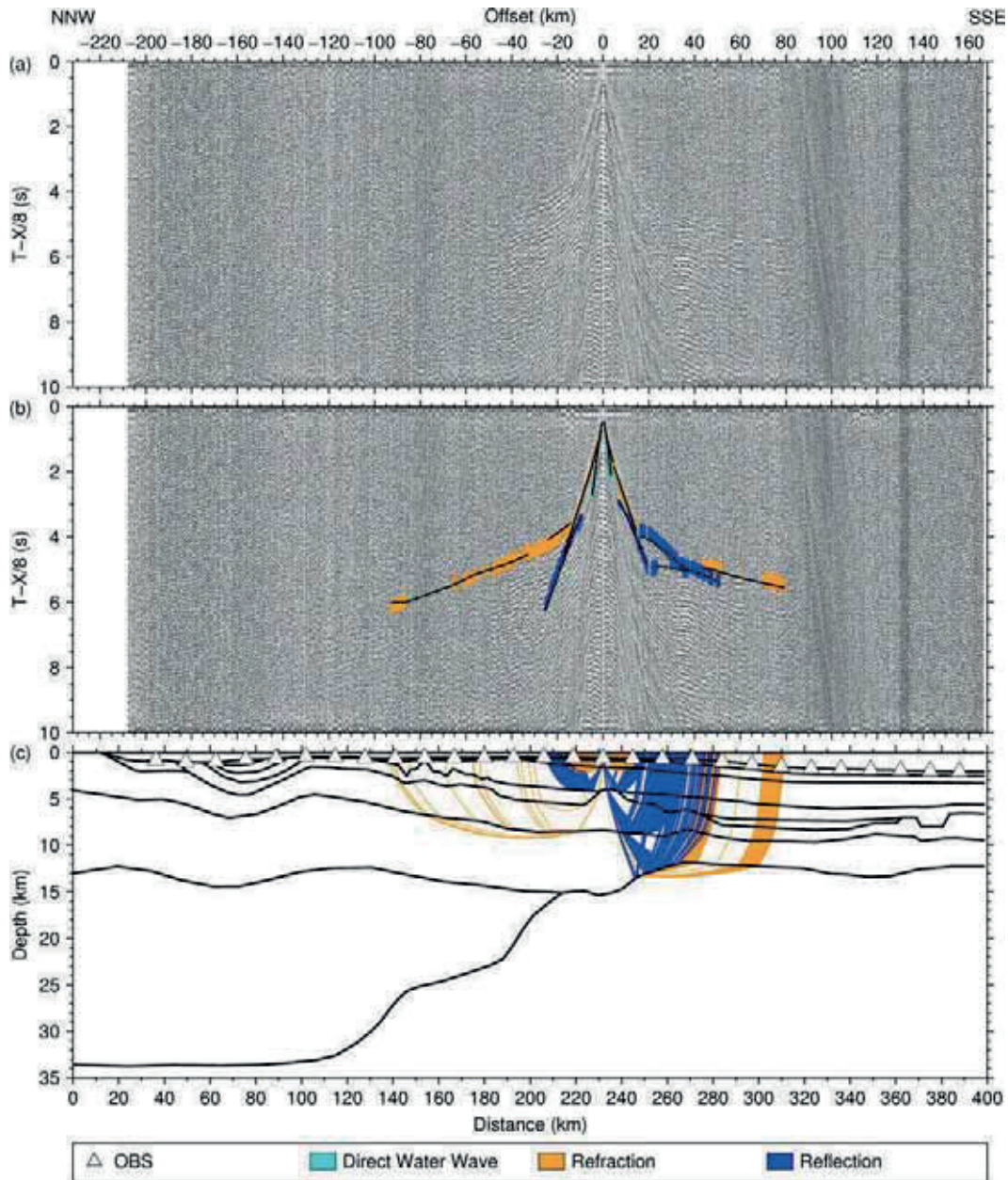


Figure B.15: Seismic section, picks and modeled raypaths of OBS 16 (AWI-20100300)
 (a) Seismic section of the hydrophone component with a reduction velocity of 8 km/s.
 (b) The colored lines mark the picked phases within the seismic section. The vertical lengths of the picks correspond to the assigned pick uncertainties. The black lines are the calculated travel times.
 (c) The black lines are the boundaries between different velocity layers of the *P* wave velocity model. The colored lines mark the modeled raypaths of the corresponding picked phases shown in the panel above.

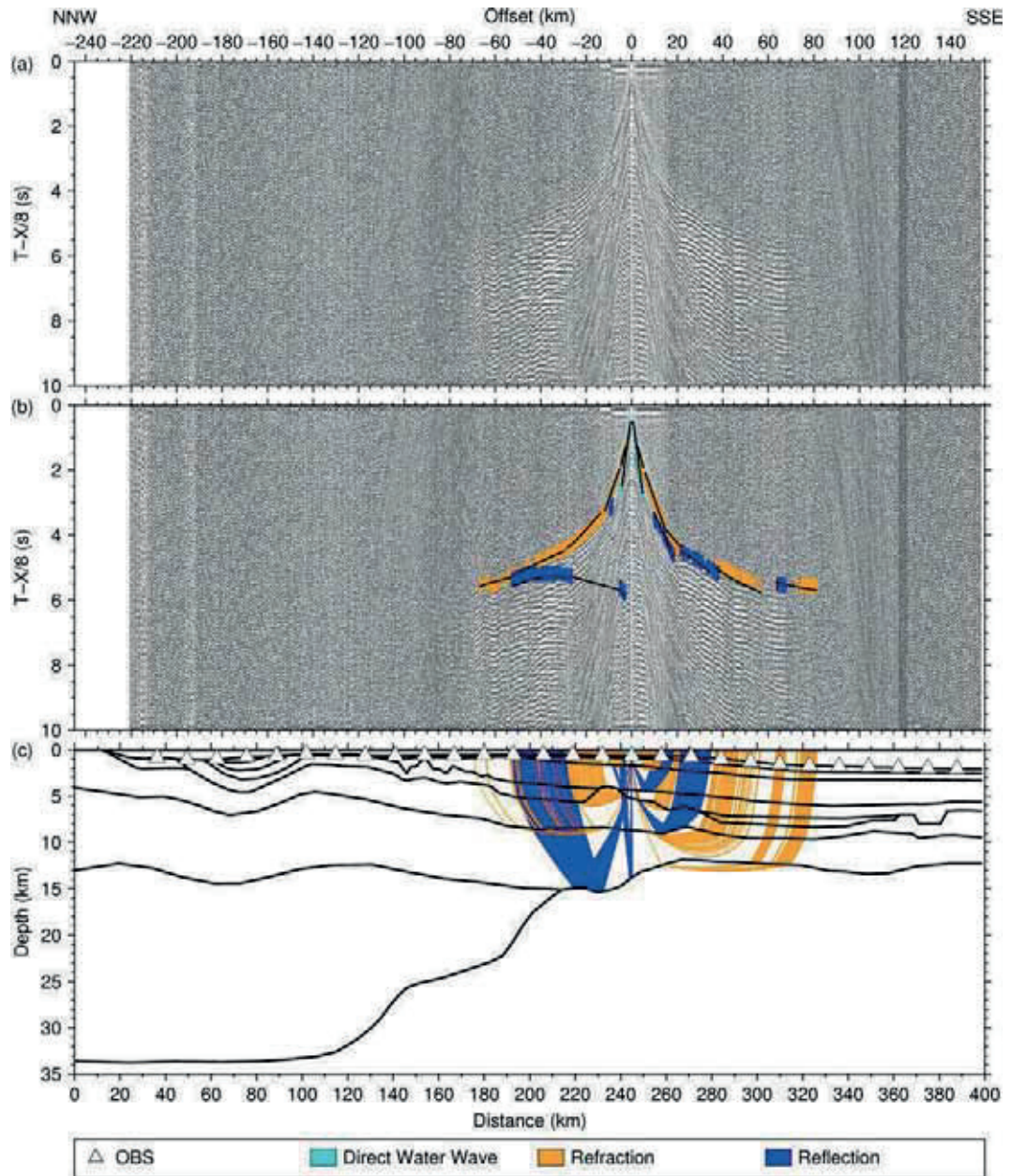


Figure B.16: Seismic section, picks and modeled raypaths of OBS 17 (AWI-20100300)

(a) Seismic section of the hydrophone component with a reduction velocity of 8 km/s.

(b) The colored lines mark the picked phases within the seismic section. The vertical lengths of the picks correspond to the assigned pick uncertainties. The black lines are the calculated travel times.

(c) The black lines are the boundaries between different velocity layers of the *P* wave velocity model. The colored lines mark the modeled raypaths of the corresponding picked phases shown in the panel above.

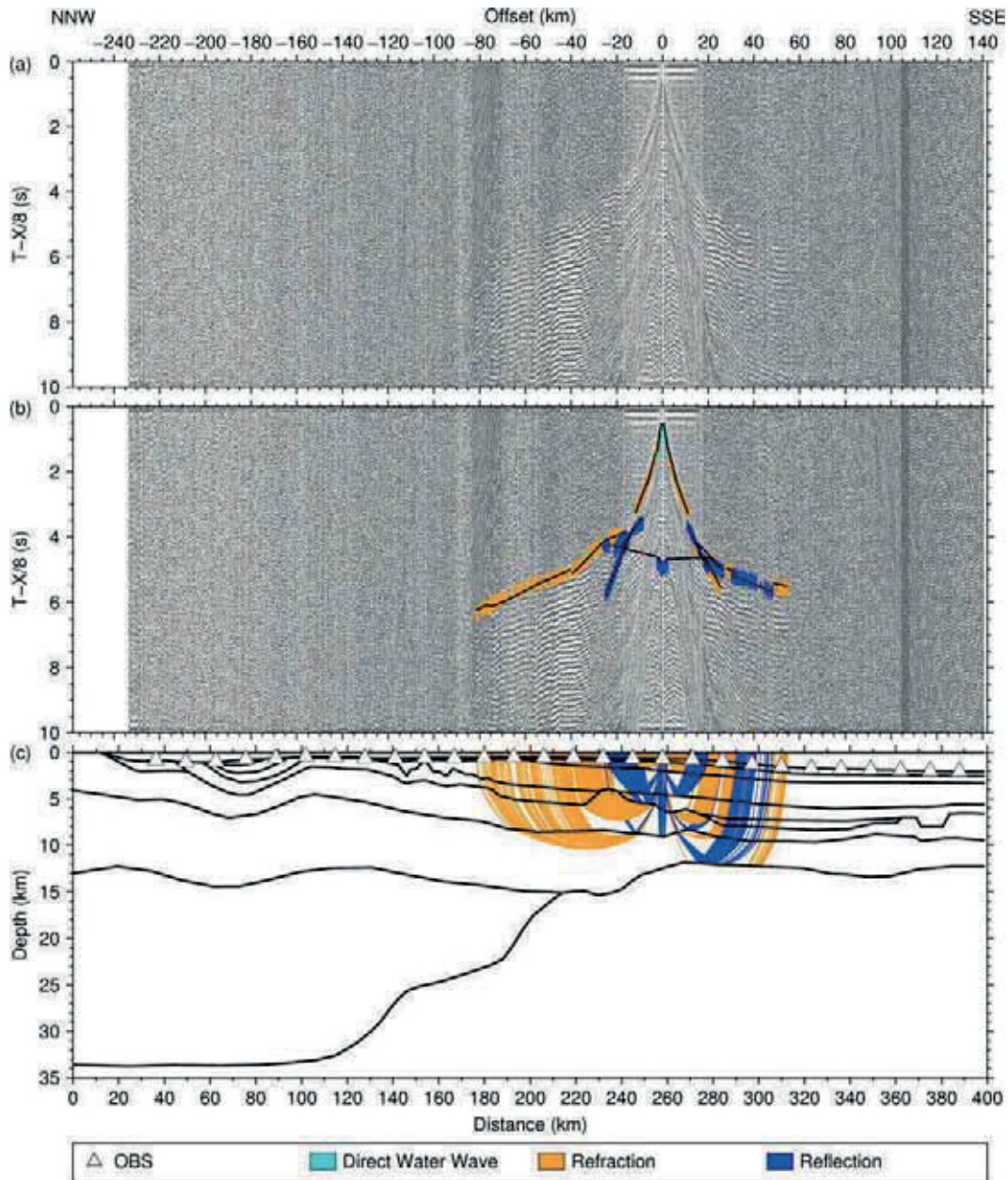


Figure B.17: Seismic section, picks and modeled raypaths of OBS 18 (AWI-20100300)
 (a) Seismic section of the hydrophone component with a reduction velocity of 8 km/s.
 (b) The colored lines mark the picked phases within the seismic section. The vertical lengths of the picks correspond to the assigned pick uncertainties. The black lines are the calculated travel times.
 (c) The black lines are the boundaries between different velocity layers of the P wave velocity model. The colored lines mark the modeled raypaths of the corresponding picked phases shown in the panel above.

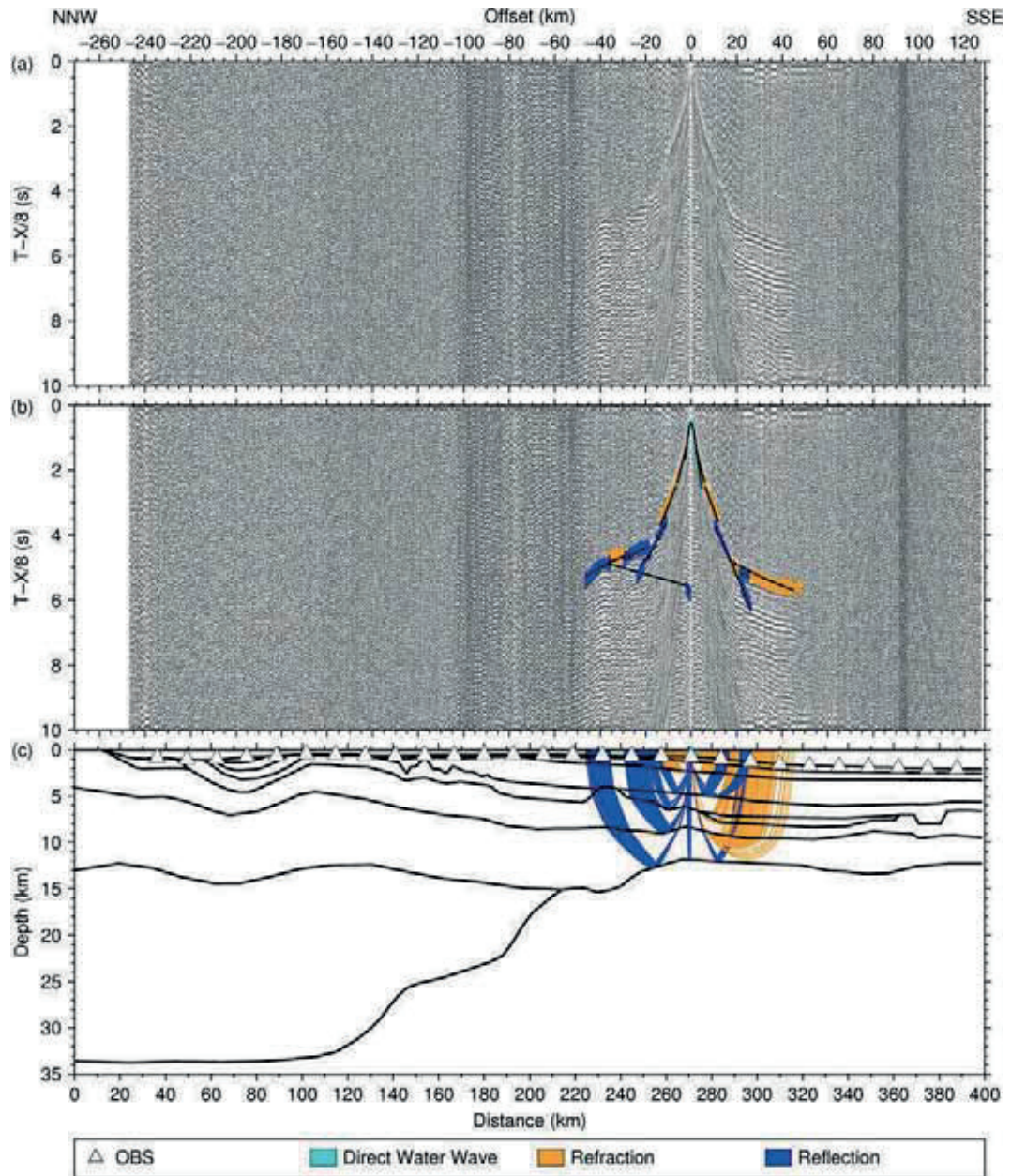


Figure B.18: Seismic section, picks and modeled raypaths of OBS 19 (AWI-20100300)

(a) Seismic section of the hydrophone component with a reduction velocity of 8 km/s.

(b) The colored lines mark the picked phases within the seismic section. The vertical lengths of the picks correspond to the assigned pick uncertainties. The black lines are the calculated travel times.

(c) The black lines are the boundaries between different velocity layers of the *P* wave velocity model. The colored lines mark the modeled raypaths of the corresponding picked phases shown in the panel above.

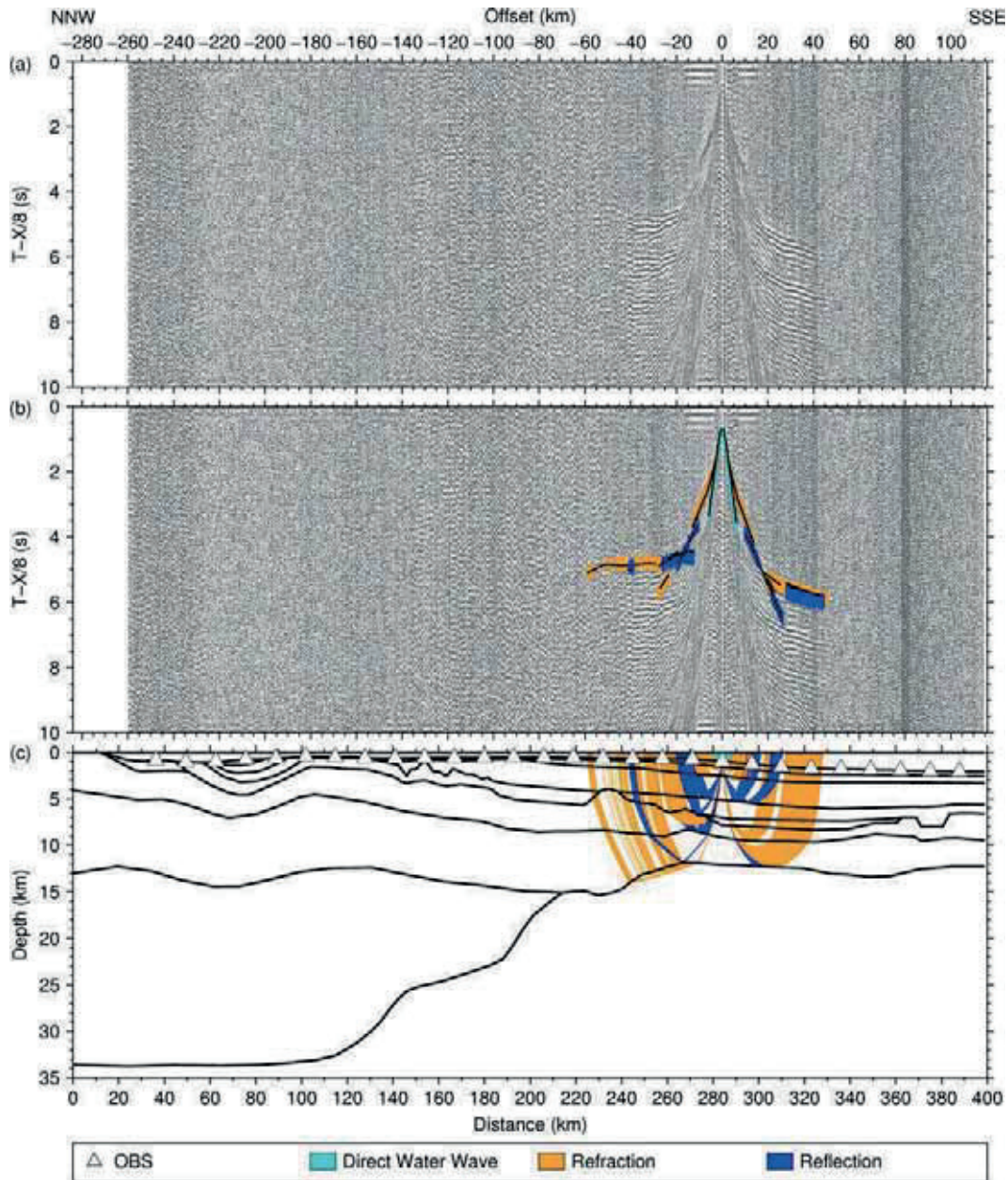


Figure B.19: Seismic section, picks and modeled raypaths of OBS 20 (AWI-20100300)
 (a) Seismic section of the hydrophone component with a reduction velocity of 8 km/s.
 (b) The colored lines mark the picked phases within the seismic section. The vertical lengths of the picks correspond to the assigned pick uncertainties. The black lines are the calculated travel times.
 (c) The black lines are the boundaries between different velocity layers of the P wave velocity model. The colored lines mark the modeled raypaths of the corresponding picked phases shown in the panel above.

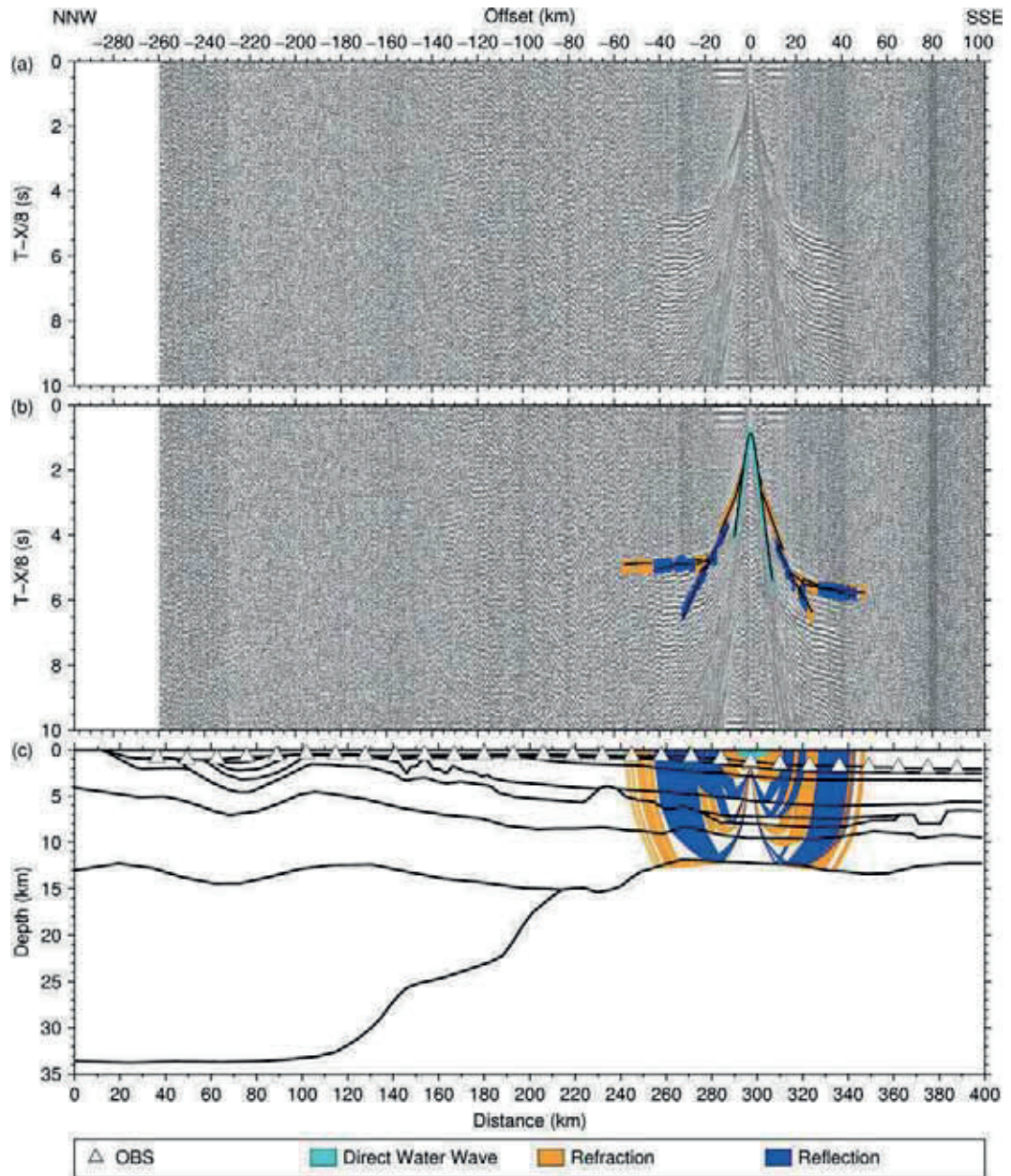


Figure B.20: Seismic section, picks and modeled raypaths of OBS 21 (AWI-20100300)

(a) Seismic section of the hydrophone component with a reduction velocity of 8 km/s.

(b) The colored lines mark the picked phases within the seismic section. The vertical lengths of the picks correspond to the assigned pick uncertainties. The black lines are the calculated travel times.

(c) The black lines are the boundaries between different velocity layers of the *P* wave velocity model. The colored lines mark the modeled raypaths of the corresponding picked phases shown in the panel above.

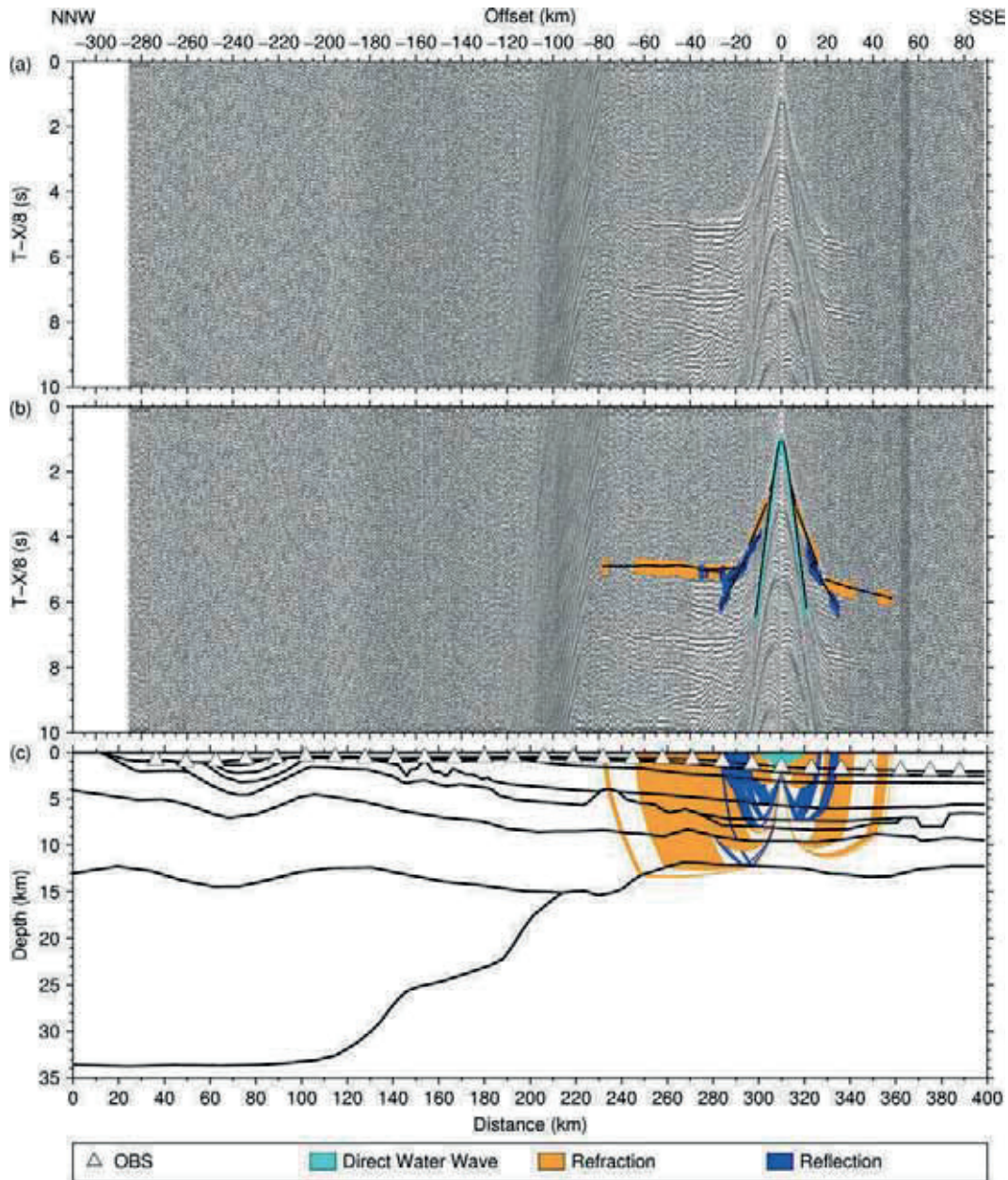


Figure B.21: Seismic section, picks and modeled raypaths of OBS 22 (AWI-20100300)
 (a) Seismic section of the hydrophone component with a reduction velocity of 8 km/s.
 (b) The colored lines mark the picked phases within the seismic section. The vertical lengths of the picks correspond to the assigned pick uncertainties. The black lines are the calculated travel times.
 (c) The black lines are the boundaries between different velocity layers of the *P* wave velocity model. The colored lines mark the modeled raypaths of the corresponding picked phases shown in the panel above.

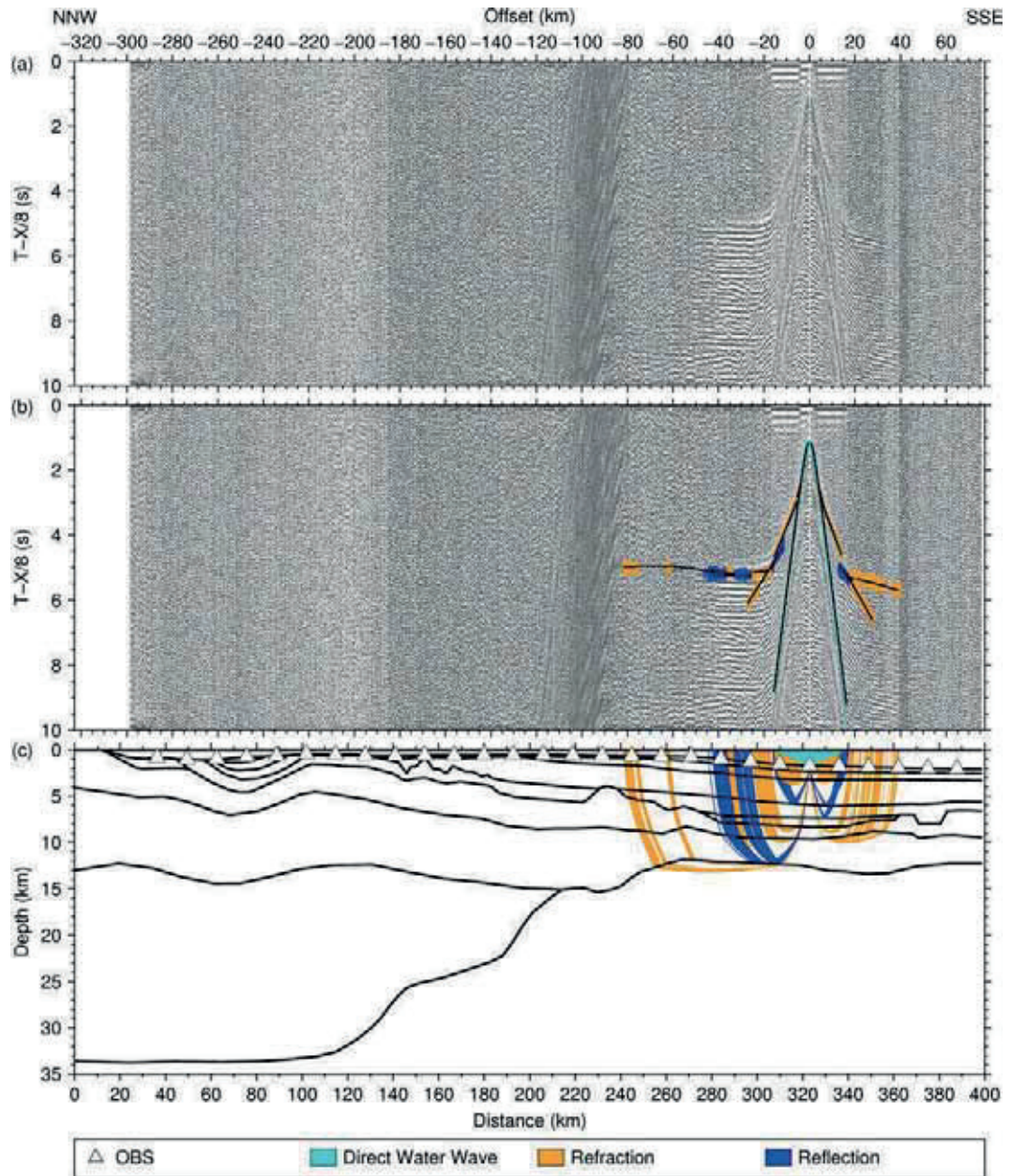


Figure B.22: Seismic section, picks and modeled raypaths of OBS 23 (AWI-20100300)

(a) Seismic section of the z-component (seismometer) with a reduction velocity of 8 km/s.

(b) The colored lines mark the picked phases within the seismic section. The vertical lengths of the picks correspond to the assigned pick uncertainties. The black lines are the calculated travel times.

(c) The black lines are the boundaries between different velocity layers of the *P* wave velocity model. The colored lines mark the modeled raypaths of the corresponding picked phases shown in the panel above.

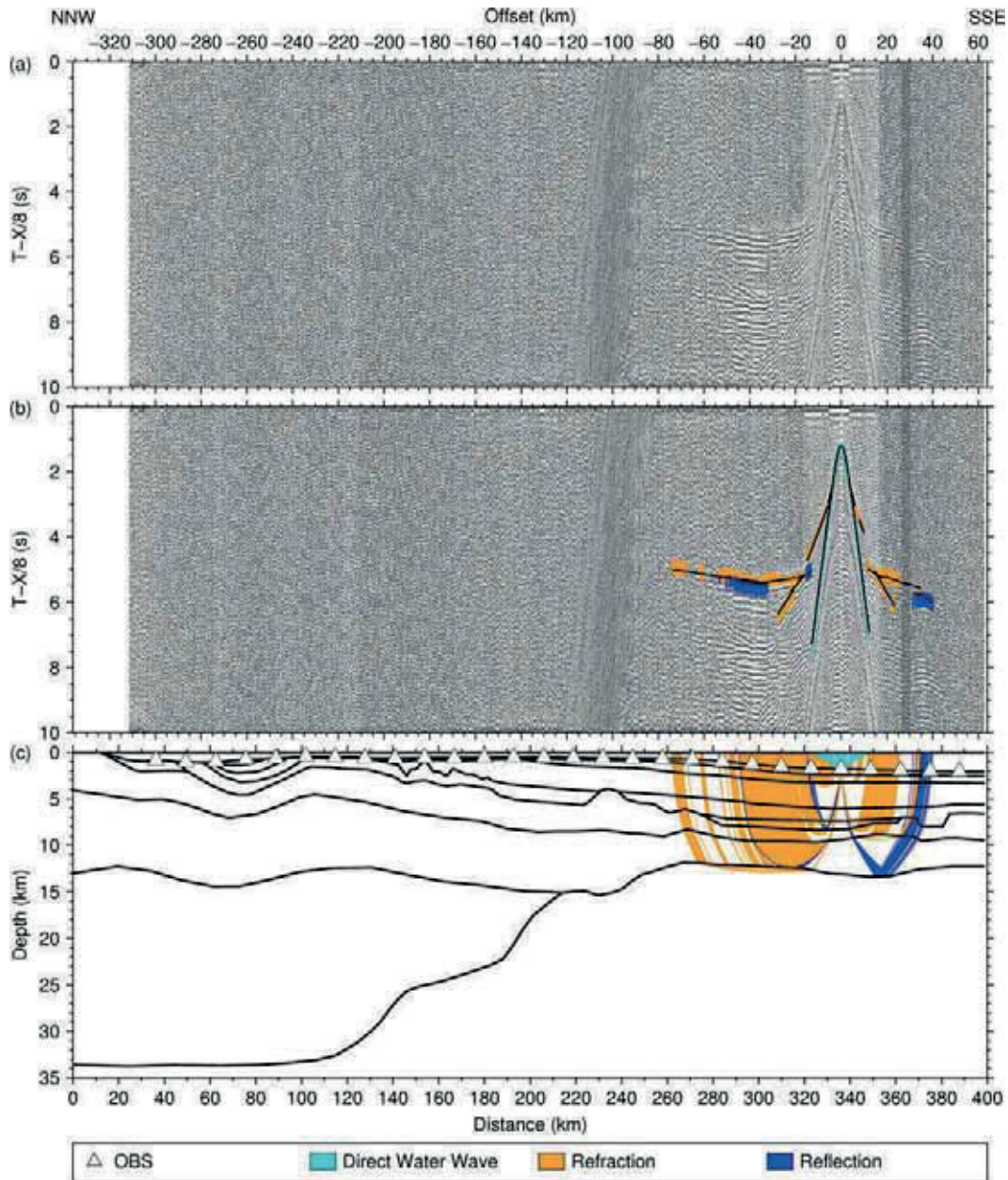


Figure B.23: Seismic section, picks and modeled raypaths of OBS 24 (AWI-20100300)
 (a) Seismic section of the z-component (seismometer) with a reduction velocity of 8 km/s.
 (b) The colored lines mark the picked phases within the seismic section. The vertical lengths of the picks correspond to the assigned pick uncertainties. The black lines are the calculated travel times.
 (c) The black lines are the boundaries between different velocity layers of the *P* wave velocity model. The colored lines mark the modeled raypaths of the corresponding picked phases shown in the panel above.

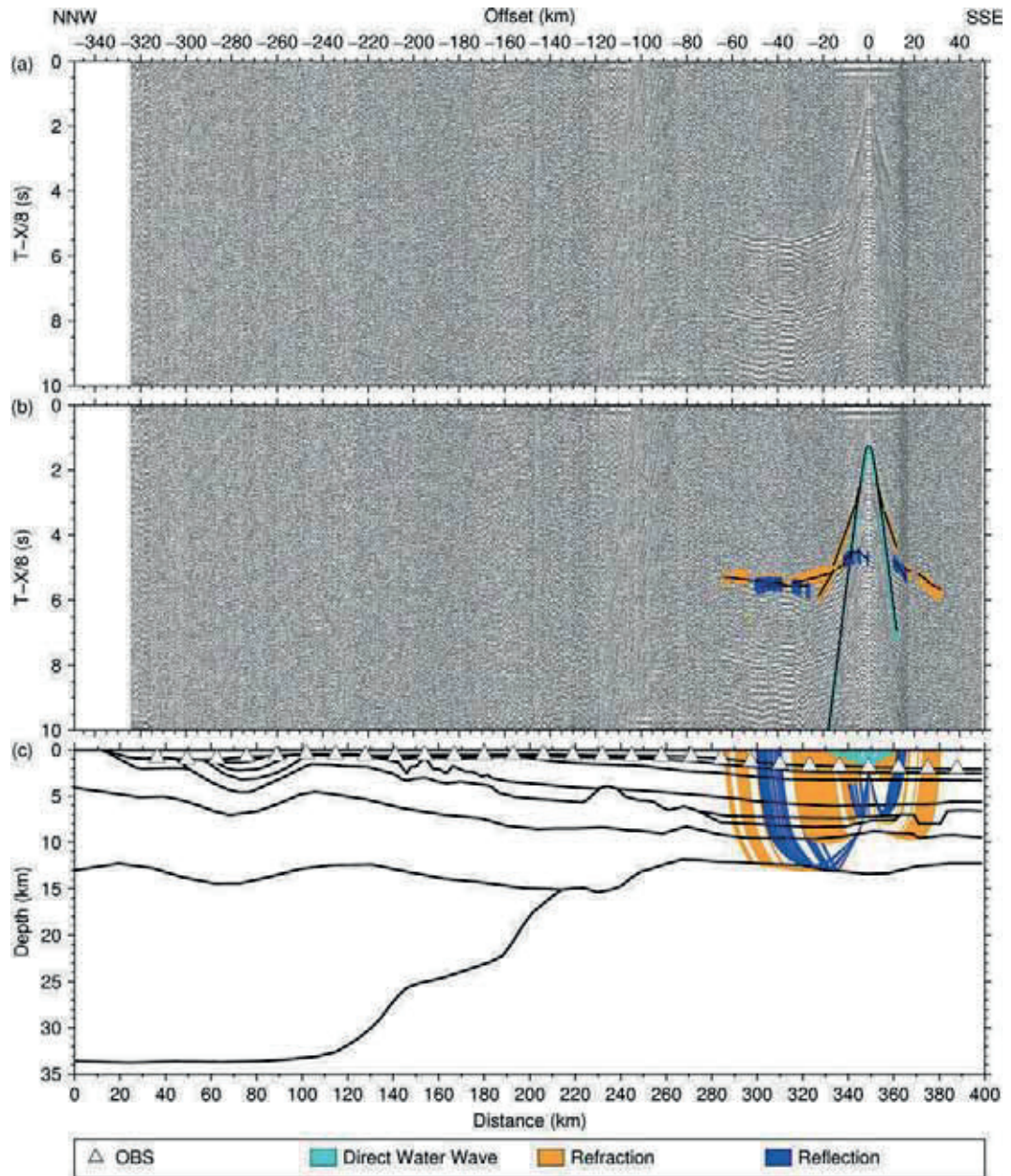


Figure B.24: Seismic section, picks and modeled raypaths of OBS 25 (AWI-20100300)

(a) Seismic section of the z-component (seismometer) with a reduction velocity of 8 km/s.

(b) The colored lines mark the picked phases within the seismic section. The vertical lengths of the picks correspond to the assigned pick uncertainties. The black lines are the calculated travel times.

(c) The black lines are the boundaries between different velocity layers of the *P* wave velocity model. The colored lines mark the modeled raypaths of the corresponding picked phases shown in the panel above.

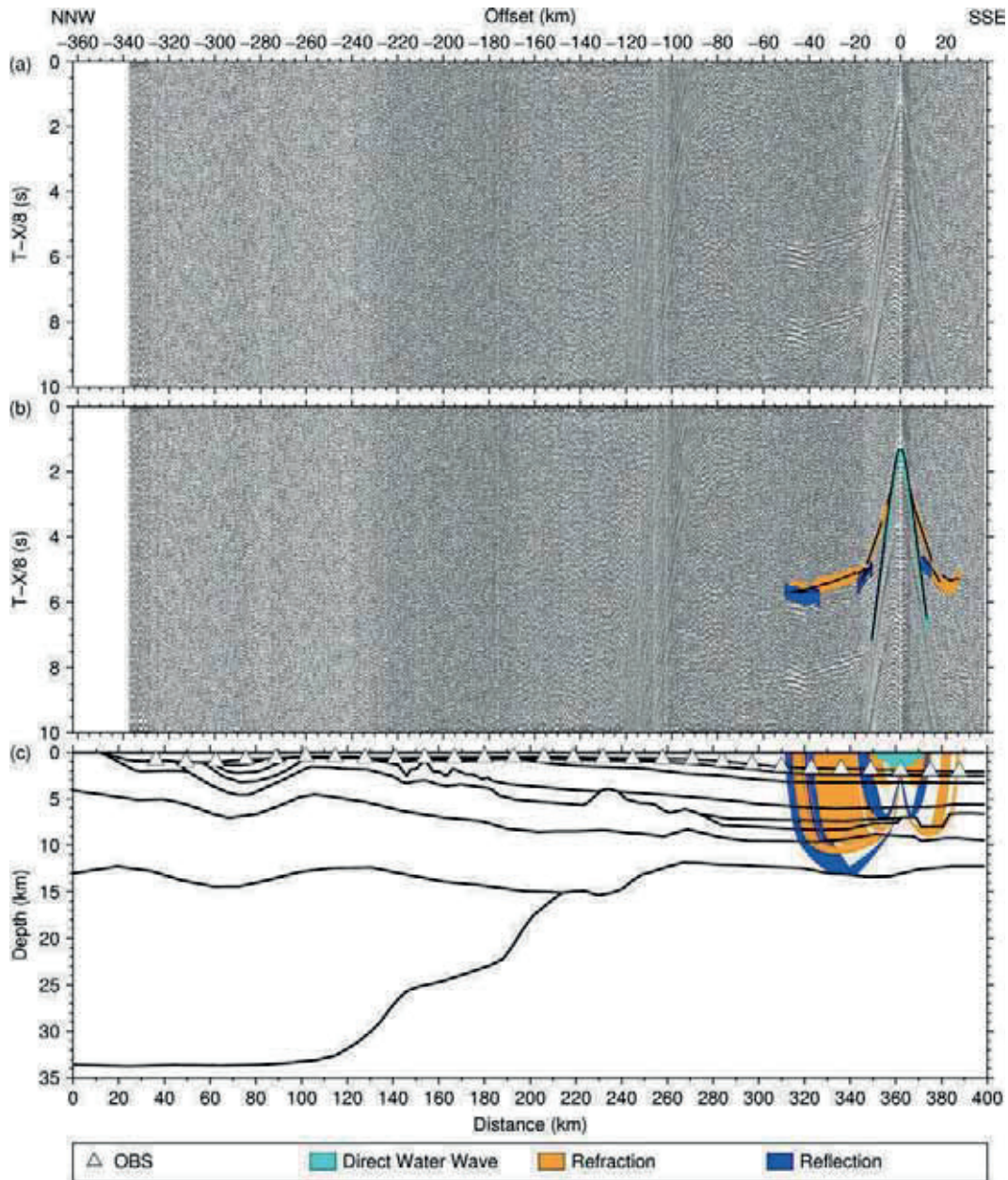


Figure B.25: Seismic section, picks and modeled raypaths of OBS 26 (AWI-20100300)
 (a) Seismic section of the hydrophone component with a reduction velocity of 8 km/s.
 (b) The colored lines mark the picked phases within the seismic section. The vertical lengths of the picks correspond to the assigned pick uncertainties. The black lines are the calculated travel times.
 (c) The black lines are the boundaries between different velocity layers of the P wave velocity model. The colored lines mark the modeled raypaths of the corresponding picked phases shown in the panel above.

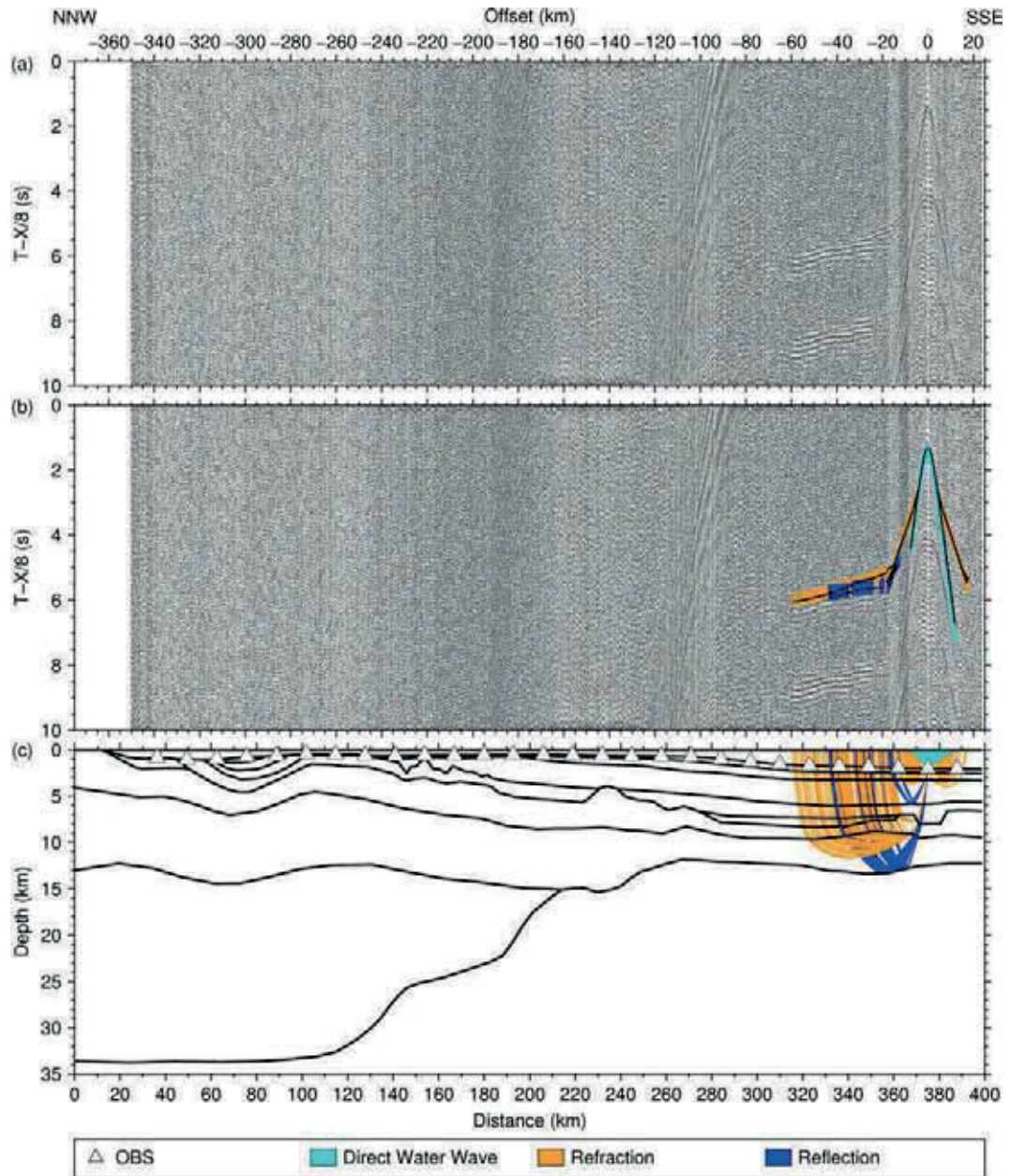


Figure B.26: Seismic section, picks and modeled raypaths of OBS 27 (AWI-20100300)

(a) Seismic section of the hydrophone component with a reduction velocity of 8 km/s.

(b) The colored lines mark the picked phases within the seismic section. The vertical lengths of the picks correspond to the assigned pick uncertainties. The black lines are the calculated travel times.

(c) The black lines are the boundaries between different velocity layers of the *P* wave velocity model. The colored lines mark the modeled raypaths of the corresponding picked phases shown in the panel above.

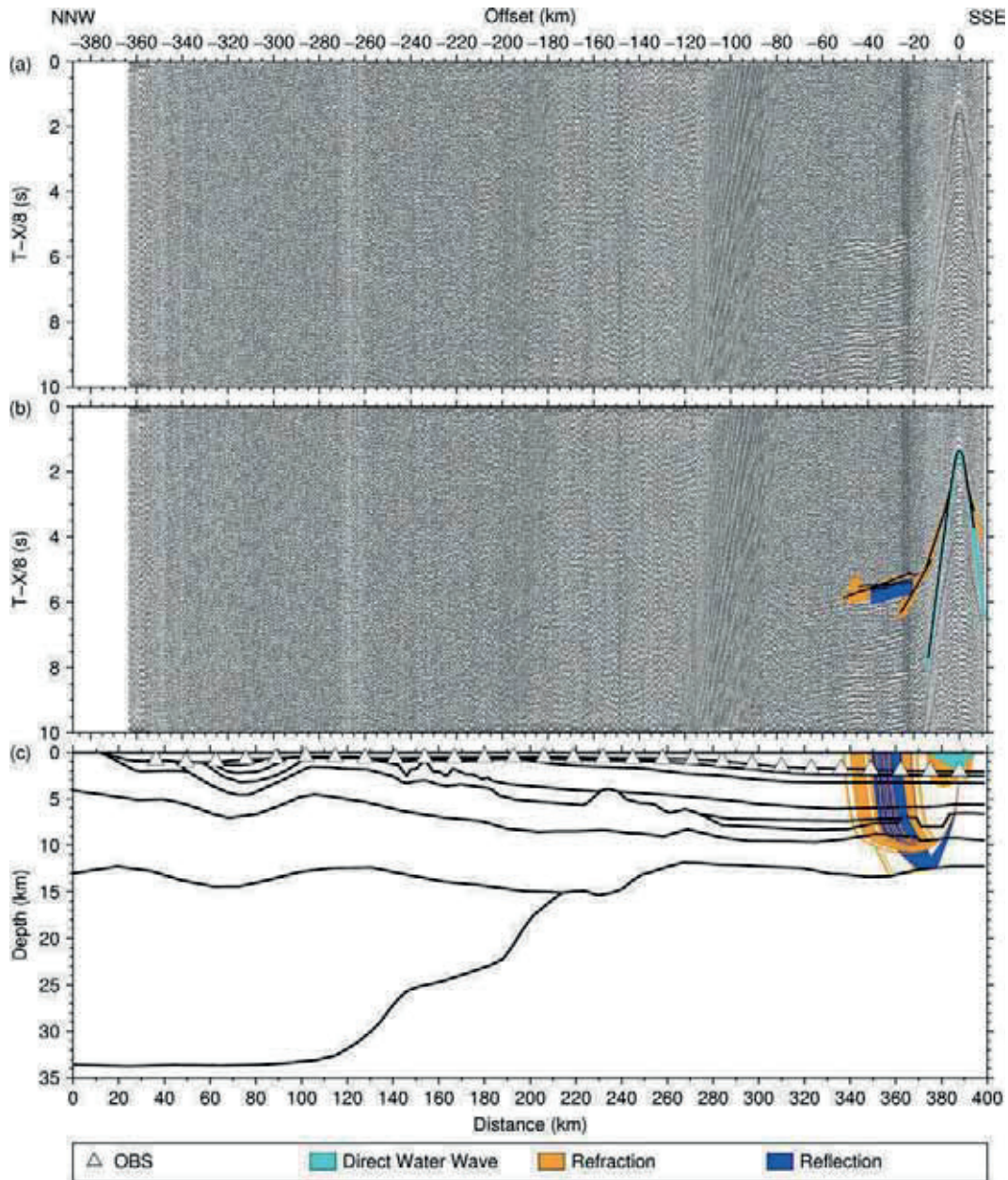


Figure B.27: Seismic section, picks and modeled raypaths of OBS 28 (AWI-20100300)
 (a) Seismic section of the z-component (seismometer) with a reduction velocity of 8 km/s.
 (b) The colored lines mark the picked phases within the seismic section. The vertical lengths of the picks correspond to the assigned pick uncertainties. The black lines are the calculated travel times.
 (c) The black lines are the boundaries between different velocity layers of the *P* wave velocity model. The colored lines mark the modeled raypaths of the corresponding picked phases shown in the panel above.

Seismic sections, profile AWI-20100450

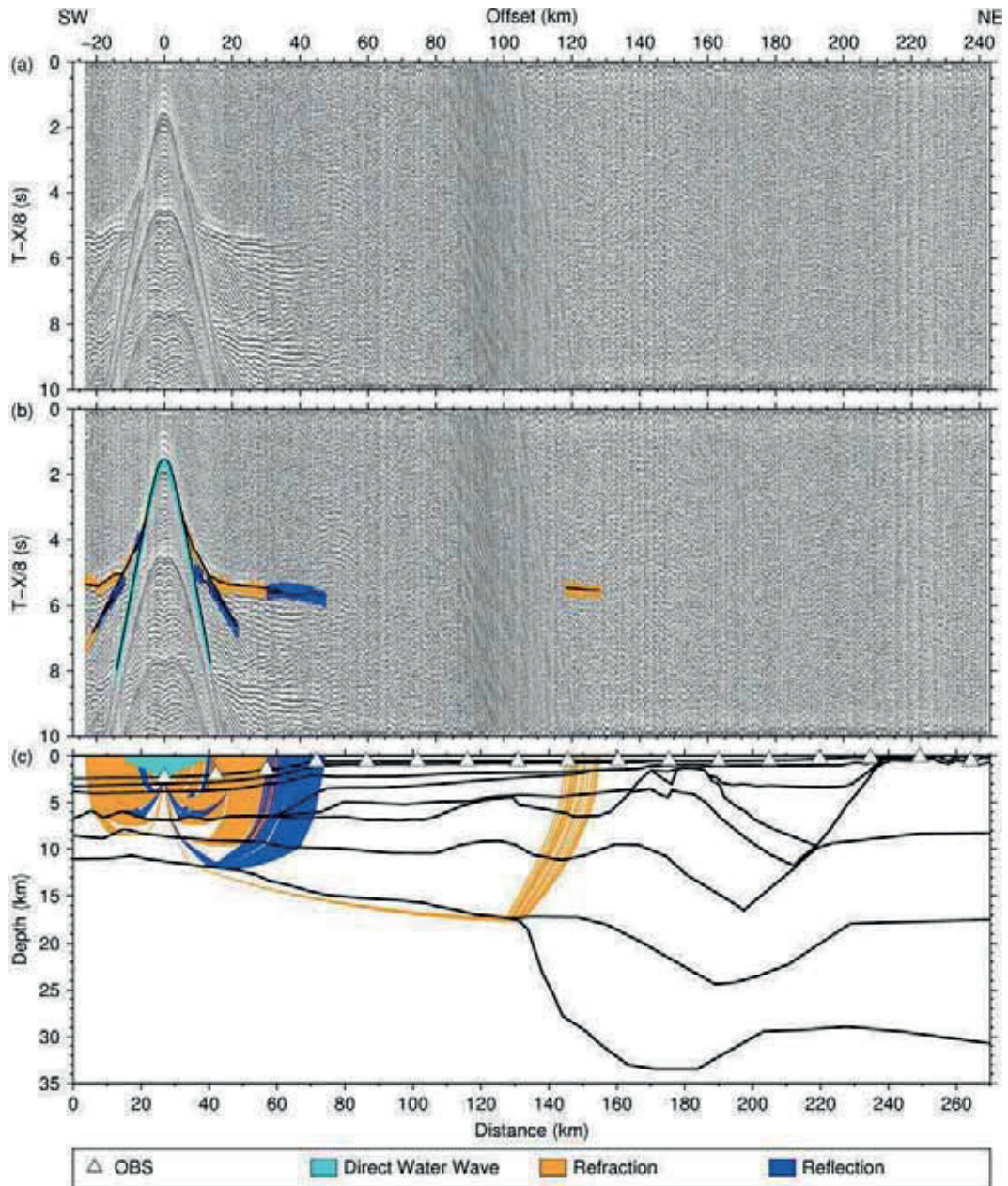


Figure C.1: Seismic section, picks and modeled raypaths of OBS 1 (AWI-20100450)

(a) Seismic section of the hydrophone component with a reduction velocity of 8 km/s.

(b) The colored lines mark the picked phases within the seismic section. The vertical lengths of the picks correspond to the assigned pick uncertainties. The black lines are the calculated travel times.

(c) The black lines are the boundaries between different velocity layers of the *P* wave velocity model. The colored lines mark the modeled raypaths of the corresponding picked phases shown in the panel above.

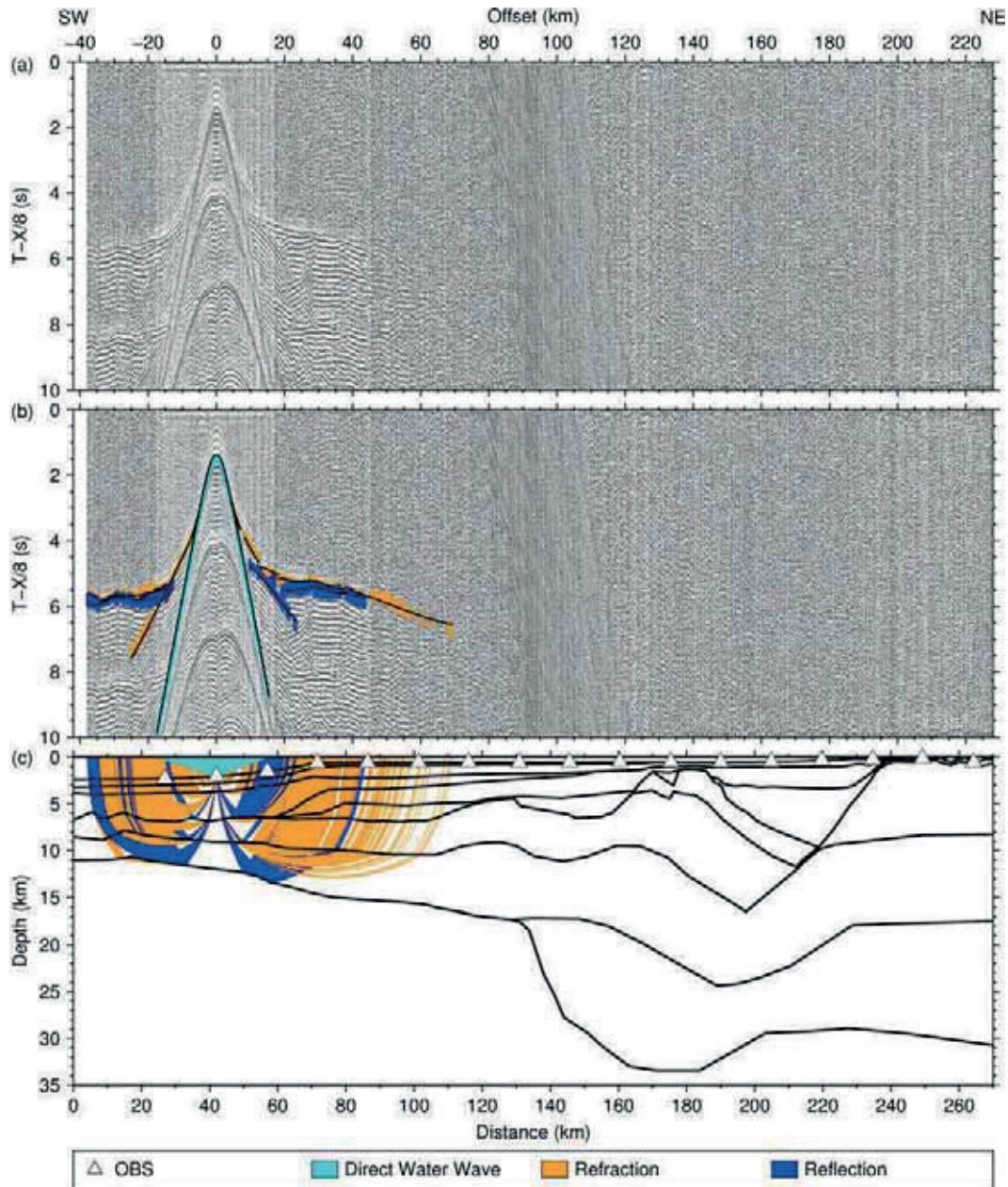


Figure C.2: Seismic section, picks and modeled raypaths of OBS 2 (AWI-20100450)

(a) Seismic section of the hydrophone component with a reduction velocity of 8 km/s.

(b) The colored lines mark the picked phases within the seismic section. The vertical lengths of the picks correspond to the assigned pick uncertainties. The black lines are the calculated travel times.

(c) The black lines are the boundaries between different velocity layers of the *P* wave velocity model. The colored lines mark the modeled raypaths of the corresponding picked phases shown in the panel above.

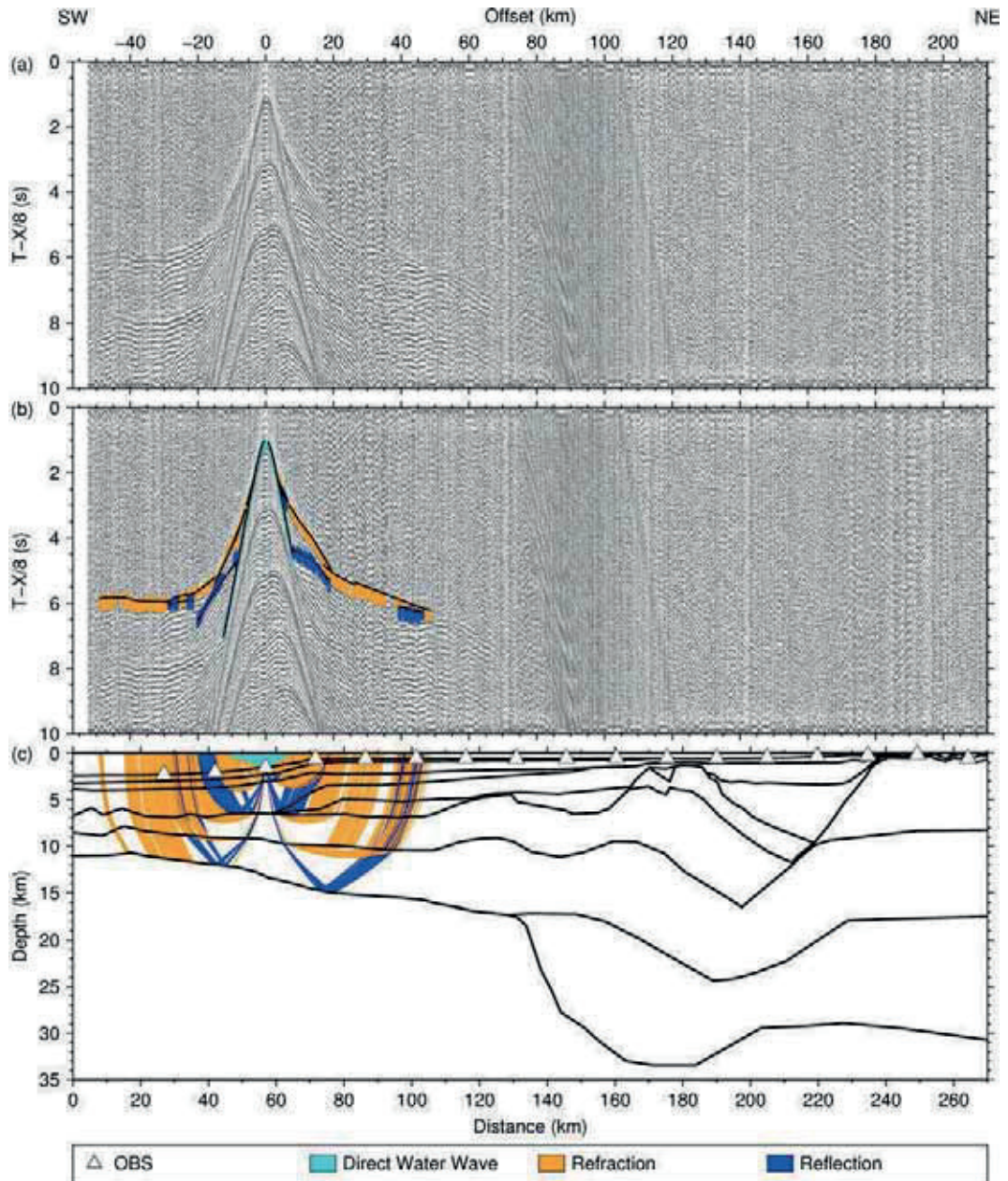


Figure C.3: Seismic section, picks and modeled raypaths of OBS 3 (AWI-20100450)
 (a) Seismic section of the hydrophone component with a reduction velocity of 8 km/s.
 (b) The colored lines mark the picked phases within the seismic section. The vertical lengths of the picks correspond to the assigned pick uncertainties. The black lines are the calculated travel times.
 (c) The black lines are the boundaries between different velocity layers of the P wave velocity model. The colored lines mark the modeled raypaths of the corresponding picked phases shown in the panel above.

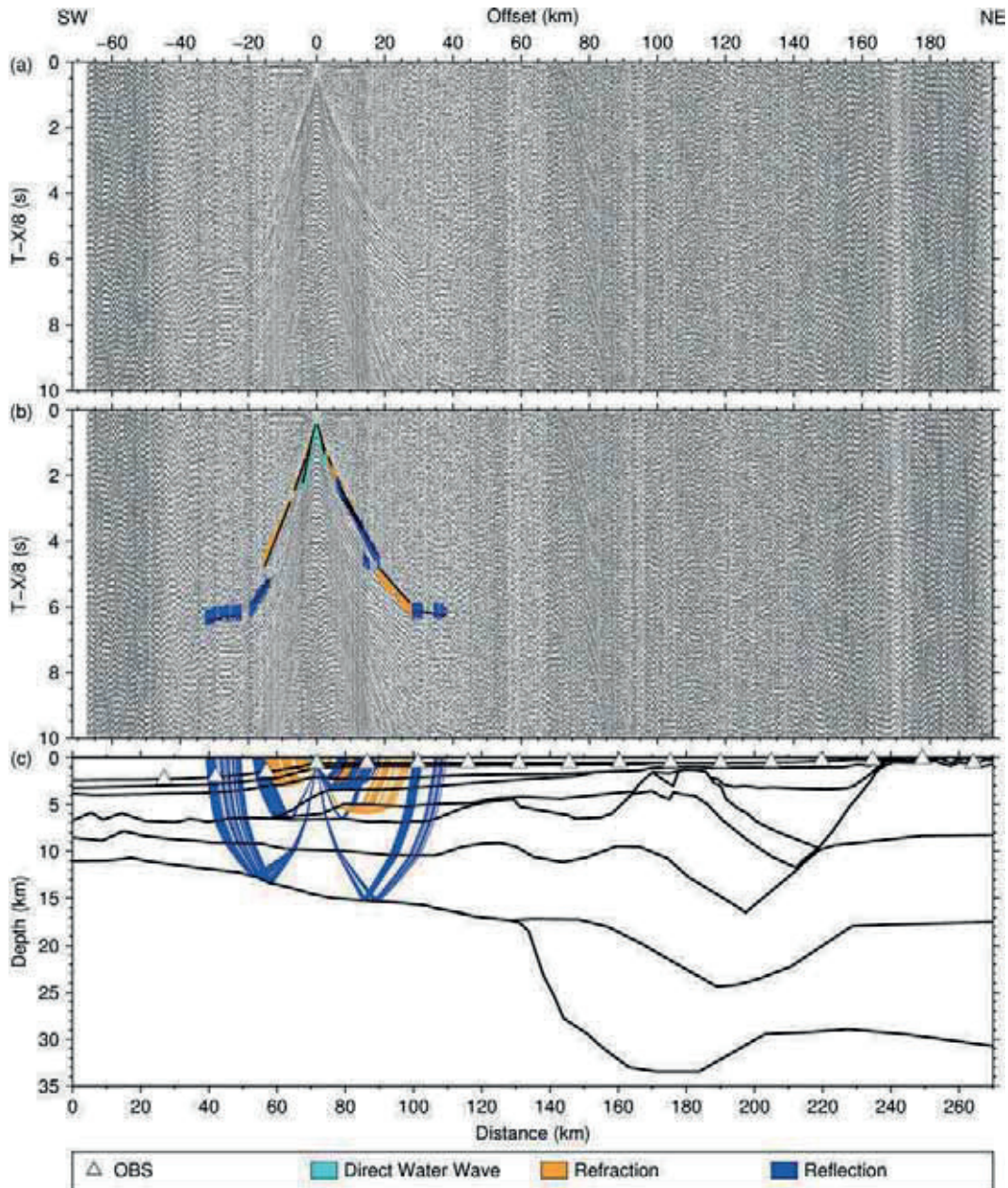


Figure C.4: Seismic section, picks and modeled raypaths of OBS 4 (AWI-20100450)

(a) Seismic section of the hydrophone component with a reduction velocity of 8 km/s.

(b) The colored lines mark the picked phases within the seismic section. The vertical lengths of the picks correspond to the assigned pick uncertainties. The black lines are the calculated travel times.

(c) The black lines are the boundaries between different velocity layers of the *P* wave velocity model. The colored lines mark the modeled raypaths of the corresponding picked phases shown in the panel above.

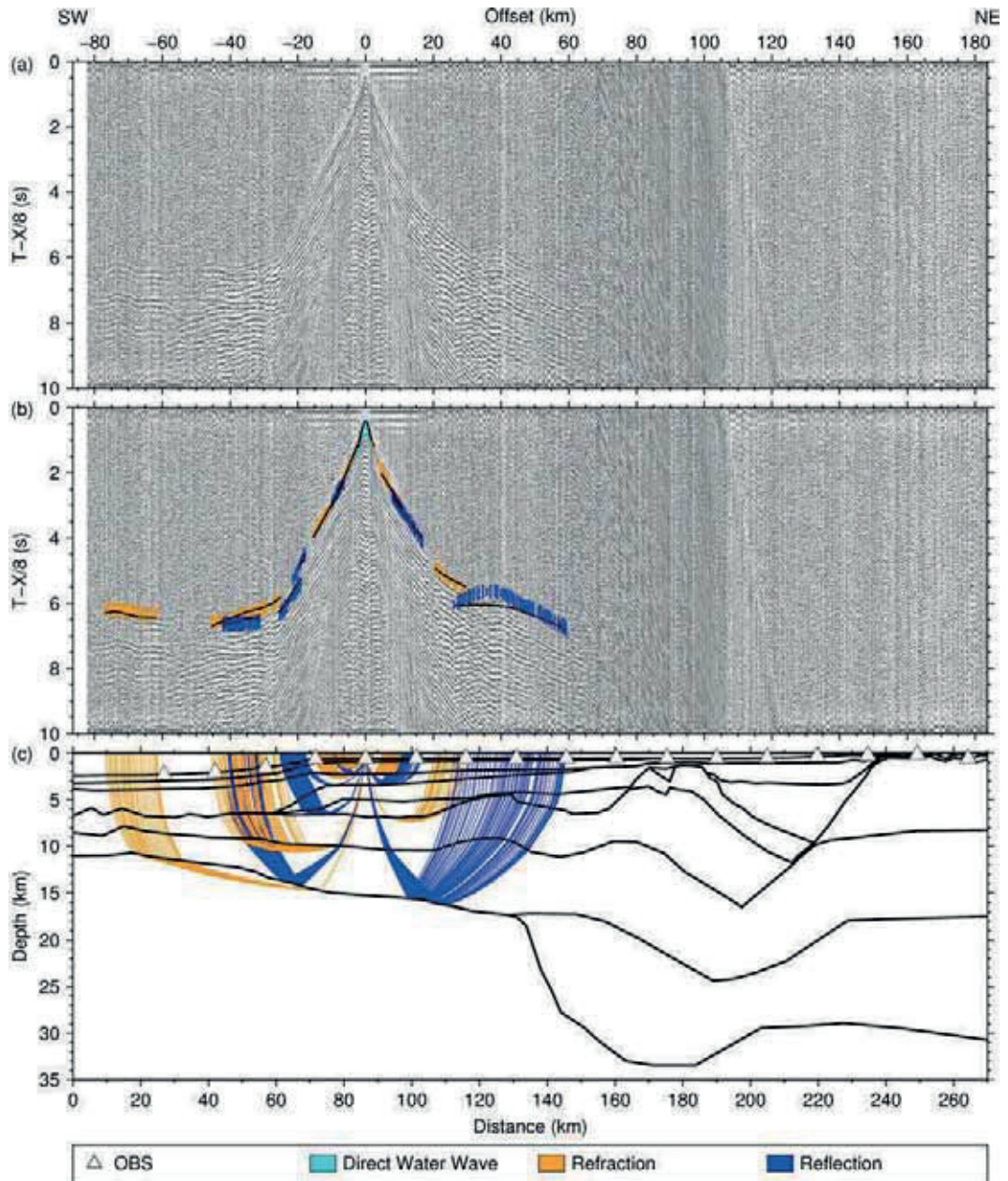


Figure C.5: Seismic section, picks and modeled raypaths of OBS 5 (AWI-20100450)

(a) Seismic section of the hydrophone component with a reduction velocity of 8 km/s.

(b) The colored lines mark the picked phases within the seismic section. The vertical lengths of the picks correspond to the assigned pick uncertainties. The black lines are the calculated travel times.

(c) The black lines are the boundaries between different velocity layers of the *P* wave velocity model. The colored lines mark the modeled raypaths of the corresponding picked phases shown in the panel above.

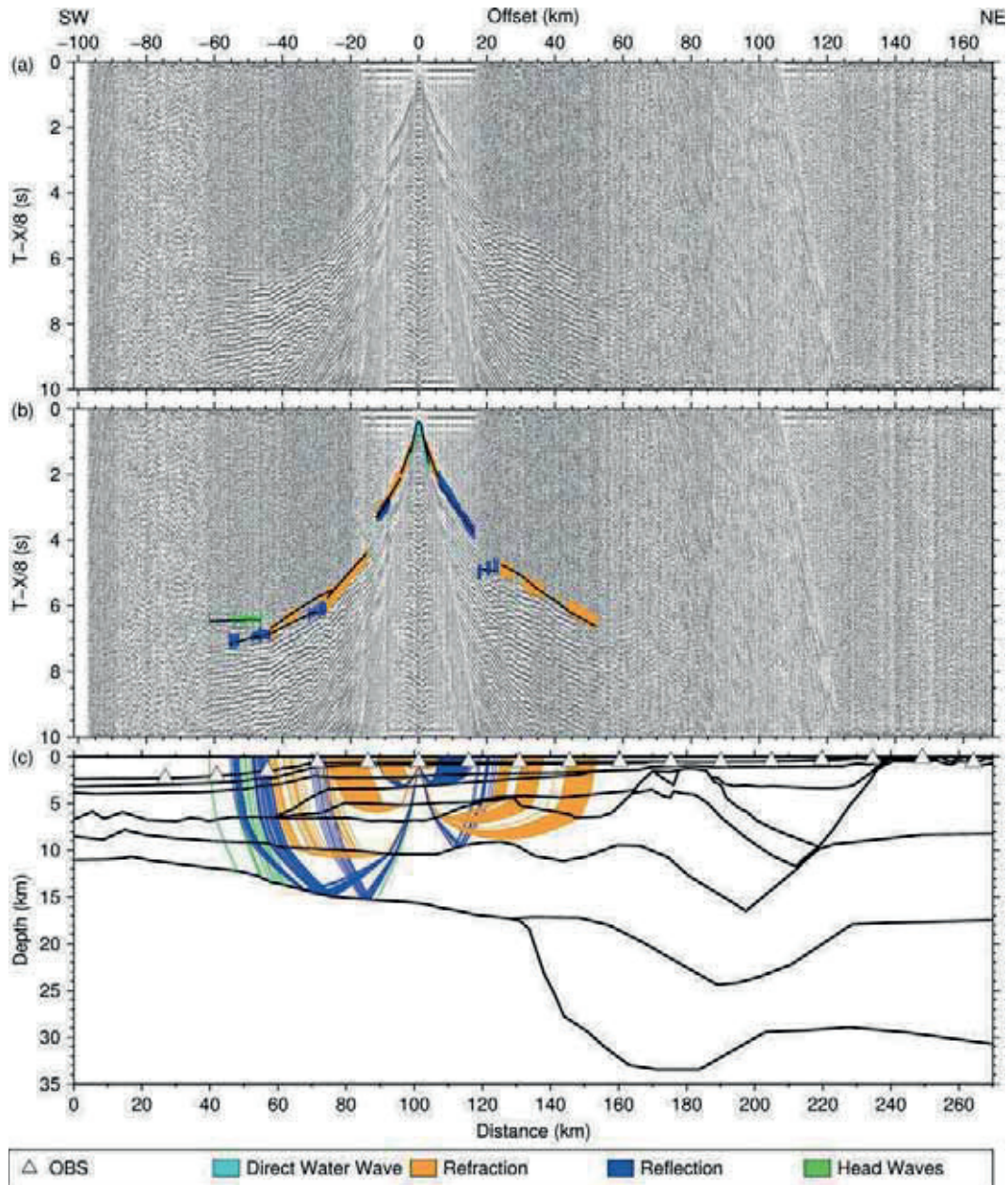


Figure C.6: Seismic section, picks and modeled raypaths of OBS 6 (AWI-20100450)

(a) Seismic section of the hydrophone component with a reduction velocity of 8 km/s.

(b) The colored lines mark the picked phases within the seismic section. The vertical lengths of the picks correspond to the assigned pick uncertainties. The black lines are the calculated travel times.

(c) The black lines are the boundaries between different velocity layers of the P wave velocity model. The colored lines mark the modeled raypaths of the corresponding picked phases shown in the panel above.

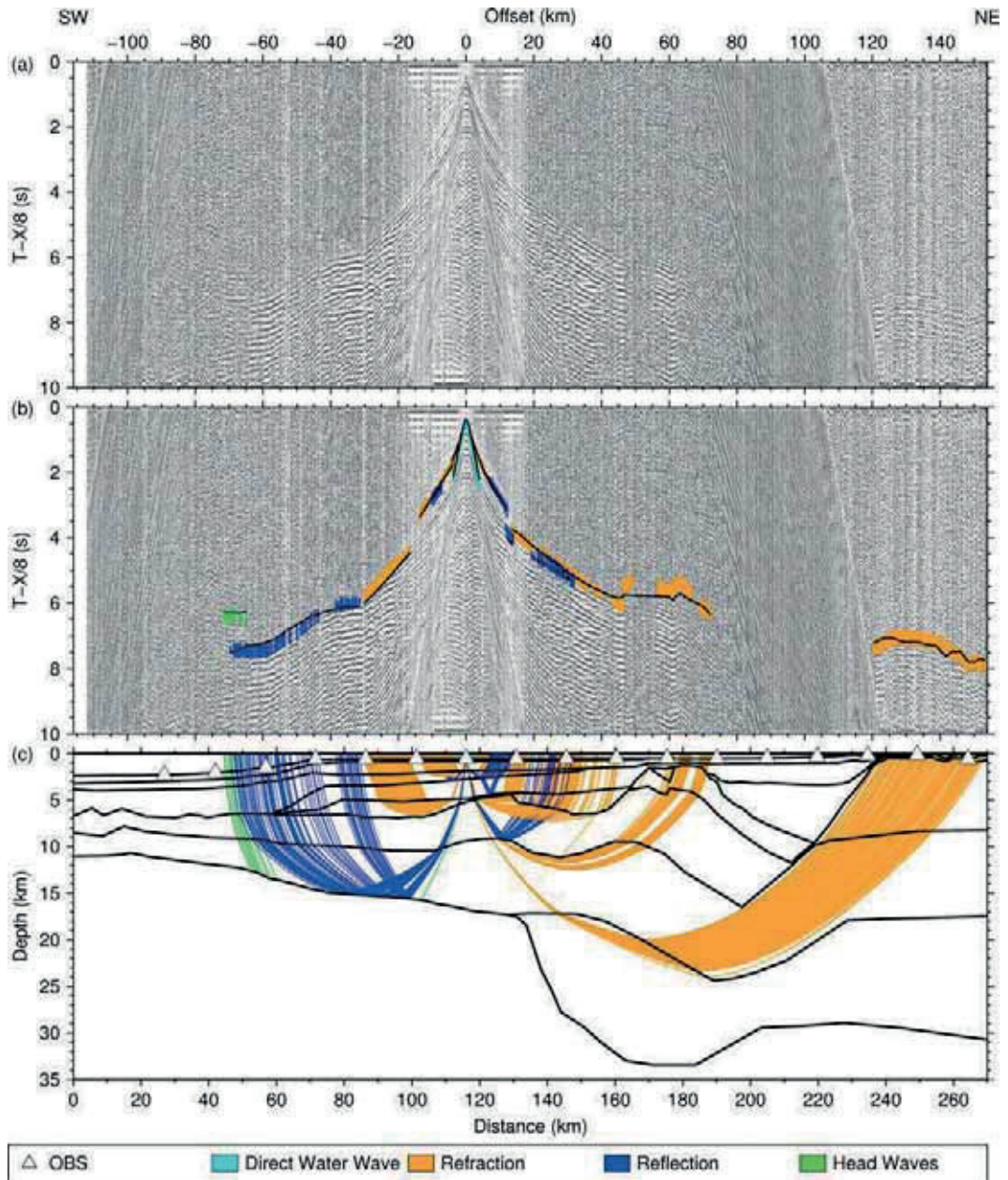


Figure C.7: Seismic section, picks and modeled raypaths of OBS 7 (AWI-20100450)

(a) Seismic section of the hydrophone component with a reduction velocity of 8 km/s.

(b) The colored lines mark the picked phases within the seismic section. The vertical lengths of the picks correspond to the assigned pick uncertainties. The black lines are the calculated travel times.

(c) The black lines are the boundaries between different velocity layers of the *P* wave velocity model. The colored lines mark the modeled raypaths of the corresponding picked phases shown in the panel above.

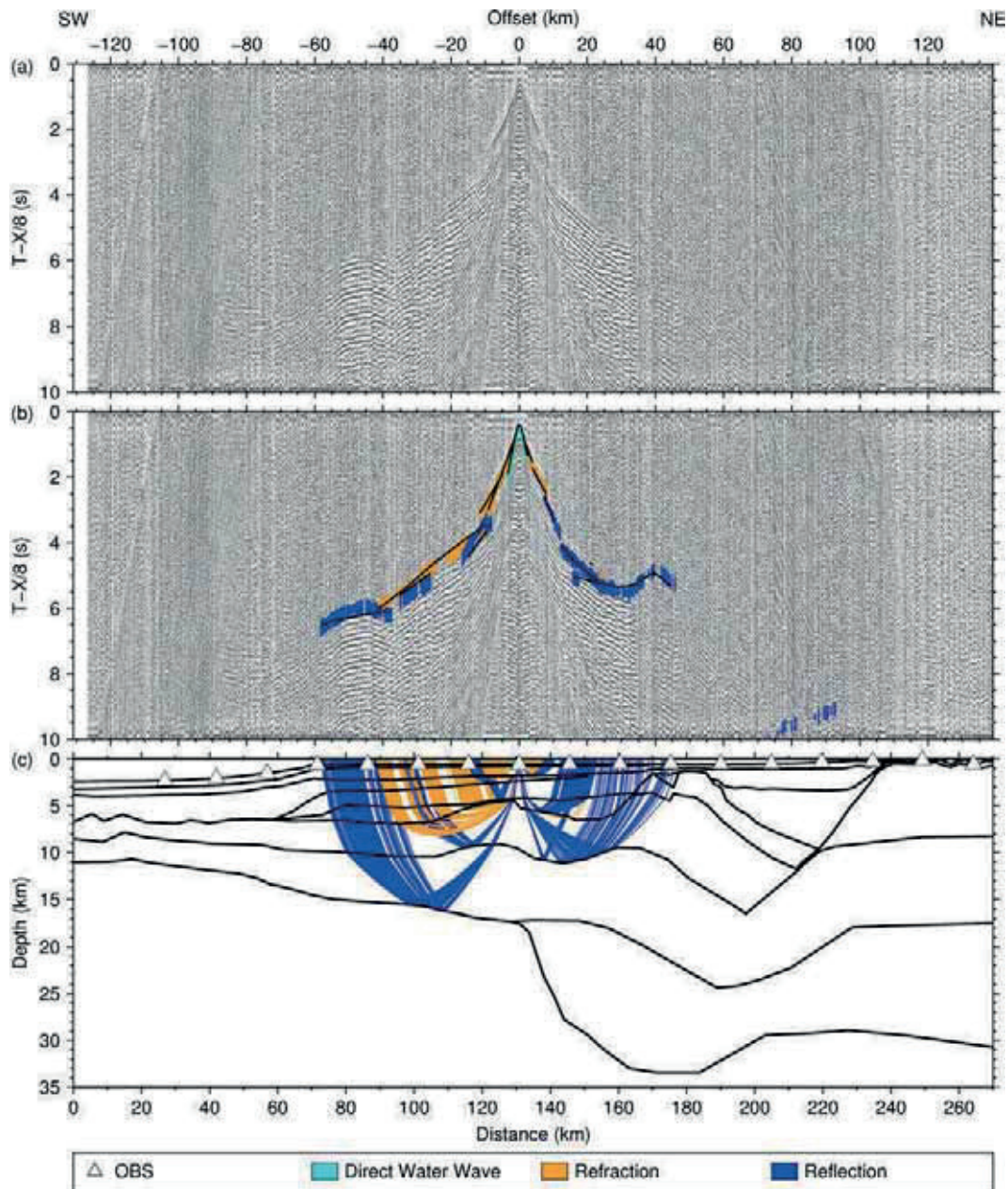


Figure C.8: Seismic section, picks and modeled raypaths of OBS 8 (AWI-20100450)

(a) Seismic section of the hydrophone component with a reduction velocity of 8 km/s.

(b) The colored lines mark the picked phases within the seismic section. The vertical lengths of the picks correspond to the assigned pick uncertainties. The black lines are the calculated travel times.

(c) The black lines are the boundaries between different velocity layers of the *P* wave velocity model. The colored lines mark the modeled raypaths of the corresponding picked phases shown in the panel above.

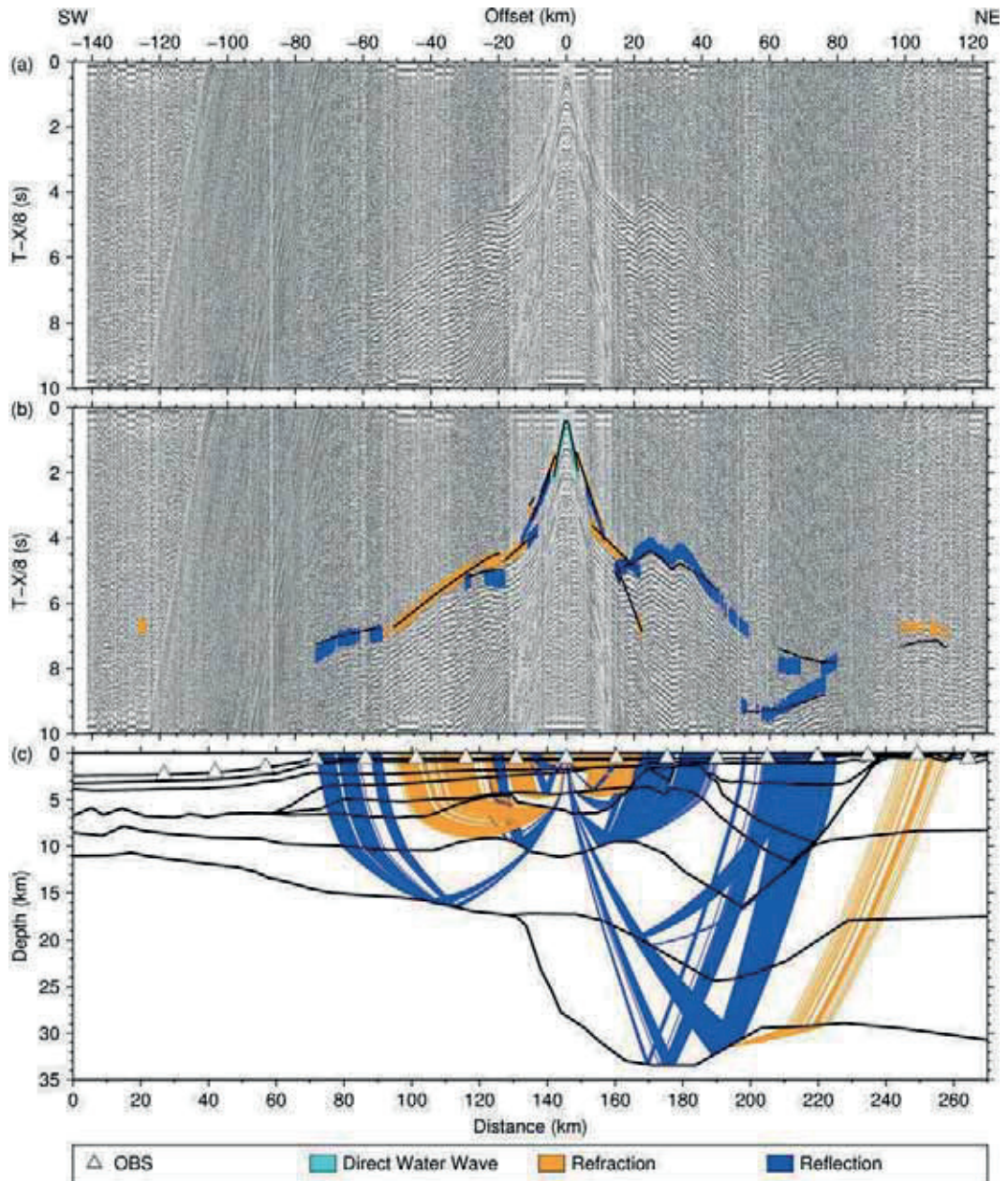


Figure C.9: Seismic section, picks and modeled raypaths of OBS 9 (AWI-20100450)

(a) Seismic section of the hydrophone component with a reduction velocity of 8 km/s.

(b) The colored lines mark the picked phases within the seismic section. The vertical lengths of the picks correspond to the assigned pick uncertainties. The black lines are the calculated travel times.

(c) The black lines are the boundaries between different velocity layers of the *P* wave velocity model. The colored lines mark the modeled raypaths of the corresponding picked phases shown in the panel above.

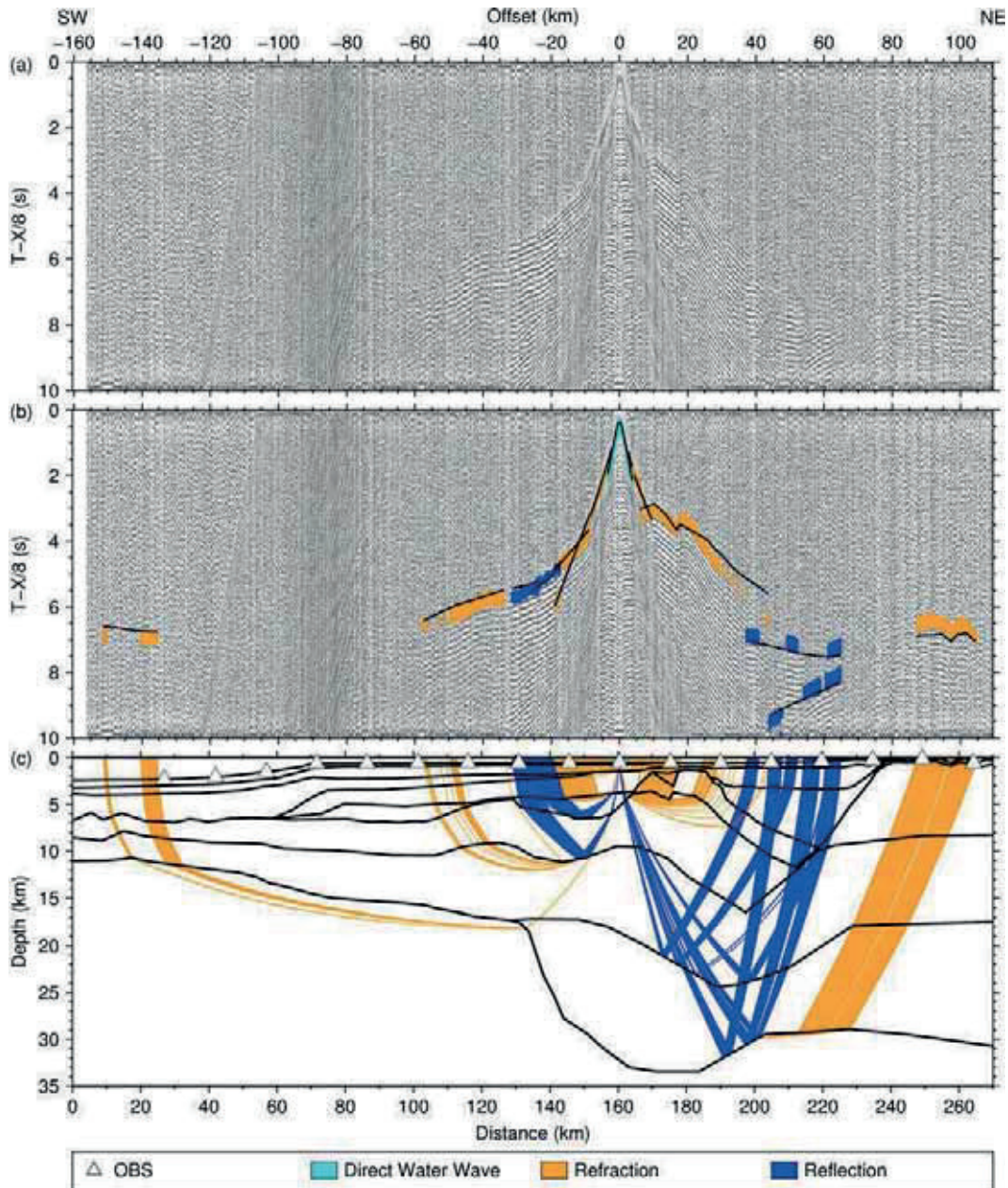


Figure C.10: Seismic section, picks and modeled raypaths of OBS 10 (AWI-20100450)
 (a) Seismic section of the hydrophone component with a reduction velocity of 8 km/s.
 (b) The colored lines mark the picked phases within the seismic section. The vertical lengths of the picks correspond to the assigned pick uncertainties. The black lines are the calculated travel times.
 (c) The black lines are the boundaries between different velocity layers of the *P* wave velocity model. The colored lines mark the modeled raypaths of the corresponding picked phases shown in the panel above.

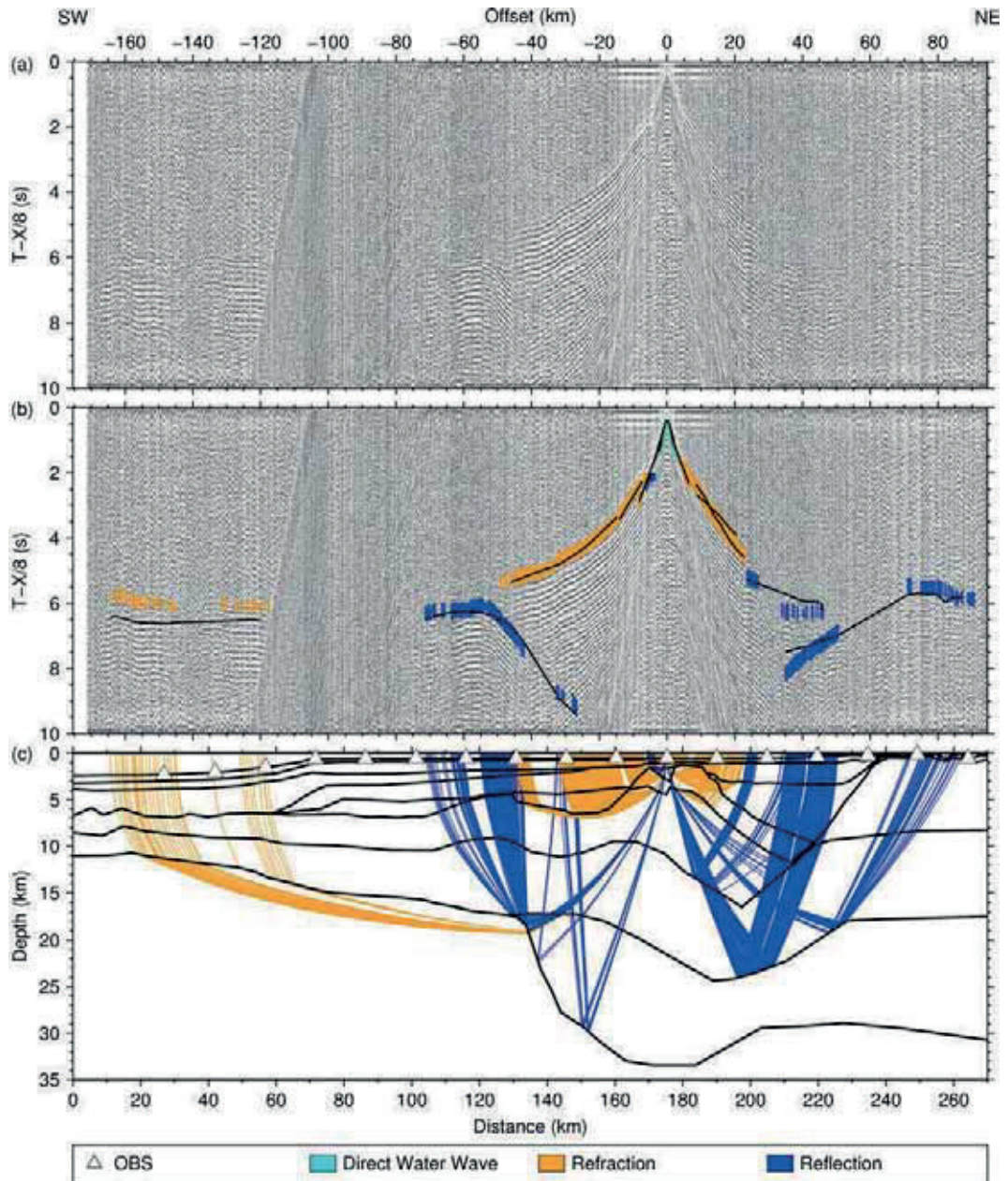


Figure C.11: Seismic section, picks and modeled raypaths of OBS 11 (AWI-20100450)

(a) Seismic section of the hydrophone component with a reduction velocity of 8 km/s.

(b) The colored lines mark the picked phases within the seismic section. The vertical lengths of the picks correspond to the assigned pick uncertainties. The black lines are the calculated travel times.

(c) The black lines are the boundaries between different velocity layers of the *P* wave velocity model. The colored lines mark the modeled raypaths of the corresponding picked phases shown in the panel above.

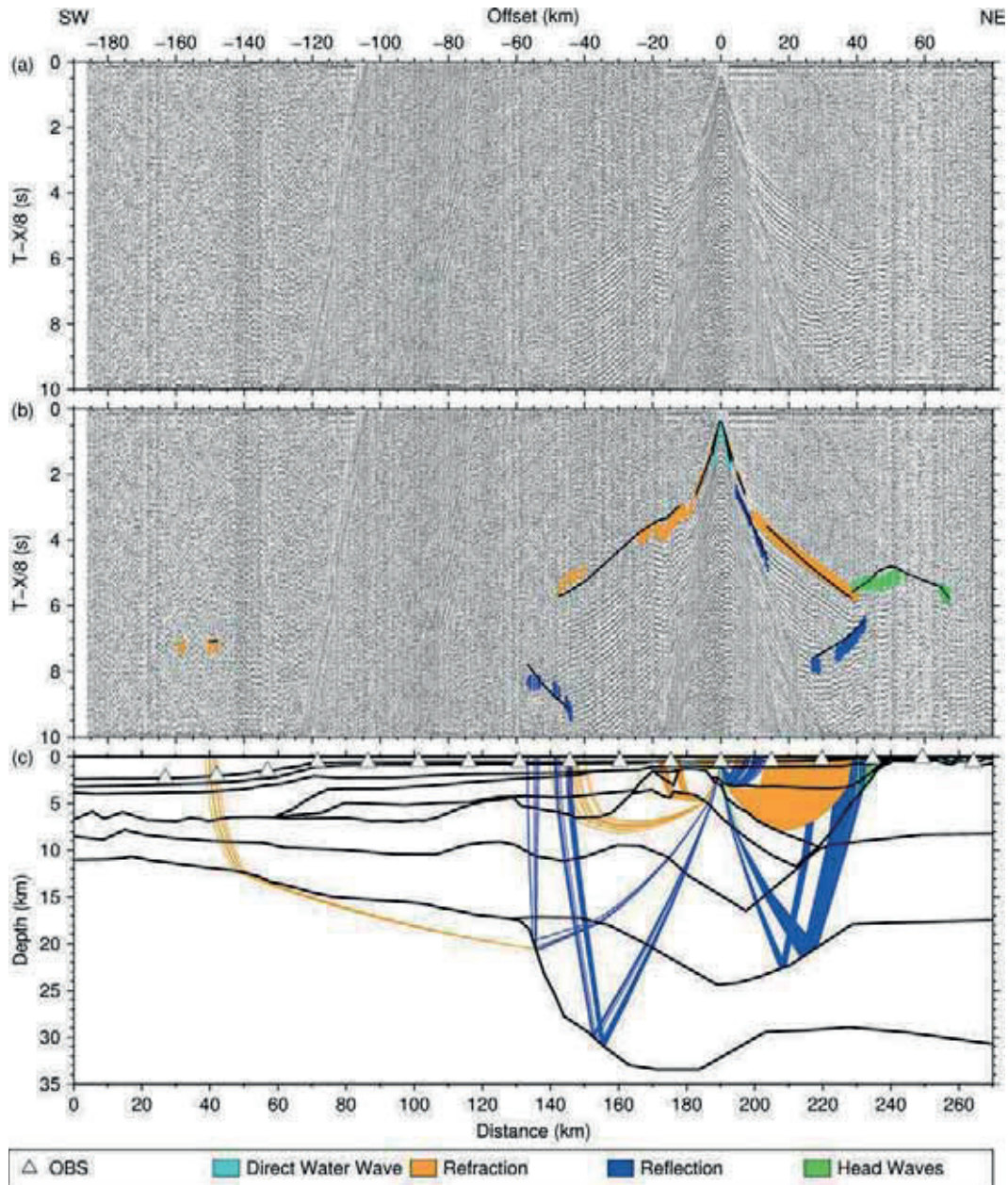


Figure C.12: Seismic section, picks and modeled raypaths of OBS 12 (AWI-20100450)
 (a) Seismic section of the hydrophone component with a reduction velocity of 8 km/s.
 (b) The colored lines mark the picked phases within the seismic section. The vertical lengths of the picks correspond to the assigned pick uncertainties. The black lines are the calculated travel times.
 (c) The black lines are the boundaries between different velocity layers of the *P* wave velocity model. The colored lines mark the modeled raypaths of the corresponding picked phases shown in the panel above.

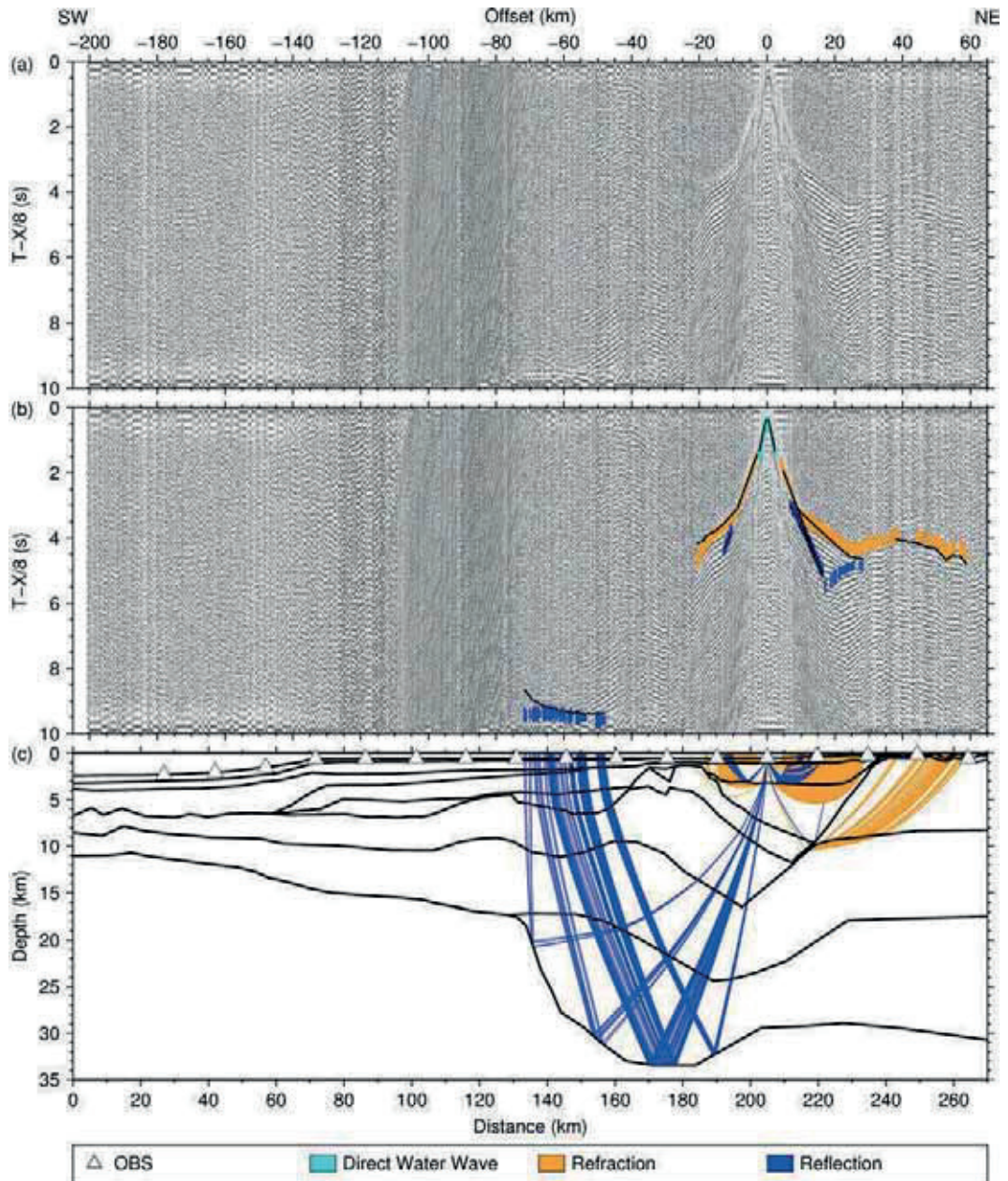


Figure C.13: Seismic section, picks and modeled raypaths of OBS 13 (AWI-20100450)

(a) Seismic section of the hydrophone component with a reduction velocity of 8 km/s.

(b) The colored lines mark the picked phases within the seismic section. The vertical lengths of the picks correspond to the assigned pick uncertainties. The black lines are the calculated travel times.

(c) The black lines are the boundaries between different velocity layers of the *P* wave velocity model. The colored lines mark the modeled raypaths of the corresponding picked phases shown in the panel above.

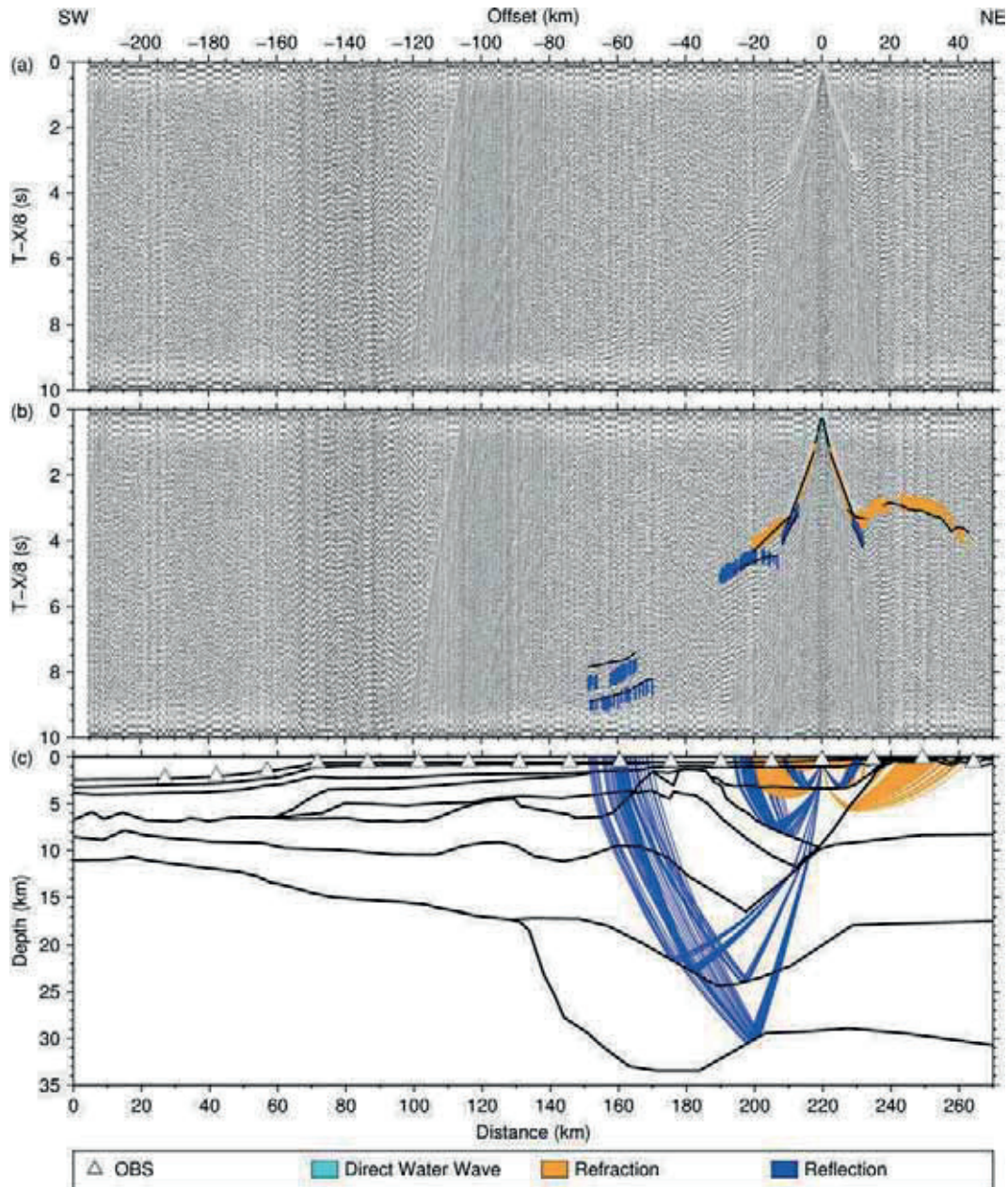


Figure C.14: Seismic section, picks and modeled raypaths of OBS 14 (AWI-20100450)
 (a) Seismic section of the hydrophone component with a reduction velocity of 8 km/s.
 (b) The colored lines mark the picked phases within the seismic section. The vertical lengths of the picks correspond to the assigned pick uncertainties. The black lines are the calculated travel times.
 (c) The black lines are the boundaries between different velocity layers of the *P* wave velocity model. The colored lines mark the modeled raypaths of the corresponding picked phases shown in the panel above.

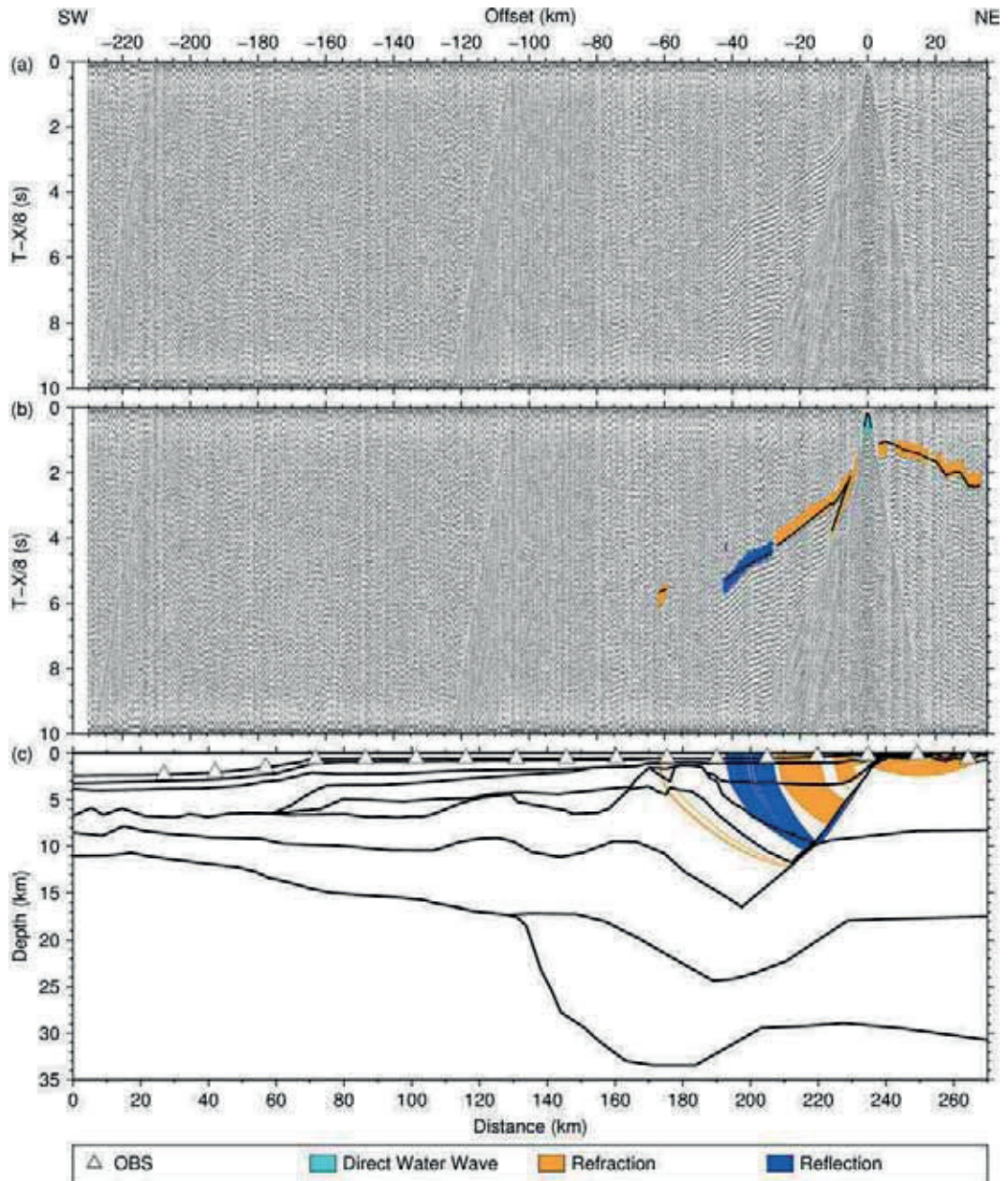


Figure C.15: Seismic section, picks and modeled raypaths of OBS 15 (AWI-20100450)

(a) Seismic section of the hydrophone component with a reduction velocity of 8 km/s.

(b) The colored lines mark the picked phases within the seismic section. The vertical lengths of the picks correspond to the assigned pick uncertainties. The black lines are the calculated travel times.

(c) The black lines are the boundaries between different velocity layers of the *P* wave velocity model. The colored lines mark the modeled raypaths of the corresponding picked phases shown in the panel above.

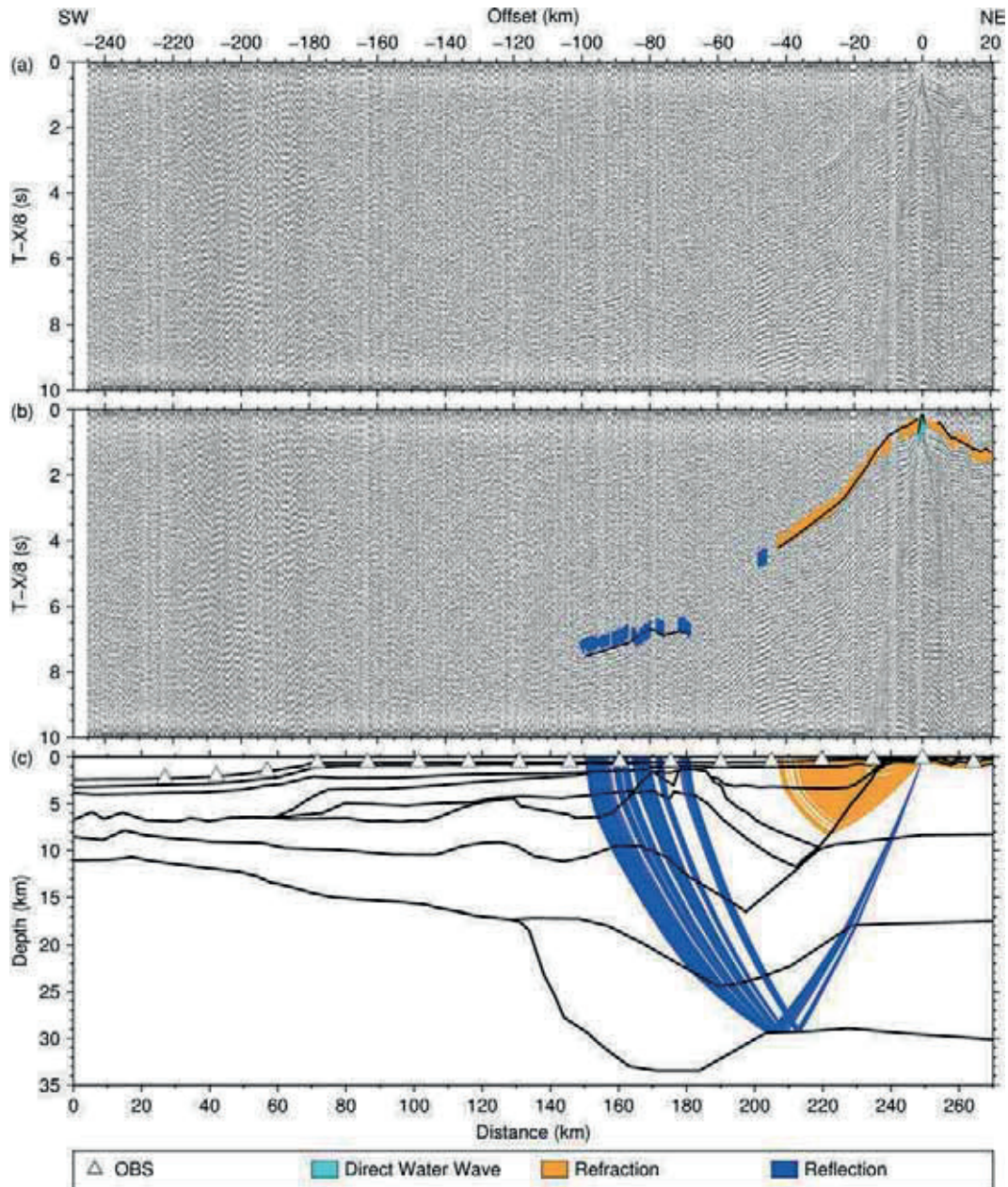


Figure C.16: Seismic section, picks and modeled raypaths of OBS 16 (AWI-20100450)
 (a) Seismic section of the hydrophone component with a reduction velocity of 8 km/s.
 (b) The colored lines mark the picked phases within the seismic section. The vertical lengths of the picks correspond to the assigned pick uncertainties. The black lines are the calculated travel times.
 (c) The black lines are the boundaries between different velocity layers of the *P* wave velocity model. The colored lines mark the modeled raypaths of the corresponding picked phases shown in the panel above.

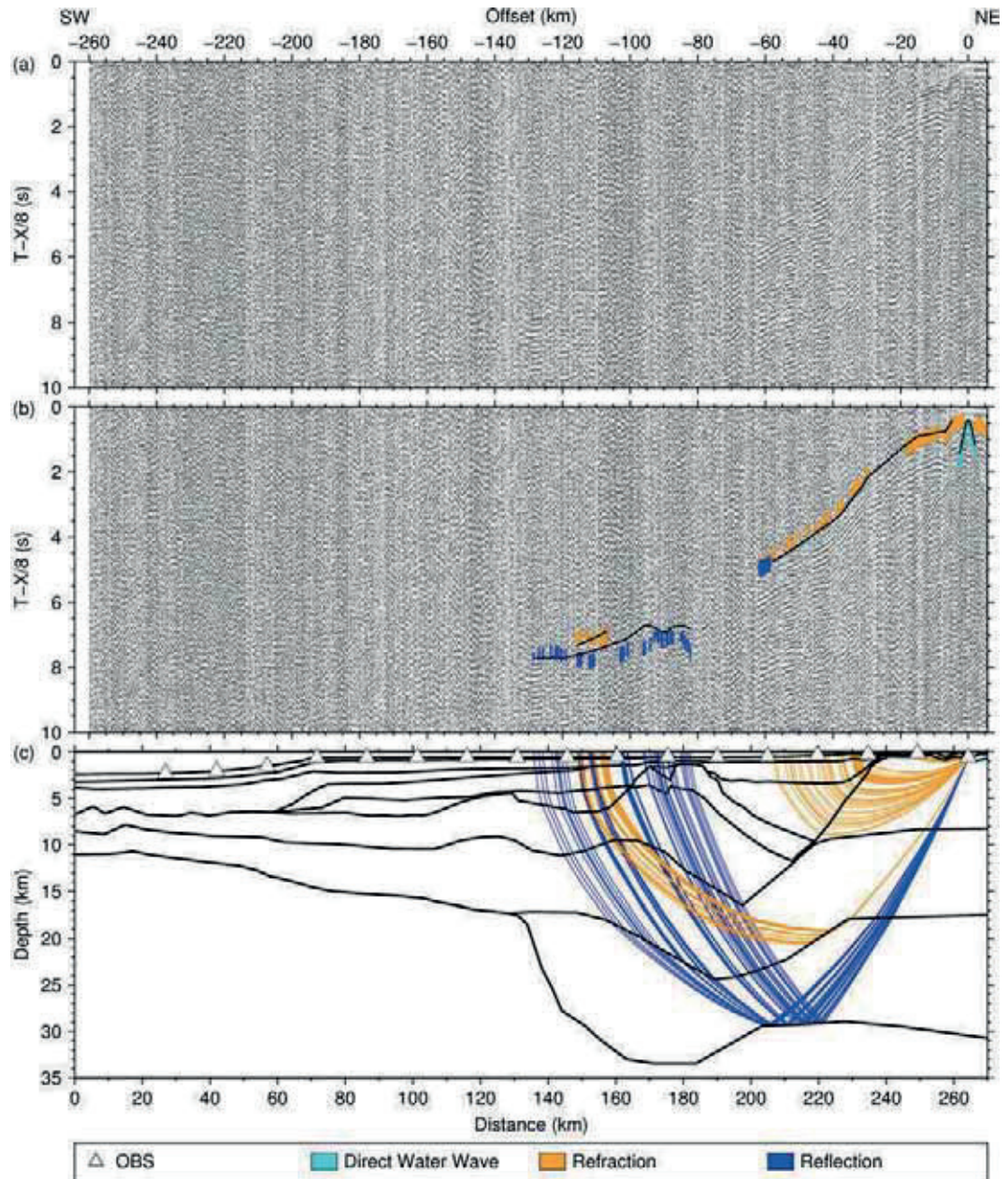


Figure C.17: Seismic section, picks and modeled raypaths of OBS 17 (AWI-20100450)

(a) Seismic section of the hydrophone component with a reduction velocity of 8 km/s.

(b) The colored lines mark the picked phases within the seismic section. The vertical lengths of the picks correspond to the assigned pick uncertainties. The black lines are the calculated travel times.

(c) The black lines are the boundaries between different velocity layers of the *P* wave velocity model. The colored lines mark the modeled raypaths of the corresponding picked phases shown in the panel above.

Danksagung

Ein herzliches Dankeschön geht an

- **Wilfried Jokat** für die Betreuung meiner Arbeit, die viele Diskussionen, seine Geduld, motivierende Worte und den ein oder anderen sanften Hintertritt. Ich hatte immer das Gefühl, in Deinem Büro willkommen zu sein.
- **Cornelia Spiegel** für die Begutachtung dieser Arbeit.
- **Volkmar Damm** und **Ingo Heyde** für ihre Unterstützung.
- die wunderbare **Geophysik-Truppe** des AWIs: Bestes Arbeitsklima und viele offene Türen machten mir das Arbeitsleben leicht.
- meinen zickigen Mac **Maggie**, die am Anfang schwer zu zähmen war und mich oft an den Rand der Verzweiflung gebracht hat. Unser Verhältnis hat sich am Ende recht entspannt. Wider Erwarten hat sie bis zum Ende durchgehalten und wurde nicht aus dem Fenster geworfen.
- **Tanja Fromm** und **Antje Schlömer** - Was wären die letzten Jahre ohne Euch , PRAY, den Garten, viel geteilte Schokolade, Abende am Kamin, weiße Hirsche, Marktbesuche und die gemeinsamen Urlaube gewesen? Ich will es gar nicht wissen!
- **Gabriele Uenzelmann-Neben** für ihre Freundschaft, Ratschläge und viele tolle Theaterbesuche.
- die wunderbaren "Bewohner" des Büros D-3170 **Katharina Hochmuth**, **Ricarda Pietsch** und **Michael Horn**. Ihr seid für jeden Quatsch zu haben und habt immer ein offenes Ohr!
- meine ehemalige Bürokollegen/in **Stefanie Kessling** und **Florian Wobbe**, die eine unglaubliche Toleranz für Wackelaugen haben.
- das "original" Baffin Bay Babe Nr. 1: **Sonja Suckro**, die mir in der Anfangszeit meiner Doktorarbeit viel erklärt und gezeigt hat. Ich hoffe, ich war eine würdige Nachfolgerin!
- meine OBS-Großmeister **Jürgen Gossler** und **Henning Kirk**, die mir viel über das Innenleben eines OBS beigebracht haben.
- **Claudia Schnabel** für unterstützende und aufmunternde Worte aus Hannover.
- die **Altenbernds** und **Brüggemanns** im fernen Billingshausen und Kachtenhausen, die in den letzten Jahren oft auf mich verzichten mußten und doch immer für mich da waren.
- meine Testleser.
- **Jörg Lang** für seine Unterstützung und all die Pendelei an den Wochenenden. Bist der Beste!

Curriculum Vitae

Personal details

Name: Tabea Altenbernd
Date of birth: 7. December 1983
Place of birth: Bielefeld, Germany
Nationality: German

Education and Employments

since Feb. 2015	Employee at Alfred Wegener Institute, Helmholtz Center for Polar and Marine Research (AWI) in Bremerhaven
June 2011 – Okt. 2014	Ph.D. at the Alfred Wegener Institute, Helmholtz Center for Polar and Marine Research (AWI) in Bremerhaven
July 2010 – May 2011	Geoscientist at the Federal Institute for Geosciences and Natural Resources (BGR), Hannover
Sept. 2003 – July 2010	Study of geosciences at the Leibniz-University in Hannover (grade 1.7)
1990-2003	School, graduation with Abitur (grade 2.5)

Research Expeditions

Apr. 2013 – May 2013	Cruise ANT-XXIX/5 from Falkland Islands to South Africa, RV Polarstern
Jan. 2012 – Mar. 2012	Cruise to the Prydz Bay, Antarctica, RV Akademik Aleksandr Karpinskiy
Aug. 2010 – Okt. 2010	Cruise ARK-XXV/3 to the Baffin Bay and Nares Strait, RV Polarstern

Scientific Publications as first author

Altenbernd, T., Jokat, W., Heyde, I. and Damm, V. (2014), A crustal model for northern Melville Bay, Baffin Bay; Journal of Geophysical Research, 119 (12), pp. 8610-8632, doi:10.1002/2014JB011559.

Altenbernd, T., Jokat W., Heyde, I. , and Damm, V., Insights in the crustal structure of the transition between Nares Strait and Baffin Bay, submitted to Tectonophysics in June 2015.

Altenbernd, T., Jokat W., Heyde, I., and Damm, V., The crustal fabric of the northeastern Baffin Bay, submitted to Journal of Geophysical Research in June 2015.

Conference Contributions as first author

Altenbernd, T., Jokat, W., Damm, V. , Heyde, I., Crustal models for the Melville Bay and Northern Baffin Bay, Talk, EGU General Assembly, Wien 2014

Altenbernd, T., Jokat, W., Heyde, I., The crustal structure of Melville Bay, Northern Baffin Bay, Talk, 3P Arctic, Stavanger 2013

Altenbernd, T., Jokat, W., Damm, V., New insights into the crustal structure of Northern Baffin Bay, Poster, EGU General Assembly, Wien 2013

Altenbernd, T., Berglar, K., Block, M., Damm, V., Schnabel, M., Ehrhardt, A., The architecture of the continent-ocean boundary in the northern Baffin Bay: New evidence based on MCS data, AAPG International Conference and Exhibition, Poster, Milan 2011

Altenbernd, T., Block, M., Damm, V., Ehrhardt, A., Schnabel, M., Geological Evolution of the Baffin Bay – new evidence for the existence of oceanic crust, Talk, 71. Jahrestagung der Deutschen Geophysikalischen Gesellschaft, Köln 2011

Bremerhaven, 1. July 2015
